UNIONE EUROPEA
Fondo Sociale Europeo

PON RICERCA E INNOVAZIONE REACT EU

UNIVERSITÀ DEGLI STUDI DI PALERMO

UNIVERSITÀ DEGLI STUDI DI PALERMO

PhD Course in Chemical, Environmental, Biomedical, Hydraulic and Materials Engineering
Dipartimento di Ingegneria
Scienza e Tecnologia dei Materiali (IMAT-01/A)

DEVELOPMENT OF BIO-POLYMERIC DEVICES FOR REMOVAL OF POLLUTANTS FROM AIR, WATER AND SOIL

PhD Candidate:
MARIA CLARA CITARRELLA

Phd Course Coordinator:
PROF. GIORGIO DOMENICO MARIA MICALE

Supervisors:
PROF. ROBERTO SCAFFARO

XXXVII CYCLE
GRADUATION YEAR 2025

Programma Operativo Nazionale Ricerca e Innovazione 2014-2020 (CCI2014IT16M2OP005), risorse FSE REACT-EU, Azione IV.4 "Dottorati e contratti di ricerca su tematiche dell'innovazione" e Azione IV.5 "Dottorati su tematiche Green"

Acknowledgements

Pursuing a PhD has been an intense and rewarding journey, filled with moments of great satisfaction as well as challenges that have helped me grow, both personally and professionally. This work would not have been possible without the guidance, support, and encouragement of several people, to whom I am deeply grateful.

I would like to express my sincere gratitude to Professor Roberto Scaffaro, my supervisor, for giving me the opportunity to develop this research and for his guidance throughout this journey.

A special thanks goes to Professor Emmanuel Fortunato Gulino, not only for his scientific support but also for his invaluable friendship and encouragement. From the very beginning, he taught me how to conduct experiments and handle laboratory work, patiently guiding me through every step of the process. His unwavering support, both in research and in the everyday moments, has been fundamental not only in overcoming obstacles but also in making this journey enjoyable. Sharing both challenges and moments of joy with him made the long hours in the lab more rewarding, and I could not have asked for a better colleague and friend.

I am also sincerely grateful to Professor Giada Lo Re from Chalmers University of Technology for her insightful collaboration and for enriching this research with her knowledge and expertise. My appreciation extends to Ecodep Srl for their valuable collaboration and for providing the FOG samples, which were essential for part of this study.

Finally, my deepest gratitude goes to my parents, my sister, and my husband, who have supported and stood by me throughout these years. Their patience, encouragement, and unwavering belief in me have been a source of strength, helping me navigate both the triumphs and the challenges of this journey.

Abstract

Environmental pollution, including air, water, and soil contamination, represents a critical challenge to public health and ecological balance. This thesis investigates the development of bio-polymeric devices for pollutant removal across these three environmental media, employing biodegradable polymers such as PLA and Mater-Bi®, enriched with vegetal and animal waste fillers. Through advanced fabrication techniques, including electrospinning, solution blow spinning, and 3D printing, bio-composite membranes and 3D devices were engineered to remove specific pollutants. Air pollution was addressed by developing fibrous composites membranes, enriched with vegetal or animal derived fillers, for particulate matter filtration, achieving high efficiency. For water remediation, porous membranes and 3D fibrous structures demonstrated the capability to adsorb dyes, oils, and greases, offering sustainable solutions for wastewater treatment. Soil pollution was mitigated through green composites designed to absorb heavy metals while promoting soil fertility via controlled fertilizer release. Comprehensive material characterization, pollutant removal performance evaluation, and reusability tests underscored the effectiveness of these bio-composites. This research not only contributes to sustainable environmental remediation but also exemplifies the integration of biodegradable materials and biomass into advanced engineering applications, aligning with circular economy principles.

TABLE OF CONTENTS

Introduction

3.1 Environmental Contamination

Air, water, and soil are the fundamental sources of life, sustaining all living beings on Earth and forming the essential element upon which ecosystems and civilizations thrive. For this reason, environmental pollution has become one of the most pressing global concerns of the 21st century, threatening the balance of natural systems and the well-being of all species. As industrialization and urbanization continually expand, the impact of pollutants on air, water, and soil grows more severe. Environmental contamination and pollution arise when toxic substances and pollutants are introduced into the air, water and soil leading to serious harm to ecosystems and posing risks to human health.

Air

The subsequent text and images have been fully extracted from the published article authored by the candidate "R. Scaffaro, M. C. Citarrella, Nanofibrous Polymeric Membranes for Air Filtration Application: A Review of Progress after the COVID-19 Pandemic. Macromol. Mater. Eng. 2023, 308, 2300072. https://doi.org/10.1002/mame.202300072" [1] and are reproduced here with the necessary permissions.

Air pollution is currently one of the major global problem. The World Health Organization (WHO) estimated that around seven million people per year die because of different medical diseases

caused by air pollution [2], including the increase of the incidence of cardiovascular and respiratory diseases and some types of cancer [3–5]. Moreover, recently, several studies confirmed a connection between infectious diseases transmission, including COVID-19, and air pollution [6–11]. According to these studies, COVID-19 consequences on human health were more severe in areas in which the presence of high levels of particulate matter (PM) was recorded [8,12–15].

Air pollution can be described as a mixture of solid particles, gases and biological pollutants such as bacteria and viruses [16,17]. In general, air pollutants are mainly derived from fossil fuels combustion processes, vehicles emission, power generation, agriculture or waste incineration [2]. Among gases, volatile organic compounds (VOCs), carbon dioxide (CO_2), carbon monoxide (CO), oxides of nitrogen (NO_x), are some of the most dangerous pollutant for human health [4]. The solid particles, instead, are mainly composed by sulfates, nitrates, sodium chloride, ammonia, black carbon, mineral dust, and water [18]. These particles are commonly labelled as particulate matter (PM) and classified according to their size: PM_{10} identifies particles with a diameter under 10 μm, $PM_{2.5}$ ones under 2.5 μm, while particles with a diameter under 0.1 μm ($PM_{0.1}$) are considered ultrafine particles (UFPs). Their hazardousness for human health, is strongly related to their dimensions. In fact, while PM_{10} are partially blocked by nasal cavities [2], long-term exposure to $PM_{2.5}$ and ultrafine dust particles provokes more adverse effects on human health causing serious respiratory diseases due to their rapid deposition in human lungs [3,4]. Therefore, the production of air filtration devices characterized by high filtration efficiency and ultrafine PM removal ability, has gained significant attention among researchers worldwide, especially after COVID-19 pandemic. In Figure 1.1 it is reported the number of published papers present in Scopus database over the years using “air filtration” as keyword. As it is possible to notice from the graph, the interest of the scientific community has progressively increased over the years especially after pandemic period.

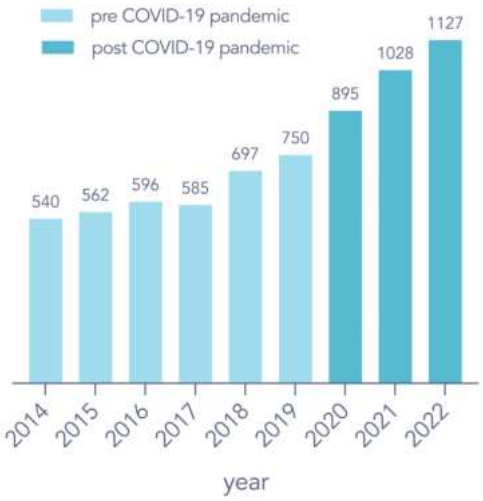

Figure 1.1 *Number of documents find in Scopus database over the years using "air filtration" as keyword.*

Based on these data, the published paper after COVID-19 pandemic (2020-2023) were analyzed using VOSViewer software and results are reported in Figure 1.2.

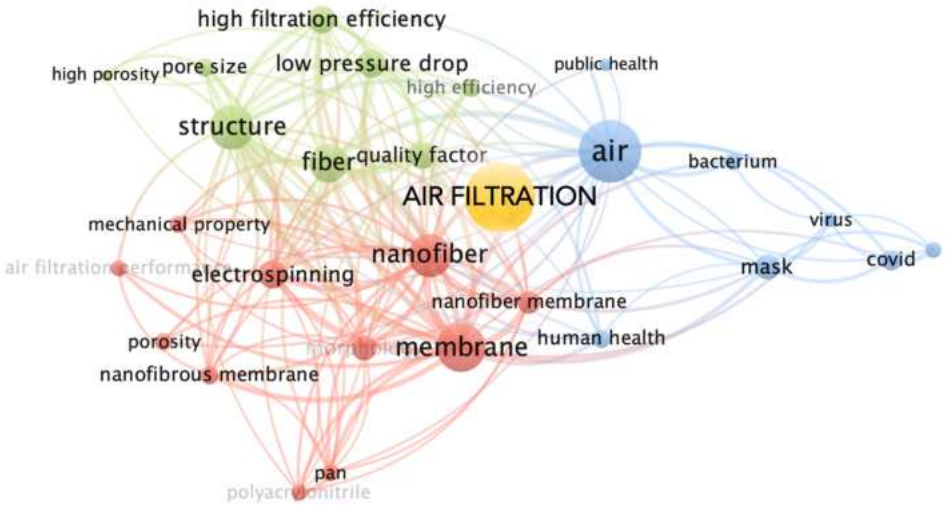

Figure 1.2 *VOSViewer map obtained by analyzing data extracted from papers present in Scopus database from 2020 to 2023 using "air filtration" as keyword. Terms have been extracted by papers titles and abstract using a binary counting. Only terms with a minimum of 10 occurrence and 60% of relevance score were taken into account.*

Outcomes reviled that three clusters could be identify. The blue cluster include all terms related to human health and COVID pandemic, confirming the importance of the development of

efficient air filtration device in order to reduce the incidence of disease connected to air pollution. The green cluster include all those goals that need to be archived in air filtrations i.e. high filtration efficiency and low pressure drop. Moreover, this cluster highlight the important role of the device "structure" in reaching these goals. The analysis of the data also suggest that mats composed by "fibers" could succeed in it. The red cluster unquestionably highlights the predominance of porous nanofibrous membranes obtained by electrospinning among all the devices recently proposed for air filtration applications. Moreover, could be noted that polyacrylonitrile (PAN) is one of the most used polymers for the production of air filtration devices.

Water

Water is one of the most vital components for living organisms and for this reason its pollution remains one of the most pressing environmental challenges of the modern world, posing severe risks to both ecological systems and human health. Defined as the contamination of water - such as rivers, lakes, oceans, and groundwater - by harmful substances, water pollution disrupts the delicate balance of aquatic ecosystems and diminishes water quality for human consumption, agriculture, and recreation.

A wide range of pollutants contribute to water pollution, including industrial, agricultural and kitchen wastewater or untreated sewage. Industrial activities often release heavy metals ions, toxic chemicals, and harmful organic compounds directly into nearby water sources, compromises the availability of clean water for human populations. Additionally, agricultural wastewater carries excessive amounts of fertilizers, pesticides and animal waste, leading to nutrient pollution that promote eutrophication, causing marine ecosystems collapse.

Water pollution caused by fats, oils, and greases (FOG) is a growing concern, especially in urban areas and regions with significant food production and processing activities. FOG, typically produced by kitchens, restaurants, and food industries, enters the wastewater system through improper disposal of cooking oils, dairy products, and other food residues. Once in the water systems, FOG solidifies and creates blockages in sewage pipes, leading to overflow and contamination of natural water bodies. Additionally, FOG can form a floating layer on the surface of water, disrupting the exchange of oxygen and leading to anaerobic conditions that harm aquatic life. In terms of environmental impact, FOG pollutants present a unique challenge as they do not dissolve easily in water, making their removal from polluted water systems particularly difficult. The accumulation of fats, oils, and greases can also promote the growth of harmful bacteria and contribute to the development of rancid, oxygen-depleted zones in water bodies. Conventional methods for removing FOG often involve costly and difficult processes, highlighting the need for more efficient and sustainable solutions.

Soil

Soil pollution is also a growing environmental concern, arising from the accumulation of harmful substances such as heavy metals, pesticides, hydrocarbons, and industrial chemicals in the soil. These pollutants not only degrade the quality of the soil, but they also disrupt natural ecosystems and pose significant risks to both human health and biodiversity. Contaminants can enter the soil through various sources, including agricultural and industrial wastewater, and improper disposal of hazardous substances. Heavy metals, for instance, can accumulate over time and become persistent environmental pollutants due to their inability to degrade, ultimately entering the food chain and causing long-term ecological damage. Pesticides, frequently based on heavy metals such as Copper (Cu) ions, can also accumulate into the soil, negatively impacting soil microorganisms and

contributing to the loss of soil fertility. Moreover, soil pollution can lead to the contamination of groundwater, affect food security and reduce agricultural productivity, posing additional risks to human populations dependent on these sources for eating, drinking and irrigation. Given the multifaceted impact of soil pollution, the development of effective, sustainable technologies to remediate polluted soils is of fundamental importance.

3.2 Biodegradable Polymers in Environmental Remediation

In recent years, the development of eco-friendly materials has emerged as a key strategy in environmental remediation applications. Among these, biodegradable polymers stand out due to their potential to provide effective, non-toxic, and sustainable solutions. Traditional remediation technologies, such as chemical treatments and synthetic filtration membranes, often suffer from drawbacks such as non-degradability, secondary pollution, microplastic generation and high operational costs. In contrast, biodegradable polymers, derived from renewable resources, offer the promise of reducing pollution while minimizing environmental impact [19].

Biodegradable polymers, such as polylactic acid (PLA) and Mater-Bi® (MB), have gained considerable attention in the fields of materials science and environmental engineering. PLA can also derive from renewable resources like corn starch and sugarcane, while Mater-Bi is a blend of biodegradable polyesters which composition is proprietary. Both materials decompose naturally, avoiding the accumulation of plastic waste in the environment [20]. These properties make them suitable candidates for creating bio-composite membranes or 3D devices designed to capture and remove pollutants from various environmental media.

3.3 Vegetal and animal waste as functional fillers

By incorporating waste materials from vegetable and animal sources - such as weeds, agricultural residues, animal or food waste - into biodegradable polymers, it is possible to enhance the mechanical and/or the functional properties of these composites. The combination of bio-polymers with organic waste results in the formation of bio-composites that can remove specific pollutants while maintaining sustainability. These bio-composite materials not only reduce environmental secondary pollution but also contribute to the circular economy by upcycling waste materials [19].

3.4 Innovative production techniques for biopolymeric devices

3.4.1 Electrospinning

Electrospinning (ES) is one the most frequently reported technique to prepare nanofibrous mats and its set-up is shown in Figure 1.3.

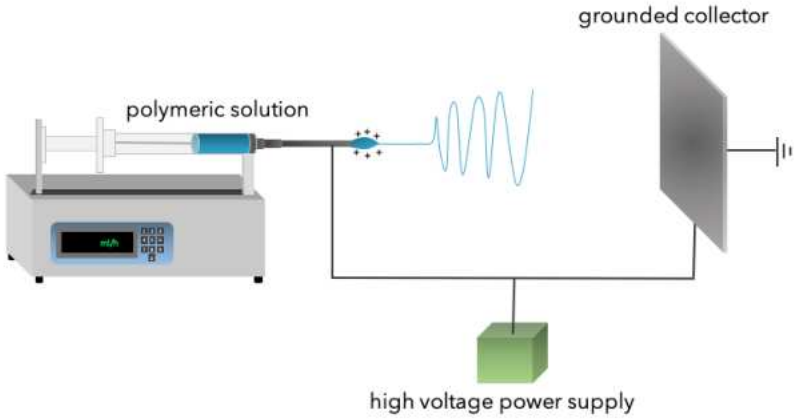

Figure 1.3 *Schematic representation of electrospinning set-up.*

The ES setup primarily consists of a collector, a spinneret, a high-voltage power supply, and a syringe pump. The polymer solution is placed in the syringe pump, which is equipped with a needle tip (the spinneret), and the solution becomes electrically charged due to the applied high voltage. When the voltage overcome the surface tension of the solution, a Taylor cone forms, allowing polymer fibers to deposit on the grounded metal collector [21].

The spinneret can be composed by a single needle or by two concentric needles connected separate syringe pumps. In this latter case the technique is referred to as coaxial electrospinning, which is used to fabricate nanofibers with core–shell structure. Additionally, by appropriately choosing the polymeric solutions, it is possible to obtain nanofiber with innovative structures, including hollow fibers.

The traditional solid collector can be replaced with a liquid one, enabling the production of three-dimensional fibrous structures. This approach can also help functionalize or crosslink nanofibers or allow hollow fibers to be formed by removing the core material.

3.4.2 Solution blow spinning

Solution blow spinning (SBS) is an emerging technique for producing polymer fibers, offering a simple and cost-efficient setup, as illustrated in Figure 1.4. In SBS, pressurized air is utilized to stretch the polymer solution and disperse the solvent, resulting in the formation of fibers. Unlike electrospinning, SBS does not require high-voltage power, making it a safer option for operators and more environmentally friendly. Additionally, it allows for the processing of polymer solutions with low conductivity, expanding its range of applications [22].

Similar to electrospinning, the solid collector in SBS can be replaced by a liquid one to achieve the same objectives discussed earlier for electrospinning.

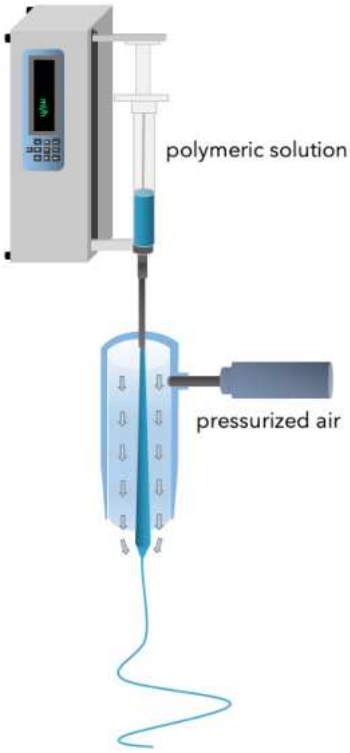

Figure 1.4 *Schematic representation of solution blow spinning set-up.*

3.4.3 3D-printing

3D printing, also known as additive manufacturing technique, is a transformative technology that constructs objects layer by layer from digital models. The core structure of a 3D printer consists of a framework supporting the movement of a extrusion system connected to a nozzle, which deposits material on a heated plate, according to pre-programmed instructions from a computer-aided design (CAD) file. The type of 3D printing technology employed in this thesis was Fused Deposition Modeling (FDM) [23].

The use of biopolymers has gained significant attention in 3D printing due to their biodegradability and reduced environmental impact. These sustainable materials enable the production of environmentally friendly devices that can be utilized in applications such as pollutant filtration, medical implants, and packaging solutions. 3D printing's integration with biopolymers offers immense potential for customized, low-waste manufacturing. The capacity to print complex

geometries with biodegradable materials has spurred innovation in the creation of specialized devices for environmental remediation, including filters and absorbent structures that remove contaminants from air, water, and soil. This approach aligns with sustainable engineering practices, promoting a circular economy through the use of renewable resources and the reduction of plastic waste [24].

3.5 Aim of the Thesis

The aim of this thesis is to investigate and develop bio-polymeric devices for the removal of pollutants from air, water, and soil. Specifically, biodegradable polymers such as PLA and Mater-Bi®, also mixed with vegetal or animal waste, will be used to fabricate bio-composite membranes and 3D devices capable of capturing a range of contaminants. The focus is on evaluating the removal efficiency of these materials in different environmental media: air, water, and soil.

This research is divided into three main sections, each corresponding to the remediation of pollutants in air, water, and soil. The study begins with air pollution, where bio-composite membranes will be evaluated for their ability to remove particulate matter. The next section focuses on water pollution, exploring how bio-polymeric membranes and 3D fibrous structures can filter and adsorb dye and oil-based contaminants. Finally, the thesis will address soil remediation by investigating how bio-composites devices can capture and stabilize heavy metals within the soil, while fertilized the crops.

By addressing pollution in these three environmental compartments, this research contributes to the broader goal of developing sustainable materials for environmental remediation, while demonstrating the potential of biodegradable polymers as a viable alternative to conventional technologies.

Chapter 2

Literature review

The growing concern over environmental pollution has led to an increase in the researches focused on the development of materials and technologies to mitigate the harmful effects of pollutants on air, water, and soil. Environmental contamination has reached alarming levels due to industrialization, urbanization, and the overuse of chemical substances in agriculture, which has compromised the quality of natural resources essential for life. In response, scientists have explored various approaches to address these challenges, with particular attention to materials that can efficiently remove pollutants from the environment. The use of advanced polymeric materials and nanotechnologies has gained significant traction as they offer promising solutions for the detection, capture, and degradation of a wide array of contaminants. This chapter provides an in-depth review of the existing literature concerning the state-of-the-art technologies for air, water, and soil remediation, highlighting recent advancements, challenges, and emerging trends in environmental pollution management. By evaluating the effectiveness of these approaches, it was possible to identify gaps in the current research and propose new directions for the development of more sustainable and efficient materials and technologies.

4.1 Air

The subsequent text and images have been fully extracted from the published article authored by the candidate "R. Scaffaro, M. C. Citarrella, Nanofibrous Polymeric Membranes for Air Filtration Application: A Review of Progress after the COVID-19 Pandemic. Macromol. Mater. Eng. 2023, 308, 2300072. https://doi.org/10.1002/mame.202300072" [1] and are reproduced here with the necessary permissions.

4.1.1 Mechanism and key parameter of nanofibers filtration

Air filtration theory has been developed for a long time, therefore the investigations in this area are mature enough to be linked to industrial and technological developments. Before going deep into the discussion of recent progresses in nanofibrous polymeric membranes for air pollutant capturing, it is useful to briefly report filtration theory and its mechanism. According to the theory, air filtration process can be divided into two states: the steady-state and unsteady-state. In the steady-state, filtration efficiency and pressure drop are constant over the time only depending on the air filter media, particle nature and dimension and airflow velocity. On the contrary, in the unsteady-state filtration efficiency and pressure drop change over time due to particles accumulation on the filter. About this latter, there is still a lack in theoretical description because of its complexity [25]. Air filtration of nanofibrous polymeric membranes is usually considered as a steady-state process. In fact, when the concentration of PM in air is moderate, particles accumulation on the filter is minimal and does not leads to any variation in membranes thickness [26]. A schematic representation of the structure of a nanofibrous membrane and its PM filtering process is reported in Figure 2.1.

The filtration theory affirms that in nanofibrous membranes particles trapping can occur following different type of mechanism: interception, inertial impaction, sieving, Brownian diffusion and electrostatic effect [27,28].

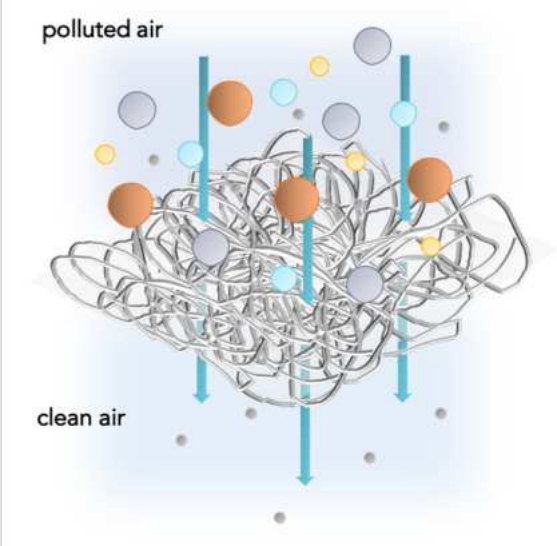

Figure 2.1 *Graphical depiction of a typical nanofibrous membrane for air filtration application. Colored spheres represent PM of different dimensions.*

Typically, particles tend to follow air streamlines and do not deviate from them unless there is another external force that force them. Particles interception occurs when they get in contact with the surface of nanofibers due to the effect of van der Waals force as shown in Figure 2.2a [29,30]. Interception is recognized as primary filtration mechanism, is not affected by air flowrate and it is efficient for capturing particles with size ranged from 0.5 to 1 μm [31,32].

UFPs, being usually smaller than the pore of the filtering mat, follow air streamlines across the nanofibrous membranes. In filtration, air streamlines are commonly tortuous due to the random orientation of the nanofibers that created extremely complex arrangement of them in the membrane. However, due to inertia force, particles can deviate from air streamlines and impact on nanofibers surface leading to an effective filtration for inertial impaction as illustrated in Figure 2.2b [33]. The efficiency of filtration for inertial impaction increases on increasing the air velocity and the particle size. This filtration mechanism, in fact, is more efficient in the capture of particles larger than 0.3–1 μm [31,32].

When the particles are larger than the pores created by fibers entanglements, a sieving mechanism occurs. In this case, nanofibers prevent particulate from passing through the membrane

blocking them as soon as the particles come in contact with fibers surface. However, after a long-term usage, particles accumulation on the filter leads to a decrease in filtration efficiency but, above all, a strong increase in pressure drop. This behaviour makes it challenging to recover the filter, removing the particles trapped in the filter, without destroying it, in order to reuse the same membrane as many as possible [31,34].

Particles could also deviate from the original streamline starting to make irregular movements due to the so-called Brownian motion. Under the action of Brownian diffusion, particles could deviate from their original air streamlines, clashing with fibers and depositing on their surface as graphically described in Figure 2.2c [29]. Brownian diffusion typically occurs for particles smaller than 1 μm, however the effect is more significant when they are smaller than 0.1 μm in size [31].

The force between charged bodies is conventionally called electrostatic force or Coulomb force. If the PM and/or the fiber are charged, particles could deviate from their original air streamlines, due to the electrostatic interaction (Coulombic attraction) with the fibers and deposit onto them surfaces (Figure 2.2d). If compared with the other forces involved in air filtration, the presence of electrostatic interaction lead to a remarkable increase in removal efficiency due to its capacity to strong attract particles also at distance. Moreover, electrostatic adsorption allows particles to adhere more firmly to the surface of the fibers [35]. Electrostatic attraction can be effectively used to capture ultrafine particles such as dust and smoke [31].

Usually, interception, inertial impaction, sieving and Brownian diffusion always occur during air filtration [36–40]. However, to archive high filtration performance it is necessary to combine all the different filtration mechanisms also exploiting electrostatic attraction [35,41–45].

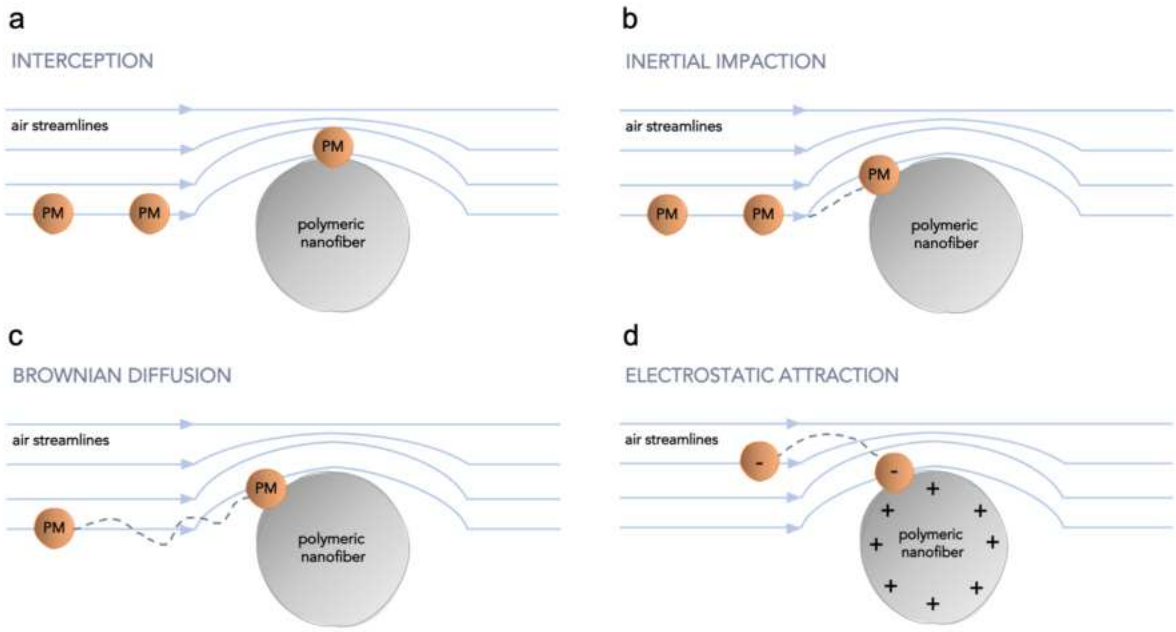

Figure 2.2 *Graphical depiction of air filtration mechanisms of nanofibers membranes: (a) interception, (b) inertial impaction, (c) Brownian diffusion, (d) electrostatic attraction.*

4.1.2 Parameters of air filtration performance

The key parameters of filter performance include filtration efficiency, pressure drop, and the quality factor. Air filtration efficiency of nanofibrous membranes, usually represented as η, can be predicted by the Kuwabara model, as follows (2.1):

$$\eta = 1 - \exp\left[\frac{-4\,\eta_s\,\alpha\,L}{\pi\,d_f\,(1-\alpha)}\right] \qquad (2.1)$$

where η_s is the filtration efficiency of a singular fiber, α represents the fiber volume fraction, d_f represents the average fiber diameter and L represents the membranes thickness [46,47]. This model highlights the strong dependence between filtration efficiency of the membranes and its structural and morphological properties. In detail, filtration performance decrease on increasing

nanofiber diameter and is directly proportional to membranes thickness. However, this model does not consider the contribution of electrostatic effect [48].

4.1.3 Materials for polymeric air filtration devices

Air filtration devices appeared for the first time in 1940 and were based on glass fibers membranes [49]. Subsequently, in 1970, also activated carbon fibers were used for filter membranes production. The firsts polymeric based air filter membranes were developed in 1990s and rapidly become the most used in air purification industry thanks to their higher filtration efficiency, lower pressure drops and better durability if compared to the previous ones [49]. Polymeric fibrous membranes, in fact, are characterized by large specific surface area, small fiber diameter and high porosity. Furthermore, they are lightweight, easy to produce, cost-effective and their fibers can be easily decorated with different type of micro- and nanoparticles [50–54].

Nowadays, air filtration membranes available on the market consist of micro-sized fibers. However, they are not efficient enough in $PM_{2.5}$ and $PM_{0.1}$ filtration and are characterize by high pressure drops, bad mechanical strength and poor thermal stability [2,50]. Therefore, is urgent to develop air filtration devices with the ability to remove also ultrafine dust from the air and contextually with low pressure drops, good mechanical properties, reusability and durability. Polymeric nanofibrous membranes have recently attracted more and more attention for the production of air filtration devices since they could allow to achieve ultrafine filtration thanks to their high porosity with interconnected pore structure, high functional surface area and customizable fiber diameter [53,55–57]. Moreover, polymeric materials have great potential for the fabrication of sensor, in fact, they have been already successfully used in different application fields [58–63]. Over the last years, also some examples of polymeric devices for air, water and soil pollution sensing have been reported [64–68]. The development of nanofibrous devices that can contextually ensure efficient air

filtration and air pollution sensing is a current challenge [66]. Moreover, also the production of air filtration devices with antibacterial ability is of great interest [69].

Polymeric materials are actually the most used for the production of air purification device thanks to their superior filtration performances [49]. Synthetic polymers (non-biodegradable), in particular, are widely used for the fabrication of air filtration devices. Thanks to their property, in fact, they can ensure good reusability, durability, appropriate mechanical properties and thermal stability to the filter membrane. In detail, as already shown in Figure 1.2, polyacrylonitrile (PAN) is the most reported polymeric material for "air filtration" topic after COVID-19 pandemic period. However, recently, due to the current need of solve environmental pollution and resources shortage issues, the development of filtration devices based on biodegradable polymeric material has become an attractive topic [18,70]. Moreover, always more often, composites polymeric membranes were proposed for air filtration application. In fact, when nanoparticles are successfully imbedded into polymeric nanofibers, they could enhance membrane filtration efficiency and contextually improve its mechanical and thermal stability [71].

4.1.4 Non-biodegradable polymers for air filtration applications

Among the wide range of non-biodegradable existing polymers, polyacrylonitrile (PAN), polyvinylidene fluoride (PVDF), polypropylene (PP), polyamide (PA) and polyvinyl pyrrolidone (PVP) are some of the most recently used ones for the production of air filtration devices, as listed in Table 2.1.

Table 2.1 Non-biodegradable polymers recently used for the production of nanofibrous filter membranes.

Polymers	**Polymer conc.** (wt%)	**Filler**	**Filler conc.** (wt%)	**Year**	**Ref.**
PAN	12	-	-	2020	[72]
PAN	12	-	-	2022	[73]
PAN	18	-	-	2019	[74]

PAN, CS	12, 1	Fe_3O_4	5	2020	[53]
PAN	10	Zn, Ag NPs	0.5, 0.5	2021	[75]
PAN, PI	10, 6	GO	0.05	2021	[50]
PAN	14	g-C_3N_4	3	2021	[76]
PAN, PCL	12, 11	β-CD, ZnO NPs	50, 27	2021	[77]
PAN, PVDF/PDMS	10, 2.5 / 2.5	-	-	2023	[78]
PVDF	16	-	-	2020	[79]
PVDF	10	-	-	2022	[80]
PVDF	16.5	Fe_3O_4	1	2020	[41]
PP	(melt)	-	-	2019	[81]
PP	(melt)	-	-	2022	[82]
Nylon-6/PEO	10 / 0.2-0.4	-	-	2023	[83]

Could be easily noted that polyacrylonitrile (PAN), as already seen in VOSViewer map (Figure 1.2), is the most reported polymeric material for air filtration device production. PAN nanofibers, in fact, due to the presence of polar chemical group on their surface, induced dipole-dipole intermolecular attraction forces with PM ensuring high capture efficiency [72,73,84]. Moreover, PAN is characterized by adequate mechanical and thermal properties [85]. However, it is possible to increase the number of functional groups on PAN fibers surface and therefore improving filtration efficiency, by combining PAN with other polymers or by adding appropriate additive of functional nanoparticles (NPs). Lv et al. [53], for example, presented a PAN based multifunctional nanofibrous membrane, reporting that the addition of chitosan (CS) to PAN provide more functional groups to nanofibers ensuring a robust interaction with pollutants. Moreover, iron oxide nanoparticles (Fe_3O_4 NPs) agglomerate (Figure 2.3) promoted the formation of a 3D porous structure improving Fe_3O_4@PAN/CS membrane filtration efficiency and also allowing antibiotic absorption. Thermal stability was also increased after the incorporation of Fe_3O_4 NPs.

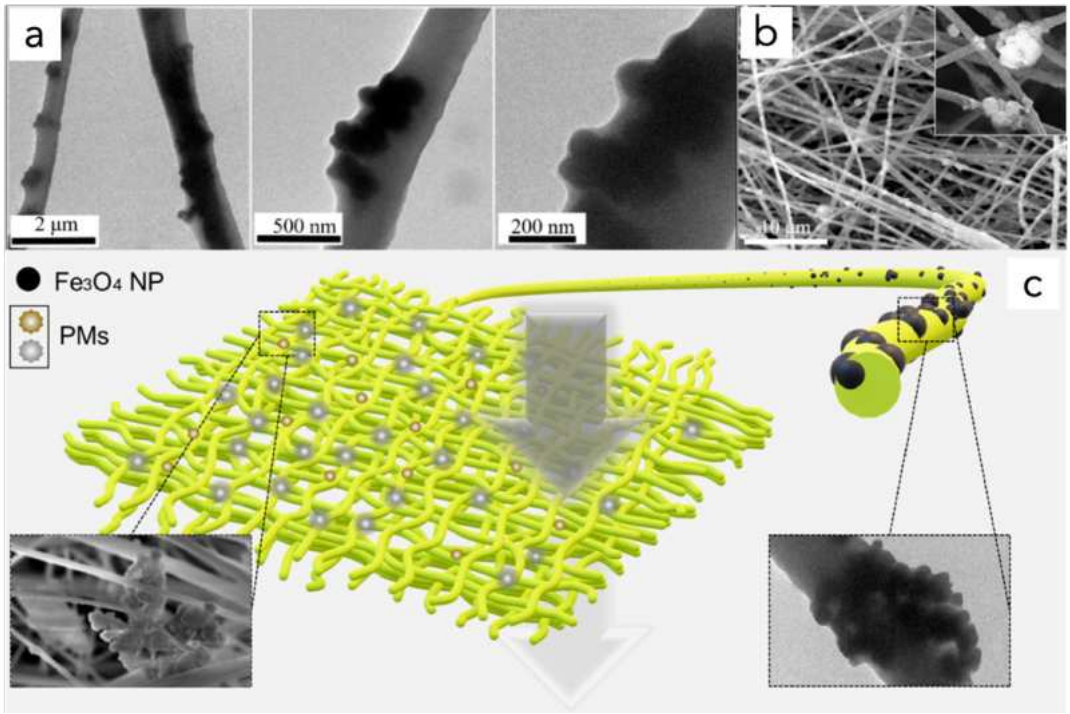

Figure 2.3 *Transmission electron microscopy (TEM) images (a), scanning electron micrographs (SEM) image after PM filtration (b) and pictorial description of PMs filtration mechanism of Fe_3O_4@PAN/CS membrane (c). Reprinted (adapted) with permission from [53], Copyright (2020), American Chemical Society.*

Multifunctional PAN based nanofibrous membrane have been also prepared by adding Zinc oxide nanoparticles (ZnO NPs) on one side of the mat and silver nanoparticles (Ag NPs) on the other side. The addition of the two NPs allowed obtaining a Janus membrane with improved filtration efficiency (if compared to neat PAN one prepared with the same procedure), organic contaminant removal ability and antibacterial properties [75].

Dai et al. [50], in 2021, prepared nanofibrous polymeric filter membranes by adding polyimide (PI) and graphene oxide (GO) into a solution containing PAN aiming to obtain a mask can be used for avoiding COVID-19 infection. If compared to neat PAN nanofibrous membranes obtain with the same procedure, PAN/GO/PI mat showed higher efficiency in capturing $PM_{2.5}$ pollutants, lower pressure drop, improved thermal stability and mechanical properties. PAN/GO/PI nanofibers could adsorb $PM_{2.5}$ more uniformly and in spherical (rather than elliptical) shape if compared to neat PAN ones, as shown in Figure 2.4. According to the authors, this behaviour can be reasonably ascribed to

the abundant hydrophilic functional groups on the PAN/GO/PI nanofibers introduced due to GO and PI addition.

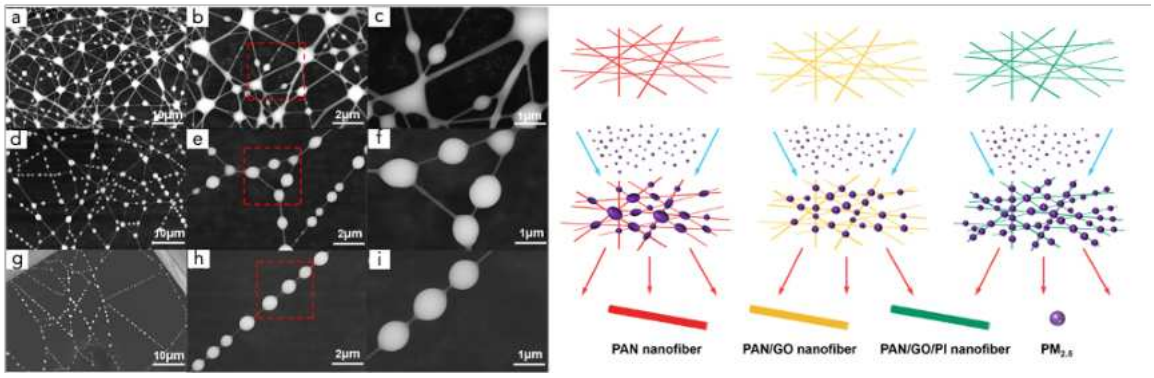

Figure 2.4 *SEM images and illustration of PAN (a − c), PAN/GO (d − f), and PAN/GO/PI-6 (g − i) nanofibers after $PM_{2.5}$ adsorption. Reprinted (adapted) from [50], Copyright (2021), with permission from Elsevier.*

In the same year, Cui et al. [76], added graphite carbon nitride (g-C_3N_4), a photocatalytic degradation material, to PAN solution obtaining a composite nanofibrous membranes. Air pollutant capture ability of PAN@g-C_3N_4 filter membrane was investigated and outcomes reviled that the addition g-C_3N_4 effectively improved filtration efficiency of $PM_{2.5}$. This behaviour has been explained by the authors considering that the addition of g-C_3N_4 lead to an increase in nanofibers surface roughness and therefore to an increase in the chance of collision between the fibers and the intercepted contaminant. Moreover, g-C_3N_4 is also a good electret which allow nanofibers charging and therefore particles electrostatic attraction, further improving filtration efficiency. Furthermore, g-C_3N_4 dispersed on nanofibers surface, under light irradiation, could oxidizes and degrades formaldehyde molecules to achieve catalytic degradation of the pollutant, making the membrane multifunctional.

Xu et al. [77] prepared multifunctional Janus membranes that can filter particulate matter (PM) and volatile organic compounds (VOCs) simultaneously. One side (the hydrophilic one) was prepared by adding β-cyclodextrin to PAN, while, in the other side, zinc oxide (ZnO) was embedded in

polycaprolactone (PCL) nanofibers in order to increase their roughness and enhance membrane hydrophobicity. The multifunctional Janus nanofibrous membrane achieved higher PM removal efficiency, lower airflow resistance and effective VOCs adsorption if compared to single side neat PAN ones.

Polymeric microbeads have been used for obtaining hydrophobic layers on filter membranes. Kim et al. [78], for example, coated PAN nanofibrous membranes (Figure 2.5a) with polymeric microbeads based on a polyvinylidene fluoride (PVDF) and polydimethylsiloxane (PDMS) 50:50 solution (Figure 2.5b). Outcomes revealed that the decorated membrane showed high filtration efficiency. Moreover, the PVDF/PDMS coating effectively created a hydrophobic layer conferring water droplet cleaning ability to the membrane.

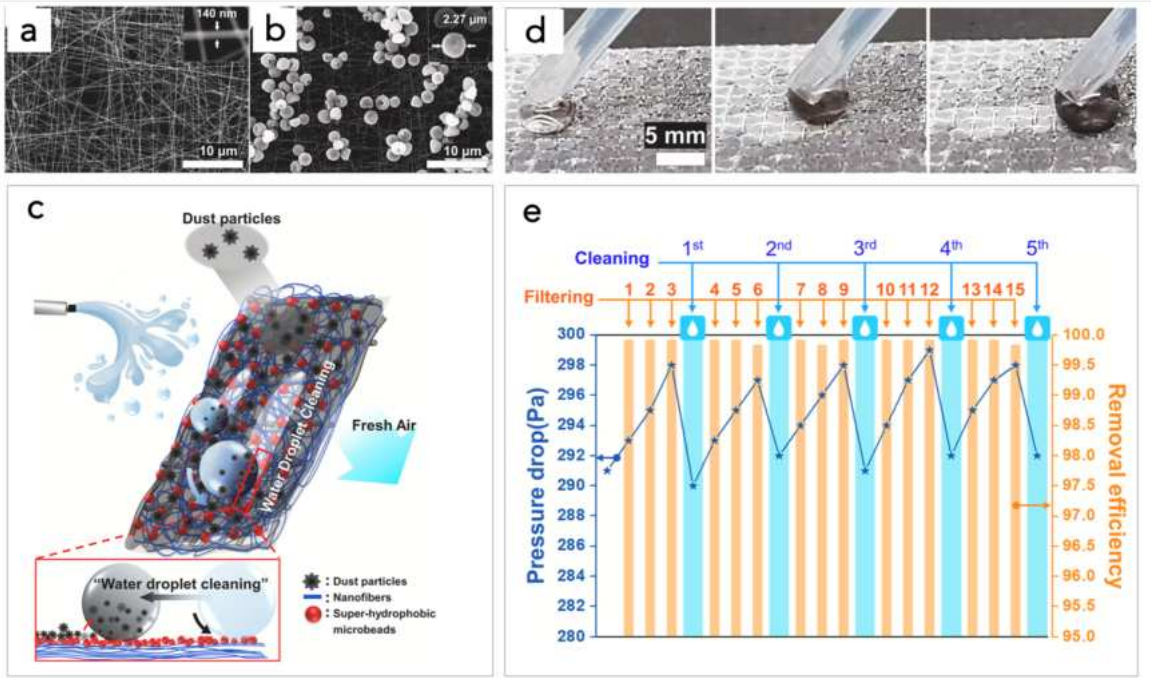

Figure 2.5 *SEM images of PAN nanofibrous membrane before (a) and after the PVDF/PDMS microbeads coating; pictorial description of filter and water droplet cleaning mechanism (c); filtration efficiency and pressure drop of PAN/PVDF/PDMS membrane during repetitive filtering and cleaning stages (e). Reprinted (adapted) from [78], Copyright (2023), with permission from Elsevier.*

When water droplets roll off membrane surface, they carry captured dust particles with them, see Figure 2.5c and d. This behaviour allowed to renew membrane filtration performance multiple

times, as it is possible to notice in Figure 2.5e. After three filtering stages, filtration efficiency remained stable, while the pressure drop gradually increased. However, after the cleaning stage, the pressure drop was almost completely restored. The reusability and durability of this membrane leads to clears economic and environmental advantages reducing maintenance cost and waste production.

Polyvinylidene fluoride (PVDF) is the second most reported polymer for the production of air filtration device. PVDF is characterized by unique properties such as good flexibility, good chemical resistance and high thermal stability [86,87]. Moreover, PVDF nanofibrous membranes have demonstrated excellent air filtration performance thanks to their electret effect that lead to a more effectively and firmly attachment of PM on fibers [79,80]. Liu et al. [41], prepared a composite filter membrane by adding Fe_3O_4 NPs to PVDF solution aiming to exploiting the electret effect (given by PVDF) and the magnetic effect (given by metallic NPs) for obtaining high filtration efficiency. Thanks to the synergy of the two effects, in fact, PVDF/Fe_3O_4 showed higher filtration performance if compare to neat PVDF ones.

Polypropylene (PP) based materials have been also reported for the fabrication of air purifiers. In detail, PP is commonly used for the production of nanofibrous mat to be employed for the production of surgical face mask used for preventing COVID-19 infection. PP membranes, in fact, are characterized by high filtration efficiency and low pressure drop [81,82].

Among the non-biodegradable polymers also Nylon-6 was investigated for the production of devices for the filtration of UFPs. Zhang et al. [83], prepared a multilayer nanofibrous membrane based on a blend of Nylon-6 and polyethylene oxide (PEO) in different concentration. The obtained filter, due to chemical functional groups of Nylon-6 molecules, exhibited extremely high filtration performance and overall optimal filtering performance. The membrane was also characterized by relatively high mechanical performance. Moreover, these membranes provided users more comfortable wearing experience and stable protection performance against COVID-19.

Combining two or more polymers with different properties has been reported as a successful strategy for the obtainment of nanofibrous membranes with high filtration performance due to the possibility of combine the respective strengths [88]. Wang et al. [89], for example, fabricated porous nanofibers using a PVP/PTFE blend in which PVP was used as a sacrificial phase. Thanks to the extremely porous nanofibrous membrane high filtration efficacy and ultralow pressure drop were achieved.

4.1.5 Biodegradable polymers for air filtration applications

The fabrication of environmentally friendly air filtration membranes with high filtration performance is still a big challenge. Most of the polymers mentioned above, in fact, need to be dissolved in toxic or, otherwise, harmful solvents and could not be biodegraded after their use. Therefore, solvents evaporation during nanofibers formation and the final disposal of the devices could induce second pollution [18,70]. Moreover, environmental impact of COVID-19 was very significant also due to the tons of raw materials exploited and plastic waste produced due to mask and indoor air filter extensive consumption [90]. The develop of air filtration devices based on bio-based and (or) biodegradable polymers would contribute to reduce these environmental issues. Although, biodegradable filters cannot ensure extensive durability or reusability they can be widely used for replacing traditional ones in all those applications in which single use only is mandatory [91]. Stimulated by these environmental needs, different nanofibrous devices based on green solvents and/or biodegradable polymers have been recently reported, as listed in Table 2.2.

Table 2.2 Biodegradable polymers recently used for the production of nanofibrous filter membranes.

Polymers	**Solvents**	**Polymer conc.** (wt%)	**Filler, additive**	**Filler, additive conc.** (wt%)	**Year**	**Ref.**
PVA	water	7	-	-	2021	[92]
PVA	water	10	zein	0 - 70	2020	[38]

PVA/CS	water / acetic acid	10 / 2	-	-	2020	[55]
PVA/CS	water / acetic acid	10 / 3	SiO_2, Ag NPs	4	2019	[93]
PVA/KGM	water	10 / 1	ZnO NPs	1	2019	[94]
PLA	EA/DMF	10	-	-	2022	[95]
PLLA	DCM/DMF	10	DC	2.5	2023	[96]

Polyvinyl alcohol (PVA) is one of the most reported biodegradable polymers used for the production of nanofibrous filter membrane. Therefore, PVA is a water-soluble polymer characterize by excellent mechanical property, thermostability and biocompatibility. Kim et al. [92], for example, fabricated a double layer device (PVA nanofibers/PP-based non-woven fabric) exploiting PVA water solubility to produce a nanofiber filter membrane that could be environmentally friendly disposed. In detail, as shown in Figure 2.6, after the filtration process, the devices could be immersed in water in order remove the PVA layer saturated with filtered particles. Subsequently, the non-woven fabric could be dried and a new PVA filtering layer could be added.

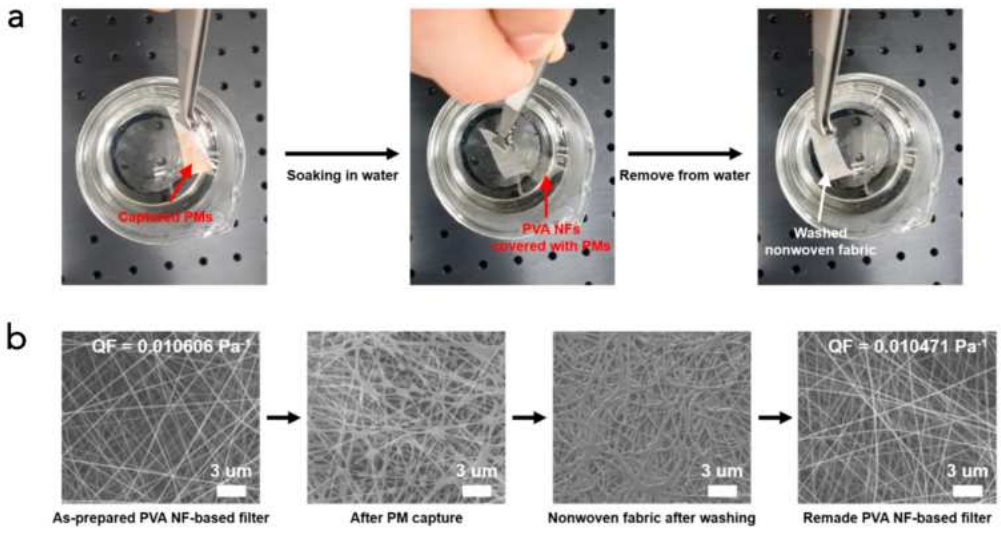

Figure 2.6 *Removal of PVA layer in water after filtration (a) and SEM images of the surface of the device during the restoring process (b). Reprinted (adapted) from [92].*

In order to expand its application, it is possible to stabilize PVA membranes through a thermal or chemical induced crosslinking. Glutaraldehyde [55] and citric acid [94] are commonly used as green additive for stabilizing PVA nanofibers. Li et al. [38], add up to 70 wt% of zein (denatured in

acetic acid/water solution) to PVA solution in order to prepare nanofibrous membrane for air filtration. Water Contact Angle (WCA) test reviled that on increasing zein amount the hydrophobicity of PVA membranes increase. Moreover, zein containing membranes showed higher air pollutant removal efficiency if compare to neat PVA ones. According to the authors, this behaviour could be reasonably ascribed to zein higher interaction with pollutants if compared with PVA. After the denaturation in acetic acid, in fact, zein exposed active group increased guaranteeing an effective interaction with pollutant of different nature. Furthermore, zein addition, leading to a decrease in solution viscosity, provoked a decrease in nanofibers diameters, resulting in an increase of their specific surface that positively contributing to membranes filtration performance.

In 2020, Zhang et al. [55] fabricated a multilayer structured membrane with excellent mechanical properties, air filtration performance and antibacterial ability by assembly PVA/CS nanofibrous membranes onto both sides of a N-halamine biopolymer fibrous mat. Zhu et al [93], similarly, exploited antibacterial activity of CS to produce PVA based filter membrane. Moreover, in this study, Ag and SiO_2 NPs were added to the nanofibrous membrane with the aim of enhance antibacterial ability and filtration performance, respectively.

Lv et al [94], successfully encapsulated ZnO NPs into PVA/konjac glucomannan (KGM, a natural polymer) nanofiber. Outcomes revealed that the presence of ZnO NPs into PVA nanofibers allow to enhance filtration performance (as shown in Figure 2.7) of the device, conferring also antibacterial and photocatalytic ability to the composite membranes.

Polylactic acid (PLA), is another biodegradable polymer widely used for the production of environmentally friendly air filtration device [36,97–99]. However, PLA is commonly dissolved using harmful organic solvents such as dichloromethane (DCM), chloroform, 1,1,1,3,3,3-hexafluoro-2-propanol (HFIP) in order to obtain nanofibers. Therefore, prepare PLA nanofibrous membranes without using toxic solvent is an urgent issue. Han et al. [95], for example, prepared PLA based nanofibrous membranes selecting two relatively green alternative non-halogenated solvents: ethyl

acetate (EA) and N, N-dimethylformamide (DMF). According to the authors, if compared to the others possible solvents (see Figure 2.8), EA/DMF mixture could significantly reduce secondary pollution related to membranes production. Moreover, once optimized the PLA concentration and the solvents ratio, the obtained morphology achieved outstanding removal efficiency and extremely low pressure drop. Filtration performance of the membrane was significatively higher to those reported for commercial masks used for avoiding COVID-19 infection.

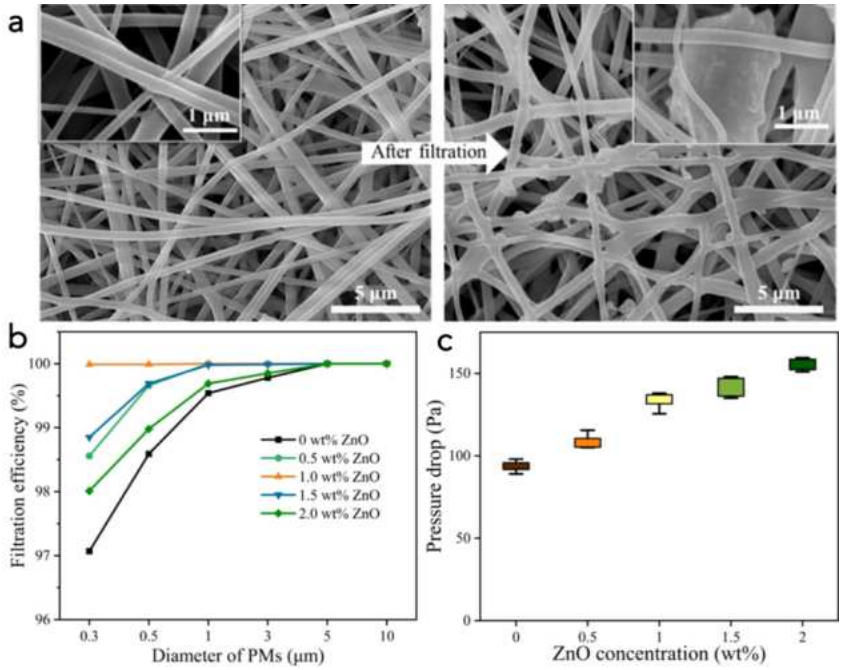

Figure 2.7 *SEM images of ZnO@PVA/KGM nanofiber membrane before (left) and after (right) filtration (a); filtration efficiency at different PM dimensions (b) and pressure drop (c) of membranes with different ZnO concentrations. Reprinted (adapted) with permission from [94], Copyright (2019), American Chemical Society.*

Wanwong et al [96], added cyclodextrins (CDs) to poly(L-lactic acid) (PLLA) in order to obtain a mask based of nanofibrous membrane that could contextually filter PM and VOCs. In fact, piezoelectric and triboelectric property of PLLA lead to an increase in membrane PM capturing ability due to the high electrostatic interaction between PLLA nanofiber and PM. On the other hand, CDs, due to their peculiar conic structure composed by a hydrophobic central cavity and a hydrophilic outer surface, entrap higher amounts of VOCs, including aniline and benzene vapors.

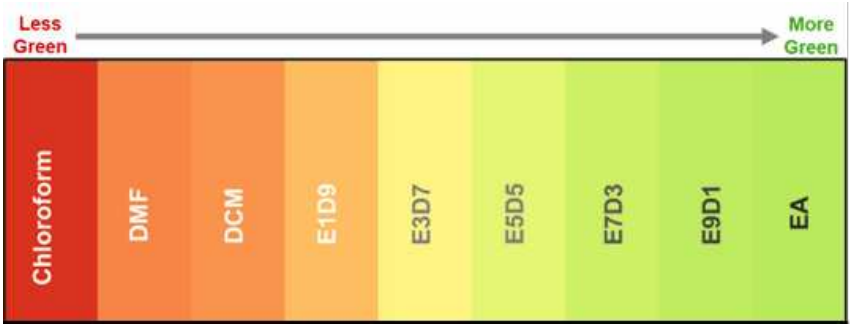

Figure 2.8 *Greenness comparison of solvents. Reprinted (adapted) from [95], Copyright (2022), with permission from Elsevier.*

It can be concluded that the choice of the polymeric matrix, together with the appropriate selection of additives and fillers, make the difference in term of filtration performance of the final nanofibrous device regardless production techniques. The addition of functionals NPs, in particular, seems to be a successful strategy to produce nanofibers with improved filtration efficiency and (or) to make membranes multifunctional.

4.1.6 Polymeric membranes for air filtration devices production

The structures of polymeric filter materials have been developed over last years. Different examples of porous polymeric filter membranes with high filtration efficiency but low porosity, poor hole connectivity and, therefore, high air resistance have been reported [48,100–103]. However, by processing the same polymeric systems with alternative production techniques it is possible to obtain different structures with higher porosity and, therefore, improved filtration performance [104–106]. In detail, polymeric membranes with nanofibrous structure turn out to perform better for air filtration if compared to other porous structure [31,107]. This behaviour confirms the strong influence of the membrane structure on filtration efficiency and, therefore, the importance of production technique choice. Table 2.3 enlist the filtration performance of various polymeric nanofibrous membranes obtained with different production technique.

Table 2.3 Filtration performance parameters of polymeric nanofibers devices obtained with different production technique.

Technique	Polymers	Structure	PM (μm)	η (%)	ΔP (Pa)	QF (Pa^{-1})	Ref.
ES	PVA	nanofibers	0.5	86.81	191	0.011	[92]
ES	PAN@g-C_3N_4	nanofibers	2.5	99.76	43	0.121	[76]
ES	PAN/GO/PI	nanofibers	2.5	99.5	92	0.058	[50]
ES	PVDF@Fe_3O_4	nanofibers	2.5	99.95	58	0.130	[41]
ES	PVA/KGM@ZnO	nanofibers	0.5	99.99	130	0.070	[94]
ES	PLLA/DCs	nanofibers	2.5	96.84	43	0.105	[96]
ES	PAN	NF/nanonet	0.3	99.99	110	0.100	[74]
ES	PVDF	NF/nanonet	0.3	99.99	93	0.110	[79]
ES	PVDF	branched NF	0.3	99.99	126	0.090	[80]
ES	PLA	bead-on-string	2.5	98.56	29	0.140	[95]
ES	PVA/CS	multilayer	0.5	99.30	183	0.027	[55]
ES	PVA/CS@SiO_2/Ag	hierarchical	0.5	96.60	306	0.011	[93]
ES	PAN@ZnO/Ag	Janus NF	0.3	80	32	0.050	[75]
ES	PAN/CD-PCL/ZnO	Janus NF	0.3	99.99	156	0.059	[77]
ES double-disc	PAN	well-ordered NF	2.5	99.60	62	0.090	[73]
ES and electrospray	PAN/PVDF/PDMS	microbeads on NF	2.5	99.80	110	0.057	[78]
centrifugal ES	PVP/PTFE	porous fibers	0.3	99.72	90	0.065	[89]
solution blow spinning	PAN	nanofibers	2.5	92.90	58	0.046	[72]
solution blow spinning	PAN/CS@Fe_3O_4	hierarchical	0.3	99.98	48	0.123	[53]
solution blow spinning	Nylon-6/PEO	multilayer	0.25	99.50	144	0.066	[83]
melt blown spinning	PP	nanofibers	0.3	99.20	29	0.170	[82]

electrospinning (ES); nanofibers (NF); particulate matter (PM); filtration efficiency (η); pressure drop (ΔP); quality factor (QF)

4.1.7 Electrospinning for air filtration devices production

Electrospinning (ES) is one the most frequently reported technique to prepare nanofibrous mats [106]. As it is possible to notice from Table 2.3, ES is widely used to prepare membranes for air filtration application, allowing to easily produce uniform, randomly oriented or aligned fibers with homogeneous diameters and leading to the fabrication of highly and interconnected porous membranes. Kim et al. [92], for example, using ES, fabricated eco-friendly air filter membranes based on PVA nanofibers. However, filtration performance of the devices was relatively low, reporting a filtration efficiency of 86.81% and a quality factor of 0.11 Pa^{-1}.

As mentioned above, the presence of functionals NPs could improve membranes filtration efficiency. ES has the great advantage of allowing easily fabrication of composite nanofibers just by

adding NPs to the polymeric solutions and electrospun them. Lui et al. [41], for example, fabricated electrospun PVDF mats containing up to 1.5 wt% of Fe_3O_4 NPs, as is possible to notice from TEM image in Figure 2.9a.

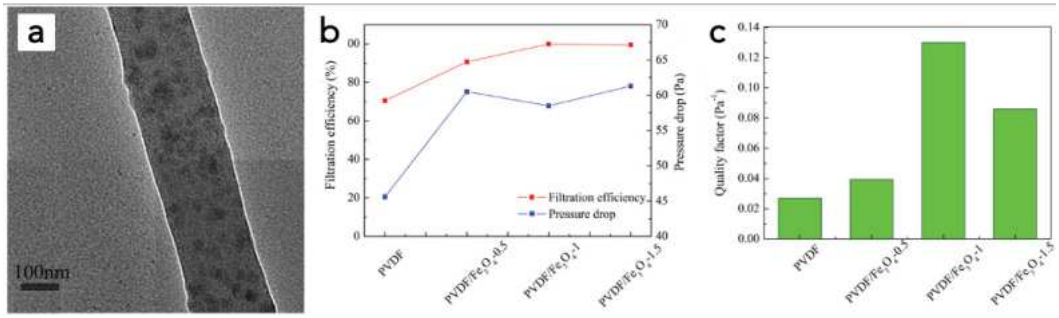

Figure 2.9 *TEM image (a); filtration performances (b) and quality factor (c) of PVDF/Fe_3O_4 membranes. Reprinted (adapted) from [41], Copyright (2020), with permission from Wiley.*

When 1 wt% of Fe_3O_4 NPs is added, the membranes achieved the best filtration performances (filtration efficacy of 99.95% and pressure drop of 58.5 Pa) as reported in Figure 2.9b,c.

Similarly, also Cui et al. [76] and Dai et al. [50] in 2021, correctly embedded graphite carbon nitride (g-C_3N_4) and graphene oxide (GO), respectively, into PAN electrospun nanofibers leading to an increase in membranes filtration performances if compared to the neat PAN ones. As regards biodegradable polymers, Lv et al. [94] fabricated PVA based filtering membranes through green electrospinning and ecofriendly thermal cross-linking. They successfully loaded ZnO NPs into PVA nanofibers during the spinning process achieving a filtration efficiency higher than 99.99% for UFPs. Moreover, recently, Wanwong et al. [96] electrospun PLLA solutions in which up to 10 wt% of CDs were added with excellent results. 2.5 wt% CDs containing membranes showed the best air filtration performance if compared to neat PLLA (16% higher) and other composites membranes with different CDs amounts. More in detail, 2.5 wt% CD/PLLA displayed filtration efficiencies of 96.84% and 99.38 % for $PM_{2.5}$ and PM_{10} capturing respectively.

Electrospinning is a very versatile technology. By tuning solution composition and concentration, processing and (or) ambient parameters it is possible to modify electrospun fibers

morphology and consequently to obtain membranes with complex structure and improved properties. Liu et al. [74] in 2019, for example, fabricated PAN nanofiber/nanonet fluffy membranes (Figure 2.10a) for air filtration application by introducing cationic surfactant tetrabutylammonium chloride (TBCA) in the polymeric solution, using a humidity-induced electrospinning/netting technique. In detail, PAN/TBAC charged droplets were formed at the exit of the needle tip due to the ion–dipole interaction between the polymer and the surfactant.

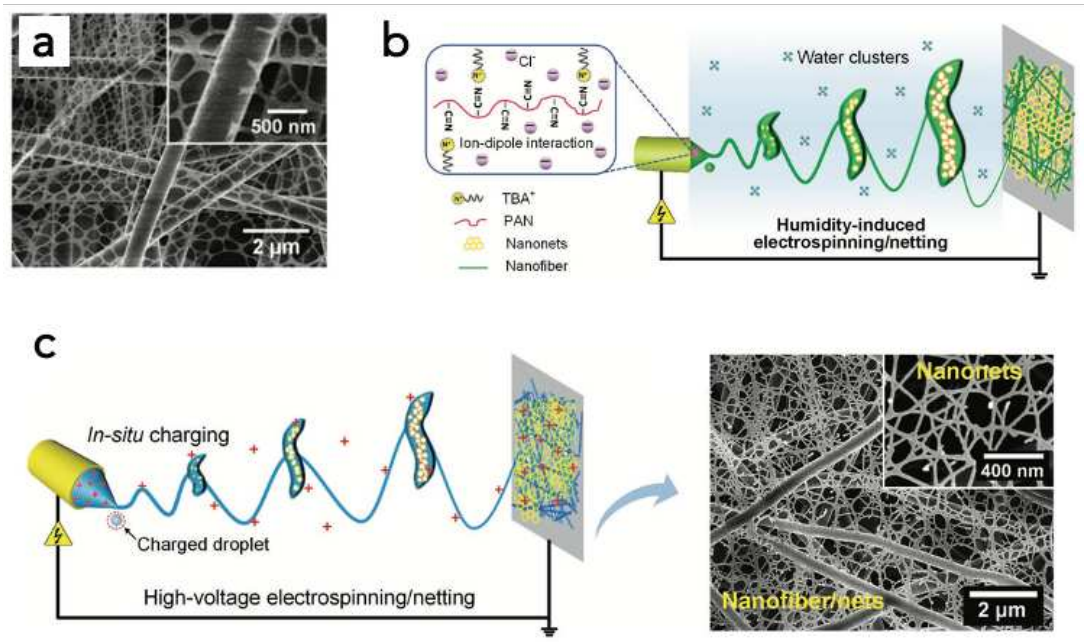

Figure 2.10 *SEM image (a) and graphical description (b) of fabrication process of PAN nanofibers/nanonet membranes. Reprinted (adapted) from [74], Copyright (2019), with permission from Wiley. Graphical description and SEM image of PVDF nanofibers/nanonet membranes (c). Reprinted (adapted) from [74], Copyright (2020), with permission from Wiley.*

Subsequently, under high-voltage electric field and humid controlled atmosphere the droplets turn in 2D nanonets due to phase separation effects, as graphically descripted in Figure 2.10b. According to the authors, thanks to the synergistic effects of nanonet and fluffy nanofiber, membranes showed extremely high filtration efficiency (99.99%) for $PM_{0.3}$ and ultralow air resistance (110 Pa). The same authors, in 2020, tested other polymeric systems in order to obtain the same nanofiber/nanonet membranes structures [79]. More in detail, by using electret PVDF was possible

to exploit electrostatic attraction to produce the nanonet (Figure 2.10c,d), keeping filtration efficiency at 99.99% and decreasing pressure drop to 93 Pa if compared with the previously obtained PAN membranes.

TBCA was also used with PVFD by Zaarour et al. [82], in order to obtain electrospun branched nanofibers. The extremely small diameter of branched nanofibers, in fact, improves van der Waals attractive forces between particles and nanofibers leading to a very high filtration efficiency (99.99%) and a quality factor of 0.09 Pa^{-1}.

Han et al. [95], fabricated electrospun membranes with bead-on-string structure by tuning the solvent ratio of PLA solution. Thanks to this complex structure, membranes achieving an outstanding removal efficiency (98%) for $PM_{2.5}$ and an extremely low pressure drop of 29.3 Pa.

Moreover, different complex structures have been obtained by electrospinning. Zhang et al. [55], for example, reported that PVA based multilayer and multifunctional nanofibrous membranes (for air filtration mask) have been prepared by consecutively electrospun superimposed different polymeric solutions. The multilayer membranes showed a high filtration efficiency of 99.3% and a relatively low pressure drop of 183 Pa for $PM_{0.5}$. On the other hand, Zhu et al. fabricated hierarchical PVA/CS based electrospun nanofibrous membrane by adding SiO_2 and Ag NPs in order to increase nanofibers surface roughness to further improve membranes air filtration performance and to give antibacterial ability to the device. The membranes could effectively serve as a personal protective mask also for COVID-19 infection.

It has been reported that ES technique allow to produce Janus membranes also for air filtration application [75]. Xu et al. [77], for example, prepared, by electrospinning, PAN/PLA based cyclodextrins and ZnO containing Janus nanofibrous membranes aiming to obtain a mask with contextually high filtration performances and VOCs adsorption ability. More in detail, the Janus membranes were obtained by consecutively electrospun superimposed PAN/β-CDs solution and

PCL/ZnO one. PAN/β-CD/PCL/ZnO device reported a filtration efficiency of 99.99% and a pressure drop of 156 Pa for $PM_{0.3}$, moreover, it effectively absorbed aniline.

By appropriately designing the grounded collector shape it is possible to modify nanofibers morphology and, therefore, the structure of the membranes in order to improve their filtration performances. Cheng et al. [73], for example, succeeded in the obtainment of well-ordered PAN nanofibrous membranes (Figure 2.11a) by using a double-disc collecting device, reported in Figure 2.11b,c. The well-ordered nanofibers membranes (ONF) showed a relatively high filtration efficiency of 99.60 % and extremely low pressure drop of 62 Pa. According to the authors, the more ordered fibers arrangement trapping particles more effectively if compared to a disordered nanofiber membrane (DNF). But, predominantly, the well-ordered structure allows to decrease significantly the air resistance (see Figure 2.11c) and improve stability over long periods of time, potentially allowing continuous air-purification applications.

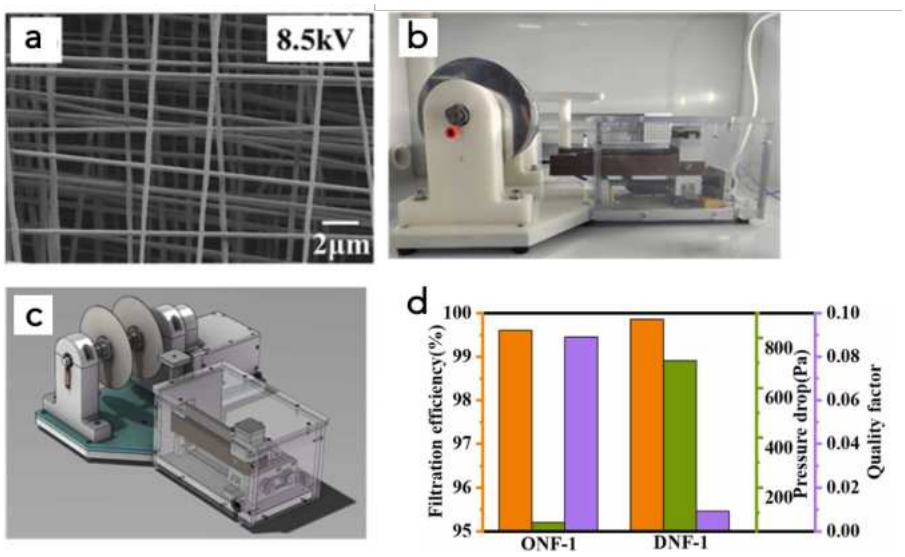

Figure 2.11 *SEM image of ONF membrane (a); picture (b) and schematic description (c) of double-disc collecting device; air filtration performance of ONF and DNF membranes (d). Reprinted (adapted) from [73], Copyright (2022), with permission from Elsevier.*

Combine ES with other similar techniques has been proved to be a successful strategy for obtaining multifunctional membranes with high filtration performance. Kim et al [78]. in 2023, for example, combined ES with electrospray (conceptually identical to ES but microbeads instead of fibers are ejected) in order to fabricate filter membranes with water droplet cleaning ability. A dual-layer structure consisting of hydrophilic PAN nanofibers coated with hydrophobic PVDF/PDMS microbead was obtained. Membranes reported a filtration efficiency higher than 99.8% and the pressure drop was recovered by 99% after each cleaning cycle, ensuring filter reusability.

ES standard set-up can be easily modified and implemented in order to obtain different fibers morphologies, improved production rate or new functionalities. Many variations of ES are reported in the scientific literature and electro-centrifugal spinning (ECS) is one of these [108–110]. Wang et al. [89], for example, reported that through ECS (the process is schematized in Figure 2.12a) and a subsequent sintering calcination was possible to improve fibers production rate and obtain ultrafine porous PTFE fibrous membrane (shown in Figure 2.12b) that exhibited excellent air filtration performance - with a filtration efficiency of 99.72% and a pressure drop of 90 Pa – and reusability, as shown in Figure 2.12c.

Figure 2.12 *Schematic representation of ECS fabrication process (a); SEM micrograph of porous fibers (b); membranes filtration performance (c). Reprinted (adapted) from [89], Copyright (2021), with permission from Elsevier.*

4.1.8 Solution Blow Spinning for air filtration devices production

Solution blow spinning (SBS) is a new technology that allow to produce polymeric fiber by using a simple and cost-effective set-up. However, usually, membranes obtained with SBS suffer from poor morphology presenting irregular fibers diameter distribution, fibers bundle and fibers in the micro-scale range [111].

Nevertheless, this non perfectly homogeneous structures achieved relatively high filtration performance [83], especially when NPs are embedded in the fibers and a wrinkled surface is obtained. Lv et al. [53], for example, used SBS technique (Figure 2.13a) aiming to fabricated ultrathin nanofiber membranes with high porosity, interconnected pore and hierarchical structure for filtration application (Figure 2.13b). In detail, they prepared multifunctional polyacrylonitrile/chitosan@Fe_3O_4 based membranes that, due to the high fibers surface roughness (achieved thanks to the presence of NPs), showed an extremely high filtration efficiency (99.98% for $PM_{0.3}$ and almost 100% for PM_1) and pressure drop of only 48 Pa. Moreover, PAN/CS@Fe_3O_4 membranes proved their reusability and durability demonstrating the potential long-term application.

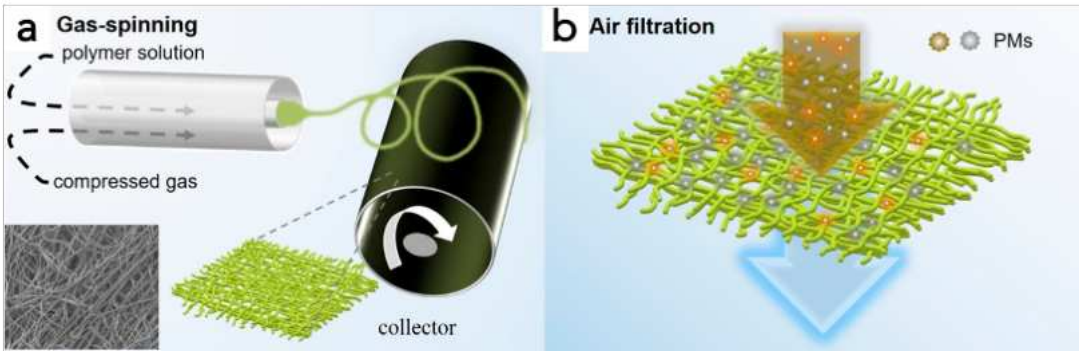

Figure 2.13 *Schematic representation of SBS technology (a) for the production of nanofibers membranes for air filtration application (b). Reprinted (adapted) with permission from [53], Copyright (2020), American Chemical Society.*

Moreover, SBS allow large-scale fabrication ensuring good industrialization prospect that, however, has not been reached up so far. Song et al. [72], for example, used SBS in order to successfully fabricate, in continuous production, 500 mm wide nanofiber membranes.

4.1.9 Melt Blow Spinning for air filtration devices production

Not all polymers can be processed for electrospinning or solution blow spinning, aiming to produce nanofibers, since not all polymers can be solvated. PP, for example, is one of these. However, PP fibrous mats were successfully fabricated for melt blow spinning (MBS) [81,82,112–114]. In MBS, fibers are created through hot and high-speed air jets that stretch the extruded molten polymer. Melt blow spinning has the great advantages of no voltage requirement, can allow large-scale fabrication and is suitable to process wide range of polymers [111]. For these reasons, MSB is actually a common method used in industry for producing microfibrous mat [115]. However, this technique is not very used for the production of innovative air filtration device since is not possible to easy obtain fibers in the nanoscale range and we have already widely discussed how the obtainment of small fiber diameter (leading to membranes with large specific surface area and high porosity) is high desirable in air filtration in order to obtain good filtration performance. In order to solve this limit, Yang el al. [82] developed a laser-assisted melt-blown (LAMB) spinning technique (illustrated in Figure 2.14) to produce PP nanofibers for fabricate facemask with a quality factor of 0.17 Pa^{-1}.

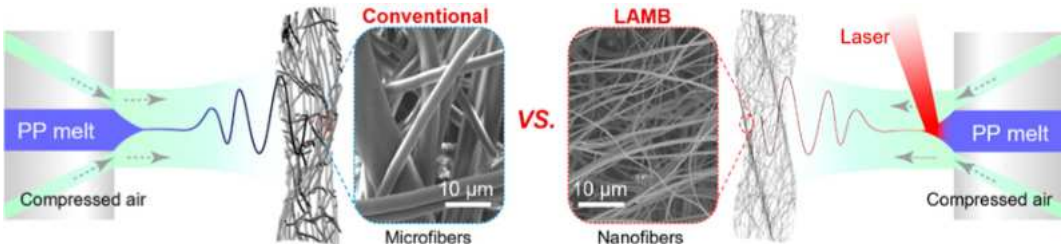

Figure 2.14 *Pictorial description and SEM images of conventional melt blow spinning and laser-assisted melt blow spinning. Reprinted (adapted) with permission from [82], Copyright (2022), American Chemical Society.*

4.2 Water and Soil

4.2.1 Mechanisms and parameters of pollutant removal

The effectiveness of devices for pollutant removal is linked to the mechanisms of adsorption, filtration, or catalytic degradation. In the literature have been reported several techniques for wastewater treatment and heavy metal absorption, including physical, chemical, and biological processes.

As regards oil removal, hydrophobicity and oleophilicity play crucial roles, allowing polymers to selectively adsorb oil from water, effectively separating it from the aqueous phase. The interaction between the device surface and oil molecules is influenced by several factors such as chemical composition and surface structure. More in detail, surface roughness and the presence of micro- and nanopores can enhance the adsorption efficiency by providing more available sites [116].

For dye removal, mechanisms often involve adsorption facilitated by electrostatic interactions, hydrogen bonding, and Van der Waals forces. The molecular structure of the dye, such as the presence of functional groups that can interact with the device material, plays a crucial role in the adsorption process. Methylene blue, for example, a cationic dye, can be efficiently adsorbed by negatively charged surfaces, which promotes strong electrostatic attraction. The adsorption kinetics are frequently modeled using pseudo-first-order or pseudo-second-order equations to better understand the rate-controlling steps and optimize the design of the devices [117].

The efficiency of devices in removing heavy metals from soil depends on different mechanisms, including adsorption and ion exchange. These processes involve interactions between the device matrix and metal ions, often facilitated by functional groups such as carboxyl, hydroxyl, and amine groups present in the device structure. The ability of polymers to form stable complexes with metal ions can significantly reduce the mobility and bioavailability of heavy metals in the soil, preventing their spread and environmental impact [118,119].

Key parameters influencing pollutant absorption mechanisms include:

- Surface area: a larger surface area provides more active sites for pollutant binding.
- Pore structure: porous materials allow deeper penetration of pollutants, increasing adsorption capacity.
- Surface charge: the zeta potential of the polymeric surface influence the interaction strength with charged pollutants.

4.2.2 Performance parameters

The performance for evaluating the efficiency of the devices in pollutant removal include adsorption capacity, removal rate, and reusability. The adsorption capacity is measured in terms of milligrams of pollutant per gram of adsorbent, while removal rate indicates the speed at which pollutants are captured. The removal efficiency is often calculated using the equation (2.2):

$$\text{Removal efficiency} = \text{RE}\ (\%) = \frac{C_0 - C_e}{C_0} \times 100 \quad (2.2)$$

where C_0 is the initial concentration of the pollutant (mg/L) and C_e is the equilibrium concentration of the pollutant (mg/L). Reusability and regeneration potential of the devices are usually assessed through multiple adsorption-desorption cycles.

4.2.3 Polymeric devices for oil and dye removal

Various polymeric materials have been utilized for pollutant removal, including synthetic polymers like polypropylene (PP), polystyrene (PS), and polyurethane (PU). For dyes, polymers such

as polyacrylonitrile (PAN) and polydimethylsiloxane (PDMS) have shown promise due to their structural adaptability and chemical stability [120].

4.2.4 Biodegradable polymers for oil and dye removal

Sustainable approaches promoted the use of biodegradable polymers, including polylactic acid (PLA), starch-based polymers, polyvinyl alcohol (PVA) and polyhydroxyalkanoates (PHAs). These polymers offer significant environmental advantages as they break down into non-toxic byproducts under appropriate conditions, reducing long-term ecological impact. Moreover, biodegradable polymers have demonstrated competitive adsorption properties [19]. Infact, characteristics such as hydrophobicity, mechanical stability, and the ability to form porous structures contribute to their effectiveness in pollutant removal. PLA, for example, is known for its biodegradability and ease of processing into various forms, including fibrous membranes and 3D structures, which can be used for oil and dye removal and heavy metals absorption [120,121].

Biodegradable polymers can be further tailored to improve their performance by using advanced fabrication techniques in order to obtain enhanced porosity, surface area, and pollutant affinity. These ensure that biodegradable devices maintain high efficiency while aligning with environmental sustainability goals.

4.2.5 Additives and fillers for enhanced removal efficiency

Both traditional and biodegradable polymers are often combined with different type of additives and fillers to improve their removal efficiency. Common fillers include activated carbon, which enhances adsorption due to its high surface area, and biochar, which provides excellent porosity and adsorption capacity. Other examples are clay minerals and zeolites, which can improve the mechanical properties and adsorptive performance of polymer composites. Natural fillers such as

cellulose fibers and chitosan are also used to increase the affinity for specific pollutants and improve biodegradability [122,123].

This strategy ensures that the polymers can capture higher concentrations of oil, dye or heavy metals, thus boosting their overall remediation efficiency.

4.2.6 Production techniques for biopolymeric devices for pollutant removal

The production of biodegradable polymeric devices for water and soil remediation typically involves inovvative techniques such as electrospinning, solution blow spinning, and 3D printing. Electrospinning and solution blow spinning are particularly useful for creating fibrous mats with high surface area and controlled porosity, while 3D printing provides the flexibility to design complex structures tailored to specific remediation needs.

Chapter 3

Materials and Methods

5.1 Materials

5.1.1 Biopolymeric matrices

In this thesis, Mater-Bi® EF51L (MB; density = 1.22 g/cm ; melt flow index = 3.5 g/ 10 min), a polymer based on blends of aromatic and aliphatic biodegradable co-polyesters which composition is proprietary, produced by Novamont SpA (Novara, Italy) and poly(lactic acid) PLA 2003D (density = 1.25 g/cm3; melt flow index = 6 g/ 10 min; 4.3% content of D-lactic acid monomer), purchased from NatureWorks® (Minnetonka, MN, USA) were selected as suitable biodegradable polymeric matrices for the fabrication of devices via melt processing techniques.

PLA was also utilized in solution-based manufacturing methods. Acetone (Ac), chloroform (Chl), deionized water and other chemicals of analytical grade were purchased from Sigma-Aldrich. In all experiments reported, PLA solutions (10 wt%) were prepared using Chl/Ac mixture (2:1 ratio). Polyethylene oxide Mw 100 kDa (PEO-A) and Polyethylene oxide Mw 600 kDa (PEO-B), used as a sacrificial phase to obtain highly porous structures after its leaching in water were purchased from Sigma Aldrich.

All the reactants were ACS grade (purity > 99%) and were used as received.

5.1.2 Fillers

For the fabrication of bio-composites devices, fillers of different nature, derived from vegetal or animal waste, were used. Invasive plants, agricultural residues, food waste, and animal-derived waste were utilized.

As regards, plant-based fillers, Kraft lignin (LIG) was obtained from black liquor using the Lignoboost technology. The cladodes from *Opuntia Ficus Indica* (OFI; cellulose: 20%, lignin: 3%, hemicellulose: 48%, ashes: 20%, other: 9%) were supplied by Bio Ecopuntia (Italy), while scraps of *Posidonia Oceanica* leaves (POL; cellulose: 31%, lignin: 29%, hemicellulose: 26%, ashes: 10%, other: 4%) were collected on the Mondello coast in Palermo, Italy. *Hedysarum coronarium* plant (HCP, syn. Sulla coronaria [L.] Medik. Species Sparacia) was kindly supplied by "Azienda Agricola Alberto Lo Dico" Petralia Soprana (PA), Sicily, Italy. *Solanum lycopersicum* plant (SLP) waste was generously provided by a local farm (Palermo, Italy). The plants were mowed after tomato harvesting and only the stems and leaves of the tomato plant were used, the roots were removed. *Juncus Maritimus* plant (JMP) were collected on the Marsala coast in Trapani (Italy).

For what concern the animal-derived filler, *Engraulis Encrasicolus* (anchovy, EE) fishbone scraps were supplied by Ballarò market (Palermo, Italy) and waste wool fibers (WF, non-textile grade) were kindly supplied by a local farm (Palermo, Italy).

NPK fertilizer with 12% of nitrogen content, 12% of phosphorus content and 17% of potassium content, purchased from Flortis, Orvital S.p.A., was used.

5.1.3 Pollutants

Air

Burning incense was used to generate the particles (PMs), with particles size ranging from 0.3 μm to 3 μm, aiming to simulate a polluted air environment.

Water

Standard oily motor 10W–40 (density = 0.87 g/cm3 kinematic viscosity = 97.7 mm2/s at 40 °C) was supplied by Total S.A. Chemical composition of oil consists in hydrocarbons between 18 and 34 carbon atoms per molecule. Commercial food grade olive oil and sunflower oil were used. The three oils were also tested in their exhausted version, i.e. at their end-of-life.

Methylene blue (MB) reagent grade was purchased from Sigma Aldrich.

Fat, Oil, and Greases (FOG), an oily effluent primarily composed of waste from kitchen processes, was provided by Ecodep Srl, Modica (Ragusa), a company specializing in the treatment of special waste. This effluent is known for its high content of lipids, oils, and grease, which makes it a significant contributor to pollution when improperly disposed of in water systems. The FOG sample was stored at room temperature and filtrate prior to any experimental use to ensure the removal of solid waste, kipping only the oil-water emulsion.

Soil

The heavy metals used within the adsorption studies included: $CuSO_4 \cdot 5H_2O$; $MnCl_2 \cdot 4H_2O$; $NiSO_4 \cdot 6H_2O$; Fe_2O_3. All of them were purchased from Sigma-Aldrich (Germany, 99.0%).

5.2 Preparation of devices

5.2.1 Electrospinning

The fibrous membranes were produced by using Linari Engineering-Biomedical Division (Pisa, Italy) conventional electrospinning apparatus, consisting of a syringe pump and a high voltage power supply. During the spinning process, the voltage applied was 15 kV, the distance from the needle to the collector was 15 cm and the flow rate was 0.3 mL/h. A regular needle with the inner diameter of 1 mm or a coaxial needle manufactured in AISI 316 stainless steel were used. As collectors a grounded collector wrapped in aluminium foil, a drum rotary collector (drum speed was 200 rpm) or a liquid collector (DI water at room temperature) were employed. The temperature during processing was kept at 23 ± 2 °C, and the relative humidity of the air was 50 ± 5 %.

5.2.2 Solution blow spinning

A home-made solution blow spinning (SBS) apparatus was design and employed to produce the membranes and the 3D fibrous structures. For the preparation of the polymeric membrane on a flat non-conductive collector, the following parameters were used: the feed rate of the polymer solution was set to 50 mL/h, and a pressure of 0.6 MPa was applied to drive the solution through the needle. The needle-to-collector distance was maintained at 15 cm, and the spinning process was carried out for 30 seconds.

The SBS process was also performed on a liquid collector (DI water at room temperature). In this latter case, the setup remained the same, except for a few parameter adjustments. The feed rate and the pressure were maintained at 50 mL/h and 0.6 MPa respectively. However, the needle-to-collector distance was reduced to 10 cm, and the blow spinning time was limited to 10 seconds. After the membrane was formed on the liquid collector, it was carefully collected from the water surface

and pressed using a perforated metallic plate to create a fluff-like device. The membranes were shaped into cylindrical structures with a height of 5 mm and a diameter of 3 mm.

5.2.3 Melt mixing

MB and PLA were melt-mixed - separately or together - with the different fillers using an internal mixer (Brabender, Germany; T = 160 °C for MB and MB/PLA, T = 190 °C for PLA, rotor speed = 64 rpm, t = 3 min) aiming to produce a homogeneous compound.

5.2.4 Extrusion

The formulations obtained through melt mixing were then extruded using a Haake Polylab, Germany single-screw extruder equipped with a cylindrical nozzle (thermal profile of 130–140–150–160 °C for MB and MB/PLA and 160–170–180–190 °C for PLA). A conveyor belt system (6 m/min) was used to draw the output extrudate, obtaining filaments with a diameter of ~ 1.75 mm.

5.2.5 Compression Moulding

The compression-moulded samples (CM) were obtained using a laboratory press (Carver, Wabash, IN, USA). All the MB based samples were pressed at 160 °C, while PLA based ones at 190 °C. For all the sample a pressure of 180 bar for 2 min was adopted.

5.2.6 3D-printing

The design of printed samples was shaped using CAD Solid Edge 2019® software. The obtained STL files were elaborated on Simplify3D® software to gain gcode files. The specimens were

printed using a Sharebot Next Generation (Italy) 3D printer. The adopted 3D printing parameters, common for all the experimental works, are summarized in Table 3.1. For the different formulations, the nozzle temperature was selected, after some trials, to avoid nozzle obstructions, while bed temperature was optimized to achieve good adhesion of the sample during printing process. The infill rate and the infill pattern were chosen, for each experimental work, aiming to promote pollutant removal ability and to optimize the mechanical performance.

Table 3.1 *3D printing process parameters common for all the experimental works.*

Parameter	Value
Nozzle diameter	0.4 mm
Bed temperature	60, 90, 60 °C
Infill pattern	Rectilinear
Layer thickness	0.1 mm
Extrusion width	0.4 mm
Printing speed	50 mm/s
Perimeter shells	4

5.3 Characterizations

5.3.1 Morphological analysis

Morphological analysis of natural particles, composites filaments, 3d printed samples and fibrous membranes was performed through Phenom ProX (Phenom-World, The Netherlands) scanning electron microscope (SEM) with electron magnification range of 80–130000x, optical magnification range of 20–135x, acceleration voltages of 15 kV and a maximal digital zoom of 12x.

Fibers diameter size distribution was measured using Image J software, equipped with Diameter J plugin. The diameters of 100 fibers for each SEM image were measurement. Each measurement was performed in triplicate.

5.3.2 Fourier transform infrared spectroscopy (FTIR)

FT-IR/ATR analysis were carried out by using a Perkin-Elmer FT- IR/NIR Spectrum 400 spectrophotometer. The spectra were recorded in the wavenumber range 4000 – 400 cm^{-1}.

5.3.3 Rheological behaviours

Rheological properties of the samples were analyzed, using a rotational rheometer (ARES-G2, TA Instruments, New Castle, PA, USA) equipped with a 25 mm parallel-plate geometry. All the tests were performed at 160 °C for MB series and 240 °C for PLA series, in frequency sweep mode in the range 0.1–100 rad/s or 1–100 rad/s, by imposing a constant stress of 1 Pa.

5.3.4 Dispersions conductivity

Conductivity meter (Xylem, Weilheim in Oberbayern, Germany) was used to test the conductivity of the polymeric dispersions.

5.3.5 Mechanical characterization

Tensile properties of the samples were investigated by tensile tests, carried out with a using a laboratory dynamometer (mod.3365, Instron, Norwood, MA, USA) equipped with a 1 kN load cell. The tests were performed on rectangular shaped specimens as described above. The measurements were performed by using a double crosshead speed: 1 mm min^{-1} for 2 min and 50 mm min^{-1} until fracture occurred. The grip distance was 30 mm whereas the sample thickness was measured before each test. Eight specimens were tested for each sample.

Tensile modulus was calculated as the slope of the initial linear portion of the stress-strain curve, tensile strength (TS) and elongation at break (EB) were calculated as the maximum stress and the maximum strain before failure. Toughness (k), calculated as the area under stress-strain curve, Eqn. 3.1:

$$k = \int_0^{\varepsilon_b} \sigma(\varepsilon) d\varepsilon \quad (3.1)$$

Where ε is the strain, ε_b is the strain upon failure, σ is the stress and k represents the energy absorbed from each material (per unit of volume) without breaking.

Flexural tests in three-point bending mode were performed according to the ASTM D790 standard, by using the same apparatus under the same environmental conditions, aiming to measure the flexural modulus (FM) and flexural strength (FS). Flexural strength (FS) was calculated according to Eqn. 3.2:

$$FS = \frac{3F_{max}L}{2bh^2} \quad (3.2)$$

Where F_{max} is the maximum applied force expressed in N, L is the span between the supports in mm, whereas b and h are respectively the width and thickness of the specimen, expressed in mm. Flexural break (FB) is the maximum flexural strain, calculated according to Eqn. 3.3:

$$FB = \frac{6hd_{max}}{L^2} \quad (3.3)$$

Where $d_{max}$is the maximum deflection (mm). Flexural modulus was calculated as the slope of the linear portion of the load deflection curve. Flexural toughness was calculated in the same manner as indicated for tensile testing.

Impact tests in Charpy mode were performed using a pendulum model 9050 by CEAST (Italy), according to the ASTM D6110 standard, to evaluate impact strength (IS).

For the fibrous membranes tensile tests were performed on rectangular shaped specimens (10 × 60 mm) cut off from the membranes. A dual crosshead speed was used: 1 mm min^{-1} for 2 min and 50 mm min^{-1} until fracture occurred. The grip distance was 30 mm, whereas the sample thickness was measured before each test. Five specimens were tested for each sample and the outcomes of elastic modulus (E), tensile strength (TS), and elongation at break (EB) have been reported as average values ± standard deviations.

5.3.6 X-ray Diffraction

X-ray diffraction patterns were collected by using a RIGAKU diffractometer (model: D-MAX 25600 HK, Rigaku, Tokyo, Japan). All diffraction patterns were obtained in the 2θ range from 5° to 80° by means of copper Kα radiation (λ = 1.54 Å) with the following setup conditions: tube voltage and current of 40 kV and 30 mA, respectively, scan speed of 4°/min with a sampling of 0.004°.

5.3.7 Thermal properties

Differential scanning calorimetry (DSC) analysis was performed on the polymeric matrices using a Chip-DSC 10 (Linseis Messgeraete GmbH, Selb, Germany). The samples were heated to 200 °C at a heating rate of 20 °C/min. Nitrogen was used as a shielding gas to avoid polymer degradation. Traces analysis was carried out using Linseis and GraphPad Prism 9 software.

5.3.8 Nanoindentation of powder

Elastic modulus of the powders were testes using an Anton Paar NHT2 nanoindenter (CSM Instruments, Switzerland) equipped with a Berkovich diamond indenter, following Baraldi et al. method [124]. In brief, SLP and NPK particles suitable for the test were selected using an optical microscopy (Leica MS5 stereo microscope, Wetzlar, Germany) and glued on a dedicated square glass slide. The indentation experiments were performed using the following protocol: a loading ramp of 30 s, a 30 s dwell period at maximum load (15.00 mN), and a final unloading step lasting 30 s. Measures were repeated at least six times, the average values and the standard deviations were calculated.

5.3.9 Density measurements

Density measurements were performed by a Thermo Pycnomatic Helium Pycnometer (Pycnomatic ATC, Thermofisher, USA), using a 99.99% pure Helium. Measures were repeated at least six times for each sample, at 25 °C.

5.3.10 Water Contact Angle (WCA) Measurements

Surface wettability of fibrous membranes bio-composites and pure matrices was determined through WCA testing (First Ten Angstroms FTA 1000, UK). An automatic liquid drop dosing system drips 4 µL of distilled water onto the samples and after 20 seconds images were taken. Five different spots of each sample were tested and WCA values have been reported as average values ± standard deviations.

5.3.11 Microbiological Analysis

A sample (10 g) of fish bones in powder form was subjected to the analysis of the main microbiological (pathogenic and environmental contaminant) groups associated to food matrices. Powdered fish bones were suspended in 90 ml of Ringer's solution (Sigma-Aldrich, Milan, Italy) and homogenized through a stomacher (BagMixer® 400, Interscience, Saint Nom, France) for 2 min at the highest speed. Cell suspensions were then inoculated in agar media as follows: plate count agar (PCA) incubated aerobically at 30°C for 72 h for total mesophilic microorganisms (TMM); Listeria selective agar base (LSAB) supplemented with SR0140E incubated aerobically at 37°C for 24 h to count and preliminary identify Listeria spp. and Listeria monocytogenes; Baird Parker (BP) supplemented with rabbit plasma fibrinogen incubated aerobically at 37°C for 48 h for coagulase-positive staphylococci (CPS); Hektoen Enteric Agar (HEA) incubated aerobically at 37°C for 24 h for Escherichia coli and Salmonella spp.; de Man-Rogosa-Sharpe (MRS) acidified at pH 5.4 with 5 M lactic acid incubated anaerobically at 30 °C for 48 h for mesophilic rod lactic acid bacteria; M17 incubated anaerobically at 30 °C for 48 h for mesophilic coccus lactic acid bacteria; yeast-extract peptone dextrose (YPD) supplemented with chloramphenicol (0.1 g/L) incubated aerobically at 25°C for 48 h for yeasts; potato dextrose agar (PDA) supplemented with chloramphenicol (0.1 g/L) incubated aerobically at 25°C for 48 h for molds. Fishbone powder was also evaluated for the

presence of spore forming bacteria after treating all cell suspensions at 85°C for 15 min. Aliquots of 0.1 mL were collected from each test tube and spread onto nutrient agar (NA) medium. Colony count occurred after incubation at 32°C for 48 h [125]. Anaerobiosis occurred in hermetically sealed jars equipped with the AnaeroGen AN25 sachets (Oxoid). All microbiological analyses were performed in duplicate.

5.3.12 UV protection performance test

UV–visible spectrophotometer (model UVPC 2401, Shimadzu Italia s.r.l., Milan, Italy) was utilized to measure the UV transmittance of the filtering membranes, with test wavelengths ranging from 200 to 400 nm. The UV protection ability of the natural fillers incorporated in the membranes was determined by comparing the fiber morphology (SEM analysis) before and after irradiation with an ultraviolet lamp (OSRAM, 315-400 nm UVA and 280-315 nm UVB), with an irradiation distance of 1 cm and an irradiation time of 2, 4 and 8 h in a climatic chamber set at 25 °C.

5.3.13 Release of NPK fertilizer

NPK release from the composites was investigated at specific time intervals by submerging pre-weighed specimens (60 mm x 10 mm × 1 mm, 0.7 g) in 50 mL of DI water at 25 °C. All the samples were immersed in 50 ml of fresh DI water after each measurement. Electrolyte resistance of the obtained solution was evaluated through electrochemical impedance spectroscopy (EIS) using an AMETEK potentiostat/galvanostat (model PARSTAT 2273) and Power Suite software. To perform the measurements a three-electrode cell was used, equipped with a gold working electrode, a platinum plate applied as the counter electrode and a saturated Ag/AgCl as the reference electrode. EIS measurements were carried out at a frequency range from 100 kHz to 100 mHz, and potential

amplitude of ±10 mV peak-to-peak versus open circuit potential (OCP). The electrolyte resistance (R) of solutions was then converted in conductivity (C) according to the equation 3.4:

$$C = \frac{1}{\rho} = \frac{R \cdot S}{l} \quad (3.4)$$

Where ρ is the resistivity, l is the length and S the cross-sectional area of the working electrode.

Control experiments were performed using free NPK (same amount present in composites) and biopolymeric matrix (without NPK). Each measurement was performed in triplicate.

Final conductivity value of free NPK was considered as 100% release and used as a standard for obtain the amount of NPK released from the devices.

5.3.14 Statistical analysis

Data obtained underwent statistical analysis with an unpaired Student t-test using GraphPad Prism 9. Statistical significance was attributed to differences between datasets when the p-value obtained was lower than 0.05 (**** $p < 0.0001$; *** $p < 0.001$; ** $p < 0.01$).

5.4 Pollutant removal performances

5.4.1 Air filtration

Air filtration performance of the membranes was evaluated on a homemade filtration test system by simulating a polluted air environment. In Figure 3.1 a schematic representation of the filtration test system is depicted. Chamber (A) and chamber (B) represent upstream and downstream chambers respectively, while the testing membrane is placed in between. More in detail, to evaluate the air filtration performance, the membranes of 100 μm thickness were fixed into a filter holder in the middle of the filtration setup. Burning incense was used to generate the particles (PMs), with particles size ranging from 0.3 μm to 3 μm, aiming to simulate a polluted air environment. The produced particles were delivered through the membranes by inject air at different flow rate (10, 32, 65, 85 L/min) in the upstream chamber (A). The particle counters (SEK-SVM4x, Sensirion, Switzerland) were used to determine the particle concentrations in the two chambers i.e. in upstream (A) and downstream (B) of the tested membrane. The micromanometer (SDP810-500PA, Sensirion, Switzerland) was used to measure the air resistance of the filter (ΔP), i.e., the difference between upstream and downstream of the test membrane. The filtration efficiency of PMs (η) was calculated according to Equation (3.5):

$$\eta = \left(1 - \frac{C_1}{C_2}\right) \times 100 \quad (3.5)$$

where C_1 and C_2 represented the PM concentration respectively in the downstream airflow and upstream airflow through the tested membrane. The PMs counting concentration was measured for 2 min and each group of membranes was tested in triplicate. Aiming to comprehensively evaluate

of the filtration performance of the membranes, the quality factor (QF) of the filtering membranes was calculated according to Equation (3.6):

$$QF = -\frac{ln(1-\eta)}{\Delta P} \quad (3.6)$$

where η represents the filtration efficiency and ΔP represents the pressure drop.

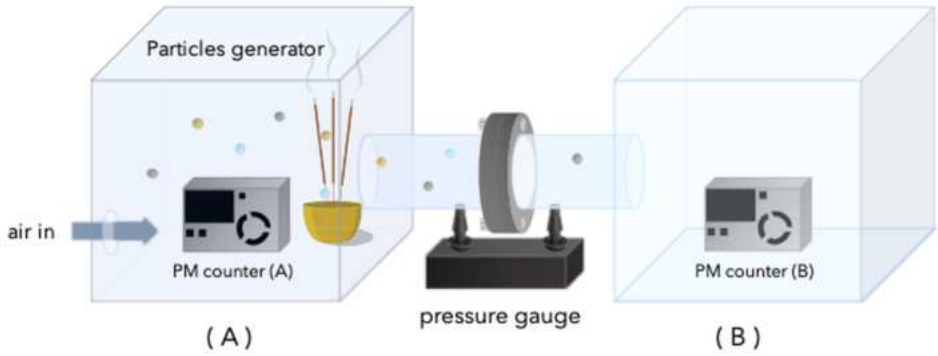

Figure 3.1 *Schematic illustration for the implemented homemade filtration test. Chamber (A) and chamber (B) represent upstream and downstream chambers respectively.*

The filtration abilities of the membranes were tested at different temperatures (35, 25, 15 °C) and relative humidity (RH, 30, 60, 80%) conditions. Air conditioners and a humidifier were employed to tune the environmental condition during the experiments. Additionally, the filtration efficiencies of the membranes were tested for five cycles to evaluate their possibility to be reused. After each cycle the membranes were cleaned by submerging them in a 70:30 water/ethanol mixture, to remove the PM deposited on the fibers. Before testing again for filtration, the membranes were left to air dry for 2 hours.

5.4.2 Wastewater treatment

5.4.2.1 Oil Spill Clean-up

The absorption capacity of fibrous membranes was evaluated by placing about 0.15 g of electrospun mat in a beaker filled with 25 g of water and 50 g of oil and taken out instantaneously. The excess oil present on the fibers, not really adsorbed by the membrane, was drained out for 30 seconds. All the experiments were carried out in triplicate.

The absorption capacity (q) have been calculated by the equation 3.7:

$$q\ (g/g) = \frac{W_a - W_i}{W_i} \quad (3.7)$$

where W_i is the initial weight of the membrane and W_a is the weight of the membrane after oil absorption. Additionally, the oil absorption ability of the electrospun membranes was monitored for five cycles to evaluate the possibility to reuse them. After each absorption cycle the membranes were squeezed with padding paper and washed with ethanol to remove the absorbed oil. After each cleaning step the membranes were left to air dry for 1 hours and reweighted. This weight was taken as a new dry reference for absorption capacity measurement. To evaluated reusability of the membranes, q variations were calculated and considered.

5.4.2.2 Methylene Blue Sorption

To perform sorption tests of the fluff, aqueous solutions of 5 mg/L of Methylene Blue (MBL) was prepared. For each experimental run, 4 fluff were immersed into 5 mL of solution. The sorption capacity of samples was assessed by monitoring at predetermined time intervals the residual pollutant concentration via UV–vis spectroscopy, carried out by using UV/ vis spectrophotometer (model UVPC 2401, Shimadzu Italia s.r.l., Milan, Italy). Absorbance values of the characteristic signals were

converted into concentrations by using opportunely constructed calibration curve. Previously, a series of aqueous solutions containing a known amount of the pollutant were analyzed in order to obtain a calibration line. The removal efficiency (%) of the samples was calculated according to equations (3.8):

$$\text{Removal efficiency} = \text{RE}\ (\%) = \frac{C_i - C_f}{C_i} \times 100 \quad (3.8)$$

where C_i (mg/L) and C_f (mg/L) are the concentration of the pollutant before and after adsorption tests. All the experiments were carried out in triplicate.

5.4.2.3 FOG (Oil-Water) Separation

For fat, oil and greases (FOG, oil-water) separation tests, a sample of wastewater from a local waste remediation plant was used. Firstly, solid wastes were filtered from the kitchen wastewater sample aiming to obtain the oil in water emulsion of FOG. For each experimental run, 0.8 g of fluff were immersed into 50 mL of emulsion under vigorous stirring and a temperature of 50 °C. The separation of the oil-in-water emulsion was evaluated using a UV/ vis spectrophotometer (model UVPC 2401, Shimadzu Italia s.r.l., Milan, Italy). The removal efficiency (%) of the samples was calculated according to equations (3.9):

$$\text{Removal efficiency} = \text{RE}\ (\%) = \left(1 - \frac{A_i}{A_f}\right) \times 100 \quad (3.9)$$

where A_i and A_f represent the areas under the UV absorption curve before and after adsorption tests. All the experiments were carried out in triplicate.

5.4.3 Heavy metal absorption

The metals ions adsorption capability was assessed by submerging the devices in 50 mL of metals aqueous solutions (1000 mg/L) at a room temperature for 30 days. The metal concentration in the collected aliquots was assessed by using UV/ vis spectrophotometer (model UVPC 2401, Shimadzu Italia s.r.l., Milan, Italy). Previously, a series of aqueous solutions containing a known amount of the selected metal ion were analyzed in order to obtain a calibration line. The maximum absorbance band of $CuSO_4$ water solution was detected at 810 nm; for $MnCl_2$ at 250 nm; for $NiSO_4$ at 395 nm and for Fe_2O_3 at 400 nm. The removal efficiency (%) of the samples was calculated according to equations (3.10):

$$\text{Removal efficiency} = \text{RE}\ (\%) = \frac{C_i - C_f}{C_i} \times 100 \quad (3.10)$$

where C_i (mg/L) and C_f (mg/L) are the concentration of the heavy metal before and after adsorption tests. All the experiments were carried out in triplicate.

The surface composition of 3D-printed samples with adsorbed metal ions were collected and analyzed by Energy Dispersive X-ray (EDX) analysis by using an EDX probe during SEM imaging to detect the presence of the metal.

5.5 Mathematical Models

5.5.1 Kinetic Models

To understand the kinetics of methylene blue adsorption onto the fibrous fluff, two widely used models, the pseudo-first-order (PFO) and pseudo-second-order (PSO) models, were applied to the experimental data. The PFO kinetic model assumes that the rate of occupation of adsorption sites is proportional to the number of unoccupied sites, and it was calculated according to equations (3.11):

$$\ln(q_e - q_t) = \ln q_e - k_1 t \quad (3.11)$$

where q_e (mg/g) is the amount of methylene blue adsorbed at equilibrium, q_t (mg/g) is the amount of methylene blue adsorbed at time t, and k_1 (min^{-1}) is the rate constant of the pseudo-first-order model.

The PSO kinetic model is based on the assumption that chemisorption is the rate-limiting step, and it is described by the following equation (3.12):

$$\frac{t}{q_t} = \frac{1}{k_2 q_e^2} + \frac{1}{q_e}\,\mathrm{t} \quad (3.12)$$

where k_2 (g/mg·min) is the rate constant of the pseudo-second-order model.

The experimental data were fitted to both the PFO and PSO models using nonlinear regression. The best-fitting model was selected based on the correlation coefficient R^2 and the comparison of predicted (by the model) versus experimental q_t values. The rate constants k_1 and k_2 and the equilibrium adsorption capacities q_e were determined for both models.

5.5.2 Halpin-Tsai Model

Halpin-Tsai model allows esteeming the modulus of composites once are known volume fractions and elastic moduli of the starting components, and the filler aspect ratio. According to Halpin-Tsai model, for composites reinforced with fibers randomly oriented, the composite modulus $E_{C,HT}$ is determined by the following equation (3.13) [126]:

$$E_{C,HT} = \frac{3}{8}E_L + \frac{5}{8}E_T \quad (3.13)$$

Where E_L and E_T are respectively the longitudinal and transverse moduli of the composite.

In this case, E_L and E_T are given by:

$$E_L = E_m\left[\frac{1 + (2\,l/d)\eta_L \upsilon_f}{1 - \eta_L \upsilon_f}\right] \quad (3.14) \qquad E_T = E_m\left[\frac{1 + 2\eta_T \upsilon_f}{1 - \eta_L \upsilon_f}\right] \quad (3.15)$$

Where υ_f and υ_m are the volume fractions of fillers and matrix respectively, l/d is the aspect ratio of the fillers while η_L and η_T are constants given by:

$$\eta_L = \frac{(E_f/E_m) - 1}{(E_f/E_m) + (2\,l/d)} \quad (3.16) \qquad \eta_T = \frac{(E_f/E_m) - 1}{(E_f/E_m) + 2} \quad (3.17)$$

Where, E_f and E_m are respectively the Young's moduli of filler and matrix.

In a ternary composite, Halpin-Tsai equation can be rewritten as follows [127]:

$$\frac{E_{C,HT}}{E_m} = \frac{3}{8}\,\frac{1 + \left(\frac{2L_{SLP}}{d_{SLP}}\right)\eta_{L,SLP}V_{SLP} + \left(\frac{2w_{NPK}}{3t_{NPK}}\right)\eta_{L,NPK}V_{NPK}}{1 - \eta_{L,SLP}V_{SLP} - \eta_{L,NPK}V_{NPK}} + \frac{5}{8}\,\frac{1 + 2\eta_{T,SLP}V_{SLP} + 2\eta_{T,NPK}V_{NPK}}{1 - \eta_{T,SLP}V_{SLP} - \eta_{T,NPK}V_{NPK}} \quad (3.18)$$

Where $E_{C,HT}/E_m$ is the reduced tensile modulus, expressed as the ratio between the moduli of composite ($E_{C,HT}$) and matrix (E_m). Moreover, for fibrous-like SLP, *l* and *d* respectively indicate length and diameter, whereas for cube-shaped NPK, *w* and *t* respectively indicate the length of a side and thickness of particles, η_L and η_T are constants given by:

$$\eta_{L,SLP} = \frac{(E_{SLP}/E_m) - 1}{(E_{SLP}/E_m) + \left(\frac{2L_{SLP}}{d_{SLP}}\right)} \quad (3.19) \qquad \eta_{T,SLP} = \frac{(E_{SLP}/E_m) - 1}{(E_{SLP}/E_m) + 2} \quad (3.20)$$

$$\eta_{L,NPK} = \frac{(E_{NPK}/E_m) - 1}{(E_{NPK}/E_m) + \left(\frac{2w_{NPK}}{3t_{NPK}}\right)} \quad (3.21) \qquad \eta_{T,NPK} = \frac{(E_{NPK}/E_m) - 1}{(E_{NPK}/E_m) + 2} \quad (3.22)$$

Volume fractions are determined from the weight fractions and the densities of each component measured experimentally by helium pycnometer, whereas elastic moduli are those obtained.

5.5.3 Peppas-Korsmeyer Model

The obtained release data were fitted according to the Peppas-Korsmeyer equation (3.23):

$$\frac{M_t}{M_\infty} = K\, t^n \quad (3.23)$$

Where M_t is the total amount of fertilizer released at time t, and M_∞ is the theoretical amount of NPK incorporated in the composites. NPK release data were fitted according to equation (3.23) in order to determinate drug transport constants (K) and transport exponents (n) of the different formulations in the range of M_t/M_∞ 0–60% [128].

Chapter 4

Result and Discussion

6.1 Air

6.1.1 Stable and Reusable Electrospun Bio-Composite Fibrous Membranes based on PLA and Natural Fillers for Air Filtration Applications

The subsequent text and images have been fully extracted from the published article authored by the candidate "R. Scaffaro, M.C. Citarrella, Stable and reusable electrospun bio-composite fibrous membranes based on PLA and natural fillers for air filtration applications, Sustainable Materials and Technologies (2024) e01146. https://doi.org/10.1016/J.SUSMAT.2024.E01146 [129]" and are reproduced here with the necessary permissions from Springer Nature.

Author contribution: Writing – review & editing, Writing – original draft, Visualization, Validation, Software, Methodology, Investigation, Formal analysis, Data curation, Conceptualization.

6.1.1.1 Abstract

Today, air pollution due to fine dust is one of the most critical environmental challenges. To mitigate the potential further environmental impact of air filtration devices, it is essential to explore the use of biodegradable polymers combined with natural fillers, preferably sourced from waste materials, to develop stable, reusable and UV-resistant air filters suitable for outdoor applications. In this work, composites fibrous membrane based on polylactic acid (PLA) and natural fillers were prepared via electrospinning and tested for air filtration applications. Air filtration performances were

evaluated at different flow rate, temperature and humidity condition, aiming to simulating outdoor conditions. The addition of 10 wt% of *Opuntia Ficus Indica* (OFI), *Posidonia Oceanica Leaves* (POL) or lignin (LIG) particles to PLA solution led to a decrease in fibers diameter increasing membranes filtration performances. PLA/OFI, PLA/POL and PLA/LIG composites membranes exhibited filtration efficiencies of 97.2%, 99.4%, 99.6% for PM_3 at a flow rate of 32 L/min, and pressure drops of 114, 103, 105 Pa, respectively. The membranes demonstrated stability maintaining good filtration efficiency across different environmental conditions and after multiple reuse cycles. The addition of OFI and LIG powders also provided effective UV resistance, crucial for ensuring the longevity and performance of air filters exposed to outdoor conditions. These findings underscore the potential of these biodegradable composite membranes for sustainable indoor and outdoor air filtration solutions.

6.1.1.2 Preparation of PLA/fillers dispersions and membranes

Firstly, OFI cladodes and POL scraps were washed in water at room temperature and dried in an oven at 60 °C for 48 hours. The two scraps were then chopped and roughly ground for 3 minutes. Subsequently, OFI, POL and LIG particles were ball-milled (Retsch MM 500 nano, Germany) for 30 minutes at 20 Hz aiming to obtain micrometric powder. PLA solution (10 wt%) was prepared using Chl/Ac mixture (2:1 ratio). After the PLA was completely dissolved, 1, 3, 5, 10 and 15 wt% (with respect to PLA mass) of OFI, POL and LIG powders, were separately dispersed in the PLA solution (Figure 4.1.1.1a, b) keeping them under magnetic stirring at 25 °C overnight. Preliminary electrospinning tests were performed on all the composites PLA dispersion. For the dispersion containing 1, 3, 5 and 10 wt% of the natural particles, no clogging of the needle (1 mm diameter) was observed during the electrospinning process. However, for 15 wt% dispersions, the spinning process experiences frequent interruptions due to the formation of agglomerates of natural particles in the needle, especially for POL containing dispersion. Aiming to maximize the presence of natural

particles in the filtering membranes and thus potentially increase fibers roughness and the chances of PMs to be caught on them [130], 10 wt% composite solutions were selected and labeled as PLA/OFI, PLA/POL and PLA/LIG respectively.

The production of composite fibrous membranes was carried out using the electrospinning technique (Figure 4.1.1.1c) with a conventional equipment consisting of a syringe pump and a high voltage power supply (Linari Engineering-Biomedical Division, Pisa, Italy). During the spinning process, the voltage applied was 15 kV, the inner diameter of the needle was 1 mm and the distance from the needle to the drum was 15 cm. The flow rate was 0.3 mL/h, and the drum speed was 200 rpm. The temperature during processing was kept at 23 ± 2 °C, and the relative humidity of the air was 50 ± 5 %. The obtained fibrous membranes were then dried at room temperature for 24 h to remove any residual solvent. According to the starting dispersions, the membranes were labeled PLA, PLA/OFI, PLA/POL and PLA/LIG (1c).

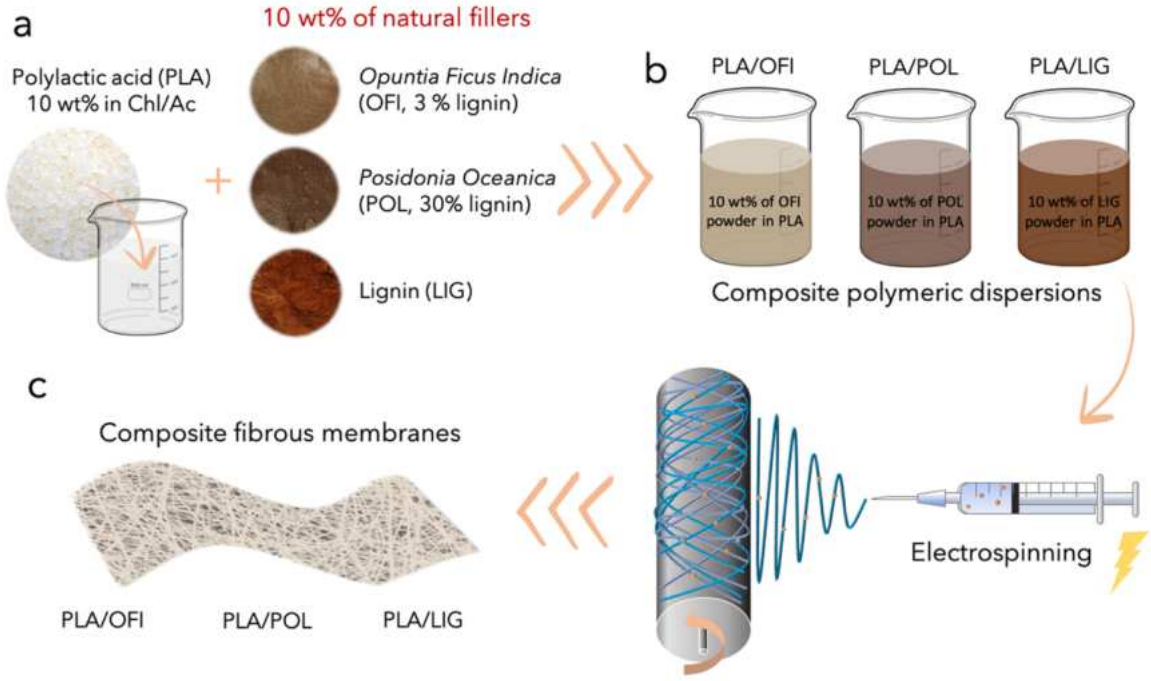

Figure 4.1.1.1 *Schematic illustration for the preparation of the composite membranes: (a) preparation of the composite dispersions; (b) composition of PLA/OFI, PLA/POL, and PLA/LIG dispersions; (c) fabrication of PLA/OFI, PLA/POL, and PLA/LIG composite fibrous membranes via electrospinning.*

6.1.1.3 Morphology of natural particles

The morphology of OFI, POL and LIG particles, after the ball-milling process, was analyzed by SEM and show in Figure 4.1.1.2a-c, while the respective particles size distribution, in terms of equivalent diameter, are reported in Figure 4.1.1.2a'-c'.

OFI and LIG particles (Figure 4.1.1.2a, c) are both characterized by a fairly spherical shape and an average diameter of about 2.5 μm (Figure 4.1.1.2a', c'). As desired, the use of ball milling allowed obtaining powders characterized by particles size in the range of few micrometer, likely facilitating the electrospinning process. However, while LIG particles are quite homogeneous in dimensions and shape, OFI powder also present few bigger and elongated particles. On the other hand, POL particles are less inclined to be reduced into spherical particles of a few micrometers during ball milling process, as shown in Figure 4.1.1.2b. In this case, irregularly shaped particles with an average diameter of about 8 μm (Figure 4.1.1.2b') are obtained, but some particles as large as 100 μm can be also noted. Differently from OFI and LIG ones, POL particles are, furthermore, characterized by a porous structure with deep channels along their entire surface. However, it can be concluded that OFI, POL and LIG powders seems to be all dimensionally compatible with electrospinning process.

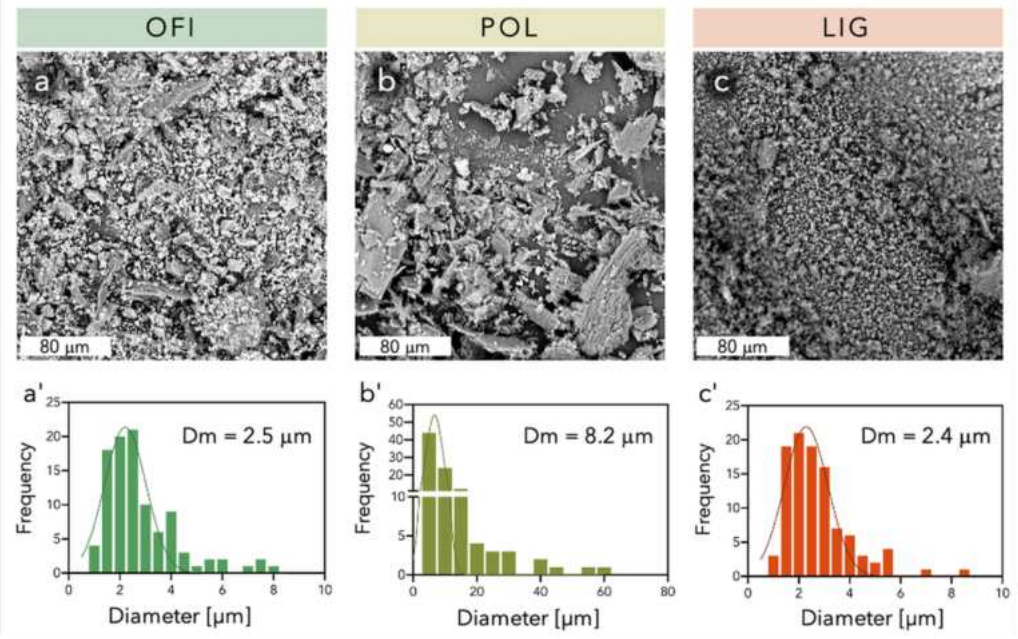

Figure 4.1.1.2 *SEM images and size distribution of OFI (a, a'), POL (b, b'), LIG (c, c') particles respectively.*

6.1.1.4 Electrospun dispersions properties

The properties of the electrospun polymeric dispersions were investigated and results are reported in Figure 4.1.1.3 Generally, in fact, differences in the composition of the spinning solution can affect their viscosity and this, in turn, can modify the morphology of the electrospun fibers [131,132]. Higher viscosity solutions typically result in thicker and more uniform fibers. This is because higher viscosity indicates greater polymer chain entanglement, which resists the stretching forces during electrospinning, leading to larger diameter fibers. Moreover, the increased viscosity stabilizes the jet formed during electrospinning, reducing fluctuations that can cause variations in fibers diameter. Conversely, lower viscosity solutions tend to produce thinner fibers.

As regards rheological tests, neat PLA shows a pronounced non-Newtonian behaviour across the entire frequency range (Figure 4.1.1.3a). When natural particles were added to the PLA solution, a significant increase in viscosity value across the entire frequency range is observed, while the overall rheological behaviour remained unchanged for all the composite dispersions. However, the presence of POL powder induces a higher increase in viscosity value if compared to the other two fillers. This apparently strange behaviour can be attributed to the porous structure of the larger POL particles (Figure 4.1.1.2b), which enhances the interfacial interactions between the polymer and the dispersed phase. In other words, the porous POL particles provide more sites for physical interactions with PLA, contributing to the viscosity increase, as already reported in similar systems [133]. Additionally, the incorporation of solid filler particles increases the effective volume fraction of the dispersed phase in the polymer solution, leading to higher resistance to deformation and increased viscosity [134]. The more rounded shape and lower porosity of OFI and LIG particles (Figure 4.1.1.2a, c) result in a reduced surface area, thus producing fewer interaction sites with the PLA chains, leading to a smaller increase in viscosity.

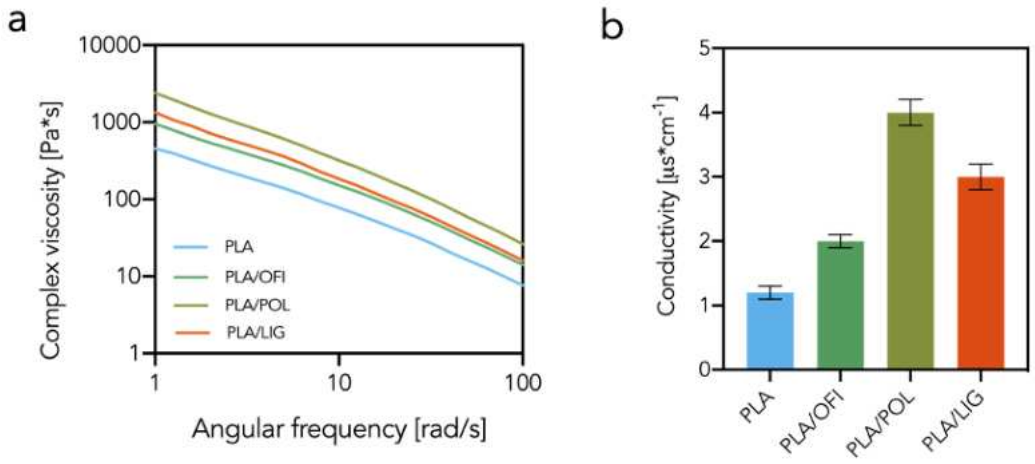

Figure 4.1.1.3 *Complex viscosity (a) and conductivity (b) of electrospun polymeric dispersions.*

Conductivity of the spinning solution is another variable that can influence morphology of the fibers. Higher solution conductivity, in fact, enhances the electric charge carried by the solution, leading to greater stretching forces on the jet during spinning and thus to obtaining thinner and more elongated fibers [131]. Therefore, to verify potential effects of conductivity changes upon adding filler to PLA solution, conductivity measurements were carried out, and results are reported in Figure 4.1.1.3b. The addition of all the fillers leads to an increase in conductivity if compared to the neat PLA solution (1.2 µS/cm). The PLA/POL dispersion displays the highest conductivity value, followed by PLA/LIG, reaching 4.1 and 3.3 µS/cm respectively. To address this issue, it is necessary to consider that when dispersed in polymeric systems, the molecular structure of lignin can release ions by interacting with the solvent and the polymer, increasing the electrical conductivity of the solution [134]. Moreover, the increase in electrical conductivity of the polymeric solution with the increase in lignin content has been extensively reported in the scientific literature [135].

6.1.1.5 Morphology of composite membranes

The electrospinning process proceeded smoothly for all the polymeric dispersion containing 10 wt% of natural particles and no clogging of the needle (1 mm diameter) was observed, even for

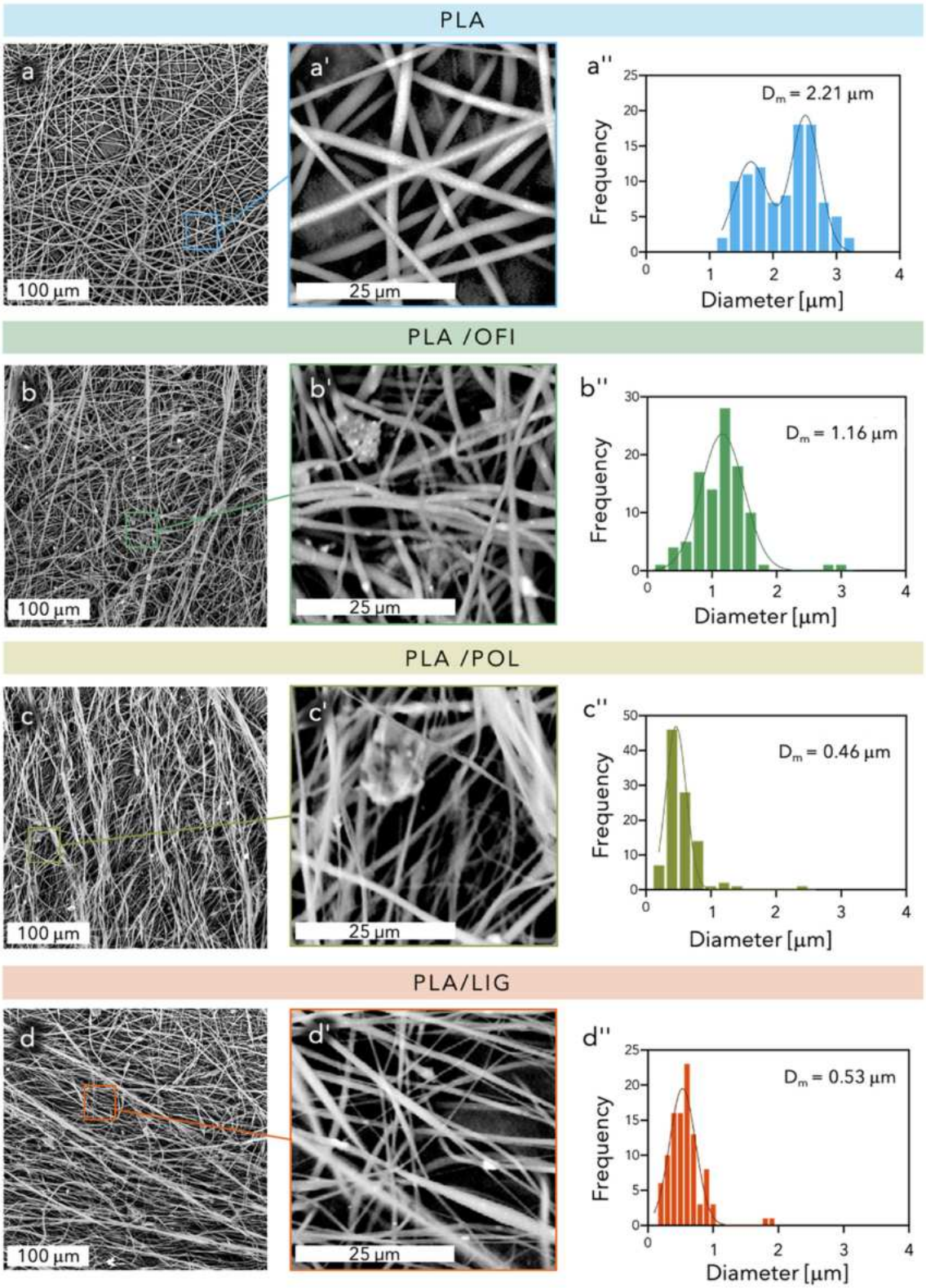

Figure 4.1.1.4 *SEM images, relative insets and fibers diameter distribution of PLA (a, a', a''), PLA/OFI (b, b', b''), PLA/POL (c, c', c'') and PLA/LIG (d, d', d'') membranes respectively.*

PLA/POL that contained the largest particles. The morphology of PLA, PLA/OFI, PLA/POL and PLA/LIG membranes was observed by SEM as shown in Figure 4.1.1.4a-d, while the respective fibers diameter distribution are reported in Figure 4.1.1.4a"-d".

PLA membranes (Figure 4.1.1.4a, a') exhibit smooth and randomly oriented fibers characterized by a bimodal fiber diameter distribution with the mean values of the two modes being 1.65 μm and 2.54 μm and the average diameter of 2.21 μm (Figure 4.1.1.4a"). The addition of natural fillers significantly affects fibers shape according to the different properties of the dispersions. PLA/OFI fibers appear randomly oriented with some OFI particles well distributed all over the membrane, as observed in Figure 4.1.1.4b. This confirms that the particles larger than a few micrometers, which cannot be embedded inside the fibers, were easily ejected through the needle, adhering to the fibers surface and thereby being incorporated into the membrane (Figure 4.1.1.4b'). The presence of these particles could be useful for improving the filtration performance of the membrane [131,132]. Moreover, the presence of OFI powder in PLA solution leads to a significative decrease in the fiber's average diameter and results in a unimodal, wide fiber diameter distribution (Figure 4.1.1.4b"). This behaviour is even more pronounced in PLA/POL and PLA/LIG membranes in which the fibers average diameters reach 0.46 and 0.53 μm respectively and unimodal, narrow fiber diameter distribution is obtained for both the membranes (Figure 4.1.1.4c", d"). Moreover, in PLA/POL and PLA/LIG membranes the fibers appear uniformly oriented and the presence of fibers bundles can be noted (Figure 4.1.1.4c, d). In PLA/POL membranes, POL particles could be extensively identified in SEM image (Figure 4.1.1.4c, c') while LIG ones seems to be almost entirely embedded into PLA fibers (Figure 4.1.1.4d, d').

It is well known in the scientific literature that an increase in viscosity value of the spinning solution usually leads to the formation of fibers with a higher diameter [136]. Surprisingly, this seems to be in contrast to what observed in OFI, POL and LIG composite systems. However, in this study, conductivity of the dispersions seems to predominantly influence fibers morphology. These

variations in the morphology of the membranes, in fact, are compatible with the different conductivity of the relative dispersions.

6.1.1.6 Fibrous composite membranes characterizations

FTIR spectroscopy analysis was performed on the electrospun membranes and the free natural powders to characterize fibers composition, and the obtained spectra are reported in Figure 4.1.1.5a-a'. The FTIR spectra of PLA/OFI, PLA/POL and PLA/LIG membranes closely resembled that of neat PLA. All the spectra show the typical PLA band of the carbonyl group (C ═ O) at 1759 cm^{-1} and the band at approximately 1081 cm^{-1}, corresponding to C–O–C stretching (Figure 4.1.1.5a). Additionally, PLA/OFI membranes displays a band at 1598 cm^{-1}, and PLA/LIG ones are characterized by a band at 1510 cm^{-1} (Figure 4.1.1.5a'). The band at 1598 and 1510 cm^{-1} can be attributed to lignin, in particular to its aromatic skeletal vibration (C ═ C) [137]. These results reasonably confirm that OFI and LIG particles are embedded in the PLA fibers, as already observed in Figures 4.1.4b and 4.1.4d, respectively. The contribution of lignin seems to be less evident in PLA/POL, probably due to the larger dimension of POL particles, which makes it more difficult to embed them in the fibers, as suggested by observing the morphology of the membrane (Figure 4.1.1.4b).

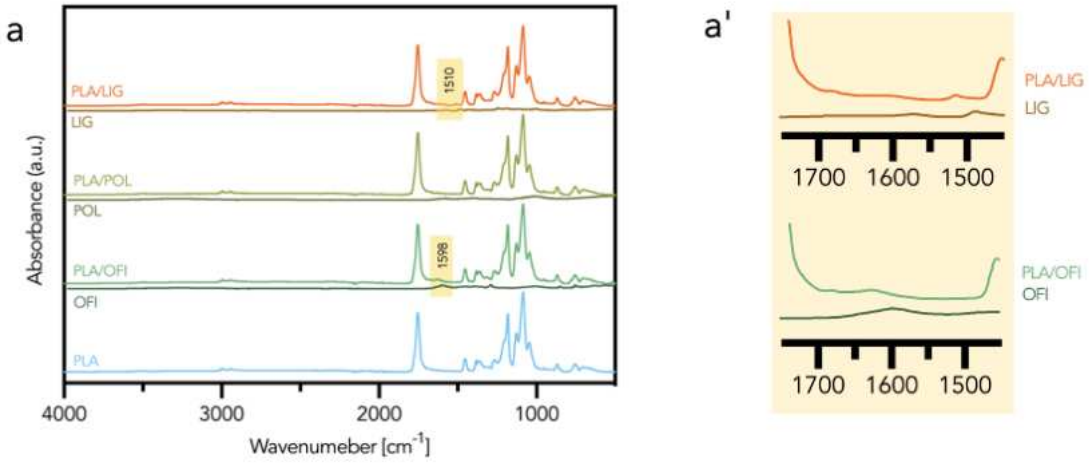

Figure 4.1.1.5 *FTIR spectra of electrospun membranes and relative natural powders (a) with PLA/OFI and PLA/LIG spectra close-up (a').*

Tensile tests were performed on the membranes, and elastic modulus (E, Figure 4.1.1.6a), tensile strength (TS, Figure 4.1.1.6b) and elongational at break (EB, Figure 4.1.1.6c) are reported for all the systems. Adding the natural fillers leads to an increase in E and a corresponding decrease in TS and EB for all the composite membranes. This behaviour can be attributed to the presence of OFI, POL and LIG fillers in/on the PLA fibers. These rigid fillers enhance the overall stiffness of the composite membranes, as evidenced by the higher modulus. However, their presence also introduces potential weakness points, resulting in a reduction of the tensile strength and elongation at break. Moreover, these variations are more pronounced in PLA/POL and PLA/LIG membranes due to their smaller fibers diameter [138]. However, the obtainment of small fibers is crucial for achieve membranes with high filtration performances. Nonetheless, the results suggest that the mechanical properties of all the composite membranes are compatible with air filtration applications [131,132,139].

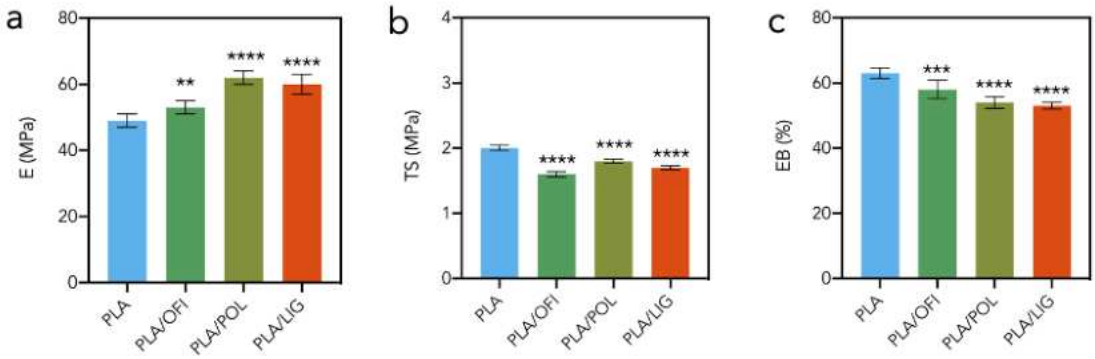

Figure 4.1.1.6 *Elastic modulus (a), tensile strength (b) and elongational break (c) of electrospun membranes. p-value (**** $p < 0.0001$; *** $p < 0.001$; ** $p < 0.01$) obtained thought statistical analysis by t-test.*

6.1.1.7 Electroactivity evaluation

It is extensively reported in the scientific literature that the enhancement of electroactivity of the filtering membranes increase the removal efficiency of PM, especially for PM_1, due to the electrostatic trapping [140–142]. Moreover, the increase of electrostatic attraction is also an effective

method for minimizing pressure drop [143]. Has been proved that the presence of lignin in PLA fibers enhances the electrostatic attraction of the composite membrane due to lignin dielectric properties [144]. As is possible to notice in Figure 4.1.1.7, the addition of POL and especially LIG particles markedly enhances the electrostatic absorption capabilities of the membranes. More in detail, pure PLA membranes exhibit slight electrostatic properties (Figure 4.1.1.7a), characteristics of the material itself [145], and PLA/OFI (Figure 4.1.1.7b) showed electrostatic behaviour comparable to pure PLA one. On the contrary, PLA/POL (Figure 4.1.1.7c) and even more PLA/LIG (Figure 4.1.1.7d), reveal excellent electrostatic adsorption capability. The photos of the membranes surfaces after the electrostatic test are shown in Figure 4.1.1.7e.

The enhanced electrostatic properties of PLA/POL and PLA/LIG membranes can be attributed to the presence of lignin that significantly amplifies the electrostatic charge of the PLA membranes. This phenomenon is due to lignin's inherent capacity to contribute to higher charge density within the polymer matrix. POL containing membranes also exhibit elevated electrostatic properties, due to its higher lignin content compared to OFI one.

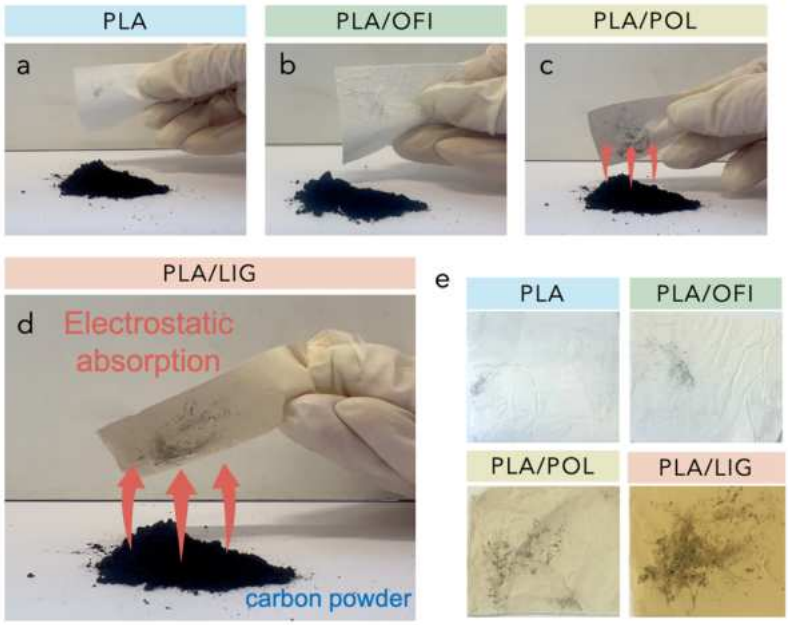

Figure 4.1.1.7 *Frames of digital videos showing carbon powder adsorbed on PLA (a), PLA/OFI (b), PLA/POL (c) and PLA/LIG (d) by electrostatic interactions and relative digital photograph of the membranes after the test (e).*

6.1.1.8 Filtration performances and mechanism of PLA composites membranes

Air filtration efficiency of neat PLA and PLA composite membranes on PM_1 and PM_3 generated from the incense burning were investigated using a self-built filtration device at an airflow rate of 10, 32, 65 and 85 L/min, and the results are reported in Figure 4.1.1.8(a, a'). The pressure drop and the quality factor of the fibrous membranes are shown in Figures 4.1.8b and 4.1.8c, respectively. From Figure 4.1.1.8 (a, a') it is possible to notice that filtration efficiency of the pure PLA membrane decreases from 85.5 % to 80.3 % for PM_1, and from 88.3 % to 82.7 % for PM_3, as the flow rate increased from 10 to 85 L/min. A similar behaviour can be noted for PLA/OFI membrane with the difference that filtration efficiencies generally increase of about 12%, reasonably due to the smaller fibers diameters of this latter membrane if compared to pure PLA one. In contrast to this behaviour, the filtration efficiencies of PLA/POL and PLA/LIG membranes remain almost stable with the flow rate increasing, potentially due to the mitigating effect given by the increase of the electrostatic attraction effect of the membrane on increase the flow rates [145].

In general, the addition of natural fillers leads to an increase in filtration efficiency for all PM dimensions if compared to neat PLA. Regarding 32 L/min flow rate and particulates smaller than 1 μm (PM_1), the filtration efficiency increases from 84.6% of neat PLA to 95.4%, 97.2% and 98.5% of PLA/OFI, PLA/POL and PLA/LIG, respectively. Moreover, with particulate of 3 μm (PM_3), PLA/OFI, PLA/POL, and PLA/LIG display filtration efficiencies of 97.2%, 99.4%, 99.6%.

The decrease in fibers diameters, the presence of natural particles, and the increase of electrostatic attraction allowed PLA/POL and PLA/LIG to achieve the highest filtration efficiency and the lowest pressure drop. The existence of electrostatic interaction between the fibers of PLA/POL and PLA/LIG membranes and PM, in fact, leads to a remarkable increase in removal efficiency, if compare to PLA/OFI membrane one, due to its capacity to strongly attract particles nearby the fibers, especially for fine particles [1].

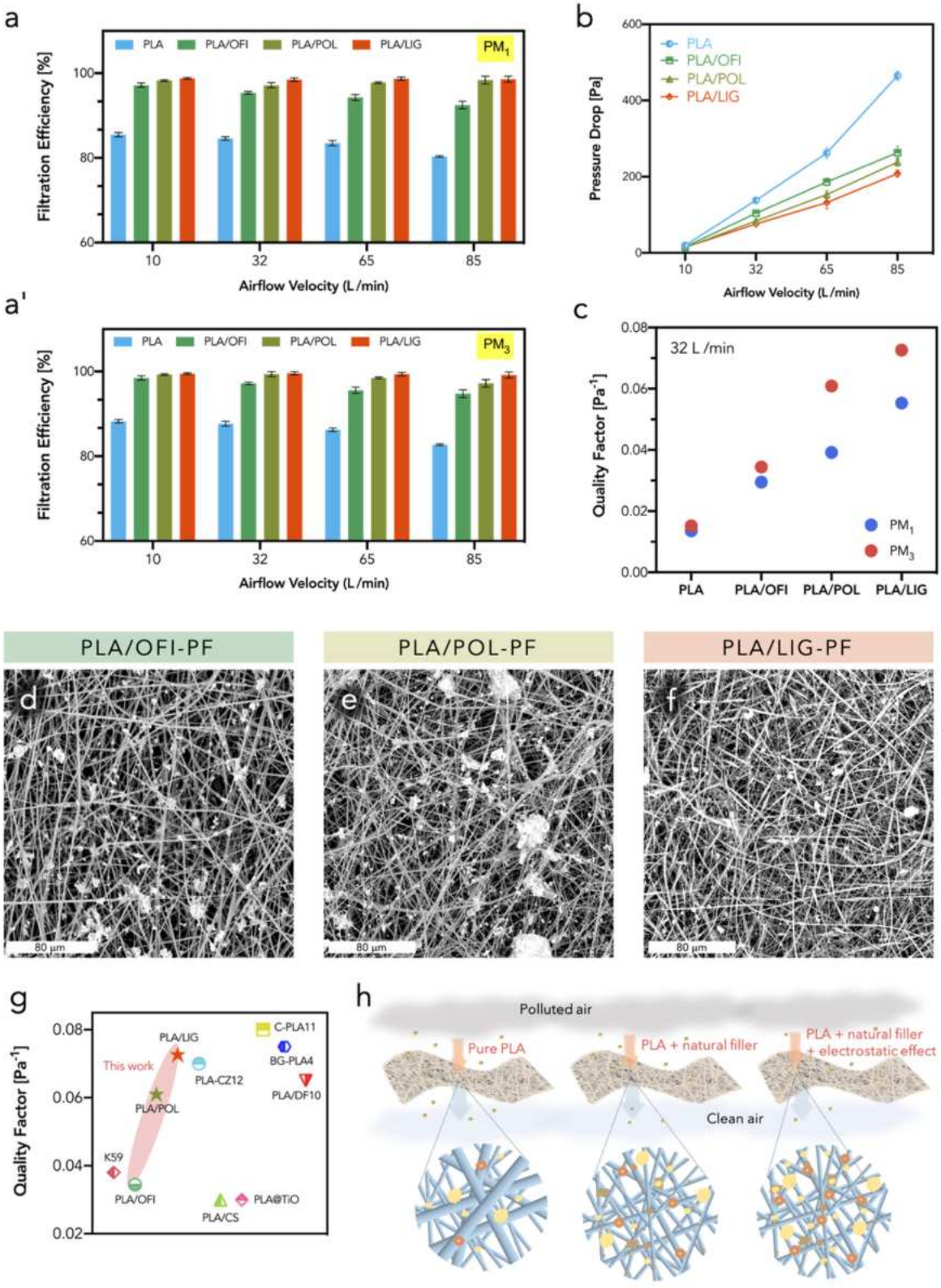

Figure 4.1.1.8. *Filtration performances of the composite membranes: filtration efficiency at different airflow rate for PM_1 (a) and PM_3 (a'); pressure drop at different airflow rate (b). Quality factor of the electrospun membranes for PM_1 and PM_3 (c). SEM images of (d) PLA/OFI, (e) PLA/POL, (f) PLA/LIG membranes after the filtration test (Post Filtration). Comparison of the QF values of this work with commercial filters and other PLA-based membranes under airflow velocity of 32 L/min (g). PMs capture mechanism (h).*

From Figure 4.1.1.8b it is possible to notice that the pressure drop of the membranes decreases when natural fillers were added. At flow rate of 32 L/min, the pressure drops of PLA/OFI, PLA/POL, and PLA/LIG were 104, 84, 76 Pa, respectively, while for pure PLA membrane pressure drop of 138 Pa were registered. The presence of the natural particles in and on the fibers surface less compaction of the membrane and induce fibers roughness, facilitating air passage and leading to an air slip effect that further decrease pressure drops.

Thanks to these behaviours, for PM_3, quality factors of 0.061 and 0.073 are obtained for PLA/POL and PLA/LIG, respectively at flow rate of 32 L/min (see Figure 4.1.1.8c). According to the SEM images, the addition of natural fillers decreases fibers diameter and increases their surface roughness, creating protrusions on the fibers surface, which improves the physical interception of particles by increasing the collision probability between particulates and fibers (Figure 4.1.1.8d-f). This behaviour can be easily observed for PLA/OFI (Figure 4.1.1.8d) and for PLA/POL (Figure 4.1.1.8e) in which this effect is further enhanced by the presence of the large POL particles set on the fibers, which act as accumulation points for the particulate.

The QFs of the produced PLA composites membranes, especially for PLA/POL and PLA/LIG, are extremely encouraging when compared to commercial filters and other PLA-based composite membranes reported in the scientific literature [131,132,140,145–147], as can be observed in Figure 4.1.1.8g. These results are obtained due to the involvement of different filtration mechanisms.

Generally, interception, inertial impaction, sieving and Brownian diffusion can occur during air filtration [1]. As depicted in Figure 4.1.1.8h, the structure of pure PLA membrane is characterized by larger fibers that create a compact structure and low electrostatic attraction (intrinsic characteristic of the material) that allow to obtain quite good filtration efficiency but also very high pressure drop due to the difficulty of airflow passing through it. On the contrary, the presence of fibers with nearly nanometric diameters in PLA/OFI, PLA/POL and PLA/LIG membranes increases the likelihood of particulates colliding with the fibers as they follow the airflow lines. Interception, in fact, is

recognized as primary filtration mechanism. Additionally, the presence of natural filler particles embedded in and on the fibers, induce roughness, further enhances the probability of particle collisions and contextually leads to an air slip effect that reduce pressure drops. Moreover, if the fibers are electrostatically charged, as in the case of PLA/POL and PLA/LIG, it becomes possible to attract nearby particles that do not directly collide with the fibers, securely trapping them on the fibers surface [53,148]. The combination of these filtration mechanisms (see Figure 4.1.1.8h) ensure higher filtration efficiencies.

6.1.1.9 Stability of the composite membranes

The membranes were also tested to evaluate their stability, i.e. to verify eventual changes of filtration efficiency across different environmental conditions, including UV irradiation (Figure 4.1.1.9). In particular, the filtration efficiency was evaluated at different relative humidity levels and temperatures to simulate possible different application scenarios. The filtration efficiency of PM_1 and PM_3 particles for all the membranes were tested at flow rate of 32 L/min. As it is possible to observe in Figures 4.1.9 a and b, across the different membranes, the filtration efficiency remains relatively stable with increasing humidity, particularly for the composite membranes (PLA/OFI, PLA/POL, and PLA/LIG), that maintain high filtration efficiency levels, close to or above 97% for both PM_1 and PM_3 particles for all humidity levels tested. More in detail, when the humidity is less than 60%, the filtration efficiency of all the membranes remains almost unchanged for both PM_1 and PM_3. On the contrary, when the humidity increases to 80%, the filtration efficiency of the PLA/POL and PLA/LIG membranes, for PM_1, slight decreases reasonably due to electrostatic dissipation that can occur at high humidity levels, as already observed in similar systems [140]. However, the filtration efficiency values remain significantly higher if compared with those of pure PLA. For PM_3, the filtration efficiency is almost insensitive to humidity variations (Figure 4.1.1.9a) since the dominant filtration mechanism in this case is mechanical interception of the particulate matter thus the electroactivity variation did not influenced the membranes performances [148].

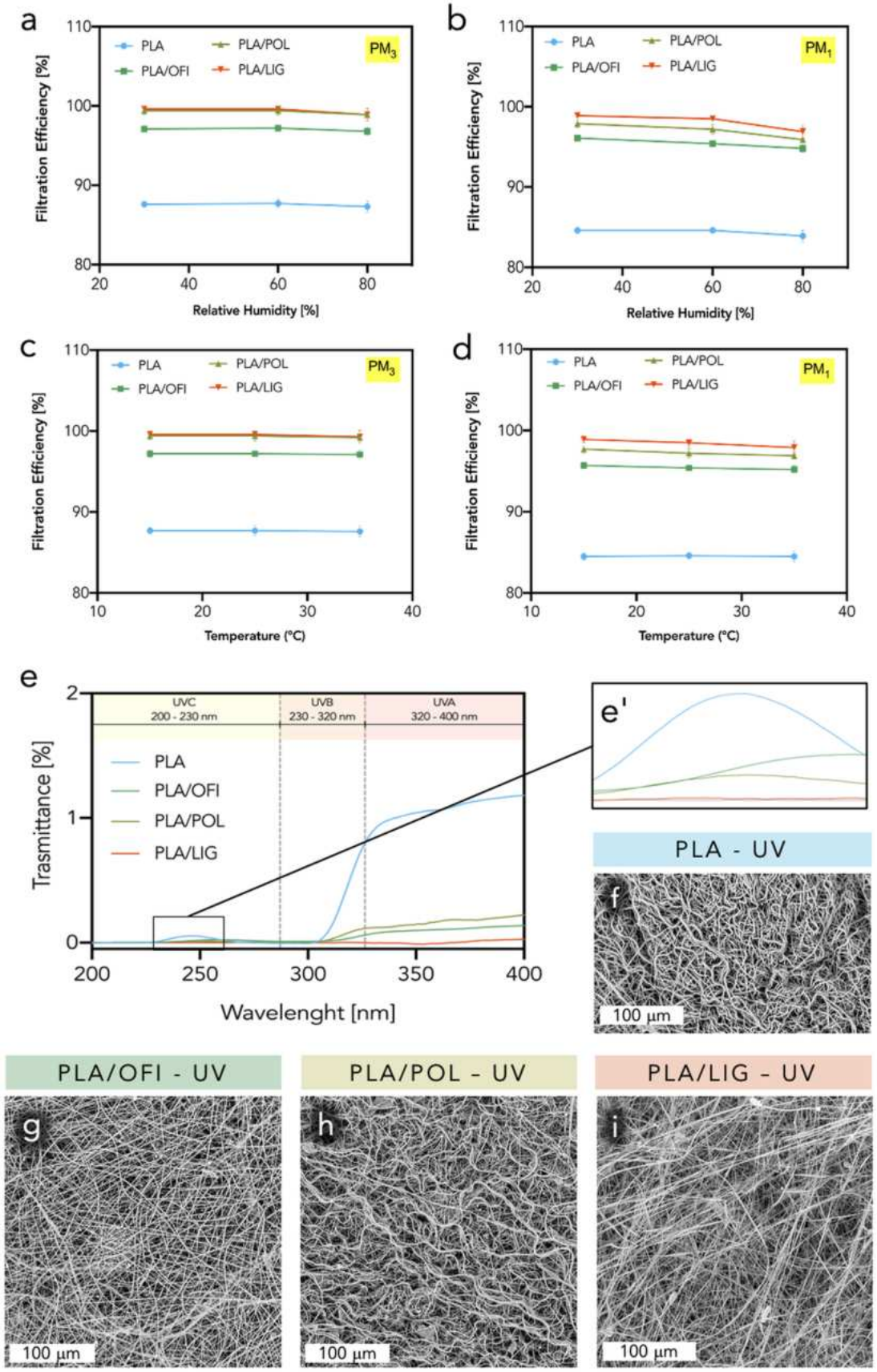

Figure 4.1.1.9 *Filtration efficiency of the composite membranes at different relative humidity for PM3 (a) and PM1 (b) and at different temperature for PM3 (c) and PM1 (d). Transmittance UV spectrum (e, e') and SEM images of PLA (f), PLA/OFI (g), PLA/POL (h), PLA/LIG (i) membranes after 2 hours exposure to UV lamp.*

Similarly, temperature variation (Figure 4.1.1.9 c and b) has a very small impact on the filtration efficiency of PM_1 and it has almost no effect on the filtration efficiency of PM_3. The composite membranes exhibit high and consistent filtration efficiency across the temperature range of 15°C to 35°C. These behaviours demonstrate that the composite membranes, particularly PLA/POL and PLA/LIG, provide superior and consistent filtration performance under varying environmental conditions, making them suitable both for indoor and outdoor applications.

The presence of plant-based fillers in PLA fibers can provide UV protection, preserving the membranes structure when exposed to sunlight [131]. To assess the resistance of the composite membranes to UV radiation, their UV transmittance was evaluated, and their morphology after 2 hours of exposure to a UV lamp was investigated. The energy radiated for 1 h is equivalent to absorbing ultraviolet energy for 75–184 days under natural conditions [131]. The UV transmittance of the membranes and their morphology after UV irradiation are reported in Figure 4.1.1.9e-i.

The composite membranes, especially PLA/LIG one, show extremely low UV transmittance in UVA (320–400 nm) spectrum (Figure 4.1.1.9e, e'). Lignin powder, in fact, contains phenol, ketone, and other chromophores that act as UV-absorbing functional groups [149]. Similarly, also *Opuntia Ficus Indica* [150] and *Posidonia Oceanica* [151] contain flavonoids and phenolic compounds that contributes to their UV protective properties by absorbing UV radiation. After 2 hours of exposure to the UV lamp, neat PLA fibers (Figure 4.1.1.9f) exhibit a notable wavy morphology. This structural alteration can be reasonably attributed UV lamp irradiation. On the other hand, PLA/OFI (Figure 4.1.1.9g) and PLA/LIG (Figure 4.1.1.9i) fibers remain almost unchanged after UV exposure. These results suggest that the inclusion of *Opuntia Ficus Indica* and lignin fillers in PLA fibers may provide some term of UV protection to the membranes. Interestingly, PLA/POL fibers show more waviness (Figure 4.1.1.9h) if compared to their unexposed structure. This may suggest that while the addition of POL powder could reduce the extent of degradation, it does not completely prevent it, reasonably because POL particles are not well embedded in the fibers.

The UV resistance of PLA/OFI and PLA/LIG membranes were evaluated also after 4 and 8 hours of accelerated UV exposures to test if them can resist longer periods of ultraviolet radiation [152] and SEM analysis were performed on them (Figure 4.1.1.10). After 4 hours of UV lamp exposure, the PLA/OFI membranes start to show signs of fiber modification, appearing wavier (Figure 4.1.1.10a). After 8 hours of exposure, the fibers are completely altered, exhibiting a highly deformed and extremely compact structure (Figure 4.1.1.10b), unsuitable for the application. PLA/LIG membranes withstand UV exposure well for up to 4 hours, maintaining an almost unaltered structure (Figure 4.1.1.10c). However, after 8 hours, the fibers undergo slight waviness and fragmentation, resulting in a compacted structure (Figure 4.1.1.10d) that is no longer suitable for filtration application.

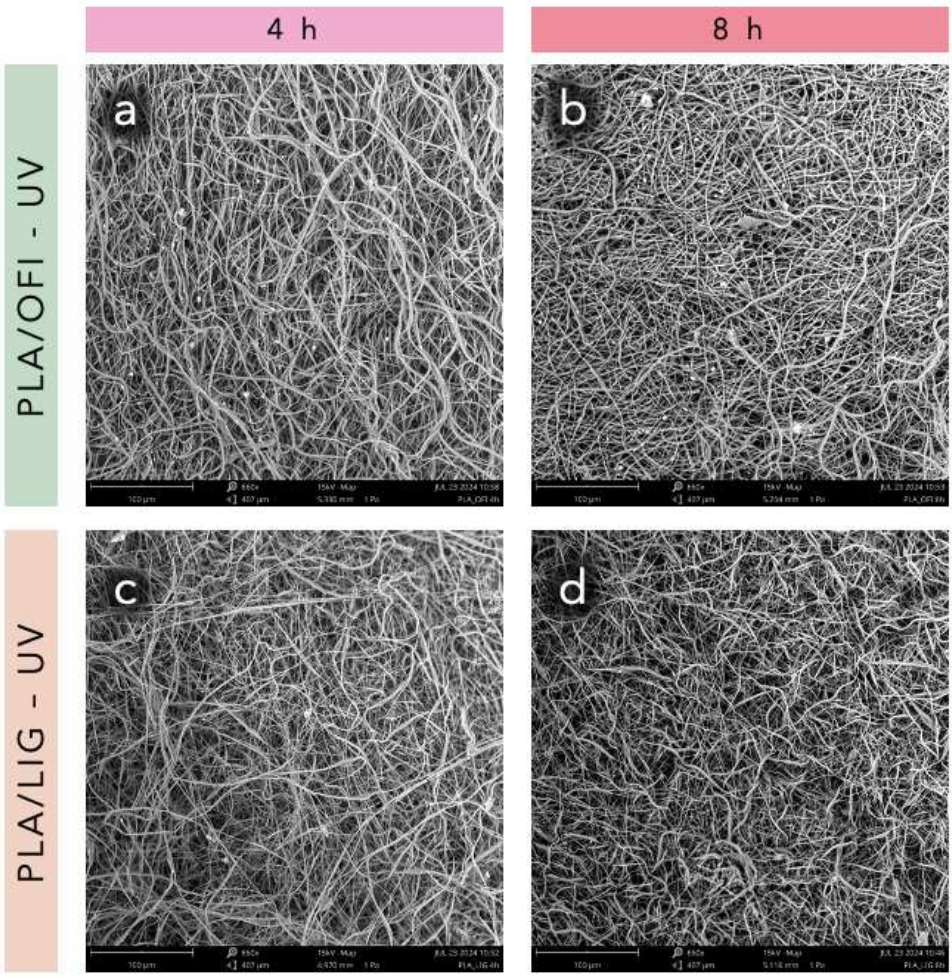

Figure 4.1.1.10 *SEM images of PLA/OFI (a, b), and PLA/LIG (c, d) membranes after 4 and 8 hours exposure to UV lamp respectively. Scale bar is 100 µm for all the SEM images.*

6.1.1.10 Reusability of the composite membranes

To evaluate their reusability, the composite fibrous membranes were washed in a water/ethanol mixture and their filtration efficiency was tested for five cycles. The obtained results, relative to PM_3, are reported in Figure 4.1.1.11a. After the second cycle, there is no significant change in the filtration efficiency of the composite membranes, and after five cycles, only a slight reduction in filtration efficiency can be observed. The washing cycles, in fact, do not damage the fibrous structure which remain almost unchanged as observed in SEM images in Figure 4.1.1.11b-e. The slight but significant reduction in filtration efficiency of PLA/POL and PLA/LIG membranes after the third cycles can be reasonably addressed to their electroactivity loss.

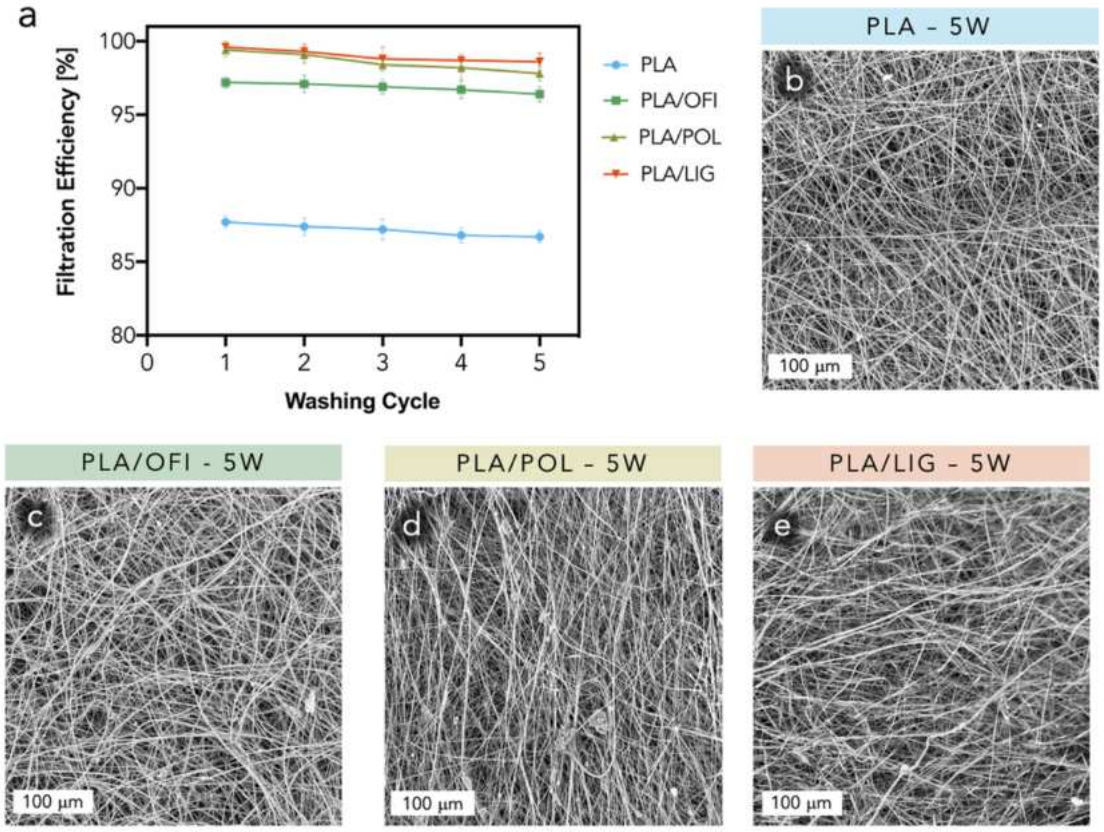

Figure 4.1.1.11 *(a) Reusability of the composite membranes: filtration efficiency of PM_3 after five cycles. SEM images of PLA (b), PLA/OFI (c), PLA/POL (d) and PLA/LIG e) membranes after five cycles of washing and filtration testing.*

6.1.1.11 Conclusions

In this study, stable, reusable and UV-resistant bio-composite fibrous membranes were successfully fabricated through electrospinning. The composite dispersions were prepared by adding 10 wt% of *Opuntia Ficus Indica* (OFI), *Posidonia Oceanica Leaves* (POL) or lignin (LIG) powders to PLA solution. The PLA/POL and PLA/LIG membranes exhibited a significant decrease in fiber diameter, attributable to the increased conductivity of the solutions. Additionally, the presence of lignin in the membranes enhanced their electroactivity. The mechanical properties of all the composite membranes are compatible with air filtration applications. The PLA/OFI, PLA/POL and PLA/LIG composites membranes exhibited high filtration performances for PM_3 at a flow rate of 32L/min, with filtration efficiencies of 97.2%, 99.4%, 99.6%, and pressure drops of 114, 103, 105 Pa, respectively. For PLA/POL and PLA/LIG membranes the contextually decrease in fibers diameters and increase in electrostatic attraction were the key factors to enhance filtration performances of the membranes. The composites membranes demonstrated satisfactory stability maintaining good filtration efficiency across different relative humidity and temperature conditions. It was also demonstrated that the inclusion of OFI and LIG powders in PLA fibers provides some term of UV protection to the filtering membranes. PLA/OFI and PLA/LIG membranes remain almost unchanged after 4 hours of accelerated UV irradiation. Moreover, the composite membranes demonstrated the ability to be reused for at least five washing cycles while maintaining their fibrous structure and preserving good filtration efficiency. Therefore, the PLA/OFI, PLA/POL and PLA/LIG membranes prepared in this study exhibits enormous potential for air filtration application both for indoor and outdoor filtering devices.

6.1.2 Bi-layer membranes based on Waste Wool Fibers for Sustainable Filtration Applications

Note: This study is ongoing, with further characterizations and application tests planned to enhance and finalize the research findings.

6.1.2.1 Abstract

Air pollution from fine dust particles remains a pressing environmental challenge. To reduce the environmental footprint of air filtration technologies, it is crucial to develop solutions based on biodegradable polymers blended with natural fillers, ideally sourced from waste materials, to create efficient, durable, and reusable air filters. In this work, bi-layer membranes based on waste wool fibers (WWF) were produced by combining a layer of hot-pressed wool fibers with a layer of composite fibrous membrane based on polylactic acid (PLA) and waste wool powder (WWP) obtained by solution blow spinning (SBS) technique. The bi-layer membrane (WWF-PLA/WWP) was tested for air filtration applications using different flow rates, temperature and humidity conditions. The addition of 10 wt% of WWP to PLA solution led to an increase of the viscosity of the solution improving the morphology of the fibers. Further characterizations and filtration performance test of the bilayer membrane across different environmental settings and after multiple cycles of reuse are ongoing.

6.1.2.2 Preparation of WWF membrane

WWF were washed in water at room temperature and dried in an oven at 60 °C for 48 hours. Once dried, 1 g of WWF where homogenously placed (random oriented) between two aluminium sheets and hot-pressed using a laboratory press (Carver, Wabash, IN, USA) a 80 °C for 10 seconds (Figure 4.1.2.1a).

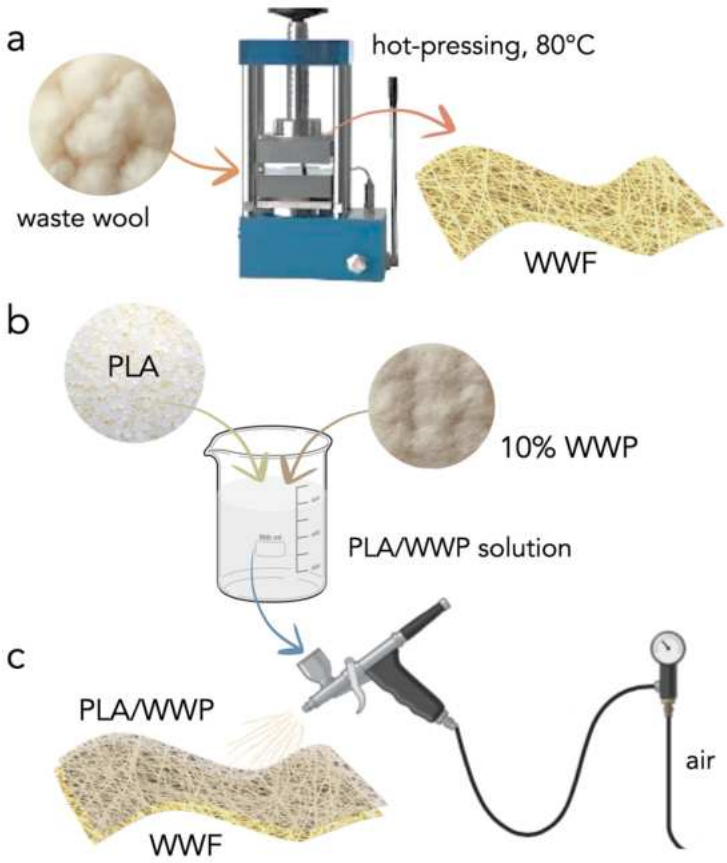

Figure 4.1.2.1 *Schematic illustration for the preparation of the membranes: (a) preparation of the WWF mat; (b) preparation and composition of PLA/WWP dispersion; (c) fabrication of PLA/WWP and WWF-PLA/WWP fibrous membranes via solution blow spinning.*

6.1.2.3 Preparation of PLA/WWP and WWF-PLA/WWP membranes

Part of the WWF were finely chopped and roughly ground for 3 minutes in a mixer. Subsequently, the obtained particles were ball milled (Retsch MM 500 nano, Germany) for 30 minutes at 20 Hz aiming to obtain micrometric powder (WWP). PLA solution (10 wt%) was prepared using Chl/Ac mixture (2:1 ratio). After the PLA was completely dissolved, 10 wt% (with respect to PLA mass) of WWP was dispersed in the PLA solution (Figure 4.1.2.1b) keeping them under magnetic stirring at 25 °C overnight. The production of PLA/WWP fibrous membranes was carried out using a homemade solution blow spinning apparatus. The feed rate of the polymeric dispersion was 50 mL/h, the air pressure was maintained at 0.6 MPa and the needle-to-collector distance was 10 cm. The temperature during processing was kept at 23 ± 2 °C, and the relative humidity of the air was

50 ± 5 %. Similarly, the bilayer membrane (WWF-PLA/WWP) was prepared by spinning the PLA/WWP dispersion directly onto the previously obtained WWF mat (Figure 4.1.2.1c). The obtained monolayer (PLA/WWP) and bi-layer (WWF-PLA/WWP) fibrous membranes were then dried at room temperature for 24 h to remove any residual solvent.

6.1.2.4 Morphology of WWF, WWF mats and WWP

The morphology of waste wool fibers (WWF) was analyzed by SEM before and after the hot-pressing process and after the ball-milling process (WWP). The relative SEM images are reported in Figure 4.1.2.2a-c, while WWP particles size distribution, in terms of equivalent diameter, are reported in Figure 4.1.2.2d. WWF fibers (Figure 4.1.2.2a) showed an average diameter of 45 μm (SD ± 10) and any significative difference can be noted in the morphological structure of the fibers after the hot-pressing process (Figure 4.1.2.2b). Through the hot-pressing process, wool fibers are compacted into a fibrous mat, allowing it to be handled as a single structure, without compromising the structural integrity of the fibers. This mat is produced to serve as a substrate for the subsequent deposition of PLA/WWP fibers applied on top using the solution blow spinning technique.

Part of the WWF were ball milled and the SEM image reviled that the obtained powder is composed by heterogenous shaped particles as it is possible to notice from Figure 4.1.2.2c. Most particles exhibit a predominantly spherical shape with nanometric or few micrometre dimensions. However, some particles tend to aggregate, forming clusters that reach sizes of several micrometres.

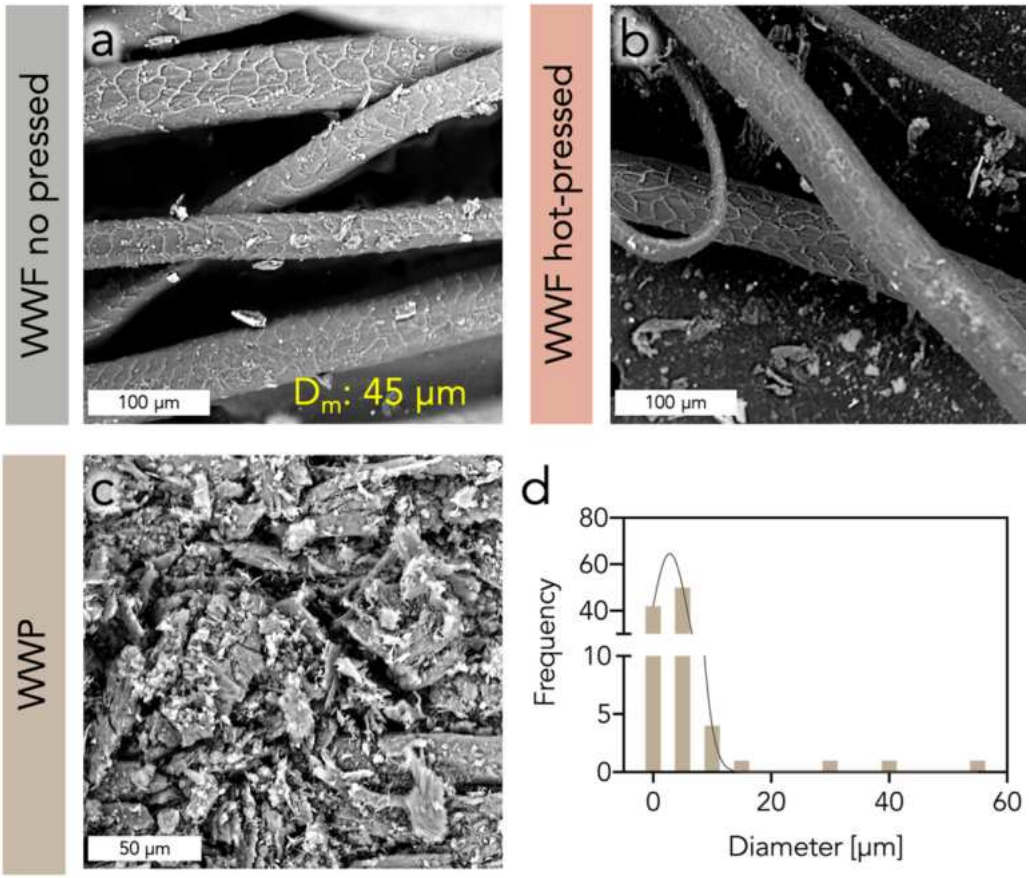

Figure 4.1.2.2 *SEM images of WWF before (a) and after (b) hot pressing process. SEM images (c) and particles size distribution (d) of WWP after ball milling process.*

6.1.2.5 PLA solutions preparation and characterization

Based on our previous study, 10 wt% of WWP was selected as the optimal filler content to add to the PLA polymeric solution, aiming to achieve both good processability in SBS and a higher incorporation of natural particles into filtering membranes. This latter objective not only aligns with sustainability goals by allowing more waste material to be integrated, but the particles may also serve as sites for pollutant accumulation, thereby improving filtration efficiency and enhancing membrane performance. Additionally, the inclusion of fillers can increase the surface roughness of the fibers, improving the likelihood of particulate matter entrapment.

The rheological behaviour of the neat PLA solution and PLA/WWP dispersion was studied and the complex viscosity curves are presented in Figure 4.1.2.3. Neat PLA exhibits its typical non-Newtonian behaviour across the entire frequency range. The addition of wool particles (WWP) to the

PLA solution does not cause any change in rheological behaviour of the dispersion. However, a remarkable increase in viscosity across the entire frequency range was observed. In fact, the inclusion of fillers in PLA solution generally leads to an increase in viscosity values [129].

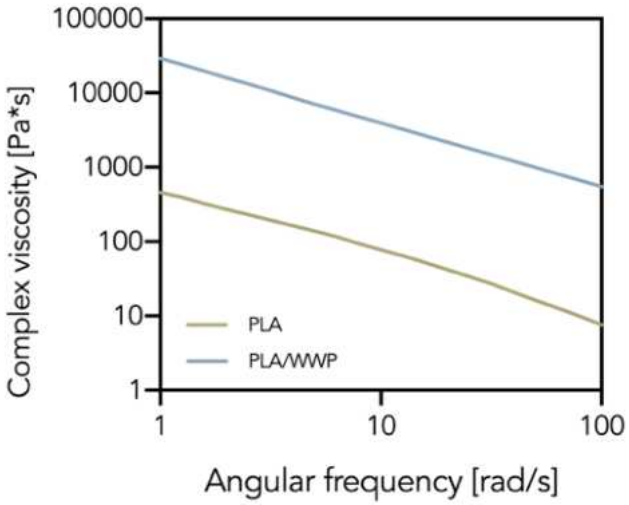

Figure 4.1.2.3 *Complex viscosity of the polymeric dispersions.*

6.1.2.6 PLA/WWP and WWF-PLA/WWP preparation and morphology

Solution blow spinning process proceeded smoothly for both PLA and PLA/WWP solutions. The bilayer membrane (WWF-PLA/WWP) was prepared by spinning the PLA/WWP dispersion directly onto the previously obtained WWF mat aiming to ensures a strong interfacial adhesion between the layers, promoting structural integrity and uniform distribution of fibers. Morphologies of neat PLA, PLA/WWP fibrous membrane and WWF-PLA/WWP bi-layer membrane were analyzed by SEM as shown in Figure 4.1.2.4a-d and a'-d'. PLA, PLA/WWP fibers diameter distributions are reported in Figure 4.1.2.4a"-b". In accordance with other studies [22,106], PLA membranes (Figure 4.1.2.4a) showed straight fibers - most of them organized in bundles – with a unimodal but wide fiber diameter distribution and an average diameter of 1.73 μm (Figure 4.1.2.4a").

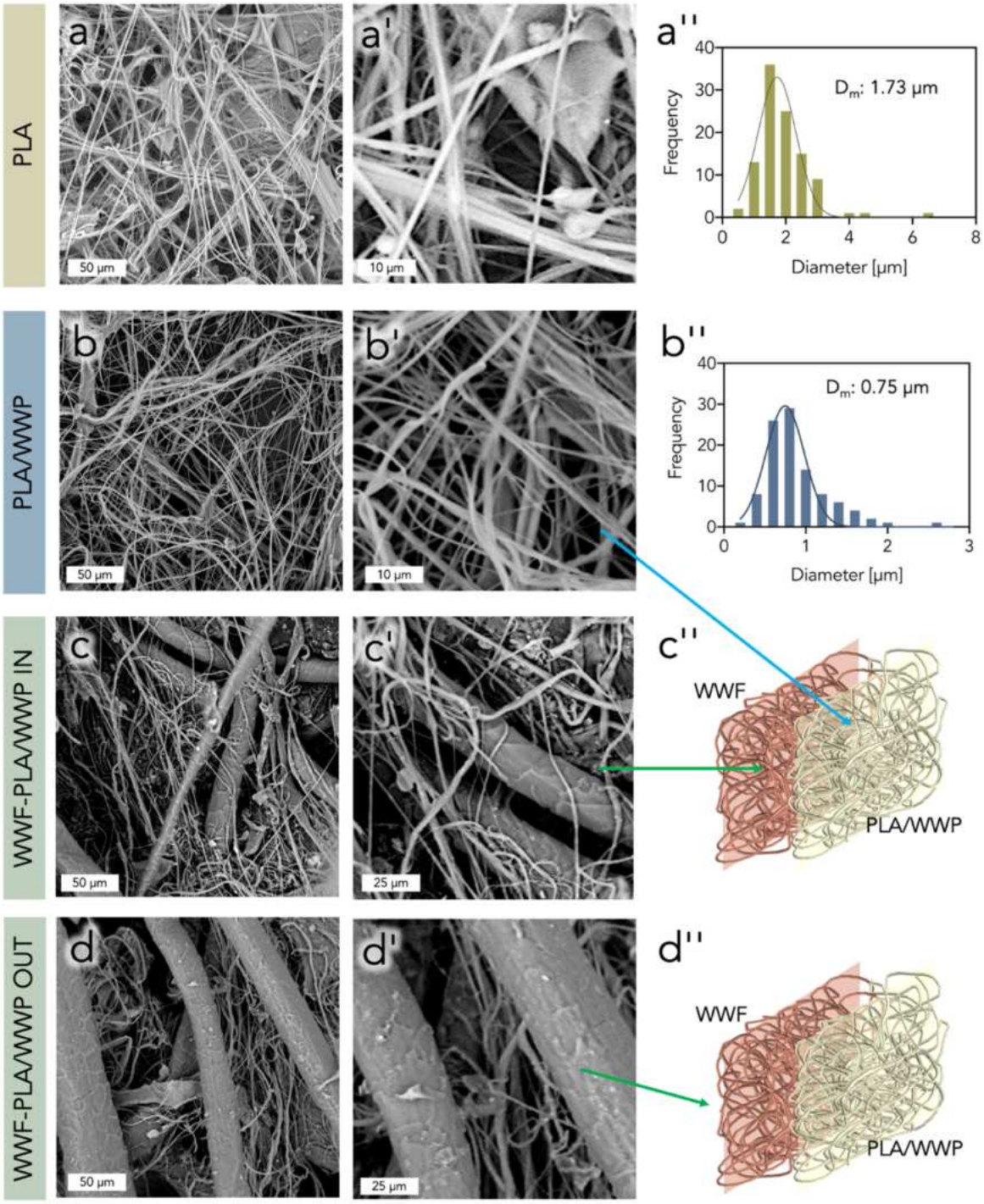

Figure 4.1.2.4 *SEM images, relative insets and fibers diameter distribution of PLA (a, a', a''), PLA/WWP (b, b', b''), WWF-PLA/WWP IN (c, c') and WWF-PLA/WWP OUT (d, d') membranes respectively. Graphical explanation of which part of WWF-PLA/WWP membrane was exanimated with SEM (c'' and d'').*

However, fibers of some micrometres can be noted too. Moreover, also beads and polymeric agglomerates (due to solution dripping phenomena) are present (Figure 4.1.2.4a'). The addition of WWP to PLA solution lead to a more uniform and randomly oriented morphology (Figure 4.1.2.4b):

no fibers bundles, beads or polymeric agglomerates can be noted (Figure 4.1.2.4b'). Additionally, a significant decrease in fiber diameter was achieved reaching an average diameter of 0.75 μm (Figure 4.1.2.4b''). This morphology could be useful for improving the filtration efficiency of the membrane [80,131]. This modification in diameter dimension and morphology could be reasonably addressed to the increased viscosity of PLA/WWP solution which affect the jet stability during the spinning process stabilizing it and thus minimizing fluctuations that may cause beads, solution dripping and inconsistencies in fiber diameter [153]. Moreover, solution whit higher viscosity can result in thinner fibers due to a better resistance to fragmentation during spinning time. This implies that the polymeric cone can further elongating under the influence of the air drag. WWF-PLA/WWP bi-layer, was analyzed considering from both sides off WWP layer after the SBS process: the side in contact with PLA/WWP (WWF-PLA/WWP IN, see Figure 4.1.2.4c'') and the free side (WWF-PLA/WWP OUT, see Figure 4.1.2.4d''). After PLA/WWP layer was peeling off, WWF-PLA/WWP IN still present some PLA/WWP strictly adherent to WWF fibers (Figure 4.1.2.4c and 4.1.2.4c'). Moreover, PLA/WWP fibers can be observed also in WWF-PLA/WWP OUT side (Figure 4.1.2.4d and 4.1.2.4d'). This confirms that a strong interfacial adhesion between the layers was achieved, ensuring structural integrity of the bilayer membrane. Additionally, the presence of PLA/WWP fibers in WWF mat further compact this layer. The WWF layer acts as a support that enhances the mechanical properties of the final membrane, while the PLA/WWP layer is responsible for pollutant capture.

6.1.2.7 Ongoing characterization and applicative tests

Characterization of the different fibrous membranes and filtration test of WWF-PLA/WWP membrane are ongoing. Moreover, reusability of the filtering membrane will be assessed.

6.2 Water

6.2.1 Biodegradable membrane with high porosity and hollow structure obtained via electrospinning for oil spill clean-up application

The subsequent text and images have been fully extracted from the published article authored by the candidate "Scaffaro, R., Gulino, E.F. & Citarrella, M.C. Biodegradable Membrane with High Porosity and Hollow Structure Obtained via Electrospinning for Oil Spill Clean-up Application. J Polym Environ 31, 3965–3981 (2023). https://doi.org/10.1007/s10924-023-02876-0 [154]" and are reproduced here with the necessary permissions from Springer Nature.

Author contribution: Methodology, Software, Validation, Formal Analysis, Investigation, Data Curation, Writing - Original Draft, Writing -Review & Editing, Visualization.

6.2.1.1 Abstract

The use of biodegradable polymers for the production of membranes to be used in wastewater treatment has attracted increasing interest considering the possibility of reducing the risk of second pollution. In this work, porous fibrous membranes based on polylactic acid (PLA) and polyethylene oxide (PEO) blends were prepared. The solutions were electrospun using two approaches: i) conventional coaxial electrospinning followed by leaching treatment (double-step, DS); ii) coaxial wet electrospinning with *in situ* leaching (single-step, SS). By varying PEO type and processing method it was possible to control membranes structure and porosity. DS leaching treatment lead to surface porosity (i.e. shell leaching), while SS allowed obtaining hollow and porous fibers (i.e. with shell and core leaching). Process, properties and structure relationships of devices were analysed trough rheological, morphological, mechanical and surface characterizations. Furthermore, the influence of the different porous structures on oil sorption capacity and reusability of the membranes was evaluated. Results reveal that different porosities lead to a variation in membranes mechanical performance, in their wettability and, consequently, in their oil spill cleanup capacity. Membranes obtained with SS displayed higher performance in oil removal if compared to the DS ones, due to their hollow structure and higher surface area.

6.2.1.2 Preparation of the polymeric porous membranes

PLA, PEO-A and PEO-B solutions ware prepared by dissolving the respective required amount of polymer in a CF/Ac mixture (2:1 ratio) under magnetic stirring at 25 °C overnight. A preliminary study of starting solutions and blends were carried out in order to verify their processability. PLA 10 wt%; PEO-A 10 wt% and PEO-B 5 wt% were selected for further investigations and from here on we will refer to these concentrations by using acronyms PLA, PEO-A and PEO-B. As regards the shell polymeric solutions, PLA was mixed with PEO-A or PEO-B at different relative ratio and PLA/PEO-A and PLA/PEO-B obtained blends were stirring overnight in order to obtain a homogeneous solution. The compositions of blends here produced are listed in Table 4.2.1.1 PEO-A (10 wt% in CF/Ac 2:1 mixture) was used as core solution for PLA/PEO-A systems and PEO-B (5 wt% in CF/Ac 2:1 mixture) for PLA/PEO-B ones.

Table 4.2.1.1 Composition of shell PLA/PEO-A and PLA/PEO-B blends.

Sample code	PLA (wt %)	PEO-A (wt %)	PEO-B (wt %)
PLA/PEO-A25	75	25	0
PLA/PEO-A50	50	50	0
PLA/PEO-A75	25	75	0
PLA/PEO-B25	75	0	25
PLA/PEO-B50	50	0	50
PLA/PEO-B75	25	0	75

Membranes were prepared by using a conventional electrospinning equipment consisting in a syringe pump and a high voltage power supply (Linari Engineering-Biomedical Division, Pisa, Italy). The polymeric solutions were filled in a 10 mL glass syringe equipped with coaxial needles manufactured in AISI 316 stainless steel. The outer needle was attached to the syringe pump containing the shell solution (PLA/PEO-A or PLA/PEO-B) and the inner was connected to a pump having, in the core solution (PEO-A or PEO-B respectively). The process was performed using the

following parameters: supplied high voltage 15 kV; flow rate, 1.5 mL/h; distance between coaxial needles tip and collector, 12 cm; temperature, 25 °C; and relative humidity, 40 %. The solutions were electrospun on a grounded collector wrapped in aluminium foil for 1 hour. Aiming to verify if the gravity could affect the electrospinning process, preliminary DS membranes were prepared with both horizontal and vertical assembly of the electrospinning set-up. Any statistically significant differences have been noted between the membranes obtained with the two set-ups from both morphological and mechanical point of view. Considering that, we decided to keep the horizontal arrangement of the set-up for convenience. In order to remove the sacrificial polymer (PEO-A or PEO-B) from the membranes (~20 mm in diameter, about 100 μm in thickness), they were submerged in 20 mL of distilled water at 25 °C for 30 minutes at 50 rpm stirring. After immersion, the membranes were dried overnight in a vacuum oven. A summary schematic of the process is depicted in Figure 4.2.1.1a.

Membranes were also prepared in single step (SS) processing using the same electrospinning apparatus, appropriately modified, with the same processing parameters reported above. More in detail, as depicted in Figure 4.2.1.1b, the polymeric solutions were filled in a 10 mL glass syringe equipped with coaxial needles that was placed on a vertically arranged syringe pump. The solutions were then electrospun for 1 hour on a liquid-bath grounded collector (known as wet collector) wrapped in aluminium foil at the bottom of the vessel. The wet collector (previously equipped with a magnetic stirrer) and was placed onto a stirrer set at 50 rpm in order to promote fibers dispersion in the liquid bath. The use of the wet grounded collector allowed the fibers to be submerged in water contextually to their formation [155–157] aiming to efficiently remove the sacrificial polymer *in situ* (single step). After processing, the membranes were dried in a vacuum oven overnight.

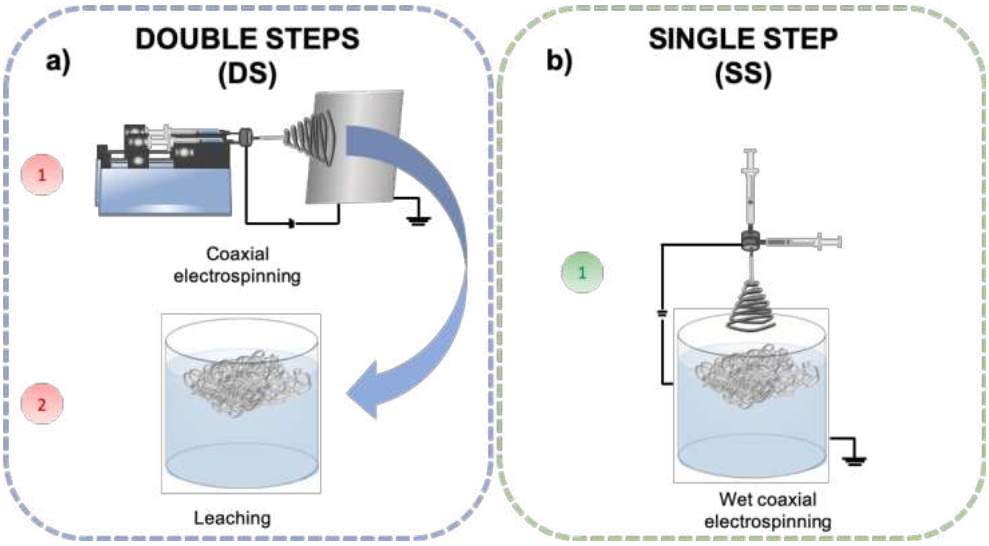

Figure 4.2.1.1 *Two-step preparation of dual porous membrane via coaxial electrospinning (a), One-step preparation of dual porous membranes via coaxial wet electrospinning (b).*

6.2.1.3 Rheological characterization of the polymeric solution

After a preliminary investigation, PEO-B 5wt% and PEO-A 10wt% have been chosen for further preparation. Different concentration of PEO-A and PEO-B in PLA blend may play a key role to obtain the desired porous structure. To investigate about processing behaviour of PLA/PEO blends, rheological tests have been performed and the results are reported in Figure 4.2.1.2a and 4.2.1.2b.

In general, all systems showed a pronounced non-Newtonian behaviour in the whole frequencies range and for both PEOs, at any PLA/PEO ratio. Moreover, all the blends displayed higher viscosity if compared to neat PLA. As regards PLA/PEO-A blends, in Figure 4.2.1.2a it can be observed that their rheological behaviour is substantially dominated by PLA up to 50wt% PEO. Differently, PLA/PEO-A75 viscosity curve, similarly to that of neat PEO-A, presents remarkable non-Newtonianism with an ensuing more pronounced shear thinning at higher frequencies, similarly to PEO-A. Regarding PLA/PEO-B blends, presented in Figure 4.2.1.2b, any dependence on PLA up to 50wt% PEO can be noted. Contrariwise, the progressive PEO-B addition induces a gradual increase in the viscosity of the solutions [158]. The non-Newtonian behaviour is preserved for all PLA/PEO-B blends in the whole frequencies range.

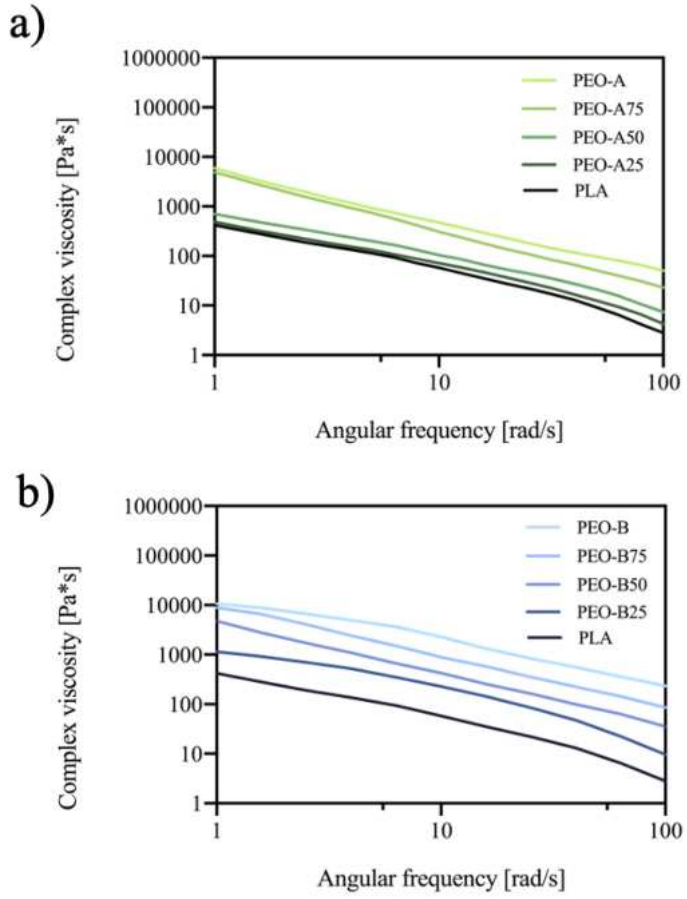

Figure 4.2.1.2 *Rheological curves of PLA/PEO-A (a) PLA/PEO-B (b) blends solutions at different PLA/PEO ratio.*

Considering that in our case the shear rate was estimated as about 4 1/s and that consequently it was found (during preliminary investigation) that the effective operating viscosity range to achieve good electrospun structures is therefore about 10^2-5*10^3 Pa*s, it is possible to observe that all PLA/PEO-A and PLA/PEO-B blend fall within this range. This outcome suggested the potential electrospinnability of all the PLA/PEO blends.

6.2.1.4 Morphological characterization of the fibrous membranes

The morphology of PLA/PEO-A and PLA/PEO-B electrospun mats together with corresponding fibers diameters distribution diagrams are shown in Figure 4.2.1.3. It is well known that electrospinning of high viscosity solutions leads to fibers with large and irregular diameters

[159]. In accordance with the scientific literature, PLA/PEO-A25 and PLA/PEO-B25 membranes (Figure 4.2.1.3a and 4.2.1.3b respectively) resulted in randomly oriented continuous fibers with rough and large surface and bead-free morphology. Moreover, they both displayed unimodal size distributions, whose mean values of 1 and 1.2 μm respectively (Figure 4.2.1.3c). PLA/PEO-A50 and PLA/PEO-B50 membranes (Figure 4.2.1.3d and 4.2.1.3e respectively) displayed fibers diameter average values of 1.2 μm and 1.23 μm respectively (not statistically significant; Figure 4.2.1.3f). Also in these cases, a unimodal size distribution can be noted (Figure 4.2.1.3f). Moreover, it is possible to observe the presence of two distinct phases along the fibers, probably identifiable with PEO agglomerations can be identify along PLA fibers (see for instance red line in Figure 4.2.1.3e). On the contrary, PLA/PEO-A75 and PLA/PEO-B75 (Figure 4.2.1.3g and 4.2.1.3h respectively) showed a multimodal size distribution with maxima and mean values of 2 and 1.9 respectively (Figure 4.2.1.3i). Furthermore, the presence of PEO agglomerations along the fibers are even more evident in these cases. In general, the presence of PEO agglomerations is more evident in PEO-B containing systems if compared to PEO-A ones, for each PEO concentrations. This behaviour can be reasonably explained considering that PEO-A and PEO-B have quite different molecular weights. PEO-A (100 kDa), in fact, is likely characterized by higher miscibility in PLA if compared to PEO-B (600 kDa) as reported elsewhere for similar systems [158,160]. Lower miscibility of PEO-B reasonably lead to the formation of larger PEO aggregates along fibers surface (see, for example, red arrow in Figure 4.2.1.3h).

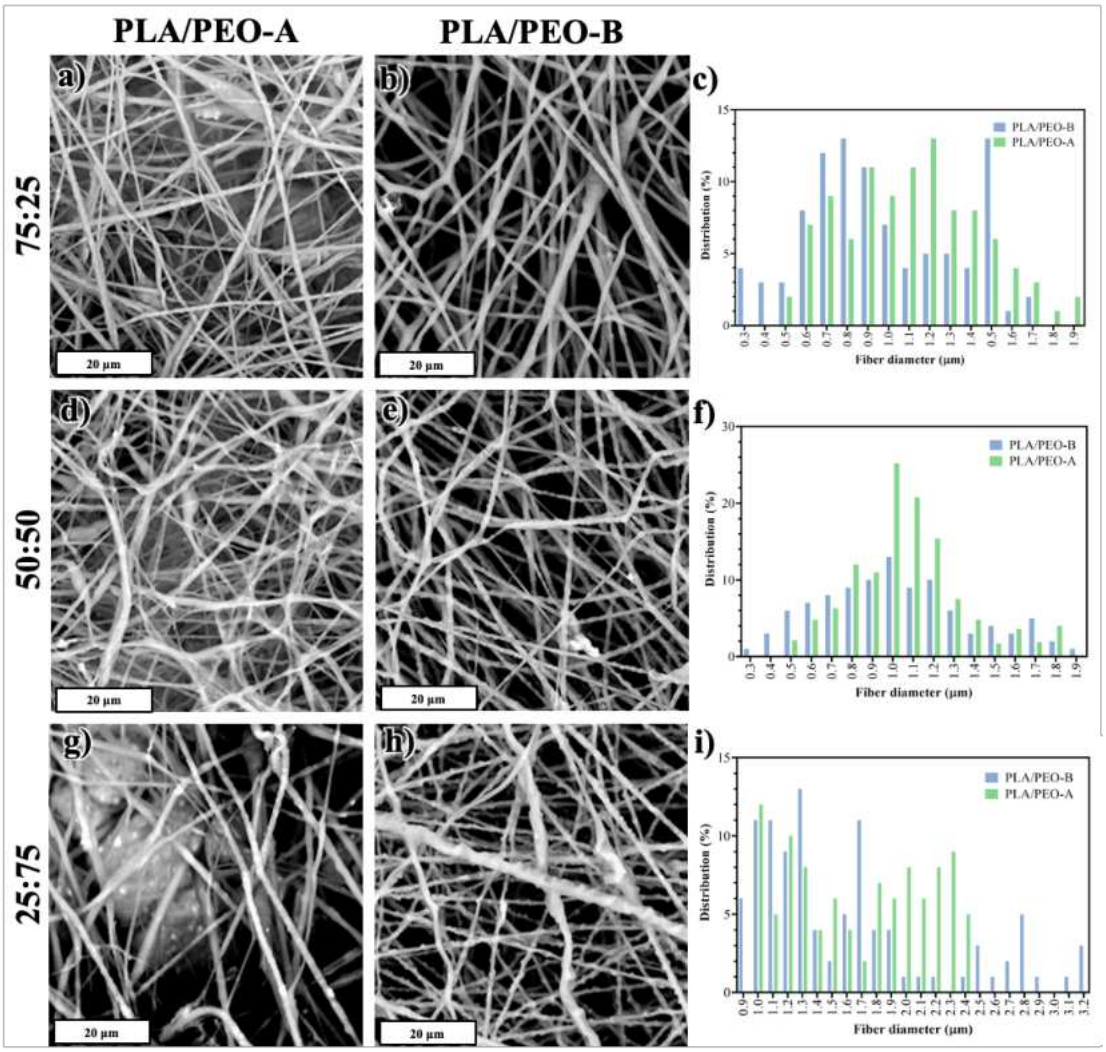

Figure 4.2.1.3 *SEM micrographs of PLA/PEO-A25 (a), PLA/PEO-A50 (b), PLA/PEO-A75 (d), PLA/PEO-B25 (e), PLA/PEO-B50 (g) and PLA/PEO-B75 (h) electrospun membranes and corresponding fibers diameters distribution diagrams (c, f, i).*

The presence of different concentrations of PEO-A or PEO-B plays a key role in obtaining membranes with different porosity. Both PEO-A and PEO-B, in fact, are totally soluble in water and for this reason they were chosen as sacrificial phases. As regards DS process, by submerging the obtained membranes in water, leaching of the PEO phase was performed and a higher porosity in electrospun membranes was verified by SEM, as shown in Figure 4.2.1.4.

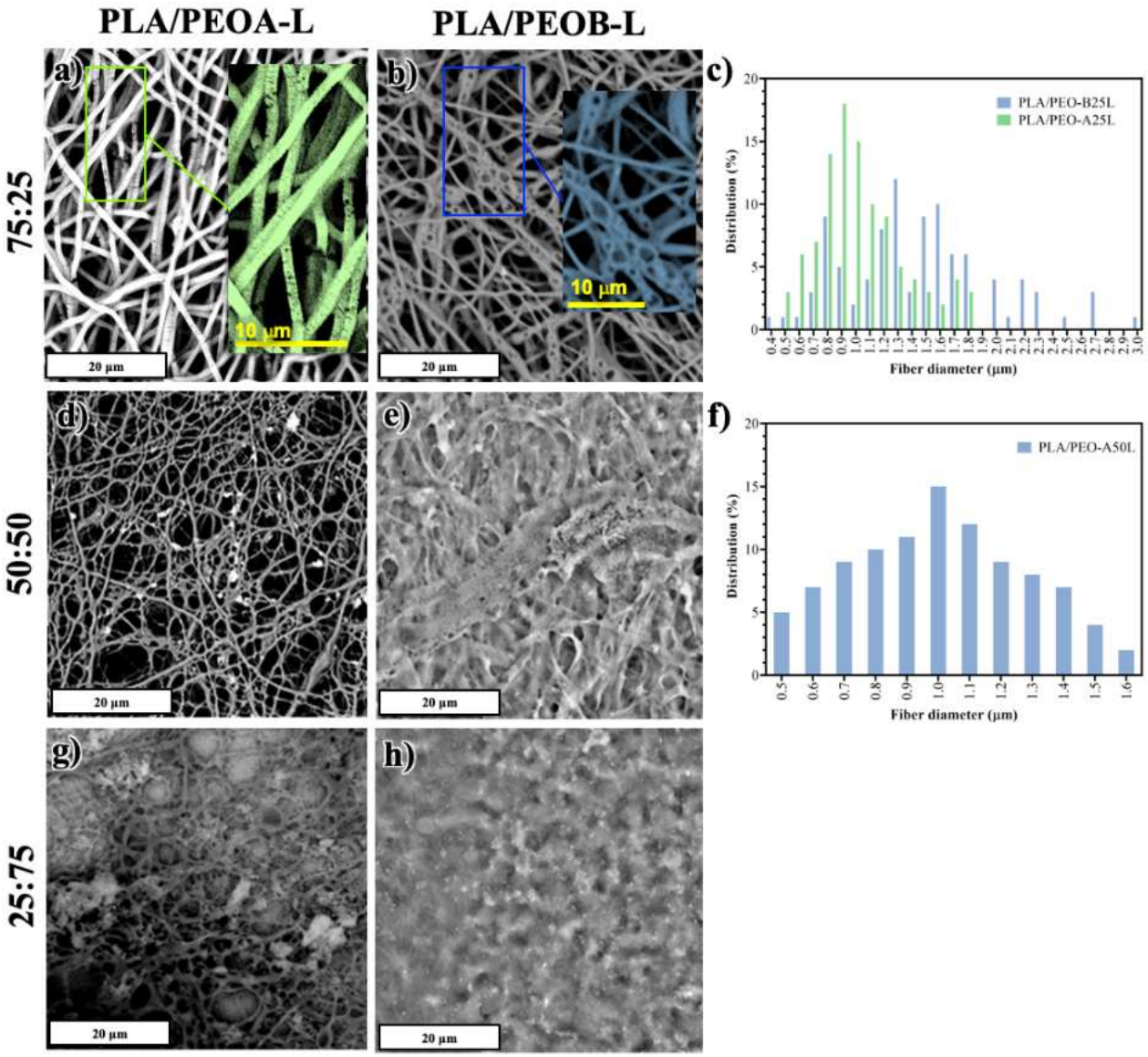

Figure 4.2.1.4 *SEM micrographs of PLA/PEO-A25L (a), PLA/PEO-B25L (b), PLA/PEO-A50L (d), PLA/PEO-B50L (e), PLA/PEO-A75L (g), and PLA/PEO-B75L (h) electrospun membranes and corresponding fibers diameters distribution diagrams (c, f).*

After leaching, PLA/PEO-A25L (Figure 4.2.1.4a) showed a quite stable structure with a good retention of fiber morphology and the presence of pores along fibers surface. On the contrary, PLA/PEO-B25L membrane (Figure 4.2.1.4b) exhibited porous and non-homogeneous fibers with coalescence between some of them. When 50% of PEO is added (Figure 4.2.1.4d, e), more marked differences can be observed between membranes before and after leaching. In particular, PLA/PEO-A50L (Figure 4.2.1.4d) showed an alteration of fibrous structure with starting coalescence between fibers. On the contrary, PLA/PEO-B50L (Figure 4.2.1.4e) showed a significant alteration of fibers

architecture with a bad retention of fiber morphology. More in detail, fibers appear flattened and non-homogeneous reasonably due to poor miscibility of PEO-B in PLA phase. In fact, when 50% of PEO-B is leached, fibers collapse due to lack of support of insoluble phase (PLA) [158]. This behaviour does not occur in the presence of PEO-A. Its better miscibility, if compared to PEO-B one, in fact, allows preserving fibers structure during leaching. Accordingly, in PLA/PEO-A75L (Figure 4.2.1.4g) only a partial collapse of the fibers can be noted while PLA/PEO-B75L (Figure 4.2.1.4h) showed a totally collapsed fibrous structure and no fibers can be observed. Considering the good fibers retention after leaching of PLA/PEO-A25 and PLA/PEO-B25, the corresponding solutions were selected to be processed by adopting single step process. The use of the wet collector (SS) lead to different morphological structure due to *in situ* leaching occurrence. In Figure 4.2.1.5 SEM micrographs and schematic description of leaching mechanism of PLA/PEO-A25W and PLA/PEO-B25W membrane are shown. PLA/PEO-A25W membrane (Figure 4.2.1.5a, b and 4.2.1.6a) shows a quite stable structure with a good retention of fiber morphology and the presence of nano-porous and hollow fibers (Figure 4.2.1.5f). Moreover, multimodal size distribution can be noted (Figure 4.2.1.5e). PLA/PEO-B25W membrane (Figure 4.2.1.5c and 4.2.1.5d) shows micro-porous and hollow fibers, however a less stable and homogeneous fibrous structure with a micro-porous fiber can be observed (Figure 4.2.1.6f). Also in this case, a multimodal size distribution can be noted (Figure 4.2.1.5g). Furthermore, fibers opening occurs (see Figure 4.2.1.5h and, for example, arrow in Figure 4.2.1.5c). This behaviour could be reasonably attributed to the presence of large agglomerations of PEO-B in the shell surface due to its poor miscibility in PLA [161]. In particular, when the fibers were projected to the wet collector, during electrospinning, sudden dissolution of PEO-B occurs inducing fiber opening with a peculiar morphology, showing a contextual intense leaching of core and shell of the fiber with pores widely distributed in both areas of the fiber, in some cases forming deep superficial furrows likely due to intense superficial leaching. This can be explained considering that PEO-B tends to form large aggregates that will turn in larger pores once leached.

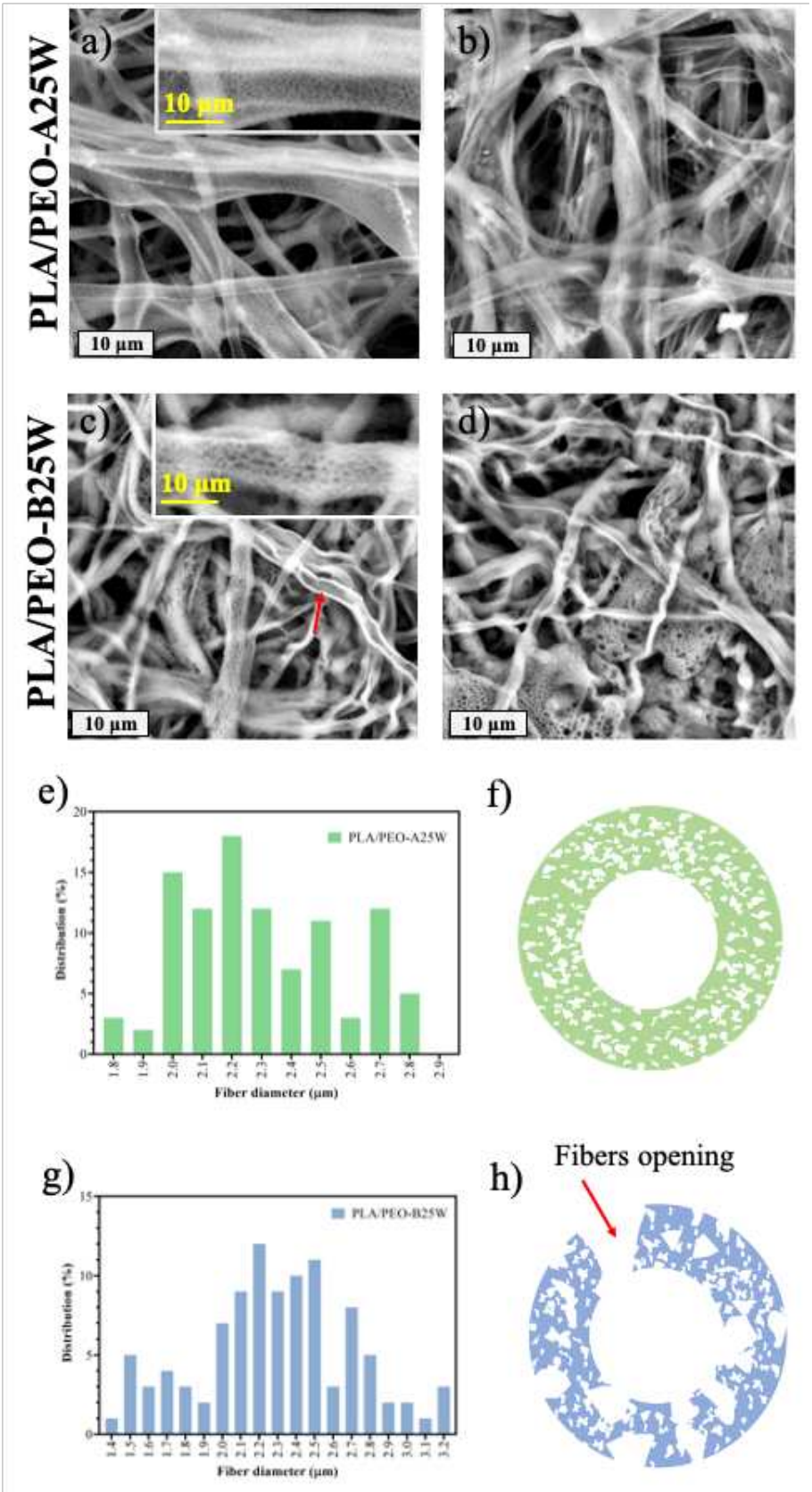

Figure 4.2.1.5 *PLA/PEO-A25W and PLA/PEO-B25W SEM micrograph (a, b and c, d respectively), corresponding fibers diameters distribution diagrams (e and g respectively) and of scheme of leaching mechanism (f and h respectively).*

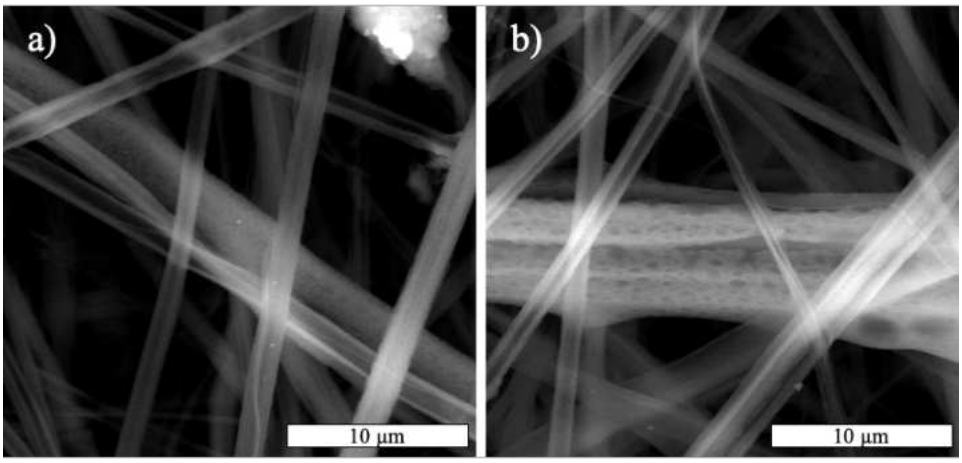

Figure 4.2.1.6 *PLA/PEO-A25W (a) and PLA/PEO-B25W (b) fibers SEM micrograph.*

Figure 4.2.1.7 shows a modelization of the leaching process in the two cases, based on the obtained results. As regards DS, Figure 4.2.1.7a, post-processing leaching treatment occur in fibers with a stabilized structure without residual solvent. Consequently, 30 minutes of leaching is evidently not enough to grant complete core leaching. On the other hand, for SS, Figure 4.2.1.7b, leaching and electrospinning occur simultaneously. During spinning, prior to fibers deposition in the wet collector, part of the solvent could remain inside the fibers. Therefore, the presence of non-stabilized fibers, containing residual solvent, promoted penetration of the leaching agent into the core. The two proposed mechanism are in full agreement with the observed morphologies in both cases.

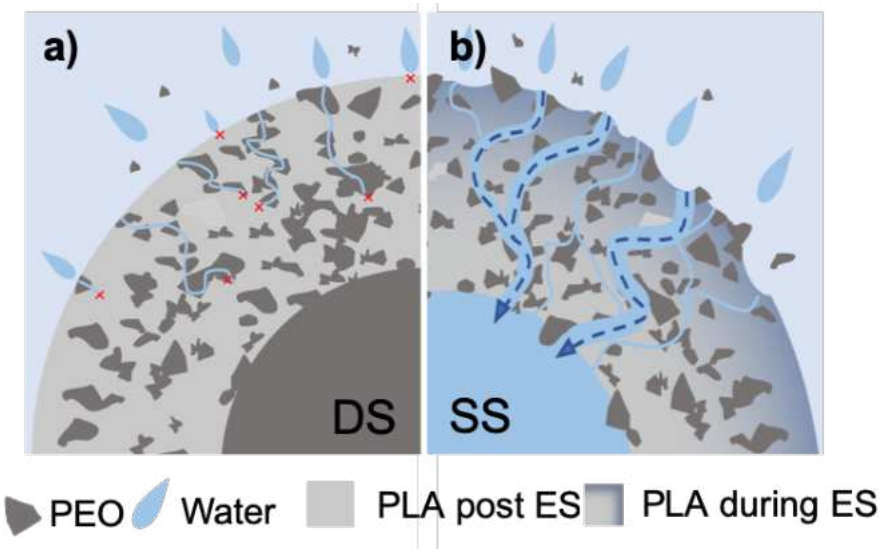

Figure 4.2.1.7 *Schematic description of fibers leaching mechanism of shell leaching achieve with double-step method (a) and core and shell leaching achieve with single-step method (b).*

6.2.1.5 FT-IR/ATR analysis

In order to get further confirmations about leaching modelization in DS and SS, ATR-FTIR measurements were carried out on neat PLA, PLA/PEO-A and PLA/PEO-B blends mats before and after leaching. FTIR analysis was performed also on PLA/PEO-A25W and PLA/PEO-B25W membranes. The related FTIR spectra are shown in Figure 4.2.1.8 and the relevant characteristic peaks are resumed in Table 4.2.1.2.

PLA revealed a neat band at 1759 cm^{-1} (–C=O band referable to PLA carbonyl groups) [162,163]. As expected, PLA/PEO-A and PLA/PEO-B blends show bands typical of both PLA and PEO-A or PEO-B. In particular, it could be noticed a band at 1344 cm^{-1} (CH_2), a peak at 1150 cm^{-1} (related to the C-O-C stretching vibration of PEO) and CH stretching mode at 2891 cm^{-1} in PEO-A and PEO-B spectra [164–166]. The same bands also appeared in PLA/PEOs blends confirming the correct incorporation of PEOs in the nanofibrous membranes. It is also possible to observe that these bands increase in intensity upon increasing the PEO-A or PEO-B amount in the blends. On the contrary, it is possible to observe a band with decreasing intensity (1759 cm^{-1} carbonyl group PLA) upon increasing the PEO-A amount in the blends [167]. However, this behaviour cannot be noticed for PEO-B blends.

Spectroscopical analysis therefore confirms that PEOs have been removed by leaching process both in DS and in SS. Moreover, in this latter case the decreasing of the related bands is more pronounced, confirming the hypotheses that more intense leaching occurs during SS process.

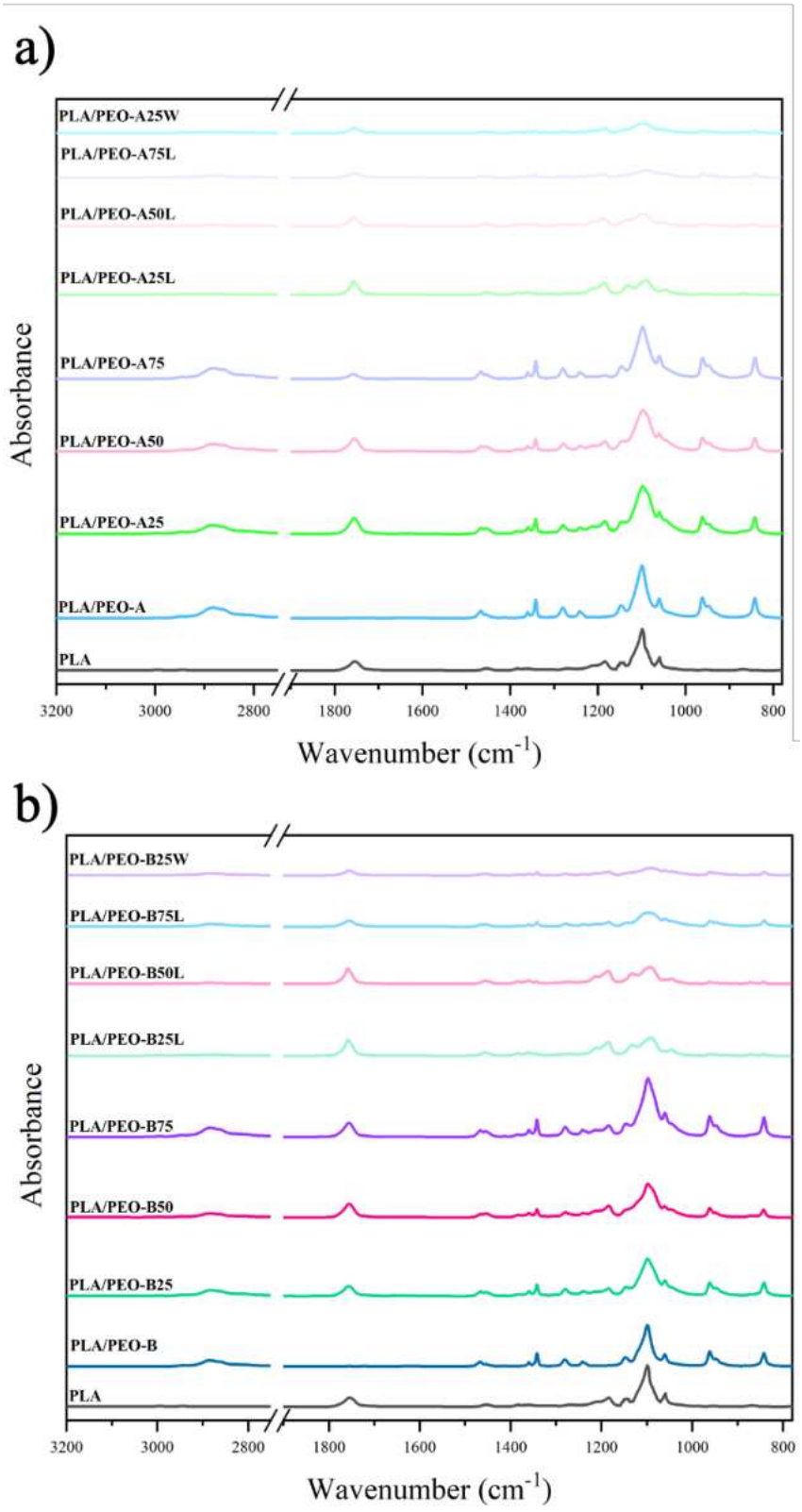

Figure 4.2.1.8 *ATR-FTIR measurements carried out on neat PLA, PLA/PEO-A, PLA/PEO-B blends mats before and after leaching and PLA/PEO-A25W, PLA/PEO-B25W.*

Table 4.2.1.2 FTIR peak values and relative functional groups.

Polymer	Wavenumber (cm^{-1})	Functional group	Vibrations	Ref.
PLA	1759	–C=O	carbonyl stretch	[162,163]
PEO	1344	CH2	symmetric stretching	[164–166]
PEO	1150	C-O-C	stretching vibration	[164–166]
PEO	2891	CH	stretching mode	[164–166]

6.2.1.6 Water contact angle (WCA) Measurements

The membranes obtained by the two methods, are formed by fibers with different architectures, also causing changes in their wettability. In this view, water contact angle (WCA) tests have been performed on all the systems and results are reported in Figure 4.2.1.9.

PLA showed a hydrophobic behaviour with a WCA of 103° in accordance with the scientific literature [168,169]. Non-leached systems containing PEO-A show higher WCA if compared to the PEO-B ones (Figure 4.2.1.9). This behaviour, according to the morphological characterization, could be explained by considering the presence of larger PEO agglomerations along the fibers in PLA/PEO-B blends if compared to PLA/PEO-A ones before the leaching step. WCA value of leached systems surprisingly showed an increase in wettability if compared to the non-leached ones. Moreover, this increase is even more evident for PLA/PEO-A25W and PLA/PEO-B25W. This behaviour, according to the morphological characterization, could be explained by considering the increase in porosity of the leached membranes: the presence of large pore and the achievement of a hollow structure in the fibers, induced by *in situ* PEO leaching, lead to the obtainment of membranes with long interconnected pores [160]. In fact, despite results seems to not match Wenzel equation, is necessary to consider that the hollow structure and the interconnected pores are responsible of liquid capillary transport through the membranes thus leading to peculiar fibers architecture and consequent lower WCA values [170].

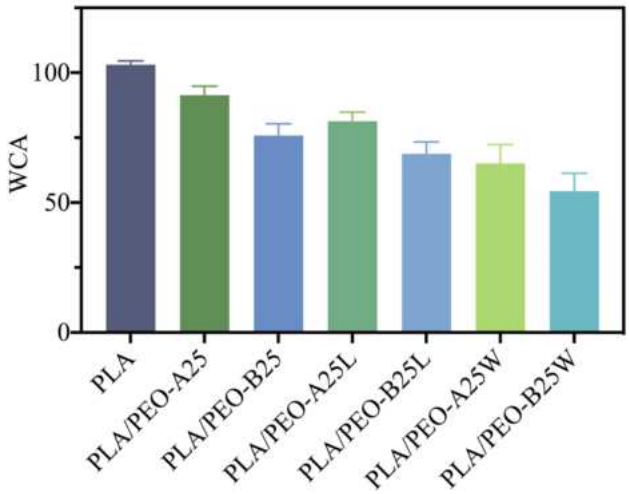

Figure 4.2.1.9 *WCA values of neat PLA, PLA/PEO-A25, PLA/PEO-B25, PLA/PEO-A25L, PLA/PEO-B25L, PLA/PEO-A25W and PLA/PEO-B25W membranes.*

Wenzel's equation state that WCA value should decrease as roughness increases. However, it is known in the scientific literature that, even though roughness increases, the presence of long interconnected channel in the membrane leads to an increase in WCA value instead of decrease. The effect of porosity on wettability, in fact, overcome the one induced by surface roughness increases [171,172]. Considering that, it is important to underline that the value obtained during WCA test are distorted by liquid capillary transport effect and shouldn't be considered as an increase of hydrophilicity. In addition, in PEO-B systems lower WCA value (if compared to PEO-A ones) are obtained due to the already commented differences in porous structure between PEO-A (smaller pores) and PEO-B (larger pores).

6.2.1.7 Mechanical properties

To evaluate different mechanical performance of the membranes, elastic modulus (E), tensile strength (TS) and elongation at break (EB) have been measured and results are reported in Table 4.2.1.3.

PLA exhibits elastic modulus, tensile strength and elongation at break of 60 MPa, 1.2 MPa and 45% respectively. If compared to PLA, all the unleached systems containing PEO-A does not show substantial differences i.e. mechanical performance that is controlled by PLA. These results are in accordance with other similar systems [158]. On the contrary, PEO-B membrane shows a different behaviour: as PEO-B content increase mechanical performance of the samples decrease. In detail, the addition of 25%, 50% and 75% of PEO-B induced a remarkable decrease in elastic modulus of PLA/PEO-B25, PLA/PEO-B50 and PLA/PEO-B75. If compared to the corresponding non-leached systems, PLA/PEO-A25W exhibits similar mechanical properties, on the contrary, PLA/PEO-B25W shows a clear decrease in E, TS and EB. PLA/PEOA-25L and PLA/PEO-B25L (DS) showed the same behaviour of their SS counterparts. The simultaneous decrease in modulus and elongation at break on increasing PEO-B content, confirms the typical behaviour of immiscible couples. In fact, poor miscibility of PEO-B phase leads to the formation of an irregular and heterogeneous fibrous structure with consequent disruption of some fibers. According to the morphological analysis, moreover, the presence of PEO-B phase agglomerations along the fibers induces discontinuity in the membranes structure leading to the formation of weak points across them. On the contrary, the good miscibility of PEO-A in PLA allows obtaining homogeneous structures leading to better mechanical performance if compare with PEO-B systems [158].

Table 4.2.1.3 Elastic modulus (E), tensile strength (TS), and elongation at break (EB) of the electrospun membranes.

Sample	E (MPa)	TS (MPa)	EB (%)
PLA	60 ± 2.3	1.2 ± 0.5	45 ± 4.6
PLA/PEO-A25	58 ± 3.7	2.0 ± 0.4	56 ± 7.2
PLA/PEO-A50	62 ± 12.8	0.9 ± 0.3	48 ± 9.5
PLA/PEO-A75	57 ± 7.7	0.8 ± 0.3	43 ± 5.6
PLA/PEO-B25	44 ± 0.2	1.4 ± 0.1	54 ± 13.9

PLA/PEO-B50	26 ± 11.2	0.1 ± 0.1	42 ± 9.2
PLA/PEO-B75	12 ± 3.5	0.4 ± 0.2	26 ± 13.1
PLA/PEO-A25W	52 ± 8.5	0.8 ± 0.2	45 ± 6.5
PLA/PEO-B25W	10 ± 2.1	0.5 ± 0.4	18 ± 3.1
PLA/PEO-A25L	55 ± 5.0	1.8 ± 0.6	38 ± 11.0
PLA/PEO-B25L	12 ± 2.0	0.5 ± 0.9	15 ± 6.0

6.2.1.8 Oil spill clean-up capacity of the porous membranes

The particular architecture observed for these membranes suggests their potential use as sorbent materials for oil spill cleanup. Six different kinds of oils (motor oil, exhausted motor oil, olive oil, exhausted olive oil, sunflower oil and exhausted sunflower oil) were chosen and their adsorption capacity by PLA, PLA/PEO-A25L, PLA/PEO-B25L, PLA/PEO-A25W and PLA/PEO-B25W were teste and results are shown in Figure 4.2.1.10. As expected, PLA membranes showed the lowest q value for all kind of oils tested. DS leached systems showed a slight increase in absorption capacity if compared to PLA membrane. The maximum absorption capacity for every type of oil was achieved by one-step leached systems. In particular, PLA/PEO-A25W and PLA/PEO-B25W showed the highest oil adsorption capacity for exhausted motor oil, with a q value of 115 and 137 g/g respectively. According to the scientific literature, the presence of high porosity, high surface area or empty channels increase oil absorption capacity of a membrane [173,174]. The low q value of PLA membrane, in fact, could be likely ascribed to its smooth and homogeneous fibers. The increase in absorption capacity values displayed by DS systems, could be reasonably attributed to the presence of fibers with porous surfaces. The best q values displayed by PLA/PEO-A25W and PLA/PEO-B25W are could be likely ascribed to the combination of a shell with large pores (also structured in furrows) and a core hollow structure. This particular structure, in fact, likely caused an increase of surface area and the formation of channels facilitated a deeper penetration of motor oil in the whole membrane.

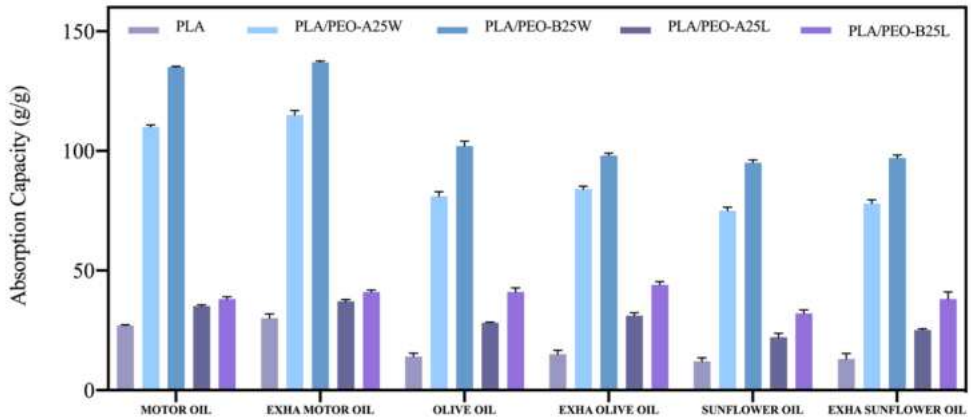

Figure 4.2.1.10 *Oil adsorption capacities of motor oil, exhausted motor oil, olive oil, exhausted olive oil, sunflower oil and exhausted sunflower oil by membranes.*

Moreover, PLA/PEO-A25W and PLA/PEO-B25W exhibit the best adsorption capacities for motor oil and the worst adsorption capacities for sunflower oil. According to the scientific literature, this behaviour should be addressed to the higher viscosity of motor oil (if compared to olive and sunflower oil ones) that make it difficult for the oil to flow out of the membranes once it enters the channels of the hollow fibers [174].

In Figure 4.2.1.11 is reported the oil spill clean-up process successfully carried out by PLA/PEO-B25W.

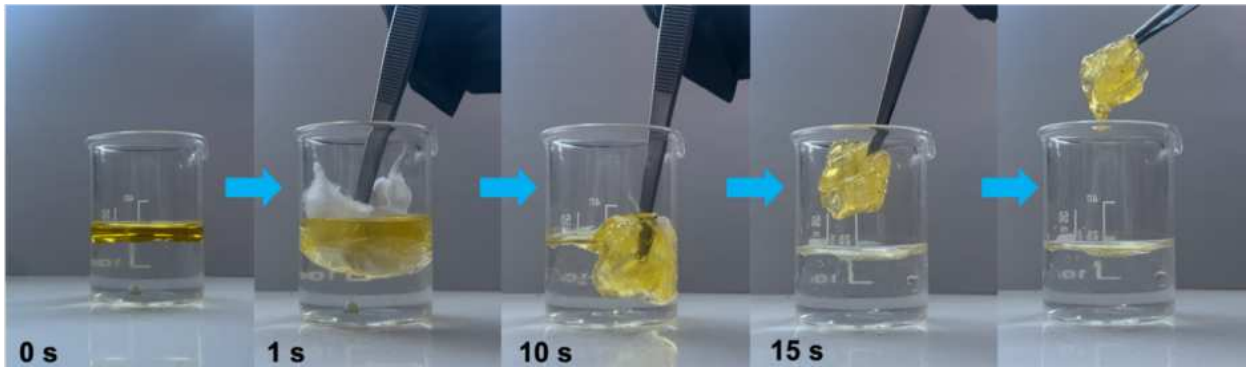

Figure 4.2.1.11 *Olive oil spill clean-up process using PLA/PEO-B25W.*

Table 4.2.1.4 shows the oil adsorption capacities of the wet coaxial electrospun PLA/PEO membranes and other adsorbents reported in literature. It can be noticed that, compared to other similar systems, wet coaxial electrospun PLA/PEO membranes exhibited excellent oil absorption capacity. Moreover, devices produced in this work were obtained in a single step process without using any additional chemicals.

Table 4.2.1.4 Comparison of oil adsorption abilities between wet coaxial electrospun PLA/PEO membrane and other adsorbents systems reported in literature.

Membrane	Materials	Additional Chemicals	Processing	Absorption Capacity [g/g]	Ref.
Coaxial and hollow fibers	PAN, PMMA	acetone, chloroform	electrospinning + stabilization + carbonization	10 - 45	[175]
Porous fibers	PLA	-	electrospinning + annealing for 12 h	22 - 42	[176]
Rough nanofibers	PLA, PHB	-	electrospinning	10 - 15	[177]
Rough nanofibers	PLA, SiO2	-	solution blow spinning	20	[178]
Fibers and micro spheres	PCL, MSO	-	electrospinning + electrospray	22 - 32	[179]
Fibers and micro spheres	PMMA, PDMS	hexane, curing agent	electrospinning + electrospray + curing 3h	55- 40	[180]
Coaxial and hollow fibers	PLA, PDLA	n-eptan	electrospinning + leaching-two steps	90 - 200	[174]
Coaxial and hollow fibers	PLA, PVA	-	electrospinning + leaching-two steps	23	[181]
Coaxial and porous hollow fibers	PLA, PEO	-	one step electrospinning and leaching	70 - 137	this work

6.2.1.9 Reusability of the porous membranes

Exhausted motor oil absorption ability of the electrospun membranes was monitored for up to five cycles to evaluate their reusability and the related performance. In this direction, membranes were washed in ethanol after used and the re-exposed to oil. The results are shown in Figure 4.2.1.12.

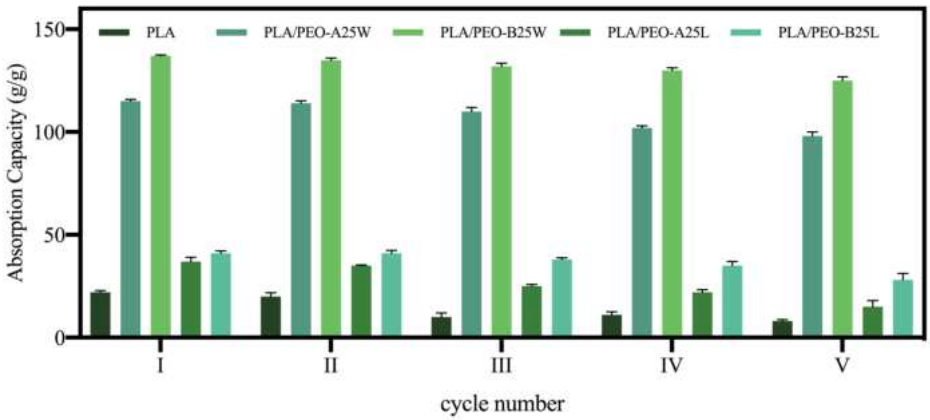

Figure 4.2.1.12 *Exhausted motor oil absorption capacity monitored for up to 5 cycles for PLA, PLA/PEO-A25W, PLA/PEO-B25W, PLA/PEO-A25L, PLA/PEO-B25L.*

After each cycle, PLA showed a decrease in absorption capacity (q). This decrease in q is probably attributable to the incomplete removal of oil from the membrane between cycles due to difficulty of penetration of the solvent during the rinsing phases.

A slight decrease (statistically significant only from the III cycle onwards) in q can be also observed for PLA/PEO-B25W after each cycle due to partial macroscopical damage of the membrane during the rinsing phase. On the contrary, no substantial variations can be evidenced for DS leached systems even after five cycle of oil absorption. The same behaviour can be observed for PLA/PEO-A25W and, again, is probably attributable to the peculiar fibers structure achieved for this system. During the rinsing phases, in fact, the penetration of the solvent is promoted by the porous and hollow structure of the fibers [180], thus granting a complete oil removal.

6.2.1.10 Conclusions

In this work, a new method for produce, in one-step, biodegradable membranes with hollow and porous fibers with high oil absorbance efficiency is presented. More in detail, membranes with hollow and (or) porous and fibers, based on polylactic acid (PLA) and polyethylene oxide (PEO) blends, were prepared using two approaches: i) conventional coaxial electrospinning followed by

leaching treatment (double-step); ii) coaxial wet electrospinning with *in situ* leaching (single-step). The relationships between materials, process, properties and structure of the obtained devices were analysed trough rheological, morphological, mechanical and surface characterizations. Results reveal that by varying PEO molecular weight and amount in the PLA/PEO blends it was possible to tune the fibers structure, especially after the leaching treatment, due to the difference in miscibility of the phases. Moreover, wet electrospinning production method allowed fabricating hollow and porous fibers (i.e. shell and core leaching) which, otherwise, could not be obtained with the double-step process that only leads to surface porosity (i.e. shell leaching). In fact, during the *in situ* leaching, not jet stabilized fibers, containing residual solvent, come into contact with the leaching agent promoting its penetration into the core creating the hollow structure.

Differences in polymeric compositions or morphology have led also to a variation in membranes mechanical performance: the occurrence of discontinuity in the fibers, due to the presence of an immiscible phase or porosity, leads to a decrease of membranes elastic modulus.

The two-step and the *in situ* leached systems both displayed morphological characteristics and mechanical property potentially suitable for oil spill cleanup application. Oil absorbance test reveal that membranes obtained via single-step method displayed higher performance in oil removal, if compared to the ones obtained through the post processing leaching, due to their hollow and porous structure that ensure higher exposed surface area.

6.2.2 Sustainable 3D Fibrous Structures based on PLA and Natural Wastes for Household Wastewater Treatment: Dye Absorption and FOG (oil/water) Separation

6.2.2.1 Abstract

Water is fundamental to life and ensuring the treatment of wastewater is crucial for both human health and the preservation of our planet. To address the growing issue of food industries and household wastewater pollution, it is essential to explore the use of sustainable devices to avoid secondary pollution. In this study, 3D fibrous structures based on PLA and natural waste fillers namely as Opuntia Ficus Indica (OFI), Posidonia Oceanica Leaves (POL) and lignin (LIG) were successfully developed via wet solution blow spinning and characterized to explore their potential application for the treatment of wastewater. Methylene blue, (MBL) and fat oil and greases mixture (FOG, oil-water) were used to verify the effectiveness of the prepared materials for the separation/removal of pollutants. The PLA composites containing LIG and POL exhibited superior performance in both MBL absorption and FOG removal, thanks to their increased surface area and the oleophilic properties of lignin both contributing to the enhancement of the hydrophobic behaviour of the structures. Although both pseudo-first-order and pseudo-second-order kinetic models were applied to the adsorption data, neither provided an adequate fit, suggesting that the adsorption process is more complex, likely influenced by surface heterogeneity. Moreover, PLA/POL and PLA/LIG fibrous structures demonstrated also satisfying stability maintaining good oil removal efficiency across four reuse cycles. These results underscore the potential of integrating biodegradable polymers and natural waste materials for creating efficient and eco-friendly solutions for wastewater treatment.

6.2.2.2 Preparation of PLA/fillers dispersions and 3D fibrous structures

OFI cladodes and POL scraps were washed with water at room temperature and then oven-dried at 60 °C for 48 hours. Afterward, both scraps were chopped and ground for 3 minutes using a conventional mixer. Following this step, OFI, POL and LIG particles were processed in a ball milling (Retsch MM 500 nano, Germany) for 30 minutes at 20 Hz to produce micrometric powder (1-10 µm). A 10 wt% PLA solution was prepared in a chloroform/acetone (Chl/Ac) mixture at a 2:1 ratio. Once the PLA had fully dissolved, 10 wt% (relative to PLA mass) of OFI, POL, and LIG powders were individually dispersed into the PLA solution (as depicted in Figure 4.2.2.1a), with magnetic stirring at 25 °C maintained overnight.

The production of composite 3D structures was carried out via wet solution blow spinning process (Figure 4.2.2.1b) with a home-made solution blow spinning (SBS) apparatus. More in detail, the SBS process was performed on a liquid collector (DI water at room temperature). The feed rate and the pressure were maintained at 50 mL/h and 0.6 MPa respectively and the needle-to-collector distance was 10 cm. After the membrane was formed on the liquid collector, it was carefully collected from the water surface and pressed using a perforated metallic plate (Figure 4.2.2.1b) to create a 3D fibrous device (Figure 4.2.2.1c). The membranes were shaped into cylindrical structures with a height of 5 mm and a diameter of 3 mm. The blow spinning time was limited to 10 seconds for the obtainment of each 3D structure. The temperature during processing was kept at 23 ± 2 °C, and the relative humidity of the air was 50 ± 5 %. The obtained fibrous membranes were then dried at room temperature for 24 h to remove any residual solvent. According to the starting dispersions, the membranes were labelled PLA, PLA/OFI, PLA/POL and PLA/LIG (Figure 4.2.2.1c).

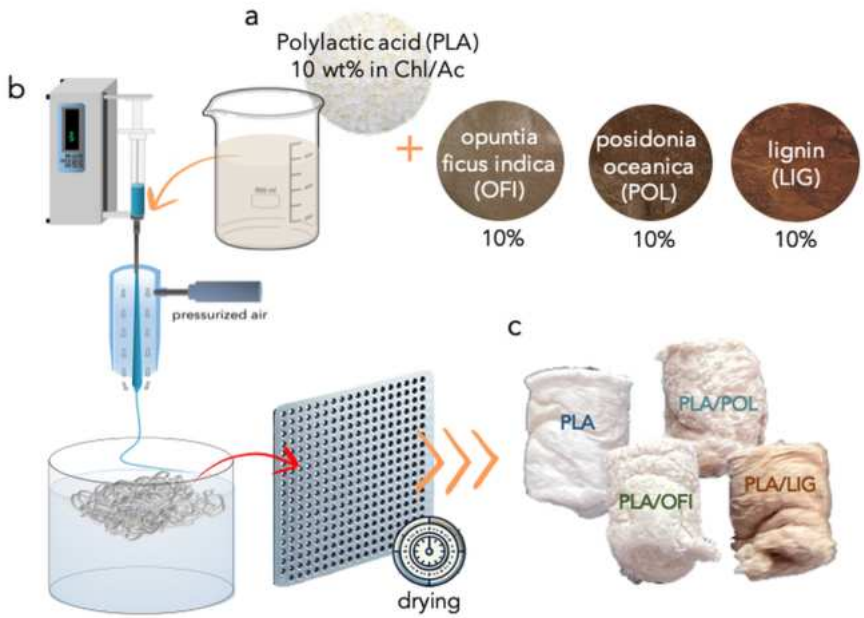

Figure 4.2.2.1 *Schematic illustration for the preparation of the composite 3D structures: (a) preparation of the composite dispersions; (b) fabrication via wet solution blow spinning of the 3D structures; (c) optical photograph of the obtained PLA, PLA/OFI, PLA/POL, and PLA/LIG composite 3D structures.*

6.2.2.3 Morphology of natural particles

The morphological analysis of OFI, POL, and LIG particles following the ball-milling process was examined through SEM, as shown in Figure 4.2.2.2a-c. The respective particles size distribution, in terms of equivalent diameter, are reported in Figure 4.2.2.2a'-c'. Both OFI and LIG particles (Figure 4.2.2.2a, c) exhibit a generally spherical shape, with an average diameter of approximately 2.2 μm (Figure 4.2.2.2a', c'). While LIG particles appear uniform in both size and shape, OFI powder includes a few larger, more elongated particles. POL particles, in contrast, showed irregularly shaped particles with average diameter of around 5 μm (Figure 4.2.2.2b'), alongside a few larger particles, up to 90 μm in size, as can be observed in Figure 4.2.2.2b. Unlike OFI and LIG, POL particles also display a porous structure with deep surface channels. Despite these differences, OFI, POL, and LIG powders all appear dimensionally compatible with the solution blow spinning process.

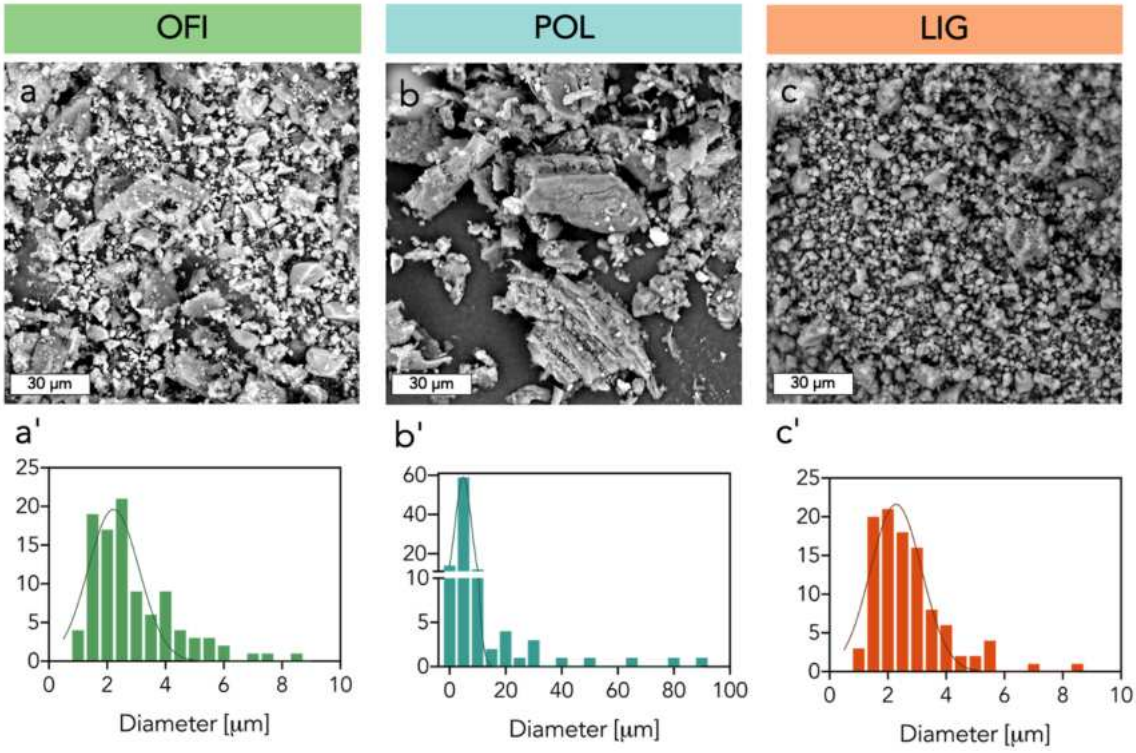

Figure 4.2.2.2. *SEM images and size distribution of OFI (a, a'), POL (b, b'), LIG (c, c') particles respectively.*

6.2.2.4 Rheological characterization

Rheological tests have been performed on the polymeric dispersions and the results are reported in Figure 4.2.2.3. Neat PLA exhibits a distinctly non-Newtonian behaviour over the entire frequency range. Upon the addition of natural particles to the PLA solution, a noticeable increase in viscosity across the frequency range was observed, although the overall rheological behaviour of all the composite dispersions remained consistent. As already observed in our previous work [129], the inclusion of POL powder causes a more pronounced increase in viscosity compared to OFI and LIG ones. To address this issue, it is necessary to consider the porous structure of the larger POL particles (Figure 2b). This porosity, in fact, offer more sites for physical interaction with PLA, resulting in greater resistance to deformation and increased viscosity, as observed in similar systems [133,134].

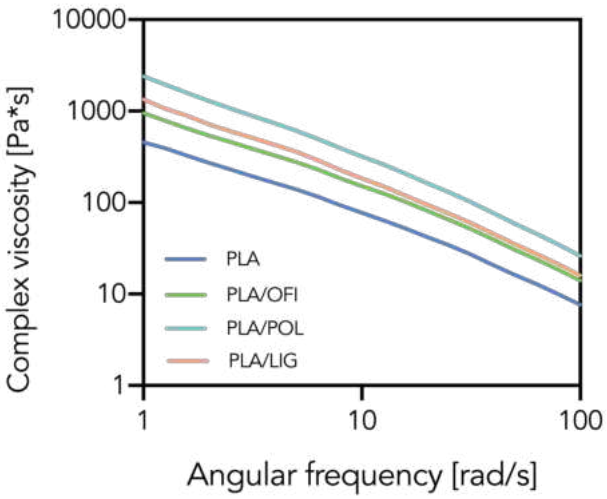

Figure 4.2.2.3 *Complex viscosity of the polymeric dispersions.*

6.2.2.5 Morphology of 3D fibrous structures

The solution blow spinning process proceeded smoothly for all the polymeric dispersion containing the natural fillers and any clogging of the needle (1 mm diameter) occurred. The morphologies of PLA, PLA/OFI, PLA/POL and PLA/LIG 3D fibrous structures were evaluated by SEM, relative fibers diameter distributions were calculated and the results are reported in Figure 4.2.2.4a-d and in Figure 4.2.2.4a"-d" are reported the respective magnifications. PLA structures (Figure 4.2.2.4a) exhibit randomly oriented fibers mainly characterized by a unimodal fibers diameter distribution with an average diameter of 1.9 µm (Figure 4.2.2.4a"), alongside a few larger fibers of about 10 µm in size, as can be observed in the magnification (Figure 4.2.2.4a'). The addition of natural fillers significantly affects fibers shape according to the rheological characterization of the dispersions (see Figure 4.2.2.3). More in detail, the addition of OFI or LIG powder in PLA solution leads to a significative decrease in the fibers diameters, resulting in a unimodal, wide fibers diameter distribution with an average of 1.3 µm (Figure 4.2.2.4b") and 0.8 µm (Figure 4.2.2.4d") respectively.

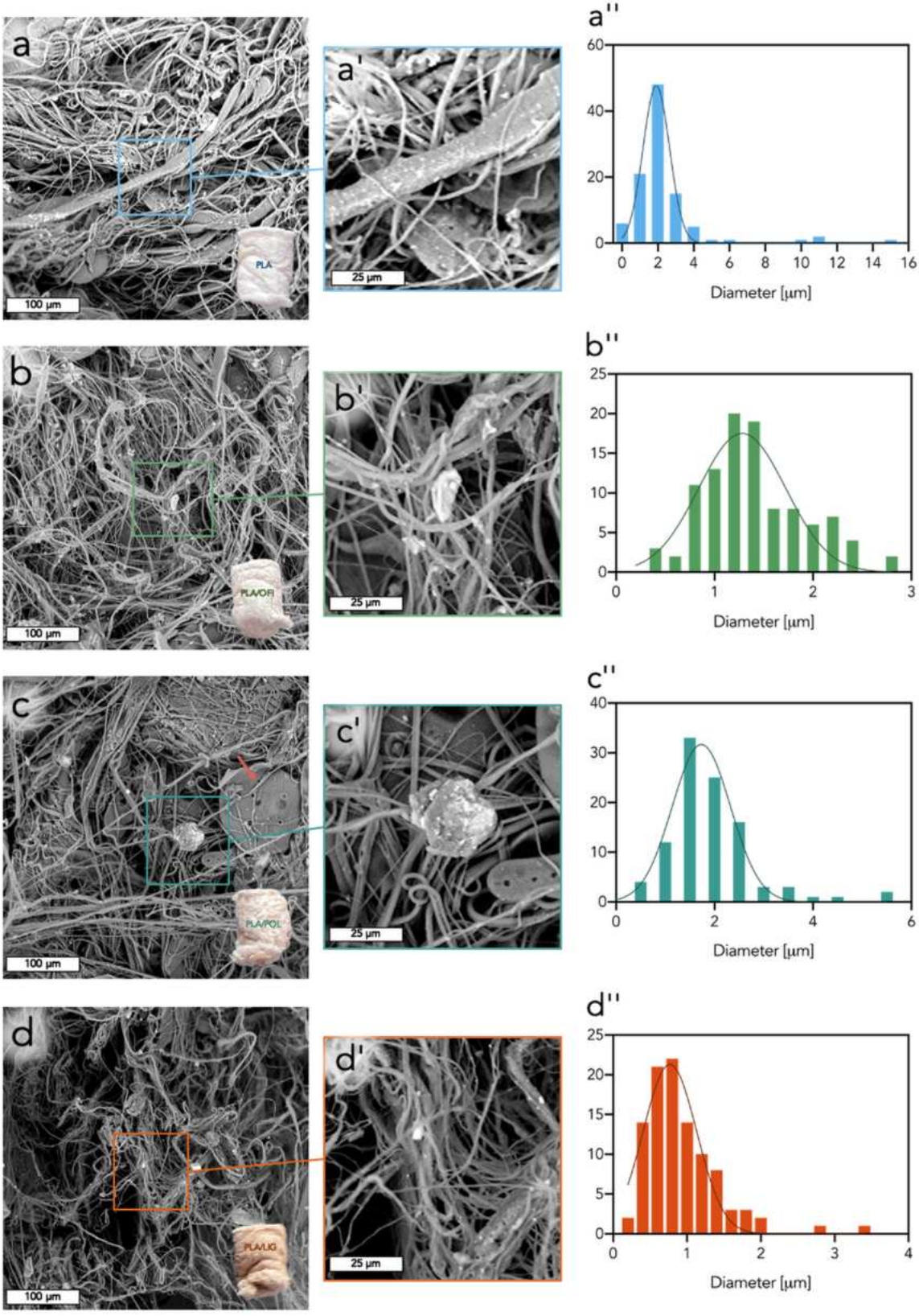

Figure 4.2.2.4 *SEM images, relative insets and fibers diameter distribution of PLA (a, a', a''), PLA/OFI (b, b', b''), PLA/POL (c, c', c'') and PLA/LIG (d, d', d'') membranes respectively.*

Additionally, PLA/OFI fibers appear randomly oriented with some OFI particles well distributed all over the membrane, as better observed in Figure 4.2.2.4b', while LIG ones seems to be almost entirely embedded into PLA fibers (Figure 4.2.2.4d, d'). This indicates that particles exceeding a few micrometres in size, which are unable to be fully embedded within the fibers, can be expelled through the needle and adhered to the fiber surfaces, becoming part of the fibrous structure.

The decrease in fibers diameters is less pronounced in PLA/POL structures in which the fibers are characterized by a unimodal, narrow fiber diameter distribution with an average diameter of 1.7 µm (Figure 4.2.2.4c''). Moreover, POL particles could be extensively identified in SEM image (Figure 4.2.2.4c, c') together with some beads (see the red arrow in Figure 4.2.2.4c).

To address the fibers diameter decrease of composites structures, it is necessary to consider that the variations in the composition of the spinning solution typically influence its viscosity, which can, in turn, impact the morphology of the fibers [153]. More in detail, higher viscosity helps to stabilize the electrospinning jet, minimizing fluctuations that may cause inconsistencies in fibers diameter [153]. Moreover, when the solution has a higher viscosity, it may resist fragmentation better and elongate further under the influence of the air drag, resulting in thinner fibers. However, if the viscosity is too high, it can inhibit fibers formation, leading to discontinuities fibers or beads formation [106,182].

6.2.2.6 Wettability of 3D fibrous structures

The wettability of the devices plays a crucial role in achieving emulsion separation. The wetting performance of the 3D fibrous structures was assessed by measuring the time-dependent evolution of water and oil contact angle in air and the relative results are reported in Figure 4.2.2.5.

Water-in-air contact angle tests revealed that the PLA 3D fibrous structures exhibit hydrophobic behaviour, as expected for the material, with a contact angle of 92°. The addition of natural fillers, leading to fibers with smaller diameters and fibers bundles, results in surfaces with increased roughness. According to Wenzel's model, this increased roughness enhances the

hydrophobic behaviour of the composite 3D structures [183]. Consequently, contact angles of 110°, 115°, and 118° were observed for PLA/OFI, PLA/POL, and PLA/LIG 3D fibrous structures, respectively. Additionally, the increasing lignin content, given by the added natural fillers, reasonably contributes to the enhancement of the hydrophobic behaviour of the structures [184,185]. The wettability tests for oil in air, shown in Figure 4.2.2.5b-e, revealed that all the 3D fibrous structures, PLA, PLA/OFI, PLA/POL, and PLA/LIG, exhibit immediate oil absorption, with contact angles approaching zero. In all the cases, the oil droplets were instantly absorbed upon contact. This is consistent with the known low barrier properties of PLA against non-polar substances like oils [186].

Figure 4.2.2.5 *3D fibrous structures water and oil wetting behaviour: water wettability in air (a); wettability of oil in air of PLA (b), PLA/OFI (c), PLA/POL (d), PLA/LIG (e).*

6.2.2.7 Methylene blue sorption and kinetics study

Methylene blue (MBL) sorption ability and kinetics of the 3D fibrous structures was evaluated by immersing them in MBL solutions for 24 hours and relative results are reported in Figure 4.2.2.6. Figures 4.2.2.6a-d show the of UV-Vis absorption spectra in the 500–800 nm range relative to MBL absorption peak (665 nm) at various time intervals (0, 3, 6, 8, 12, 18, and 24 hours) for PLA (a), PLA/OFI (b), PLA/POL (c), and PLA/LIG (d). Each panel (a-d) includes photographs of the corresponding solution before (0 h) and after 24 hours of adsorption. The progressive reduction in the absorption peak indicates a decreasing in concentration of MBL in the solution. The most pronounced reduction can be observed for PLA/POL and PLA/LIG structures, in accordance with the colour of the solutions after 24 hours of absorption. As it is possible to notice from Figure 4.2.2.6e, PLA/LIG shows the highest removal efficiency reaching almost 90 % in the first 10 hours (92 % after 24 h) of the absorption test, followed closely by PLA/POL (80 % after 10 h and 87 % after 24 h) and PLA/OFI (65 % after 10 h and 70 % after 24 h). Neat PLA exhibited the worst performance, with only 40 % of MBL removed after 10 h and 55 % after 24 h. In Figure 4.2.2.6e are also reported the digital photos of PLA/LIG (top left corner) and PLA (bottom right corner) 3D structures after 24h of absorption test.

The high removal efficiency observed in the PLA/LIG and PLA/POL can be primarily attributed to the presence of lignin. Lignin is known for its complex aromatic structure, rich in functional groups such as hydroxyl and methoxy, which facilitate strong chemical interactions with MBL [185]. These functional groups enable both hydrogen bonding and π-π interactions between the lignin and the aromatic rings of MBL, enhancing the adsorption process. In particular, POL contain significantly higher lignin content compared to OFI [129]. Furthermore, in accordance with SEM images (Figure 4.2.2.4), the addition of the natural fillers results in smaller fibers diameters compared to neat PLA. This reduction in fibers diameter likely leads to an increased surface area, which provides more exposed active sites for adsorption, further enhancing the removal efficiency of PLA fibers.

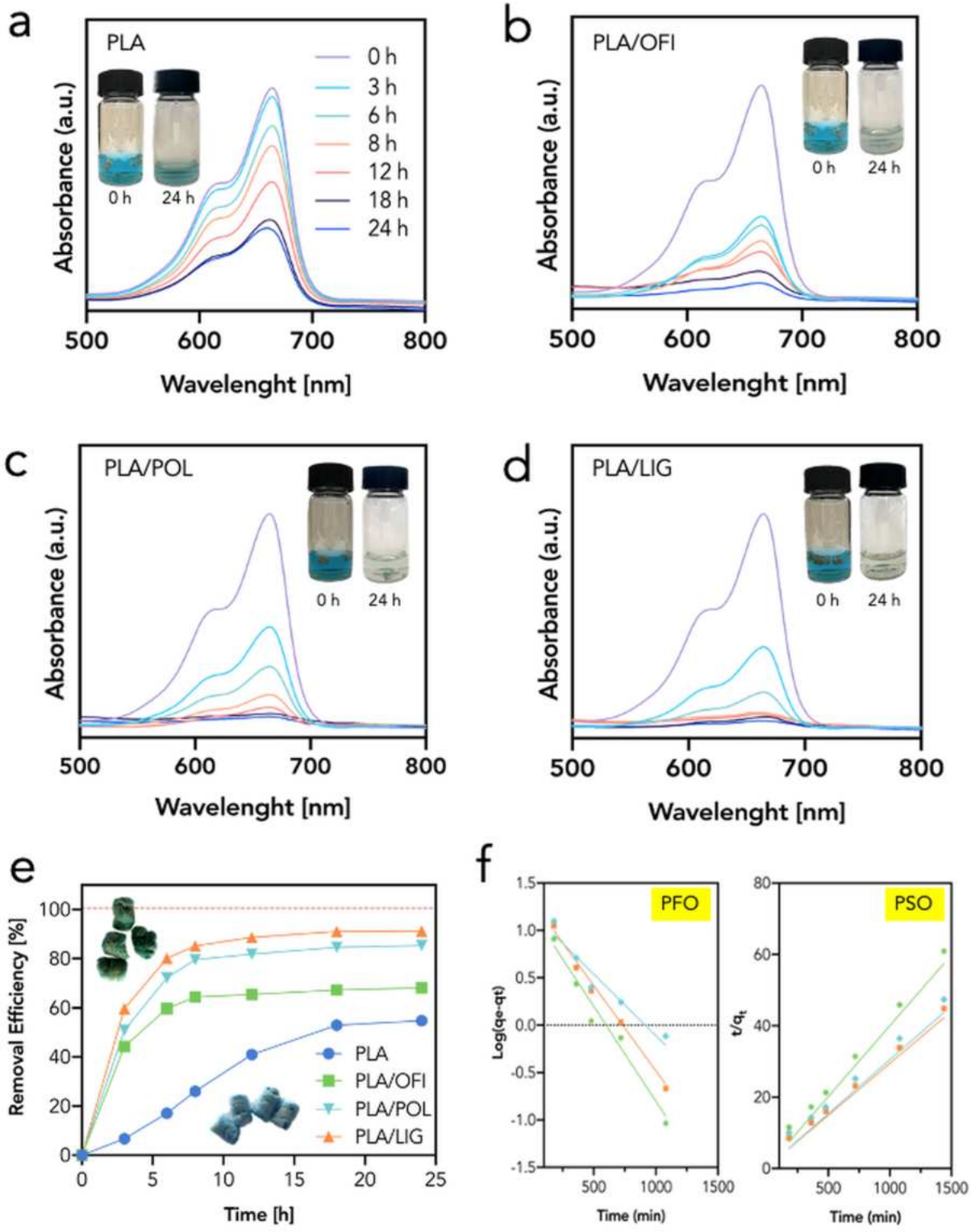

Figure 4.2.2.6 *Time-dependent adsorption of MBL: UV-Vis absorption spectra of MBL over time (0-24 h) for PLA (a), PLA/OFI (b), PLA/POL (c), and PLA/LIG (d). Insets show the appearance of the MBL solution at 0 h and 24 h. MBL removal efficiency (%) as a function of time (e) and linearized pseudo first and pseudo second order kinetic plots of the adsorption process, symbols represent experimental points and lines the theoretical ones (f).*

Therefore, the superior performance of both PLA/LIG and PLA/POL can be directly correlated with the combination of lignin-derived functional groups and the morphological changes induced by filler addition, which together maximize the adsorption capacity of the composites.

Pseudo first and pseudo second order kinetic models were studied for the adsorption of the MBL. Neither the pseudo-first-order (PFO, Figure 4.2.2.6f) nor the pseudo-second-order (PSO, Figure 4.2.2.6f) kinetic models provided an adequate fit for the adsorption behaviour of MBL. The PFO model is generally applicable when the rate of adsorption is controlled by the difference between the concentration of the adsorbate in solution and the amount adsorbed at the surface. The PSO model is more suitable when chemisorption dominates, where the rate depends on the number of active sites on the adsorbent surface and the interaction between the adsorbent and adsorbate [187]. Herein, the failure of both models can be attributed to the highly irregular surface morphology of the 3D fibrous structures, with each sample exhibiting distinct shapes. Additionally, as already seen in SEM images (Figure 4.2.2.4), during SBS process, fibers bundles were formed and this behaviour further complicating the adsorption process by creating heterogeneous and complex surfaces. Moreover, natural filler particles are randomly distributed both in location and quantity in the 3D fibrous structures, introducing further variability. These irregularities in surface structure, combined with the random distribution of the filler particles, likely result in adsorption mechanisms that cannot be described by simple kinetic models like PFO or PSO. The complexity of the system suggests that the adsorption process is influenced by a range of factors, including surface heterogeneity and possibly diffusion limitations, which are not accounted for in these kinetic models.

6.2.2.8 FOG (Oil-Water) Separation

The wastewater sample used for the separation test was provided by a waste management company (Ecodep Srl) that handles, among other, liquid waste from the food industry or restaurant kitchens.

The solid wastes were filtered aiming to separate only the liquid part of the oil in water emulsion. FOG sorption ability of the 3D fibrous structures was evaluated by immersing them in the oil in water emulsion for 24 hours and relative results are reported in Figure 4.2.2.7.

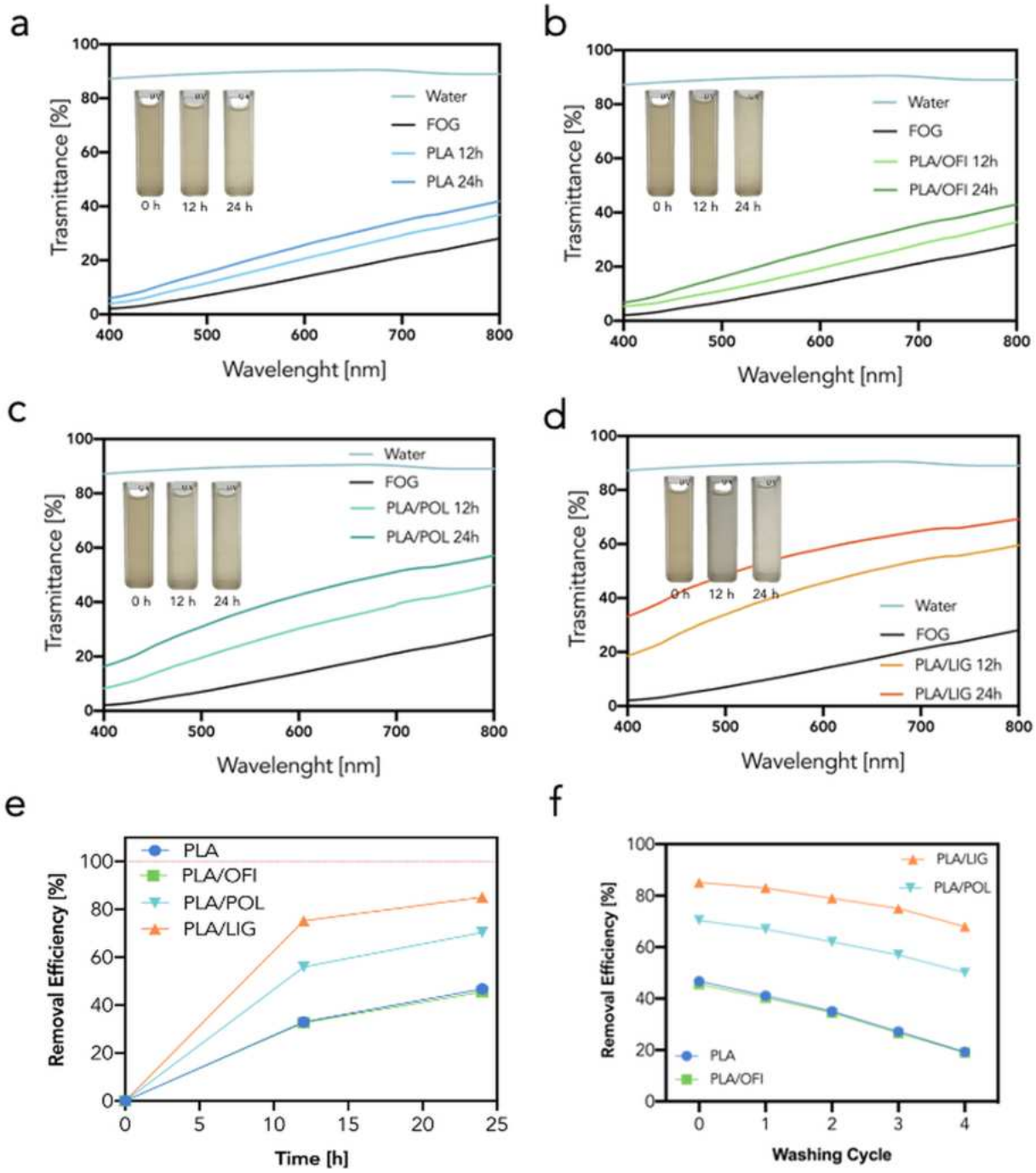

Figure 4.2.2.7 *Time-dependent separation of FOG: UV-Vis absorption spectra of water, FOG, and FOG-treated with PLA (a), PLA/OFI (b), PLA/POL (c), and PLA/LIG (d) 3D fibrous structures. Insets show the appearance of the oil in water emulsion at 0 h, 12 h and 24 h. FOG removal efficiency (%) as a function of time (e) and reusability of the 3D fibrous structures (f).*

The removal efficiency of the 3D structures was evaluated by investigating the transmittance spectra of the emulsions through UV-vis spectroscopic analysis. Neat PLA (Figure 4.2.2.7a) and PLA/OFI (Figure 4.2.2.7b) structure, exhibits a gradual but modest increase in transmittance over time, indicating partial FOG removal. As can be seen from the insets, even after 24 hours of testing, the emulsion remains quite cloudy. PLA/POL structures (Figure 4.2.2.7c), shows further improvement in FOG removal, as evidenced by higher transmittance levels at both 12- and 24-hours. PLA/LIG structures (Figure 4.2.2.7d) exhibit the most effective FOG removal, with a remarkable increase in transmittance, particularly after 24 hours. The inset of Figure 4.2.2.7d highlight that after 24 hours of absorption, the emulsion is substantially clear if compared to the starting condition. The integral value under the absorption curve before and after treatment were used to calculate the removal efficiency of the different 3D fibrous structures aiming to comparing their adsorption performance (Figure 4.2.2.7e) [188]. The PLA/LIG structures emerges as the most efficient, reaching about 85% of removal efficiency after 24 hours, followed by PLA/POL, with 72%. PLA/OFI, and pure PLA, showed quite the same behaviour with approximatively 45% of removal efficiency. To address these issues, it is necessary to consider that PLA exhibited limited oil removal efficiency due to its relatively hydrophobic nature but lack of strong oleophilic characteristics [186]. The similar efficiencies of PLA and PLA/OFI suggest that the addition of OFI did not provide any significant benefit for oil removal under the tested conditions. To address this issue, it is necessary to consider that OFI is richer in cellulose rather than lignin and cellulose hydrophilic behaviour may results in competitive absorption of water, thereby not contributing to the oil absorption process. On the contrary, the higher content of lignin in POL powder results in improved oil absorption of PLA/POL structures compared to PLA ones. Obviously, this behaviour is even more marked when pure lignin is added to PLA in PLA/LIG structures. Lignin, in fact, it is well known for its hydrophobic and oleophilic properties, due to its complex aromatic structure that facilitates strong interactions with oil molecules, promoting higher absorption rates [185]. Moreover, in accordance with SEM images (Figure 4.2.2.4) and with MBL absorption (Figure 4.2.2.6), the addition of the natural particles leads

to a decrease in fiber diameters of the composite structures, resulting in a larger surface area, offering more exposed active sites for adsorption and thereby improving oil removal efficiency. As a result, also for FOG sorption, the enhanced performance of both PLA/LIG and PLA/POL can be directly attributed to both the fibers diameter decrease due to fillers addition and the presence of lignin-derived functional groups. More in detail, the coexistence of hydrophilic oxygen-containing groups and hydrophobic methyl oxygen groups and benzene rings in lignin structure allow to improve oil-water separation [189].

Removal efficiency of the 3D fibrous structures was tested across multiple washing cycles and results are reported in Figure 4.2.2.7f. Progressive reduction in the removal efficiency of PLA and PLA/OFI was observed across the four washing cycles. Significant changes in removal efficiency of PLA/POL and PLA/LIG occur only after the second cycle. However, starting from the third cycle, a slight but progressive reduction in removal efficiency was observed also for PLA/POL and PLA/LIG. After four washing cycles the fibrous structure of PLA and PLA/OFI devices appear damaged while fibers structures of PLA/POL and PLA/LIG showed only minor modification as observed from SEM images in Figure 4.2.2.8a-d. Although the fibrous structures of PLA/POL and PLA/LIG exhibited only minimal visual damage after multiple washing cycles, the progressive decline in removal efficiency suggests that the absorbed oil may not be entirely removed during the washing process. Residual oil trapped within the fibers and absorbed by the natural fillers could progressively occupy more surface area and partially occlude POL and LIG pore, reducing the available sites further limiting oil absorption capacity in subsequent cycles.

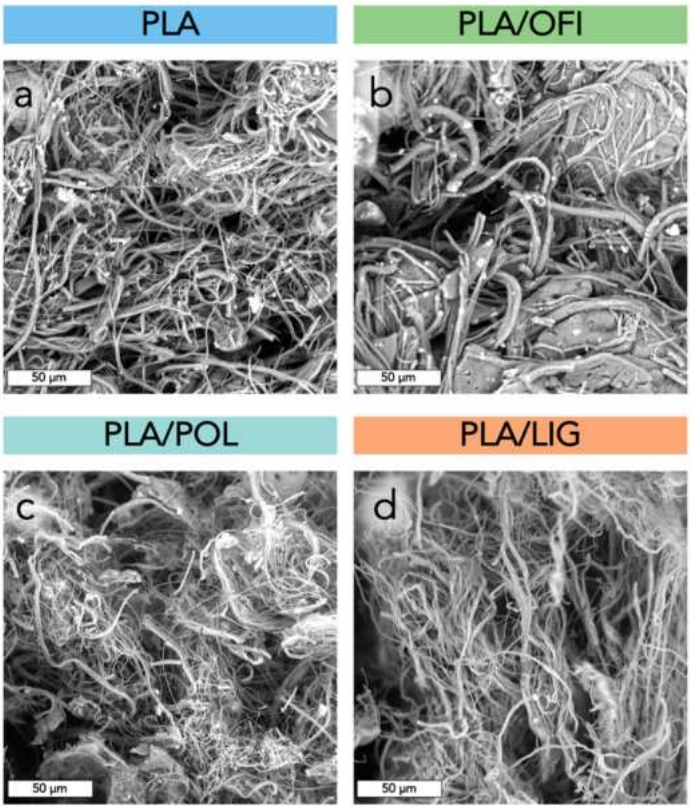

Figure 4.2.2.8 *SEM images of PLA (a), PLA/OFI (b), PLA/POL (c) and PLA/LIG (d) membranes after four cycles of washing and FOG removal.*

The removal efficiencies herein reported are remarkable, especially when considering that typical evaluations are often conducted using model systems where pure oil is employed to assess absorption performance. In contrast, the system used in this work is based on a real sample obtained from a wastewater treatment plant. It is important to acknowledge that FOG (fats, oils, and grease) derived from household waste is a complex mixture, containing both saturated and unsaturated fats, oils, and emulsifying agents. The presence of emulsifiers and the heterogeneous nature of the mixture can make separation more challenging compared to pure oils. Kitchen-derived FOG often contains natural emulsifiers, such as soaps and detergents, which can form stable emulsions. These emulsions can reduce the separation efficiency, as the oil droplets become too small to be easily absorbed.

6.2.2.9 Conclusions

In this work, 3D fibrous structures based on PLA and natural fillers were successfully prepared using solution blow spinning process. The composite dispersions were prepared by adding 10 wt% of *Opuntia Ficus Indica* (OFI), *Posidonia Oceanica Leaves* (POL) or lignin (LIG) powders to the PLA solution. The incorporation of natural fillers led to an increase in the viscosity of the PLA solutions, which in turn improved the fibers morphology by reducing their diameters. This effect was particularly evident in PLA/LIG and PLA/POL composites, which exhibited smaller fiber sizes and a more uniform distribution. Additionally, the presence of natural fillers, particularly LIG and POL (due to its high lignin content), significantly enhanced the hydrophobicity of the materials, improving their oil absorption capacity. This improvement in surface wetting behaviour, combined with the smaller fiber diameters, made the PLA/POL and PLA/LIG structures more suitable for oily pollutant removal and oil-water separation applications. The methylene blue adsorption and FOG (oil-water) separation tests demonstrated that the PLA/LIG and PLA/POL composites outperformed the other samples. The addition of OFI particles to PLA increased MBL removal efficiency, rising from 55% of the neat PLA to 68% (after 24 hours). PLA/POL and PLA/LIG achieved the best methylene blue sorption with removal efficiencies of 85% and 91% respectively (after 24 hours).

Similarly, the best FOG separation efficiencies were achieved by PLA/POL and PLA/LIG, reaching 70% and 85% of oil absorbed after 24 hours, respectively, while also maintaining good performance over four reuse cycles.

The promising results obtained with real wastewater samples (FOG) further validate the practical applicability of these materials, paving the way for future studies on the scalability and long-term use of such systems in industrial settings.

6.3 Soil

A series of preliminary studies were conducted to assess the printability of PLA and Mater-Bi® based composites using Fused Deposition Modelling (FDM) technology, incorporating different natural fillers: *Hedysarum Coronarium, Solanum Lycopersicum, Opuntia Ficus Indica*. The materials produced via FDM were first compared with those created using the same formulations but through compression moulding. These comparisons focused on mechanical properties and the ability of the composites to release active compounds, for which NPK fertilizer was used as a test case.

FDM technology was ultimately selected as the optimal method due to its superior capability to produce stable and porous structures. These porous features were essential for improving the composites' performance in pollutant removal applications.

Subsequent studies explored the ability of the composites to remove heavy metals, such as Cu(II) ions, using fillers of different natural origins and varying polymer matrices. Specifically, 3D-printed composites made with tomato plant fillers in PLA, Mater-Bi, and PLA/Mater-Bi blends were evaluated for their dual functionality in releasing NPK fertilizer and removing Cu(II) ions. Composites incorporating anchovy fishbone scraps with PLA or Mater-Bi were also tested for Cu(II) ion removal. Finally, *Juncus Maritimus* and PLA-based composites were examined for their effectiveness in removing a range of heavy metals.

6.3.1 *Hedysarum coronarium-based Green Composites Prepared by Compression Moulding and Fused Deposition Modelling*

The subsequent text and images have been fully extracted from the published article authored by the candidate "Scaffaro, R.; Citarrella, M.C.; Gulino, E.F.; Morreale, M. Hedysarum coronarium-Based Green Composites Prepared by Compression Molding and Fused Deposition Modeling. Materials 2022, 15, 465. https://doi.org/10.3390/ma15020465 [190]" and are reproduced here with the necessary permissions.

Author contribution: methodology, software, validation, formal analysis, investigation, data curation, writing—original draft preparation, writing—review and editing, visualization.

6.3.1.1 *Abstract*

In this work, an innovative green composite was produced by adding *Hedysarum Coronarium* (HC) flour to a starch-based biodegradable polymer (Mater-Bi®, MB). The flour was obtained by grinding together stems, leaves and flowers and subsequently sieving it, selecting a fraction from 75 µm to 300 µm. Four formulations have been produced by compression moulding (CM) and fused deposition modelling (FDM) by adding 5%, 10%, 15% and 20% of HC to MB. The influence of filler content on the processability was tested, and rheological, morphological and mechanical properties of composites were also assessed. Through CM, it was possible to obtain easily homogeneous samples with all filler amounts. Concerning FDM, 5% and 10% HC-filled composites proved also easily printable. Mechanical results showed filler effectively acted as reinforcement: Young's modulus and tensile strengths of the composites increased from 74.3 MPa to 236 MPa and from 18.6 MPa to 33.4 MPa, respectively, when 20% of HC was added to the pure matrix. FDM samples, moreover, showed higher mechanical properties if compared with CM ones due to rectilinear infill and fibers orientation. In fact, regarding the 10% HC composites, Young's modulus of the CM and FDM ones displayed a relative increment of 176% and 224%, respectively.

6.3.1.2 *Preparation of Composites*

Firstly, the dried HC was ground for 3 min and then sieved in order to obtain particles of a size suitable for the 3D printer, which, therefore, do not lead to obstructions in the nozzle. To this

aim, the sieving fraction from 75 μm to 300 μm was selected. In order to obtain a homogeneous dispersion of the filler, the filler amounts chosen to prepare MB-based bio-composites were 5, 10, 15 and 20 wt%. All of the composites (namely MB/HC5, MB/HC10, MB/HC15, MB/HC20) and neat MB, for comparison, were prepared by melt compounding in an internal mixer. The obtained materials were then ground into pellets and processed in a single-screw extruder. The compression-moulded samples (CM) were obtained using a laboratory press. For each formulation, 60 mm × 10 mm × 1 mm samples were printed using a 3D printer. Some representatives of obtained CM and FDM samples are shown in Figure 4.3.1.1.

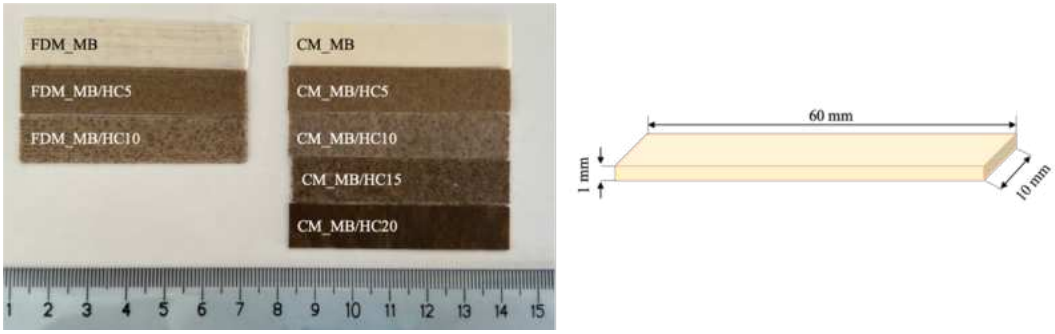

Figure 4.3.1.1 *FDM- and CM-obtained samples.*

6.3.1.3 Results and discussion

Neat MB and HC composite filaments were easily extruded with a diameter suitable for the printer (1.75 mm), and part of them were pelletized and processed by compression moulding. Through CM, it was possible to obtain homogeneous samples with all filler amounts. Regarding the FDM samples' printability, pure MB and the ones containing 5% and 10% of HC proved easily printable once the appropriate parameters were found. The bio-composite containing more than 10% of HC, in fact, could not be produced by FDM with the printer used in this study. In detail, 15% and 20% of HC-containing filament does not even flow in the melting chamber.

It is known from the scientific literature that rheological properties of the polymeric filament have a strong influence on printability [191]. For this reason, rheological properties of bio-composites have been investigated. In Figure 4.3.1.2, the rheological curves of MB and its HC composites are shown. For MB, a pseudoplastic behaviour was generally observed, with remarkable shear thinning at higher frequencies. In general, the addition of HC leads to a variation of polymer viscosity: when increasing filler content, the viscosity values monotonically increase in the entire investigated frequency range. It is worth observing that MB/HC15 and MB/HC20 show a remarkably non-Newtonian behaviour with the presence of apparent yield stress in the low frequency region. This behaviour could reasonably justify the non-printability of 15% and 20% of HC-containing composites. As soon as filament reaches the melting chamber, in fact, the very first part of the filament melts and, due to its high viscosity, creates a plug at the entrance of the chamber that clogs it, not allowing the filament to advance. Therefore, filaments do not melt in the chamber, leaving it empty and thus preventing the sample printing.

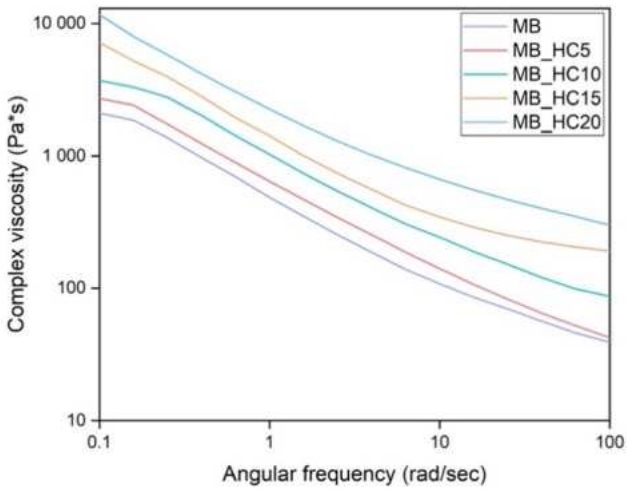

Figure 4.3.1.2. *Complex viscosity of pure MB and its HC composites.*

Morphology of MB samples, HC powder and obtained composites were analyzed by SEM. Relevant optical image and micrograph of the natural organic filler are shown in Figure 4.3.1.3. From SEM micrograph (Figure 4.3.1.3b), it is possible that the HC powder contains elements with different

morphology, reasonably belonging to different parts of the plant: the solid line highlights a part probably belonging to the stem, while the dashed line highlights a flower.

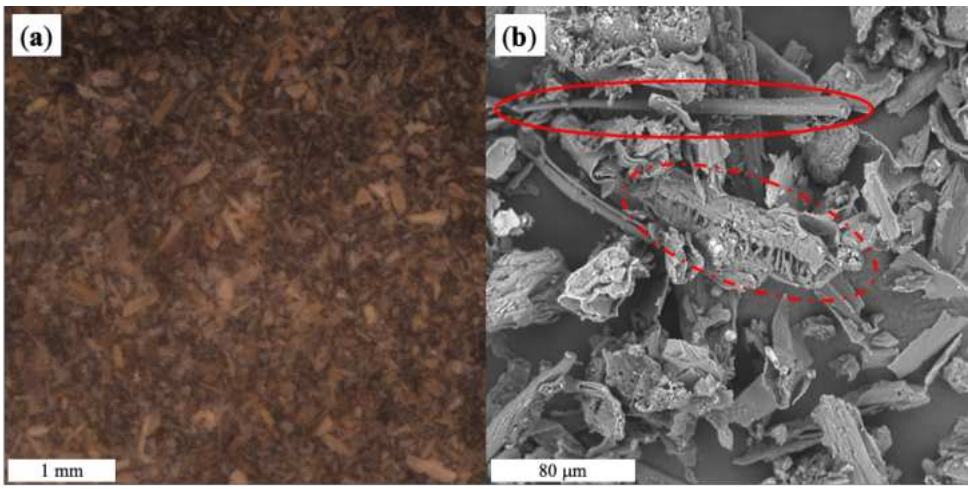

Figure 4.3.1.3. *Optical image (**a**) and SEM micrograph (**b**) of HC powder.*

Morphological analysis was also performed on the transverse fracture surfaces of CM samples, for which relevant SEM micrographs are reported. In Figure 4.3.1.4, it is possible to notice an almost homogeneous dispersion of the filler in each CM sample. In addition, matrix–filler adhesion appears to be good for all CM series. However, as filler content increases, the wettability of the matrix decreases. In particular, when the filler level is 15 wt%, the matrix is not able to homogenously wet the filler, as the red circle in Figure 4.3.1.4c clearly highlights. This behaviour is obviously more remarkable when the 20% HC is added (red circle, Figure 4.3.1.4d). As evidence, poor wettability does not prevent the production of specimen for CM, whereas, on the contrary, the FDM printability of 15% and 20% of HC-containing samples was totally inhibited.

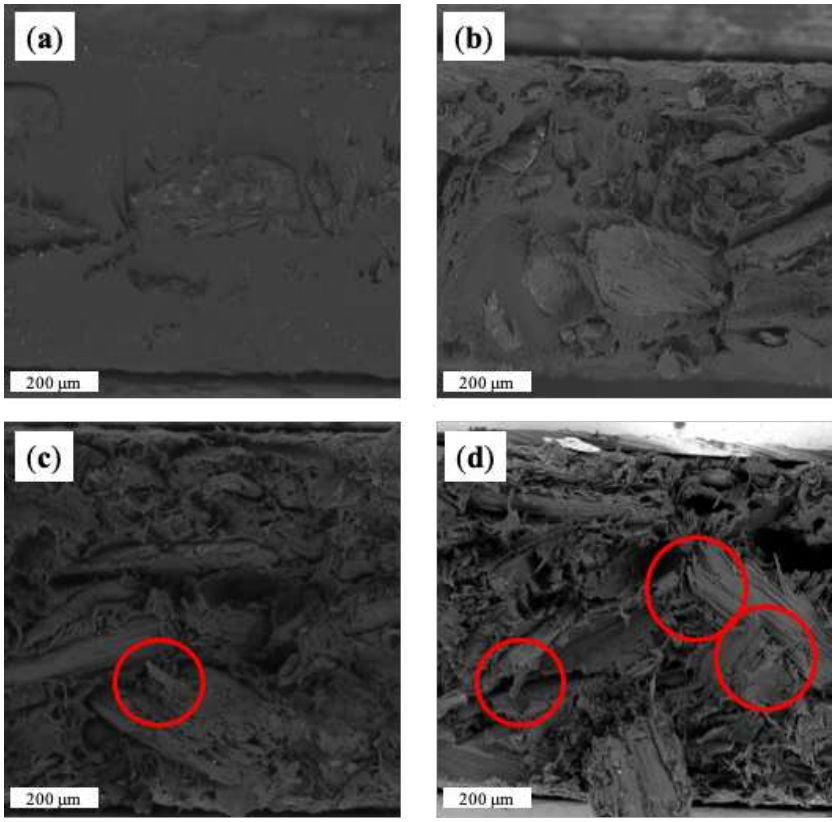

Figure 4.3.1.4 *SEM micrograph of fractured cross-sections of CM_MB/HC5 (**a**), CM_MB/HC10 (**b**), CM_MB/HC15 (**c**) and CM_MB/HC20 (**d**). Red circles highlight poor filler wettability parts.*

Mechanical performance of samples was investigated by tensile tests. The values of elastic modulus (E), tensile strength (TS) and elongation at break (EB) of neat MB and MB composites with different amount of HC produced via CM and FDM are reported in Table 4.3.1.1. Regarding CM samples, CM_MB showed a Young's modulus of 74.3 MPa a tensile strength of 18.6 MPa and an elongation-at-break of 821%. As the filler content increased, Young's modules and tensile strengths of the composites increased too. On the contrary, EB decreased significantly when the filler was added to the matrix. CM_MB/HC20 exhibited a Young's modulus value of 236 MPa while the EB value dropped to 20.3%. Concerning FDM composites, the same trend was observed. In particular, FDM_MB showed a Young's modulus of 83.9 MPa. When 5% or 10% filler amount was added, Young's modulus values of the composites reached 166 MPa and 188 MPa, respectively. It is well known from the scientific literature, in fact, that the addition of organic fillers to a biopolymeric matrix typically brings an enhancement of the mechanical properties. Moreover, the FDM prepared

samples showed a more remarkable improvement of the mechanical performance if compared to the ones obtained by CM. Regarding the 10% HC composites, in fact, Young's modulus of CM and FDM samples displayed a relative increment of 176% and 224%, respectively. This behaviour could be reasonably ascribed to 100% rectilinear infill [192]. Moreover, SEM micrograph of FDM_MB/HC5 (Figure 4.3.1.5a) and FDM_MB/HC10 (Figure 4.3.1.5b) showed that, during the printing process, HC fibers aligned along printing orientation. This fiber alignment could reasonably improve the mechanical properties of the FDM composites [193].

Table 4.3.1.1 Elastic modulus (E), tensile strength (TS) and elongation at break (EB) of sample obtained by compression molding and FDM.

Sample	E (MPa)	TS (MPa)	EB (%)
CM_MB	74.3 ± 0.84	18.6 ± 0.5	821 ± 1.8
CM_MB/HC5	121 ± 11.3	23.7 ± 2.33	43.6 ± 3.39
CM_MB/HC10	131 ± 8	24.5 ± 2.16	39.8 ± 2.75
CM_MB/HC15	145 ± 12	27.2 ± 0.88	24 ± 0.88
CM_MB/HC20	236 ± 8.49	33.4 ± 0.29	20.3 ± 0.37
FDM_MB	83.9 ± 1.34	27.2 ± 0.16	58.2 ± 0.75
FDM_MB/HC5	166 ± 8.8	41.5 ± 1.39	42.3 ± 4.19
FDM_MB/HC10	188 ± 1.54	45 ± 1.36	34.6 ± 0.82
FDM_MB/HC15	-	-	-
FDM_MB/HC20	-	-	-

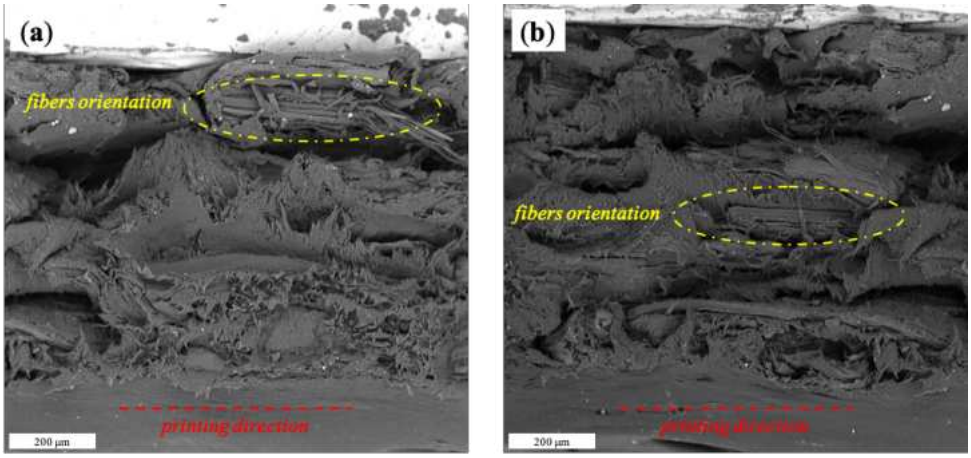

Figure 4.3.1.5 *SEM micrograph of fractured cross-sections of FDM_MB/HC5 (a); FDM_MB/HC10 (b).*

6.3.1.4 Conclusions

An innovative green composite was produced for the first time by adding 5%, 10%, 15% and 20% of *Hedysarum Coronarium* (HC) flour to Mater-Bi®. Through CM it was possible to obtain homogeneous samples with all percentages of fillers. Moreover, neat MB and the samples containing 5% and 10% of HC proved easily printable too. The findings of this study outline that it is possible to replace up to 20% of bioplastic with a low-cost and ecofriendly organic filler, enhancing the mechanical performance at the same time. Mechanical results, actually, showed that filler effectively acted as a reinforcement: Young's modules and tensile strengths of the composites increased from 74.3 MPa to 236 MPa and from 18.6 MPa to 33.4 MPa, respectively, when 20% of HC was added to the pure matrix. FDM samples, moreover, showed higher mechanical properties if compared with CM ones due to rectilinear infill and fibers orientation. In fact, regarding the 10% HC composites, Young's modulus of CM and the FDM ones displayed a relative increment of 176% and 224%, respectively. The improvement of the mechanical properties together with other advantages of FDM, such as reduction of production times and costs, and the possibility to produce extremely elaborated geometries, make MB/HC promising for the creation of manufactured products based on green composites that, thanks to their wood-like colour, can find application in green fabrication of panels for different use, in the structural sector, in the production of furniture and so on. In the scientific literature, indeed, other similar systems (biodegradable polymeric matrices and natural fillers) are already proposed for these types of applications. Panels for sound adsorption, thermal insulation or for the interior design industry, in fact, do not require extremely high mechanical properties.

6.3.2 Green Composites Based on Hedysarum Coronarium with Outstanding FDM Printability and Mechanical Performance

The subsequent text and images have been fully extracted from the published article authored by the candidate "Scaffaro, R.; Gulino, E.F.; Citarrella, M.C.; Maio, A. Green Composites Based on Hedysarum coronarium with Outstanding FDM Printability and Mechanical Performance. Polymers 2022, 14, 1198. https://doi.org/10.3390/polym14061198 [194]" and are reproduced here with the necessary permissions.

Author contribution: software, validation, formal analysis, investigation, data curation, writing—original draft preparation, writing—review and editing, visualization.

6.3.2.1 Abstract

The addition of natural scraps to biodegradable polymers gained particular interest in recent years allowing to reduce environmental pollution related to traditional plastic. In this work, new composites were fabricated by adding 10% or 20% of *Hedysarum Coronarium* (HC) flour to Poly (lactic acid) (PLA). The two formulation were first produced by twin screw extrusion and the obtained filaments were then employed for the fabrication of composites either for compression moulding (CM) or by Fused Deposition Modelling (FDM) and characterized from a morphological and mechanical point of view. Through FDM it was possible to achieve dense structures with good wettability of the filler that, on the contrary, cannot be obtained by CM. The results indicate that the filler effectively acts as reinforcement, especially for FDM composites. The most remarkable enhancement was found in flexural properties (+100% of modulus and ultimate strength) followed by tensile resistance and stiffness (+60%) and impact strength (+50%), whereas a moderate loss in tensile deformability was observed especially at the highest loading. By adding HC to the polymeric matrix, it was possible to obtain a green, performing and cost-effective composite that can find applications for the fabrication of panels for furniture or automotive.

6.3.2.2 Preparation of composites

In this study, the whole plant was ground as received in order to optimize production time and costs. Dried HC was grinded for 3 min and then sieved. Sieving fraction under 150 μm was selected in order to obtain particles of a size suitable for the 3D printer which, therefore, do not cause obstruction in the nozzle. PLA composites containing 10 wt% and 20 wt% of HC (label as PLA/HC10 and PLA/HC20) were prepared by extrusion. Pure PLA was also extruded for comparison. Compression-moulded samples (CM) were obtained using a laboratory press. The sample were finally cut into specimens of appropriate geometry for further characterizations: 60 mm × 10 mm × 2 mm for tensile tests, 40 mm × 10 mm × 2 mm for flexural tests and 80 mm × 10 mm × 2 mm for impact tests. As regards fused deposition modelling (FDM), samples of each formulation were 3D printed in appropriate geometry (60 mm × 10 mm × 2 mm for tensile tests, 40 mm × 10 mm × 2 mm for flexural tests and 80 mm × 10 mm × 2 mm for impact tests). 100% infill rate and a rectilinear infill pattern with ± 45° raster angle were chosen in order to optimize mechanical properties; 30 mm/s printing speed was chosen as a compromise solution between better properties and higher production rate. Some representative of obtained CM and FDM samples are shown in Figure 4.3.2.1.

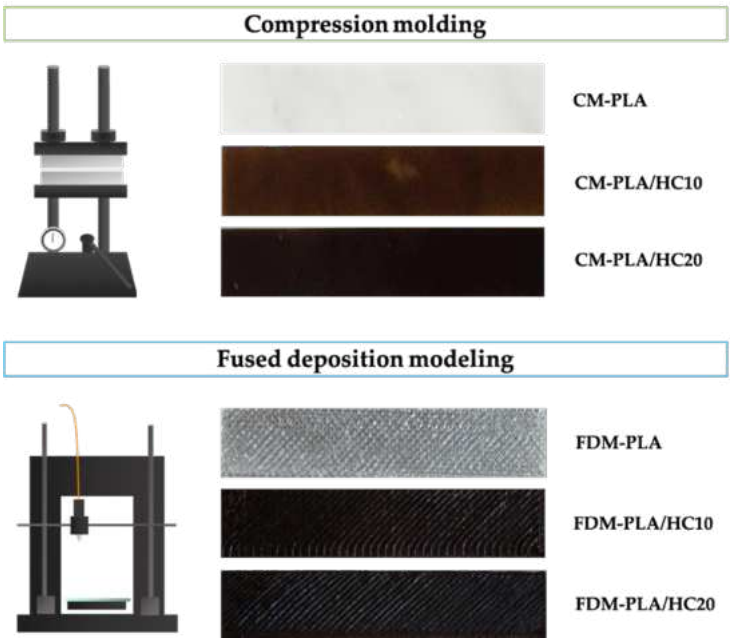

Figure 4.3.2.1 *Digital photographs of CM and FDM obtained samples.*

6.3.2.3 Results and Discussion

Morphology of HC particles and composites were analyzed by SEM and relevant micrograph of the natural organic filler is shown in Figure 4.3.2.2.

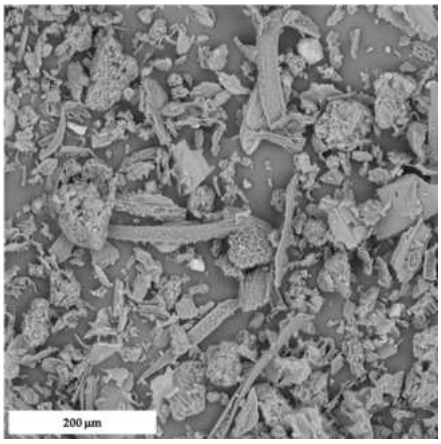

Figure 4.3.2.2 *SEM micrograph of HC.*

HC filler was characterized by the coexistence of fibers, platelets and globular microparticles, reasonably due to the presence of stems, leaves and flowers. Indeed, this heterogeneity is supposed to impart benefits to the mechanical performance of resulting composites [190], whether the different types of element HC in are able to exert synergistic effect, as already reported in several studies focused on hybrid composites containing either micro- or nano-sized fillers [195–197].

The morphology of composites prepared by compression-moulding is reported in Figure 4.3.2.3, whereas those prepared via FDM is provided in Figure 4.3.2.4. As one can see, the former technique was found to be inadequate to grant satisfactory levels of filler dispersion and adhesion, with the presence of aggregates and voids due to lack of mutual affinity. On the contrary, FDM has proven a good suitability to achieve dense structures with enhanced wettability of the fillers, as already observed with another polymeric matrix [190]. In Figure 4.3.2.5 it is possible to notice the peculiar structure of FDM samples induced by the selected raster angle (±45°).

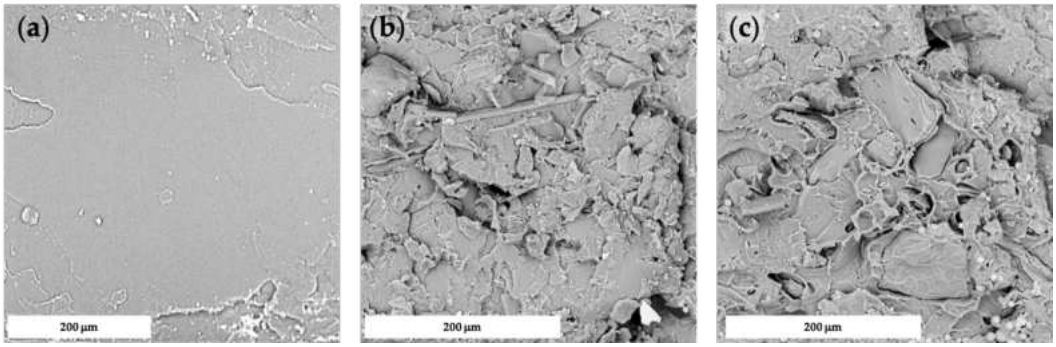

Figure 4.3.2.3 *SEM micrographs of fractured cross-section of CM_PLA (a), CM_PLA/HC10 (b) and CM_PLA/HC20 (c).*

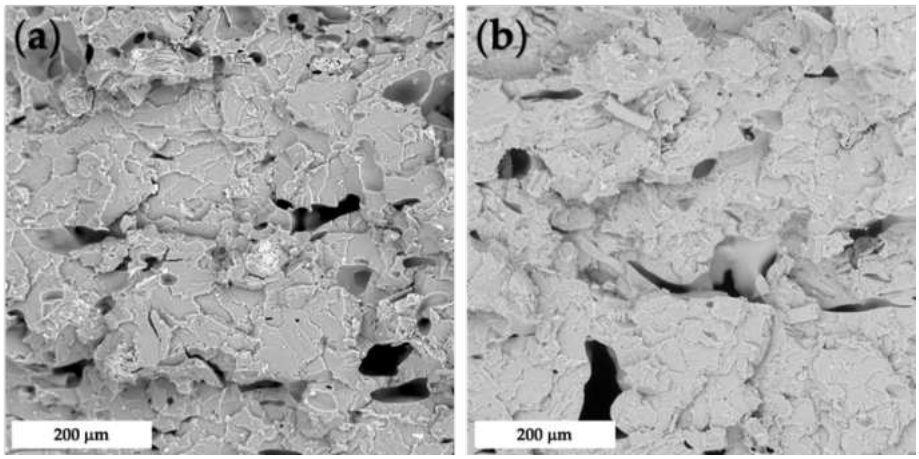

Figure 4.3.2.4 *SEM micrograph of fractured cross-section of FDM_PLA/HC10 (a) and FDM_PLA/HC20 (b).*

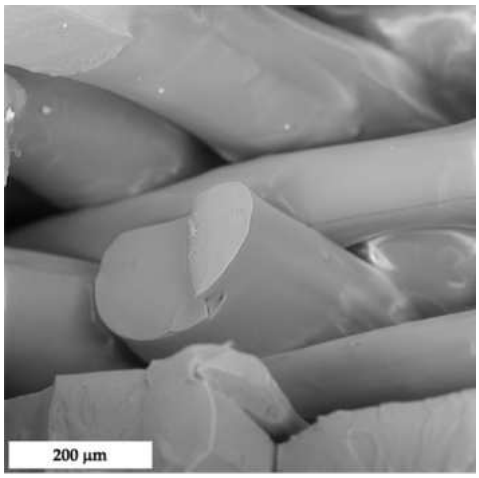

Figure 4.3.2.5 *SEM micrograph of fractured cross-section of FDM-PLA.*

The representative tensile stress-strain curves of the materials are provided in Figure 4.3.2.6, whereas their salient tensile features are listed in Table 4.3.2.1.

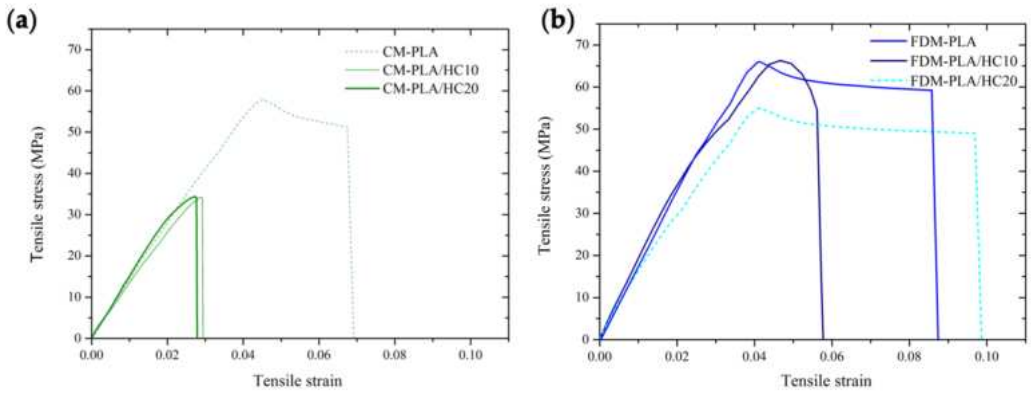

Figure 4.3.2.6 *Representative stress-strain curves of CM- (**a**) and FDM-series composites (**b**) during tensile tests.*

Table 4.3.2.1 Main tensile properties of the samples investigated.

Sample	E (MPa)	TS (MPa)	EB (%)	k (MJ/m^3)
CM-PLA	1580 ± 19	54 ± 2	5.6 ± 0.4	2.64 ± 0.01
CM-PLA/HC10	1730 ± 15	32 ± 3	2.5 ± 0.4	0.55 ± 0.01
CM-PLA/HC20	1830 ± 22	34 ± 2	2.4 ± 0.2	0.55 ± 0.01
FDM-PLA	1260 ± 13	56 ± 4	10 ± 0.3	4.09 ± 0.02
FDM-PLA/HC10	1843 ± 20	63 ± 4	9 ± 0.5	3.60 ± 0.02
FDM-PLA/HC20	2070 ± 31	62 ± 3	7 ± 0.1	2.43 ± 0.01

The shape of the tensile curves lets envisage that pure PLA and FDM-bio-composites (Figure 4.3.2.6b) experience a ductile fracture, owing to the presence of a well-defined necking, otherwise not observed in the case of CM-bio-composites (Figure 4.3.2.6a), which displayed a fragile mode fracture. Moreover, it can be easily noted that samples prepared by FDM are much more ductile and resistant than their counterpart prepared by CM. The quantitative analysis of tensile moduli points out that the choice of processing technique affects the tensile properties of the neat matrix, with CM-PLA being stiffer than FDM-PLA. This aspect could be reasonably explained by considering the eventual differences imparted by the type of printing, either in terms of porosity, surface texture, or degradation.

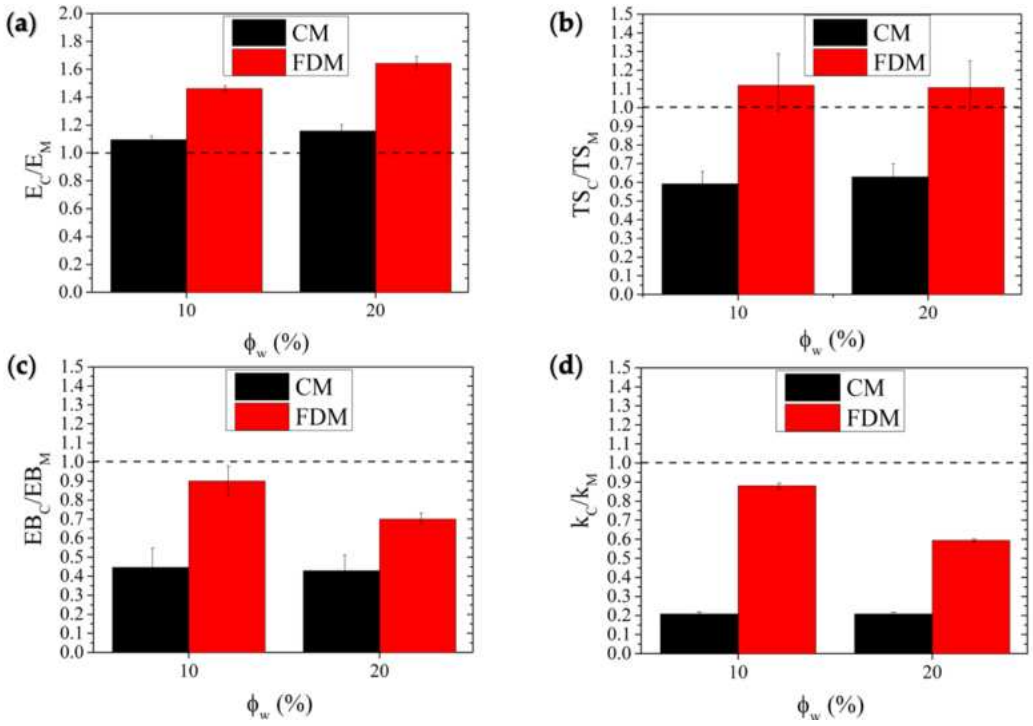

Figure 4.3.2.7 *Elastic modulus (**a**), tensile strength (**b**), elongation at break (**c**), and toughness (**d**) of composites normalized with respect to those of matrix.*

Furthermore, the effect of filler loading was found to be quite different depending on the fabrication technique adopted. In fact, although the incorporation of HC imparted a relevant stiffening effect in all the cases, the relative increments achieved were higher in FDM-samples, as visible by comparing the reduced moduli of CM- and FDM-series systems (Figure 4.3.2.7a), i.e. normalized to that of the respective processed matrix. The analysis of breaking properties is reported in Figures 4.3.2.7b and 4.3.2.7c. With regard to reduced tensile strength (Figure 4.3.2.7b), it can be observed that filler incorporation exerts a fair strengthening effect in FDM-bio-composites (10% more resistant than neat matrix), while being detrimental in CM bio-composites, which experienced 35-40% loss in TS with respect to PLA, likely due to the premature failure of specimens. In fact, although all the bio-composites have proven less deformable than the corresponding matrices, a more remarkable decay upon filler loading was observed in CM bio-composites that retained less than half of the matrix EB (Figure 4.3.2.7c). Toughness (Figure 4.3.2.7d) followed the same trend as EB, with all the bio-composites displaying a lower ability to absorb energy and plastically deform without fracturing, when compared to the corresponding matrices. However, even in this case, FDM bio-composites

retained 60-90% of the initial toughness of PLA, while CM bio-composites showed toughness values equal to only 20% of that of PLA.

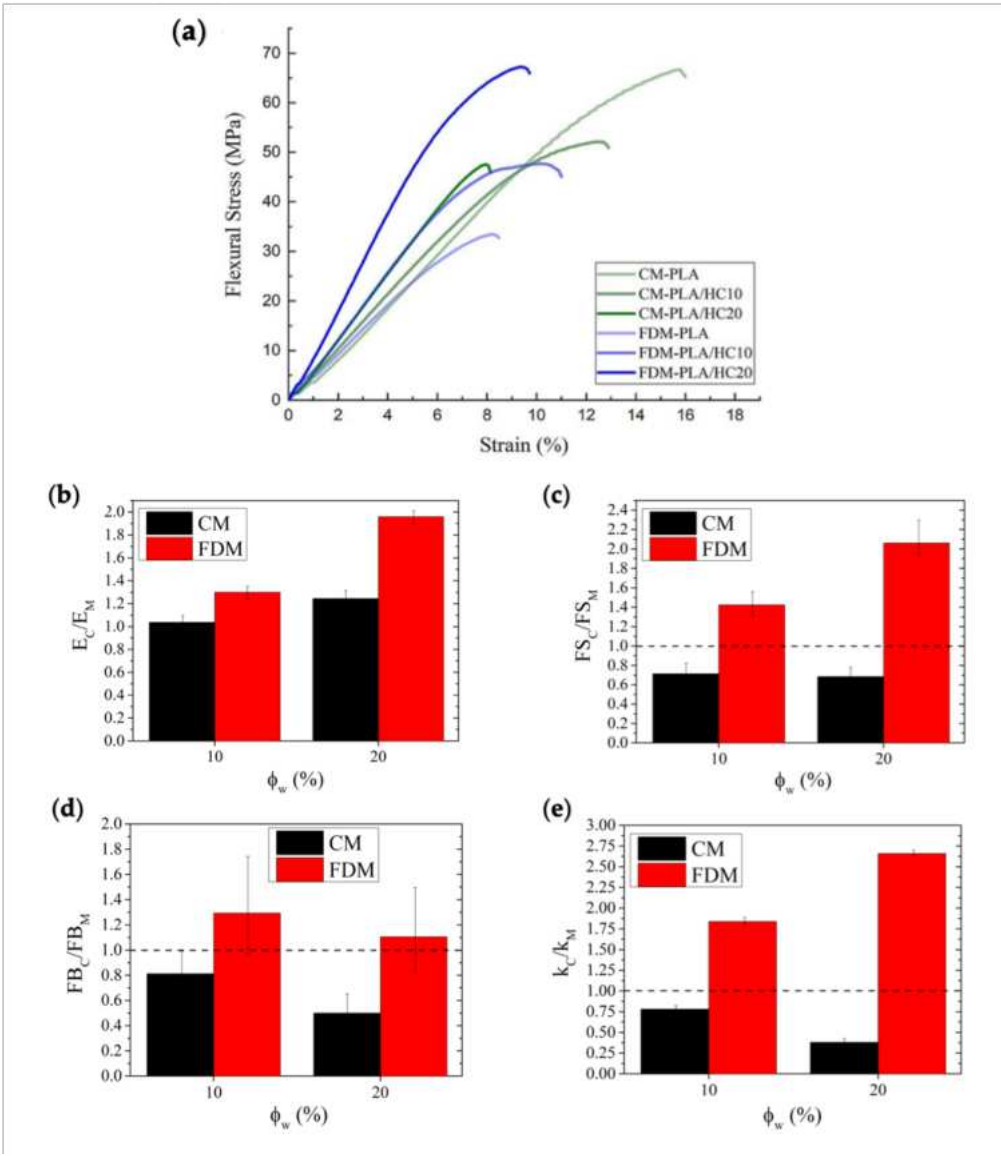

Figure 4.3.2.8 *Representative flexural stress-strain curves (**a**), along with behaviour of reduced flexural elastic modulus (**b**), strength (**c**), deformability (**d**), and toughness (**e**) as a function of filler content and processing technique.*

Figure 4.3.2.8 reports the representative stress-strain curves of the materials subjected to flexural testing (Figure 4.3.2.8a), along with the behaviour of reduced flexural properties, namely elastic modulus (Figure 4.3.2.8b), flexural strength (Figure 4.3.2.8c), deformability (Figure 4.3.2.8d), and toughness (Figure 4.3.2.8e) as a function of filler content and processing technique, whereas

salient data are listed in Table 4.3.2.2. Even in this type of solicitation, the behaviour of neat polymer is greatly affected by the processing technique, although an opposite trend was observed with respect to tensile testing. In fact, in this case CM-PLA displays breaking properties much higher than those of FDM-PLA, while being substantially similar the values of elastic modulus. However, the effect of filler incorporation showed remarkable differences depending on the different printing mode. FDM-composites displayed the monotonic increase of both flexural stiffness and strength upon filler content and proved to be slightly more deformable than pure matrix, while CM-series composites displayed the typical embrittlement upon filler addition, with monotonic decay of both flexural strength and deformation. As a consequence, the toughness (Figure 4.3.2.8e) of FDM-bio-composites increases linearly upon filler content (up to +166% relative increase), whereas that of CM-bio-composites was found to decrease monotonically with the filler content, up to halving at 20% loading.

Table 4.3.2.2 Main flexural properties of the samples investigated.

Sample	E (MPa)	FS (MPa)	FB (%)	k (MJ/m^3)
CM-PLA	530 ± 10	70 ± 3	16 ± 2.0	5.12 ± 0.04
CM-PLA/HC10	550 ± 10	50 ± 5	13 ± 1.1	3.99 ± 0.04
CM-PLA/HC20	660 ± 25	48 ± 3	8 ± 1.3	1.93 ± 0.02
FDM-PLA	500 ± 10	33 ± 2	8.5 ± 1.2	1.44 ± 0.01
FDM-PLA/HC10	650 ± 10	47 ± 1	11 ± 1.6	2.65 ± 0.01
FDM-PLA/HC20	980 ± 20	68 ± 3	9.4 ± 1.5	3.83 ± 0.02

These outcomes were confirmed in impact properties, measured by Charpy tests, provided in Figure 4.3.2.9. Even in this case, an opposite behaviour as a function of filler content was found depending on the technique used: CM-samples showed a monotonic decrease of impact strength whereas FDM-composites displayed values higher than that of pure matrix, with a maximum observed at 10% HC.

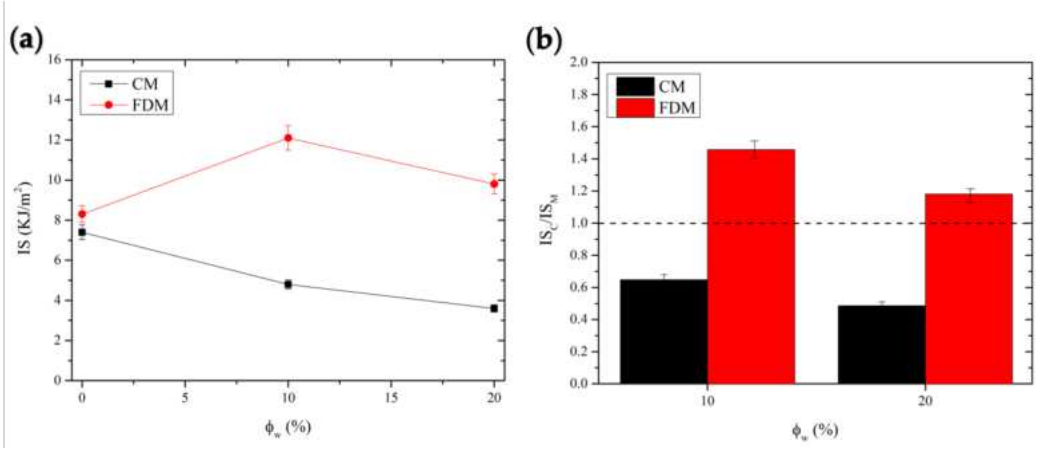

Figure 4.3.2.9 *Plots of impact strength (**a**) and reduced impact strength (i.e., normalized to that of each matrix) as a function of filler content and processing technique (**b**).*

Taken together, these outcomes point out that PLA/HC system is particularly suitable for 3D printing, which leads to materials with mechanical performance higher than those achieved by compression-molding. Among the bio-composites, FDM-PLA/HC10 gave the overall best performance, while FDM-PLA/HC20 represents the best compromise between mechanical properties and sustainability, given the fact that 20% of PLA can be replaced with inexpensive and renewable biomass fillers, without altering the processing protocol usually adopted for neat polymer.

6.3.2.4 Conclusions

Natural fillers achieved from *Hedysarum Coronarium* waste were assessed as reinforcing agents for polylactic acid-based bio-composites prepared by twin-screw extrusion and printed by either FDM or compression-molding. The materials were fully characterized from a morphological and mechanical point of view. The results point out the excellent 3D printability of such bio-composites, which showed uniform dispersion of the filler throughout the matrix and a strong interfacial adhesion, which led to remarkable improvements of all the mechanical properties, when compared to either neat matrix or their compression-molded counterparts. In detail, the most remarkable enhancement was found in flexural properties, where a doubling of modulus and strength was recorded, followed by tensile resistance and stiffness (up to +60%) and impact strength (+50%),

whereas a moderate loss in tensile deformability was observed especially at the highest loading. Moreover, these formulations, relying on an inexpensive and inedible biomass waste that can be processed in the same way as neat polymer and in the absence of particular purification/chemically treatment steps, represent an outstanding sustainability from both an economic and ecological point of view. The encouraging results carried out in this study let envisage a great potential of such bio-composites in many application fields, including panels for automotive and furnishes.

6.3.3 Green composites based on Mater-Bi® and Solanum lycopersicum plant waste for 3D printing applications

The subsequent text and images have been fully extracted from the published article authored by the candidate "Scaffaro, R.; Citarrella, M.C.; Morreale, M. Green Composites Based on Mater-Bi® and Solanum lycopersicum Plant Waste for 3D Printing Applications. Polymers 2023, 15, 325. https://doi.org/10.3390/polym15020325 [198]" and are reproduced here with the necessary permissions.

Author contribution: Conceptualization, methodology, software, validation, formal analysis, investigation, data curation, writing—original draft preparation, writing—review and editing, visualization.

6.3.3.1 Abstract

3D printability of green composites is currently experiencing a boost in importance and interest, envisaging the way to valorise agricultural waste, in order to obtain affordable fillers for the preparation of biodegradable polymer-based composites with reduced cost and environ-mental impact, without undermining processability and mechanical performance. In this work, an innovative green composite was prepared by combining a starch-based biodegradable polymer (Mater-Bi®, MB) and a filler obtained from the lignocellulosic waste coming from Solanum lycopersicum (i.e. tomato plant) harvesting. Different processing parameters and different filler amounts were investigated, and the obtained samples were subjected to rheological, morphological and mechanical characterizations. With regard to the actually adopted filler amounts, processability was found to be good, with adequate dispersion of the filler in the matrix. Mechanical performance was satisfactory, and it was found that this is significantly affected by specific pro-cess parameters such as the raster angle. The mechanical properties were compared to those predictable from the Halpin-Tsai model, finding that the prepared systems exceed the expected values.

6.3.3.2 Composites preparations

The dried SL plant was ground for 3 min and the resulting powder was then sieved to obtain particles of a size suitable for the 3D printer. The sieving fraction under 150 μm was selected. In order to obtain a homogeneous dispersion of the filler, according to previous studies, the filler

amounts chosen to prepare the MB-based bio-composites were 5, 10, 15 wt%. All of the composites (namely MB/SL5, MB/SL10, MB/SL15) and neat MB, for comparison, were prepared by melt compounding in an internal mixer. The obtained materials were then ground into pellets and processed in a single-screw. The extrudates were drawn with the help of a conveyor belt system to obtain filaments with a diameter suitable to the printer (1.75 mm). For each formulation, 60 mm × 10 mm × 1 mm samples were printed using a 3D printer. 100% infill rate and a rectilinear infill pattern with a 0° or ± 45° raster angle were chosen in order to evaluate its influence on the tensile properties of the composites; 45 mm/s printing speed was chosen to maximize the production rate without compromising the mechanical performance. Sample formulations and sample codes are reported in Table 4.3.3.1.

Table 4.3.3.1 Formulation of investigated samples.

Sample Code	MB Content (wt%)	SL Content (wt%)	SL Mesh Size (µm)	Raster Angle
MB 0°	100	0	-	0°
MB/SL5 0°	95	5	< 150	0°
MB/SL10 0°	90	10	< 150	0°
MB/SL15 0°	85	15	< 150	0°
MB 45°	100	0	-	± 45°
MB/SL5 45°	95	5	< 150	± 45°
MB/SL10 45°	90	10	< 150	± 45°
MB/SL15 45°	85	15	< 150	± 45°

6.3.3.3 SL powder and filament characterization

The samples loaded at 5% (MB/SL5), 10% (MB/SL10) and 25% (MB/SL25) filler where properly extruded into the related filaments, to be subjected to FDM thereafter. Filament printability (i.e. processability in FDM mode) is directly correlated to the morphological properties. More in details, not only the diameter of the filament must be suitable to the specific 3D printer used, but its surface must be as even and homogeneous as possible [199]. In addition, printability depends also on the rheological and mechanical properties of the filaments, that were thus investigated as well.

Morphological characterization was carried out first. The main results are shown in the SEM micrographs reported in Figure 4.3.3.1 for SL powder and in Figure 4.3.3.2 for MB/SL5, MB/SL10

and MB/SL15, respectively. From SEM micrograph of the powder (Figure 4.3.3.1), it is possible to notice that SL powder contains elements with different morphology, reasonably belonging to different parts of the plant: stem and leaf. From the samples cross-section micrographs (Figure 4.3.3.2), it can be observed that the SL particles are homogeneously dispersed in the MB matrix, only few voids are present, and the general adhesion between the matrix and the particles is good. Furthermore, the diameters of the MB/SL5 and the MB/SL10 filaments are even and homogeneous, in the range 1.6 – 1.8 mm (respectively) which is suitable to the actual printer used. On the other hand, the MB/SL15 filaments showed uneven diameters.

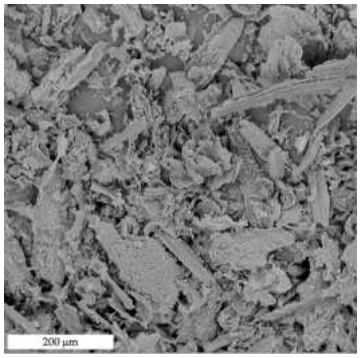

Figure 4.3.3.1 *SEM images of SL powder.*

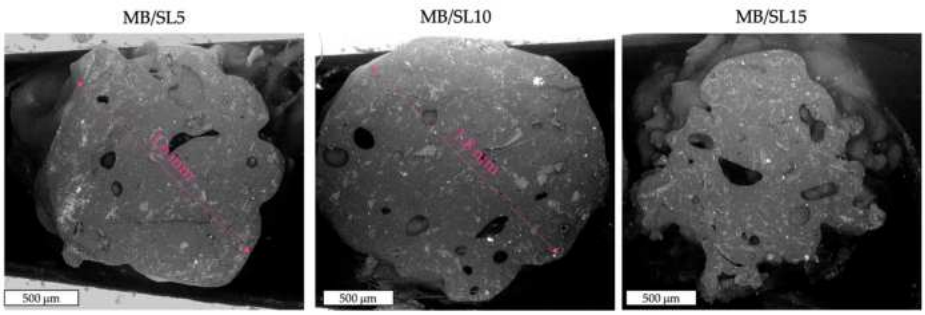

Figure 4.3.3.2 *SEM images of MB/SL5, MB/SL10 and MB/SL15 filaments.*

Rheological measurements were performed on specimens obtained from the filaments, in order to evaluate the actual processability for FDM purposes. Figure 4.3.3.3 reports the rheological values of MB and the composite filaments, on increasing the filler content. As predictable, MB shows a clear non-Newtonian behaviour. The addition of 5% SL leads to an increase of viscosity over the entire frequency range, as well as a more marked non-Newtonian behaviour. This tendency further

increases by adding 10% SL. When 15% SL is added to the MB matrix, there is a much more drastic increase of the viscosity and the onset of yield stress phenomena. Such results suggest that only the rheological behaviour of MB/SL5 and MB/SL10 appears compatible with the 3D printing process, whereas MB/SL15 may be not adequately printable, due to the excessively high viscosity which may lead to nozzle clogging during the process.

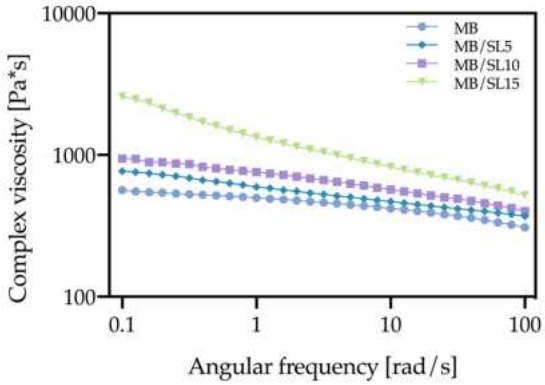

Figure 4.3.3.3 *Rheological curves of MB/SL5, MB/SL10 and MB/SL15 filaments.*

Anyway, optimal printability depends also on the tensile properties of the filaments. Figure 4.3.3.4 reports the values of elastic modulus (E), tensile strength (TS) and elongation at break (EB), on increasing the SL content. It can be noticed that the filaments become stiffer on increasing the SL content, although the effect is much more significant only in the case of MB/SL15; the tensile strength is similar to that of the neat MB, or even higher, and this is a satisfactory result since it suggests that the filament should not undergo rupture too easily, during the process; on the other hand, the deformability drops even at just 5% SL content.

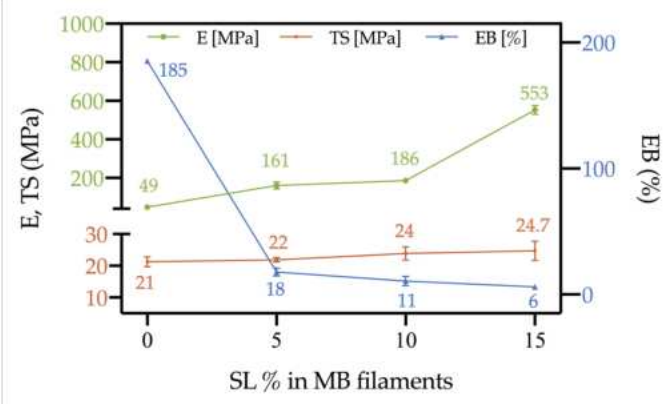

Figure 4.3.3.4 *Tensile properties of MB/SL5, MB/SL10 and MB/SL15 filaments as a function of the SL amount.*

In Figure 4.3.3.5 photos of MB/SL5, MB/SL10 and MB/SL15 filaments before (Figure 4.3.3.5a, b, c respectively), during (Figure 4.3.3.5a', b', c' respectively), and after (Figure 4.3.3.5a'', b'', c'' respectively) tensile test are reported. MB/SL5 and MB/SL10 filaments present a homogenous shape and their fracture occurs some second after the 50 mm min^{-1} speed was applied. On the other hand, the MB/SL15 filament present an irregular shape due to the high content of filler. In this latter case the fracture occurred instantaneously when the 50 mm min^{-1} speed was applied.

The results of the rheological and mechanical tests allow drawing some general considerations, propaedeutic for the FDM stage, since viscoelasticity and tensile strength measurements help to predict problems in printability and possible printing errors. In particular, too high viscosities are not suitable to the process, since the low deformability can lead to filament blocking at the nozzle of the 3D printer, and subsequent clogging and rupture (Figure 4.3.3.6a). On the other hand, if the filament is too soft (high decline of viscosity at low temperatures), it tends to flow too easily while not pulling correctly, resulting in nozzle clogging (Figure 4.3.3.6b); furthermore, if it is too brittle, it will break (Figure 4.3.3.6c). These considerations therefore suggest that MB/SL5 and MB/SL10 should be easily printable and without significant defects in the obtained samples (on the other hand, neat MB may lead to some uncertainty due to the relatively high deformability), while problems may arise with MB/SL15.

Actual 3D-printing was then carried out. As expectable, based on the previous considerations, neat MB as well as MB/SL5 and MB/SL10 were easily processed, while the filament containing 15% SL showed to be not printable, since the high viscosity caused obstruction of the nozzle and the filament broke easily. The samples were printed with both 0° and 45° raster angles, in order to evaluate the printability and the effect of the angle on the mechanical properties of the obtained 3D specimens.

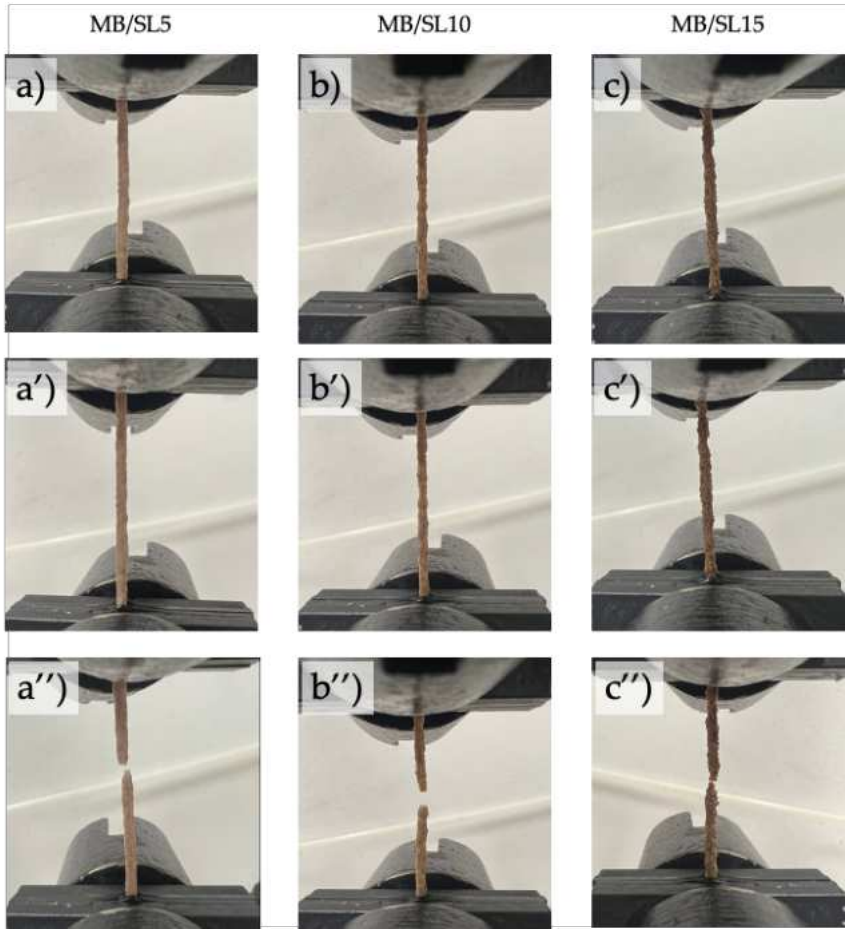

Figure 4.3.3.5 *Photos of MB/SL5, MB/SL10 and MB/SL15 filaments before (a, b, c respectively), during (a', b', c' respectively), and after (a'', b'', c'' respectively) tensile test.*

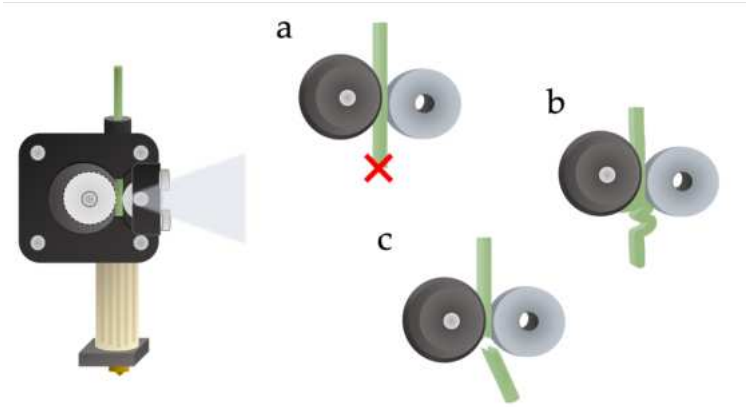

Figure 4.3.3.6 *Different behaviours of the filament upon entering the melting chamber, at different viscoelastic and mechanical properties.*

6.3.3.4 Characterizations of 3D printed samples

First, the 3D-printed samples were subjected to morphological analysis on cryofractured surfaces. Figure 4.3.3.7 shows SEM images of fractured surfaces, at increasing magnification from left to right, of MB/SL10, 0° raster samples. In general, it can be stated that filler dispersion and adhesion are good, as clearly visible from the filler particle circled in green (right), where no significant voids can be found at the filler-matrix interface.

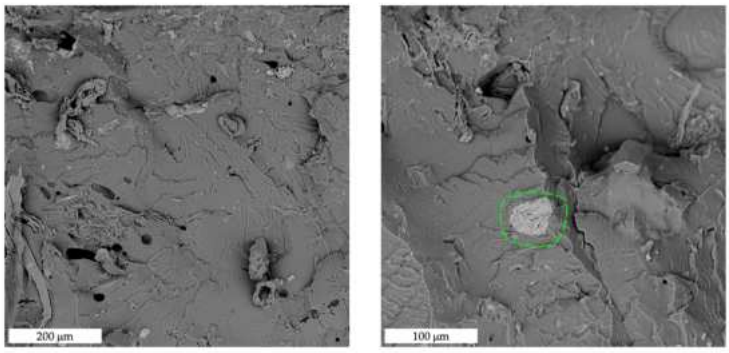

Figure 4.3.3.7 *SEM images of fracture surfaces of MB/SL10 0° samples at increasing magnification (from left to right).*

Figures 4.3.3.8-11 show the fracture surfaces after tensile tests of the composite samples. Overall, it may be stated that some fibre pull-out and debonding phenomena are more visible in the SL5 rather than in the SL10 samples and, especially, in 45° samples (Figure 4.3.3.11) as opposed to 0° ones (Figure 4.3.3.10).

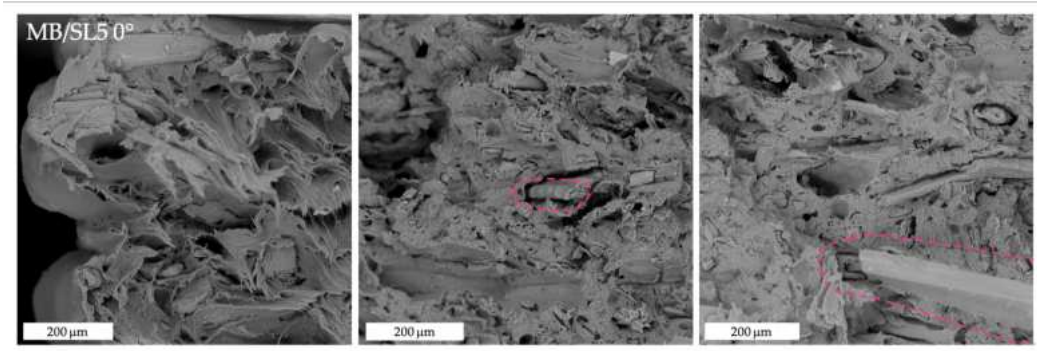

Figure 4.3.3.8 *SEM images of tensile fracture surfaces of MB/SL5 0° samples.*

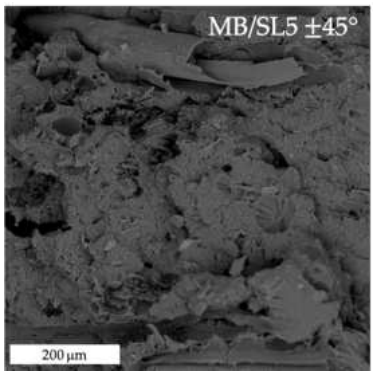

Figure 4.3.3.9 *SEM image of tensile fracture surface of MB/SL5 ±45° sample.*

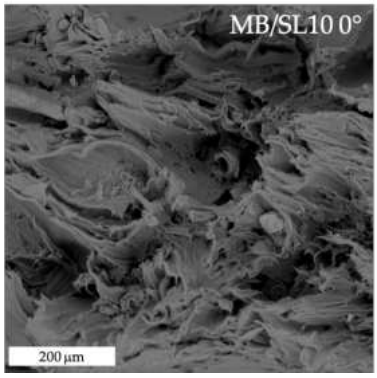

Figure 4.3.3.10 *SEM image of tensile fracture surface of MB/SL10 0° sample.*

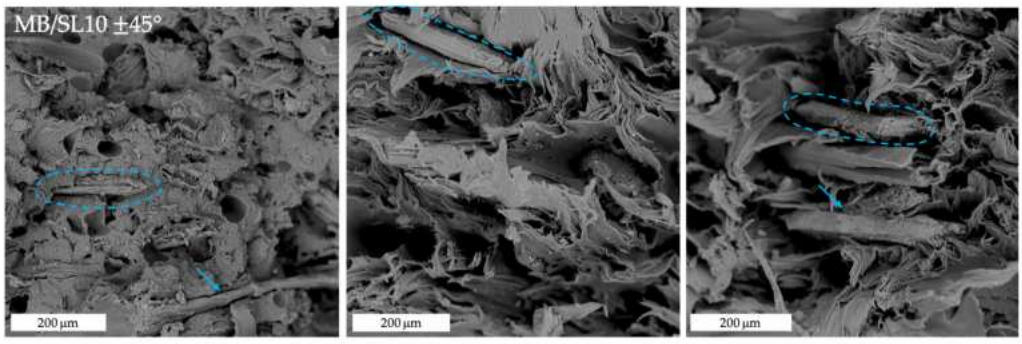

Figure 4.3.3.11 *SEM images of tensile fracture surfaces of MB/SL10 ±45° samples.*

The actual tensile properties of the 3D-printed samples are shown in Figure 4.3.3.12, in the case of raster angle = 0 ° (left) and raster angle = 45 ° (right). It can be observed that, in both cases, the elastic modulus and the tensile strength increase on increasing the filler content, while the deformability decreases. However, such decrease is significantly less marked in the case of raster angle = 0 °, and the overall results of all the tensile properties are better, with excellent reproducibility.

This confirms the first indications from the morphological analysis, which could allow to suppose higher breaking resistance of the 0° samples, in comparison to the 45° ones.

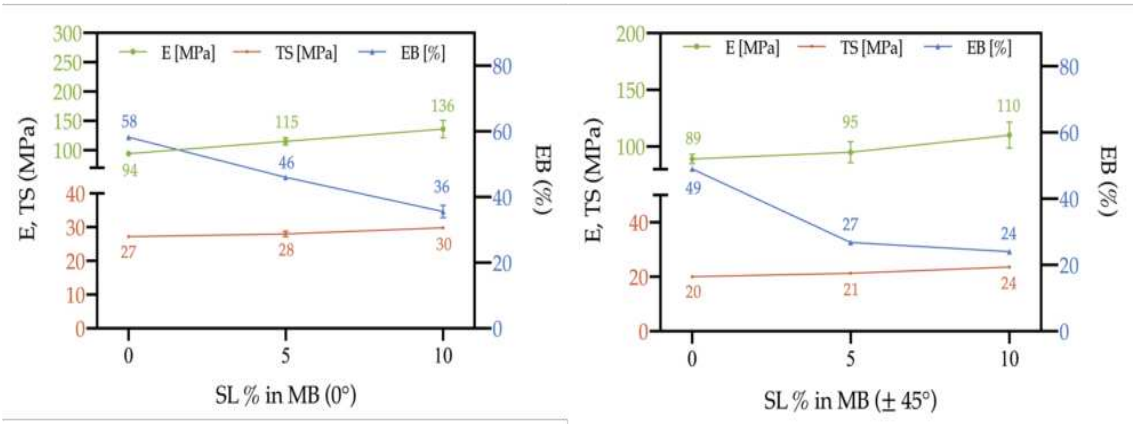

Figure 4.3.3.12 *Elastic modulus (E), tensile strength (TS) and elongation at break (EB) of 3D-printed samples as a function of the filler content; raster angle = 0° (left) and raster angle = 45° (right).*

Such evidence can be further deduced from Figure 4.3.3.13. The 0° raster angle during printing definitively optimizes the tensile properties, confirming data from the literature, obtained on similar systems, where 0° raster angle usually optimizes tensile properties, whereas 45° leads to optimization of flexural and impact properties [200].

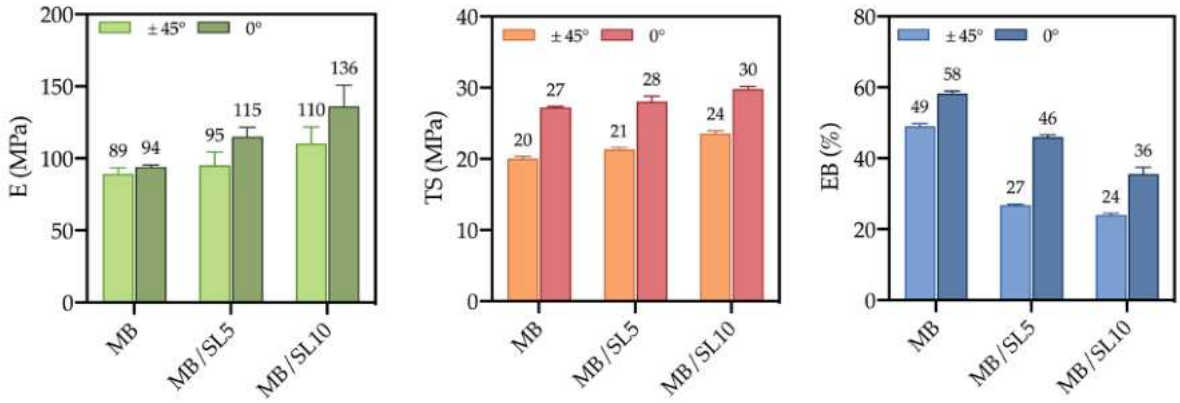

Figure 4.3.3.13 *Elastic modulus (E), tensile strength (TS) and elongation at break (EB) of 3D-printed samples with different filler content and raster angle.*

6.3.3.5 XRD and DSC characterizations

In order to verify if the addition of SL filler leads to some crystallinity variation in the polymeric matrix, XRD and DSC analysis were performed on neat MB and MB/SL printed composites and relative outcomes are reported in Figure 4.3.3.14a and 4.3.3.14b respectively. No differences can be noted in XRD curves (Figure 4.3.3.14a) when 5 or 10% of SL is added to the polymeric matrix. Moreover, the addition of SL powder to MB do not lead to any change in its melting temperature or melting enthalpy (see Figure 4.3.3.14b and Table 4.3.3.2).

These outcomes confirm that the increase in tensile property of SL composites, if compared to the pure matrix, can be effectively attributed to the reinforcing effect given by the filler.

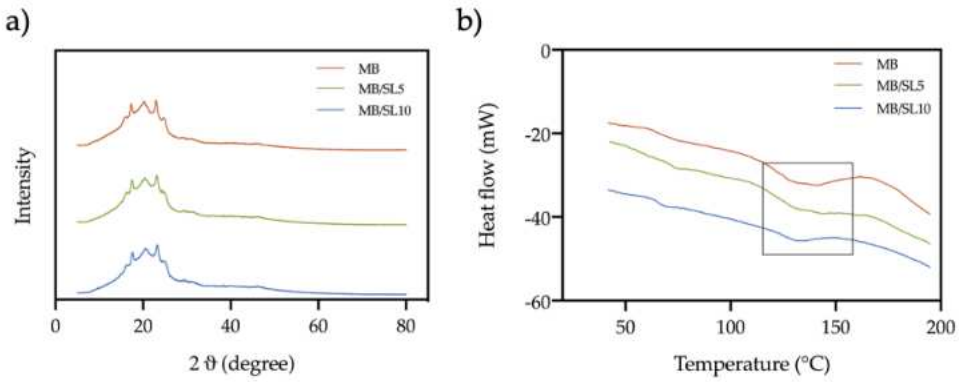

Figure 4.3.3.14 *XRD spectra (a) and DSC analysis (b) of neat MB and MB/SL printed composites.*

Table 4.3.3.2 Melting temperature and melting enthalpy of 3D printed samples obtained by DSC analysis

Sample	weight (mg)	melting temperature (°C)	melting enthalpy (mJ/mg)
MB	10.9	132.3	15.8
MB/SL5	8.8	132.7	16.3
MB/SL10	3.3	131.7	15.9

6.3.3.6 Halpin-Tsai model

Figure 4.3.3.15 shows the trends of Ec/Em (ratio between the elastic modulus of the composite and that of the matrix) on increasing the SL content, both from the experimental (Exp) results (at 0- and 45-degrees raster angles) and the theoretical trend calculated according to the Halpin-Tsai model

(HT). This semiempirical model allows assessing the composite modulus (Ec), once five parameters are known, i.e. the elastic modulus of matrix (Em) and filler (Ef), their volume fractions and the filler aspect ratio [201].

The trends clearly outline that the model significantly underestimates the values of Ec, especially at higher filler contents. This may be due to the filler particles coming from different parts (wastes) of the tomato plant, thus presenting some natural differences in terms of morphology and/or mechanical properties. An additional likely explanation may involve the capability of the polymer matrix to, at least partially, enter the void channels of SL particles, as presumable on the basis of the SEM images and of the results from our previous studies on similar (i.e. biodegradable polymer/natural-organic plant waste filler) systems [202].

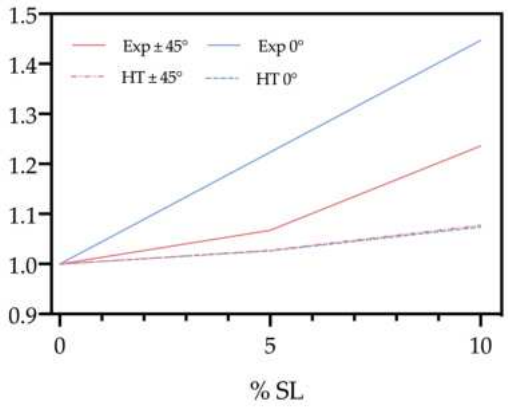

Figure 4.3.3.15 *Ratio between elastic modulus of the composite and the polymer matrix, as a function of the SL content, according to the Halpin-Tsai model (HT) and the experimental results (Exp).*

6.3.3.7 Conclusions

In this work, composites based on a Mater-Bi® polymer and wastes coming from *Solanum lycopersicum* were prepared and processed via FDM, in order to explore the actual suitability to 3D-printing applications. Different processing parameters and different filler amounts were investigated, and the obtained samples were characterized from the rheological, mechanical, and morphological point of view. The adopted processing parameters allowed optimal processability up to 10% filler content, with satisfactory dispersion of the filler in the matrix; the same holds for the interfacial

adhesion. Mechanical characterization showed that the tensile strength was kept or even improved upon increasing the filler content, the elastic modulus was enhanced and only a “physiological” reduction of the elongation at break was found; moreover, the processing parameters and, in particular, the raster angle significantly affected the tensile resistance, with 0° being preferable to ±45°. The experimental mechanical behaviour was compared to the Halpin-Tsai model, finding positive deviations for the prepared systems. Moreover, the addition of a natural waste would allow to lower the final cost of the product. In fact, the cost of *Solanum Lycopersicum* plant waste used in this work is virtually zero, since these are residues from the harvesting and they would not find much significantly valuable alternative uses. Overall, these green composites let expect a bright potential for the development of sustainable bio-based materials aimed to several applications.

6.3.4 Opuntia Ficus Indica based green composites for NPK fertilizer controlled release produced by compression moulding and Fused Deposition Modelling

The subsequent text and images have been fully extracted from the published article authored by the candidate "Roberto Scaffaro, Maria Clara Citarrella, Emmanuel Fortunato Gulino, Opuntia Ficus Indica based green composites for NPK fertilizer controlled release produced by compression molding and fused deposition modeling, Composites Part A: Applied Science and Manufacturing, Volume 159, 2022, 107030, ISSN 1359-835X, https://doi.org/10.1016/j.compositesa.2022.107030. [203]" and are reproduced here with the necessary permissions from Elsevier.

Author contribution: Methodology, Software, Validation, Formal analysis, Investigation, Data curation, Writing – original draft, Writing – review & editing, Visualization.

6.3.4.1 Abstract

Excessive fertilization causes ecological problems due to leaching issues. To solve this problem and promote agriculture sustainability an innovative green composite for controlled release fertilizers was produced by adding NPK fertilizer flour to a biodegradable polymer with or without *Opuntia Ficus Indica* (OFI) particles. Six formulations were produced and employed for the fabrication of devices both for compression molding and fused deposition modeling (FDM). Both fillers displayed a good dispersion in the composites, excellent adhesion with the polymeric matrix and effectively acted as reinforcement. The decrease of NPK release rate (up to 30 days) was achieved using whole composites prepared. By appropriately selecting the dimension of the particles, the addition of OFI and the production technique, was possible to modulate the NPK release rate: FDM samples containing fine particles of OFI and NPK displayed the fastest release. Release data were fitted according to Peppas-Korsmeyer model to understand the release mechanism.

6.3.4.2 Preparation of composites

Firstly, OFI and NPK were separately grinded for 3 min and the obtained particles were sieved selecting two different mesh sizes : under 75 μm (labelled as OFI-A and NPK-A) and from 75 μm to 300 μm (labelled as OFI-B and NPK-B). Particle size were selected to be suitable for the 3D printer

preventing nozzle obstruction. In order to obtain a homogeneous dispersion of the filler, according to previous studies [202,204], the amount of filler to prepare hybrid bio-composites (ones containing both OFI and NPK) was chosen with the aim to not overcome total amount of filler of 20 wt.%. Six formulations namely MB/OFI-A, MB/OFI-B, MB/NPK-A, MB/NPK-B, MB/OFI-A/NPK-A and MB/OFI-B/NPK-B were produced by melt mixing. Hybrid composites, composites and pure MB, for comparison, were prepared by melt compounding. The obtained blends were then extruded and to obtain filaments suitable to be used for the 3D printer (diameter ~ 1.75 mm), the output extrudate were then drawn using a conveyor belt system set at a speed of 5.5 m/min.

Plaques for further characterization tests were obtained by compression molding and fused deposition modeling (FDM). After some trials, nozzle temperature of 160° was chosen aiming to achieve good printability avoiding nozzle obstructions. The other processing variables were selected considering previous works [204–207]. Other processing parameter were also chosen to promote NPK release and to optimize the mechanical performance [192,205]: infill rate 100%, rectilinear infill pattern, raster angle $\pm$ 45°. Code names of different produced samples together with their formulation are reported in Table 4.3.4.1 and some representative of them are shown in Figure 4.3.4.1.

Table 4.3.4.1 Formulation and production technique of investigated samples.

Sample code name	MB content (wt%)	OFI content (wt%)	OFI Mesh size (µm)	NPK content (wt%)	NPK Mesh size (µm)	Production technique
CM_MB	100	0	-	0	-	CM
CM_MB/OFI-A	90	10	< 75	0	-	CM
CM_MB/OFI-B	90	10	300 < 75	0	-	CM
CM_MB/NPK-A	90	0	-	10	< 75	CM
CM_MB/NPK-B	90	0	-	10	300 < 75	CM
CM_MB/OFI-A/NPK-A	80	10	< 75	10	< 75	CM
CM_MB/OFI-B/NPK-B	80	10	300 < 75	10	300 < 75	CM

FDM_MB	100	0	-	0	-	FDM
FDM_MB/OFI-A	90	10	< 75	0	-	FDM
FDM_MB/OFI-B	90	10	300 < 75	0	-	FDM
FDM_MB/NPK-A	90	0	-	10	< 75	FDM
FDM_MB/NPK-B	90	0	-	10	300 < 75	FDM
FDM_MB/OFI-A/NPK-A	80	10	< 75	10	< 75	FDM
FDM_MB/OFI-B/NPK-B	80	10	300 < 75	10	300 < 75	FDM

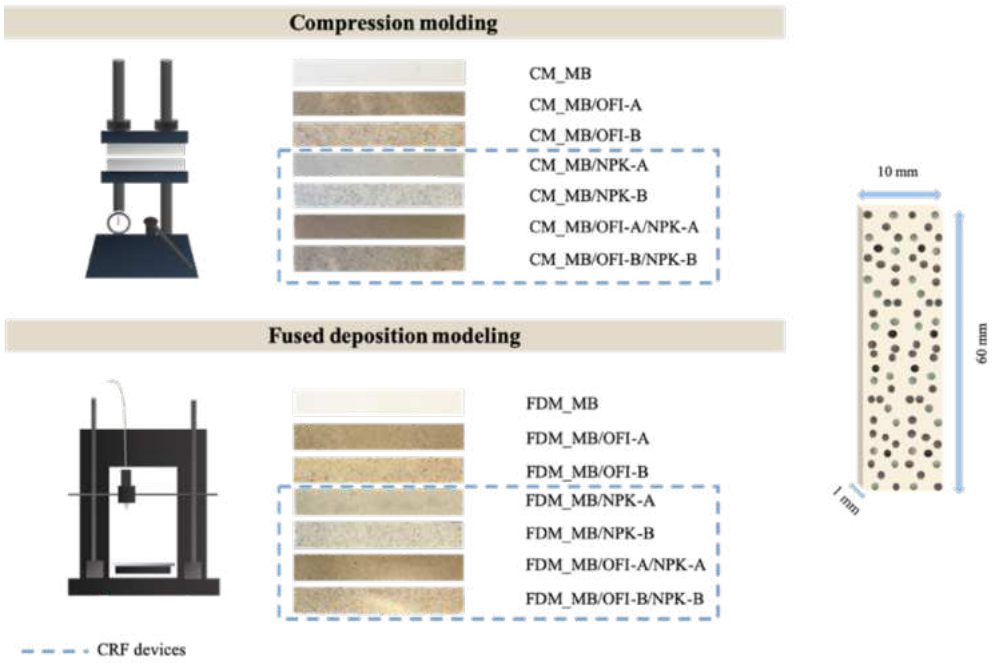

Figure 4.3.4.1 *FDM- and CM-obtained samples (photo) and their dimensions. CRF composites have been highlighted with dashed rectangles.*

6.3.4.3 Morphological analysis

Morphology of OFI particles, NPK powder and obtained composites were analyzed by SEM. Relevant micrograph of natural organic filler and fertilizer in both mesh sizes (A and B) are shown in Figure 4.3.4.2. OFI and NPK particles showed a well distinguishable morphology. Even if both present inhomogeneity in shape and size, the natural filler displayed an elongated shape while the fertilizer is characterized by a more rounded form and a clear white colour that makes it easily to

identify. Morphological analysis was also performed on the cross section of composites and SEM micrographs of compression moulded and FDM specimens are reported in Figure 4.3.4.3.

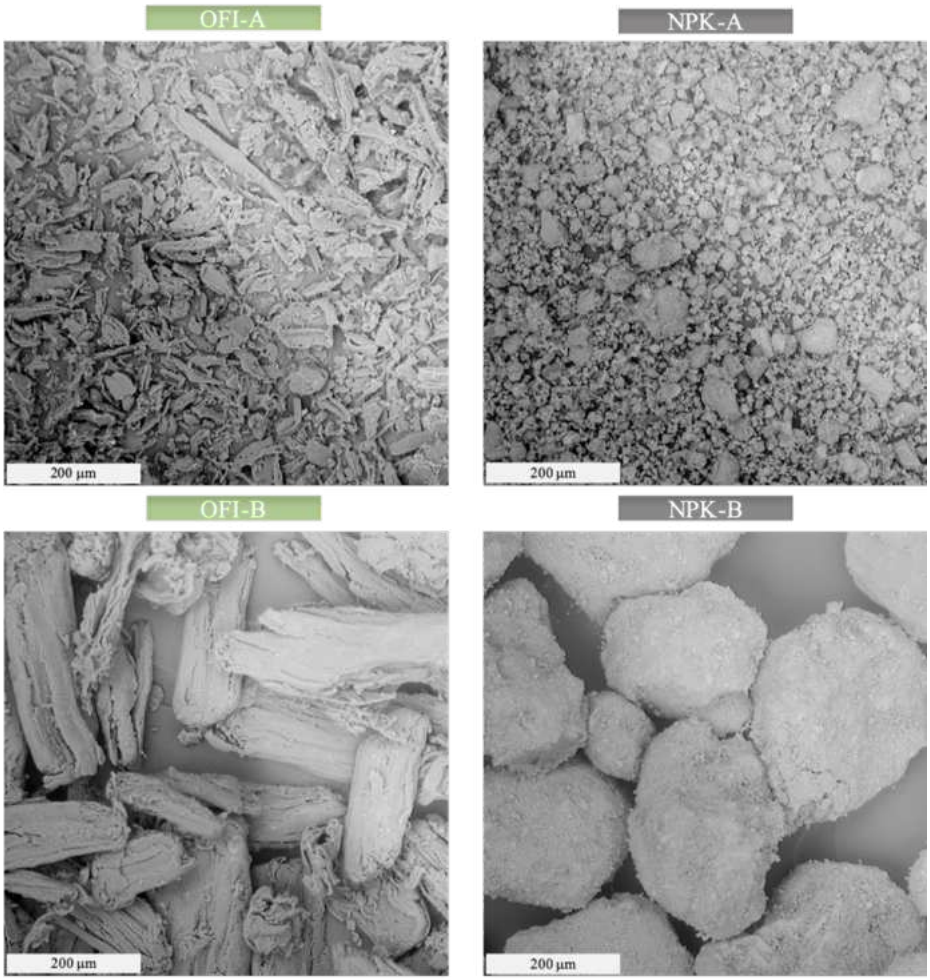

Figure 4.3.4.2 *SEM micrograph of OFI and NPK particles (A < 75 µm, B = 75–300 µm).*

It is possible to observe an almost homogeneous dispersion of filler and/or fertilizer in all samples. In addition, particles appear well embedded in the polymeric matrix and the adhesion between matrix and particles seem to be good for both OFI and NPK in both sizes (A and B). For FDM samples is possible to notice good adhesion between layers (see FDM samples micrograph in Figure 4.3.4.3 and Figure 4.3.4.4a). The selected raster angle (± 45°), moreover, allowed to obtain a porous structure by creating separation points among adjacent raster layers (see FDM samples micrograph in Figure 4.3.4.3 and Figure 4.3.4.4b).

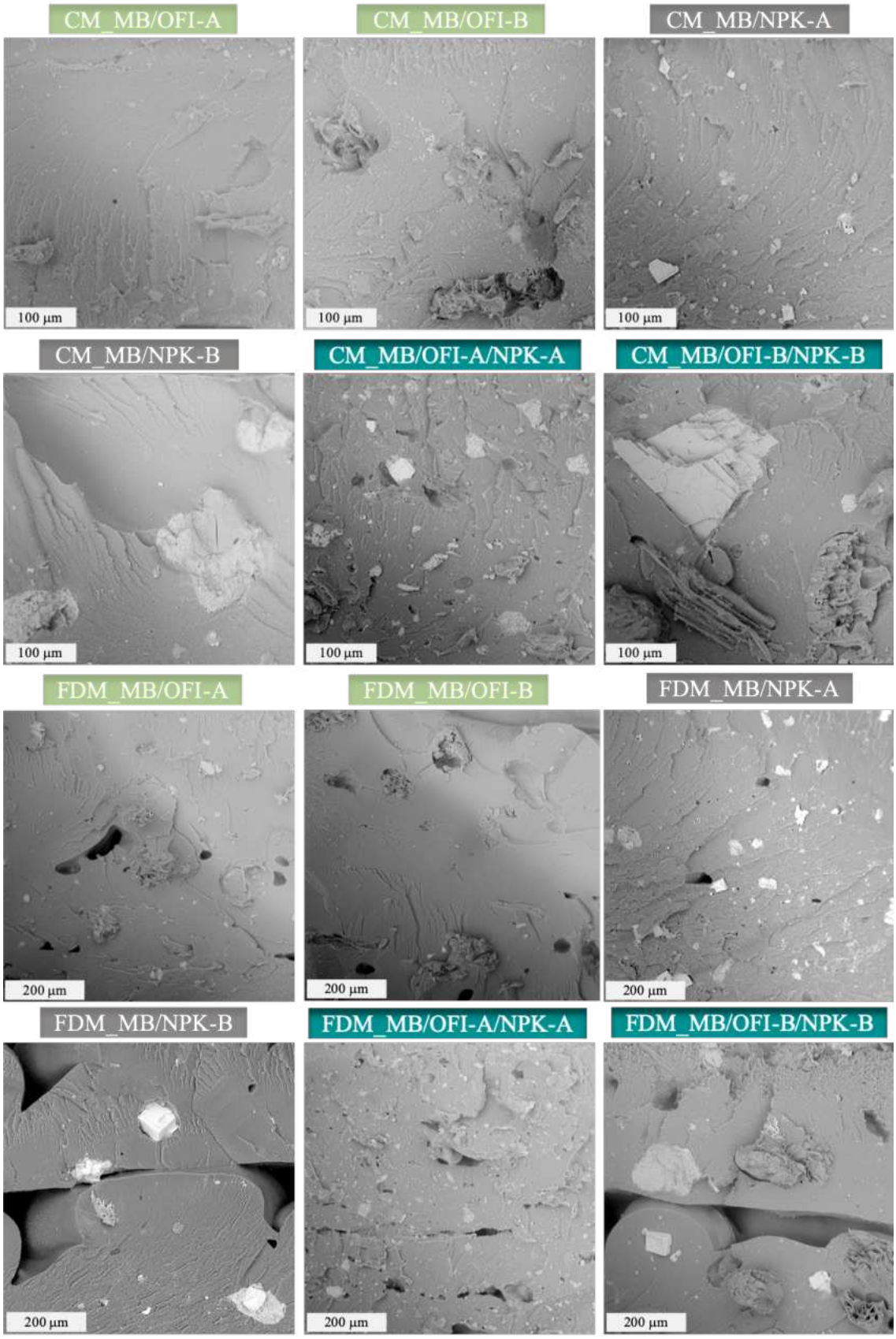

Figure 4.3.4.3 *SEM micrograph of fractured cross-section of green composites and CRF devices fabricated for compression moulding and FDM.*

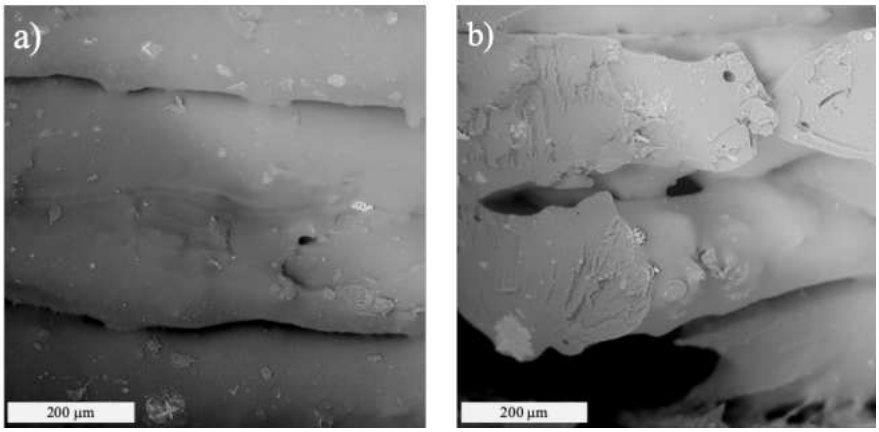

Figure 4.3.4.4 *SEM micrograph of adhesion between layers (a) and porous structure (b) of FDM samples.*

6.3.4.4 Mechanical characterization before NPK release

Mechanical performance of samples was investigated by tensile tests. The values of elastic modulus (E), tensile strength (TS) and elongation at break (EB) of pure MB, MB composites (OFI or NPK) and MB hybrid composites (OFI and NPK) produced via compression molding and FDM are reported in Table 4.3.4.2. Regarding compression molded samples, CM_MB shows a Young's modulus of 74.3 MPa a tensile strength of 19 MPa and an elongation-at-break of 821%. The addition of filler, fertilizer, or both in either mesh size (A and B), lead to an increase in E value (statistically significant, being $p < 0.0001$ for whole compositions), a decrease in EB (statistically significant, being $p < 0.0001$ for whole compositions) while TS remained almost unchanged (not statistically significant, being $p > 0.05$). This behaviour could be reasonably ascribed to the homogeneous dispersion of fillers and their good adhesion with the polymeric matrix (according to the morphological analysis). In particular, CM_MB/OFI-B showed a Young's modulus of 112 MPa and so an increase slightly higher if compared with CM_MB/OFI-A (98.1 MPa). On the contrary, no difference is observed between CM_MB/NPK-A and CM_MB/NPK-B. In fact, both showed a Young's modulus of ~ 95 MPa and an EB of ~ 64%. Hybrid composites (CM_MB/OFI-A/NPK-A and CM_MB/OFI-B/NPK-B) exhibited the highest increase in Young's modulus (~ 206%) and the lower value of elongation at break for the compression molded samples (~ 30%). This behaviour

could be reasonably explained considering that the total amount of fillers (i.e. OFI and NPK) for these latter is 20% being 10% in the previous cases. FDM composites and hybrid composites showed the same trend: the addition of filler, fertilizer, or both in either mesh size (A and B), lead to an increase in E value (statistically significant, being $p < 0.0001$ for whole compositions). Moreover, the FDM prepared samples showed a slightly higher improvement of mechanical performance if compared to the ones obtained by compression molding (statistically significant, $p < 0.0001$ for whole compositions except for OFI-A and OFI-B/NPK-B series that showed $p = 0.067$ and $p = 0.08721$ respectively). This behaviour could be reasonably ascribed to 100% rectilinear infill [192,205] and the good adhesion between layers achieved during the printing process (according to morphological analysis). Mechanical property of FDM samples could be improved even more if a 0° raster angle had been selected [192]. On the contrary, an angle of ± 45° was selected in order to achieve in the composites a good compromise between optimization of tensile properties and promotion of NPK release due to its porous structure (see FDM samples micrograph in Figure 4.3.4.3 and Figure 4.3.4.4) that ± 45° raster angle allow to obtain.

Table 4.3.4.2 Elastic modulus (E), tensile strength (TS), and elongation at break (EB) of sample obtained by compression molding and FDM.

Sample code name	E (MPa)	TS (MPa)	EB (%)
CM_MB	74.3 ± 1.2	19 ± 0.1	821 ± 0.5
CM_MB/OFI-A	98.1 ± 11	17 ± 0.3	49 ± 0.9
CM_MB/OFI-B	112 ± 8.5	16 ± 0.3	38 ± 1.8
CM_MB/NPK-A	95 ± 1.4	15 ± 1.2	65 ± 2.3
CM_MB/NPK-B	96 ± 1.5	16 ± 0.1	63 ± 2.5
CM_MB/OFI-A/NPK-A	151 ± 7.7	17 ± 0.1	30 ± 0.0
CM_MB/OFI-B/NPK-B	155 ± 8.1	16 ± 0.3	26 ± 1.0
FDM_MB	89 ± 1.3	20 ± 0.2	49 ± 0.8
FDM_MB/OFI-A	113 ± 1.6	17 ± 0.8	21 ± 0.6

FDM_MB/OFI-B	128 ± 1.5	18 ± 1.5	30 ± 1.5
FDM_MB/NPK-A	116 ± 1.6	19 ± 1.7	33 ± 1.3
FDM_MB/NPK-B	120 ± 1.2	20 ± 0.6	49 ± 1.4
FDM_MB/OFI-A/NPK-A	168 ± 1.4	17 ± 1.3	26 ± 1.5
FDM_MB/OFI-B/NPK-B	162 ± 1.8	15 ± 1.5	23 ± 0.1

6.3.4.5 Water Contact Angle (WCA) Measurements

In Figure 4.3.4.5 WCA of compression molded and FDM samples are reported. The addition of filler and / or fertilizer do not lead to a significative variation in surface wettability of the samples (statistically not significant, $p > 0.05$). Contrariwise, all FDM samples showed a decrease in WCA value if compared with their compression molded counterpart (statistically significant, $p < 0.05$ for whole compositions). This behaviour could be reasonably ascribed to the pattern of the surface obtained with the selected raster angle. It is known in the scientific literature that wettability of FDM manufactured is affected by raster angle [208,209].

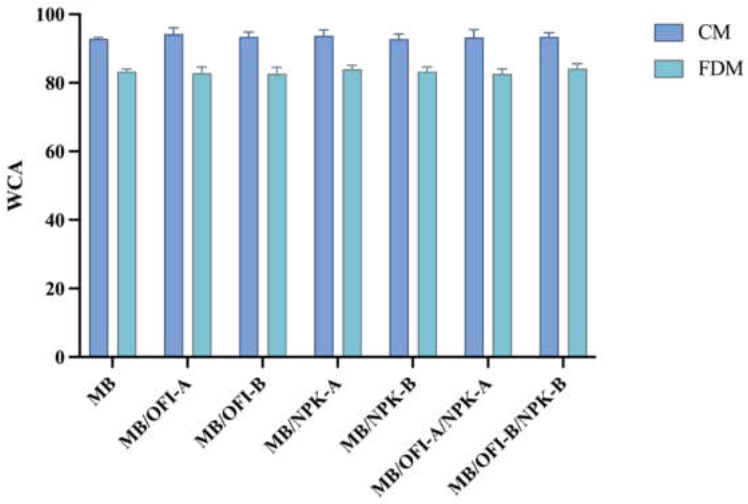

Figure 4.3.4.5 *WCA values of compression molded and FDM samples.*

Moreover, despite results seems to not match Wenzel equation, is necessary to consider that the wetting behaviour of composites obtained by FDM depends not only on surface roughness but also

on pore morphology [209]. FDM samples, printed using ±45° raster angle, are characterized by interconnected worm-like pores as could be noticed in Figure 4.3.4.6. According to Wenzel's equation, hydrophobicity is supposed to be further increased as roughness increases. However, it is known in the scientific literature that, despite surface roughness increases, the presence of long interconnected worm-like pores leads to an increase of hydrophilicity instead of hydrophobicity. The effect of porosity on wettability, in fact, overcome the one induced by surface roughness increases [172,210].

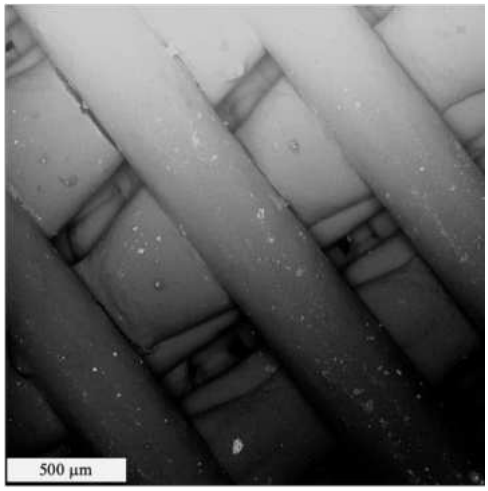

Figure 4.3.4.6 *SEM micrograph of FDM composite porous structure, plan view.*

6.3.4.6 NPK release

Release profile of NPK from the samples was performed through conductivity measurements. Electrolyte resistance, in fact, can give information about the total concentration of electrolytes in solution. Electrolyte resistance was measured also for NPK (same content as in the composites) and for composites without NPK for control and results are shown in Figure 4.3.4.7a. The conductivity values for pure NPK reached rapidly a plateau region. In this case a complete release of the fertilizer is achieved in the first 24 hours of immersion. On the contrary, for all composites without NPK (CM_MB, CM_MB/OFI-A, CM_MB/OFI-B, FDM_MB, FDM_MB/OFI-A, FDM_MB/OFI-B) a low concentration of electrolytes was slowly and constantly released. The behaviour of these latter

could be reasonably attributable to some substances originate from the matrix and from the OFI which were released in water when the samples were submerged. It is necessary taking into account that this evaluation method overestimate the NPK release since in real condition, the NPK release occurs in soil and not in a liquid medium.

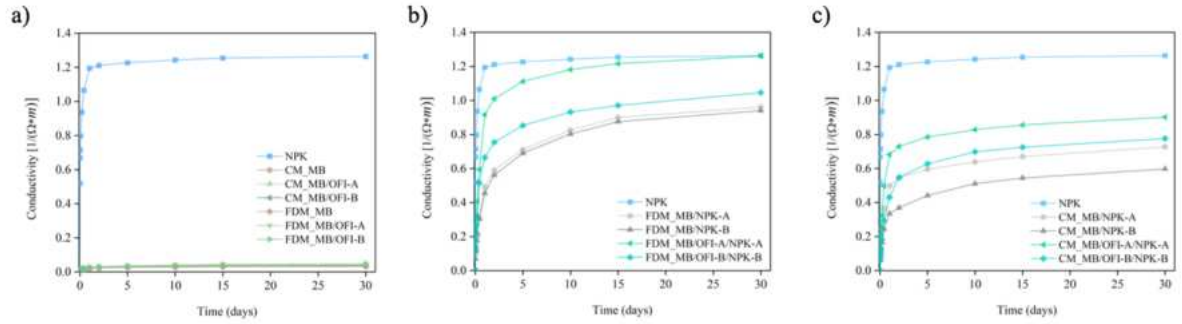

Figure 4.3.4.7 *Fertilizer release monitoring by conductivity measurements as function of time for free NPK (reported in each graph for comparison), composites without NPK (a), FDM CRF devices (b) and compression moulded CRF devices (c).*

Conductivity tests of composites with NPK obtained by FDM and compression moulding, carried out as a function of time in water at 25 °C, are shown in Figure 4.3.4.7b and 4.3.4.7c respectively. The NPK release kinetics of FDM composites (Figure 4.3.4.7b) is characterized, for all the specimens, by at least three phases: a burst release until 24 hours of immersion time, a second phase characterized by the progressive and slower release rate of NPK, and a final plateau region observed after 15 days of immersion. In detail, FDM_MB/OFI-A/NPK-A show a remarkable burst delivery with about 70% of NPK released in the first 24 hours. Other FDM composites showed a lower release of NPK, in particular, after 24 hours, FDM_MB/OFI-B/NPK-B released about 50% of NPK while FDM_MB/NPK-A and FDM_MB/NPK-B released about 40% and 45% respectively. This behaviour could be reasonably be explained taking into account that, during immersion, OFI particles create channels along the polymeric matrix allowing the water to be conveyed inside the sample. This imply that NPK particles, present in the inner part of the samples, could be easier released. Moreover, as expected, the A series showed a faster release if compared with the respectively B counterparts for both normal and hybrid composites. A smaller particle size, in fact,

allow a faster dissolution of the dispersed particles thanks to their greater exposed surface area. Compression moulded specimen (Figure 4.3.4.7c) showed the same behaviour of FDM ones but the compact structure of them significantly slow down the release of NPK. High porosities induced by FDM, in fact, significatively contribute to water transport allowing the release of the NPK also from the more inner layer of the composites [211]. After 24 hours, in fact, CM_MB/OFI-A/NPK-A released about 25% of the fertilizer only.

The sustained release of NPK fertilizer, in general, was achieved using whole composites and hybrid composites prepared both from compression moulding and FDM. All composites, in fact, if compared with free NPK, showed a significant reduction in conductivity, and so in the content of released compounds, especially in the first 24 hours. Moreover, appropriately selecting the dimension of the particles, the addition of OFI and the production technique it is possible to modulate the NPK release rate. More in detail, if a faster release is required CRFs devices should be prepare through FDM, OFI particles should be added to the polymeric matrix and NPK and OFI particles of 75 μm should be preferred. Moreover, this solution allows achieving a complete release of the fertilize. FDM_MB/OFI-A/NPK-A, in fact, act as the best CRF device considering its 100% release of NPK after 30 day. The total amount of NPK released for each composite at the end of the test, after 30 days, is resumed in Table 4.3.4.3. Compared with other CRFs reports in the literature, devices fabricated with this innovative method exhibited excellent ability to slow the release rate of NPK [212–217].

Table 4.3.4.3 Total amount of NPK released after 30 days.

Sample code name	**NPK released [%]**	
	CM	**FDM**
MB/NPK-A	58	76
MB/NPK-B	47	74
MB/OFI-A/NPK-A	71	100

MB/OFI-B/NPK-B	61	83

6.3.4.7 Peppas-Korsmeyer model

Logarithmic plots of obtained NPK release data as a function of time (Figure 4.3.4.8) were evaluated to understand better the fertilizer release mechanism. On the firsts 5 hours of release test (Figure 4.3.4.8, region 1), the devices showed a burst release region in which reasonably the fertilizer available in composites surface is immediately delivered (first 30 min) and subsequently the delivery is driven by diffusive phenomena (Figure 4.3.4.8, region 2). After this first stage the slope of the release curves increases, likely due to the occurrence of some swelling phenomena across the polymeric matrix (Figure 4.3.4.8, region 3). This latter stage results more marked for FDM samples. The higher porosity induced by the process itself, in fact, reasonably lead to a relevant increase in water uptake and swelling for FDM structure if compared with the compact structure of compression moulded devices [211].

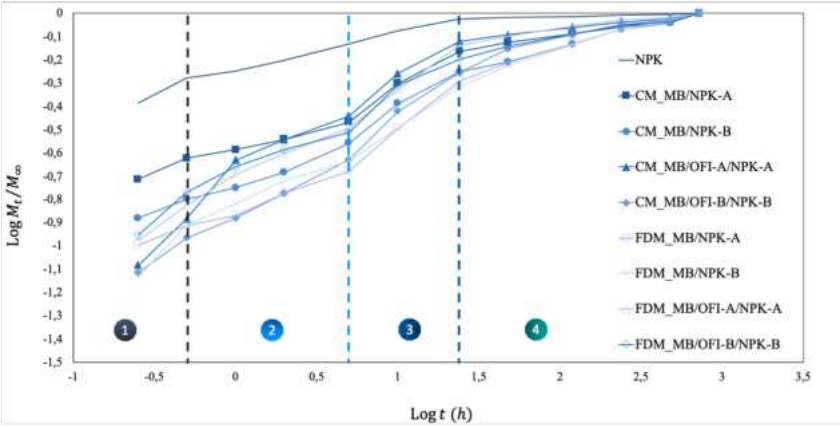

Figure 4.3.4.8 *Logarithmic plot of the release data expressed as M_t/M_∞ as function of time for free NPK and CRF devices. Vertical lines and numbers identify different regions of fertilizer release mechanism.*

After 24 hours, the fertilizer delivery is reasonably governed by both swelling and diffusive phenomena (Figure 4.3.4.8, region 4). Figure 4.3.4.9 provides a pictorial description of the release mechanism of the CRF composites.

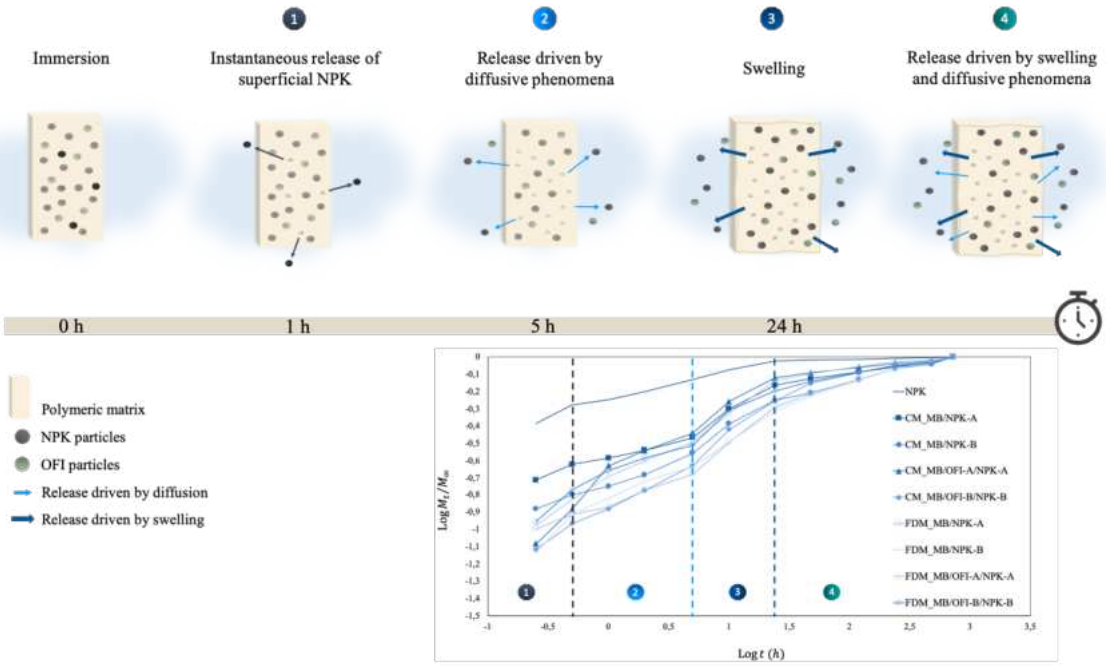

Figure 4.3.4.9 *Pictorial description of NPK release mechanism.*

In order to confirm these hypotheses on NPK release mechanism, the obtained release data were fit according to Peppas-Korsmeyer mathematical model [54,218,219]. Moreover, this model has previously been successfully used to describe fertilizer release kinetics from CRFs [220,221]. Value of K and n of the different formulations were determined and reported Table 4.3.4.4. Through n value is possible to obtain information about the release mechanism. In fact, when n is approximately 0.5, the fertilizer delivery is driven by diffusive phenomena; $n = 1$ indicates that release mechanism is governed by swelling and n values between 0.5 and 1 indicate an anomalous release, governed by swelling and diffusive phenomena [54,128,218]. However, the biopolymeric matrix may hinder diffusion, thus giving $n < 0.5$, while the presence of the organic filler and the interconnected pore in

FDM structure could provide the formation of internal channels in the samples allowing the release of the fertilizer incorporated in the innermost areas of the composite.

Table 4.3.4.4 Values of slopes (n) and intercepts (k) of fitting of Peppas-Korsmeyer model power law applied to the release data collected in the burst region ($M_t / M_\infty < 0.6$).

Sample code name	Step 1		Step 2	
	K	n	K	n
CM_MB/NPK-A	1.96	0.30	1.83	0.16
CM_MB/NPK-B	1.52	0.25	-	-
CM_MB/OFI-A/NPK-A	1.71	0.78	1.72	0.27
CM_MB/OFI-B/NPK-B	1.36	0.35	-	-
FDM_MB/NPK-A	1.38	0.24	-	-
FDM _MB/NPK-B	1.61	0.74	1.42	0.27
FDM _MB/OFI-A/NPK-A	1.55	0.34	-	-
FDM _MB/OFI-B/NPK-B	1.67	0.46	1.67	0.21

In particular, CM_MB/NPK-A (Figure 4.3.4.10a) showed a burst region that can be divided into two sub-regions, one characterized by faster kinetics ($n = 0.30$), probably attributable to some NPK particles available in the composite surface and thus faster delivered, and a second region that provide information about the actual capability of the system to establish a controlled release ($n = 0.16$). However, in both regions $n < 0.5$, especially in the second region, therefore the composite could indeed slow the fertilizer release. CM_MB/OFI-A/NPK-A (Figure 4.3.4.10b) showed the same scenario but with a first region characterized by a much faster kinetics ($n = 0.75$). This behaviour could be reasonably imputable to the presence of OFI particles in the matrix as already discussed. CM_MB/NPK-B and CM_MB/OFI-B/NPK-B (Figure 4.3.4.10c), instead, showed a single region characterize by a hinder diffusion of the NPK ($n = 0.25$ and $n = 0.35$), ensuring an almost Fickian release mechanism. Likewise, FDM_MB/NPK-A and FDM_MB/OFI-A/NPK-A (Figure 4.3.4.10d) showed a hinder diffusion of fertilizer with n value of 0.24 and 0.34 respectively. On the contrary, FDM_MB/NPK-B (Figure 4.3.4.10e) and FDM_MB/OFI-B/NPK-B (Figure 4.3.4.10f) showed two

sub-regions, one characterized by faster kinetics, especially for FDM_MB/NPK-B ($n = 0.74$), and the second that confirm the capability of the systems to establish a controlled release ($n = 0.27$ and $n = 0.21$ respectively). In general, all composites showed a significant hinder diffusion of the NPK, especially in the first 24 hours, that can be modulated by appropriately selecting the dimension of the particles of the fertilizer, the addition of OFI and the production technique. The obtained CRFs composites ensuring an almost Fickian release mechanism, unlike NPK grain, where NPK is immediately released because of its instantaneous dissolution.

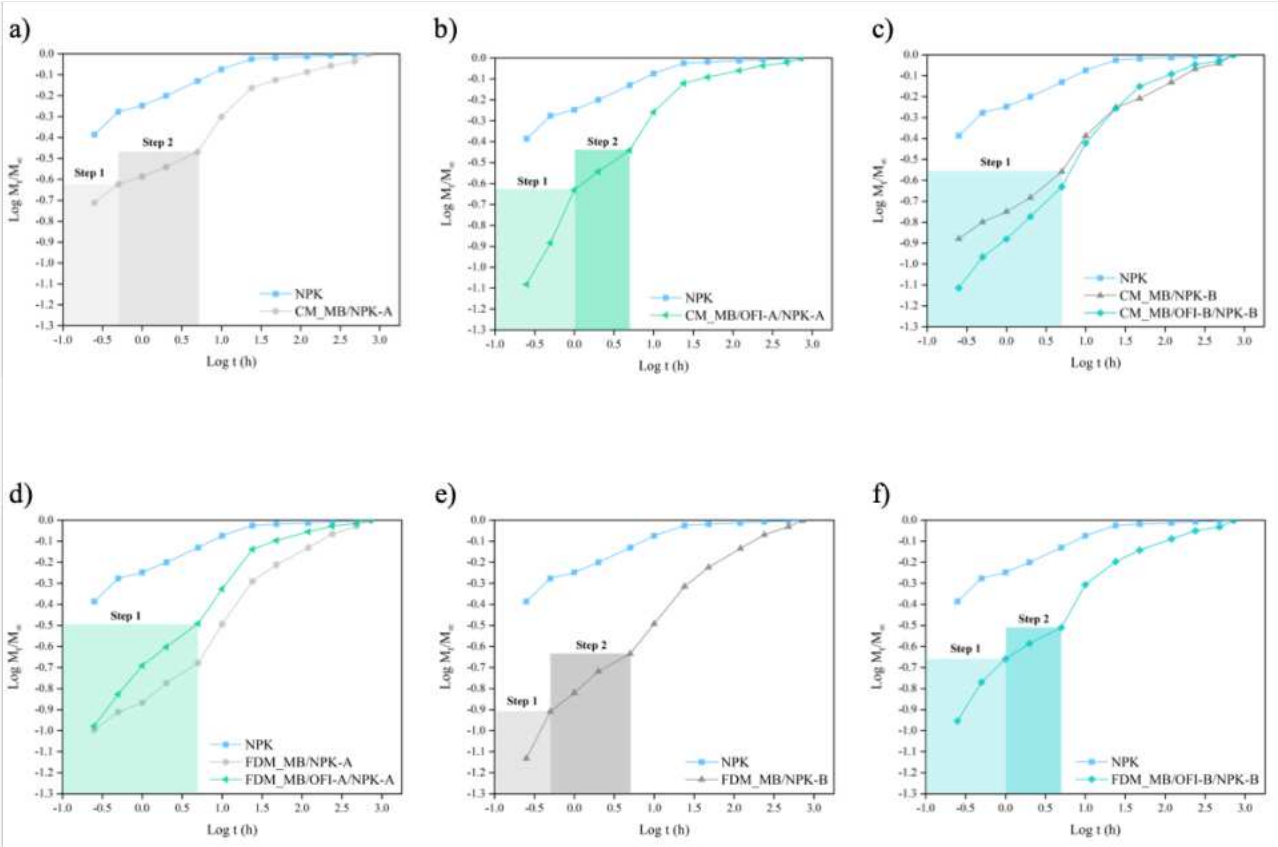

Figure 4.3.4.10 *Logarithmic plots of power law model applied to the release data collected in the burst region ($M_t/M_\infty < 0.6$, highlighted by coloured portion of the plot) for CM_MB/NPK-A (a); CM_MB/OFI-A/NPK-A (b); CM_MB/NPK-B and CM_MB/OFI-B/NPK-B (c); FDM_MB/NPK-A and FDM_MB/OFI-A/NPK-A (d); FDM_MB/NPK-B (e); FDM_MB/OFI-B/NPK-B (f).*

6.3.4.8 Morphological analysis of CRF devices after NPK release

Morphology of CRF were analyzed also after NPK release (30 days of soaking in distilled water) and relevant SEM micrograph of them are showed in Figure 4.3.4.11.

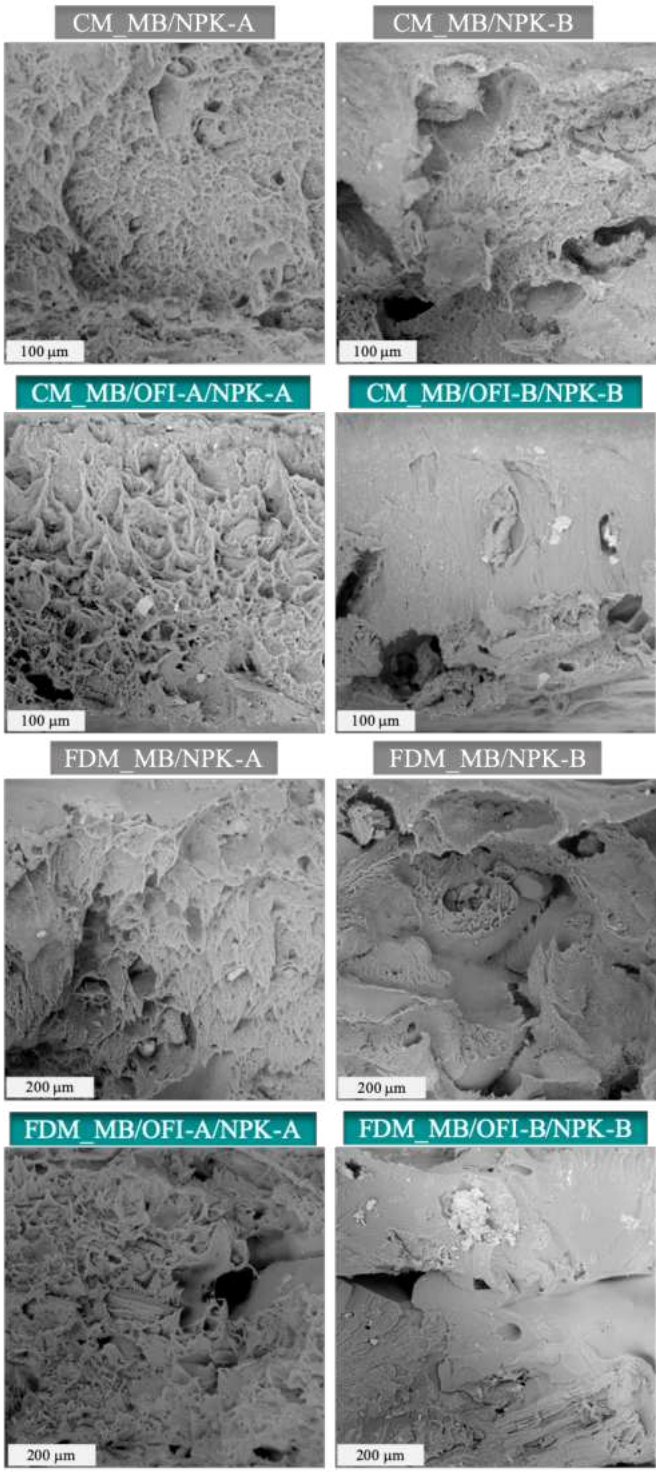

Figure 4.3.4.11 *SEM micrograph of fractured cross-section of CRF devices, fabricated for both compression moulding and FDM, after soaking in water for 30 days.*

It is possible to notice that all CRF devices displayed an evident degradation of the polymeric matrix. Moreover, all the composites showed voids in the matrix (not detectable in the samples before the release) reasonably produced by the dissolution of released NPK. Some NPK particle are still present in all device except FDM_MB/OFI-A/NPK-A. In this latter, in fact, no particles of fertilizer can be detected confirming the 100% NPK release. Furthermore, optical image (Figure 4.3.4.12a) and micrograph of the FDM samples before (Figure 4.3.4.12b) and after (Figure 4.3.4.12c) the release were reported. In Figure 4.3.4.12b it is possible to notice the good adhesion of adjacent layer in FDM samples before NPK release. After soaking in water for 30 days, instead, the samples showed a detachment of the layers (Figure 4.3.4.12c). This behaviour testifies the occurrence of swelling of the polymeric matrix confirming the supposed mechanism of release.

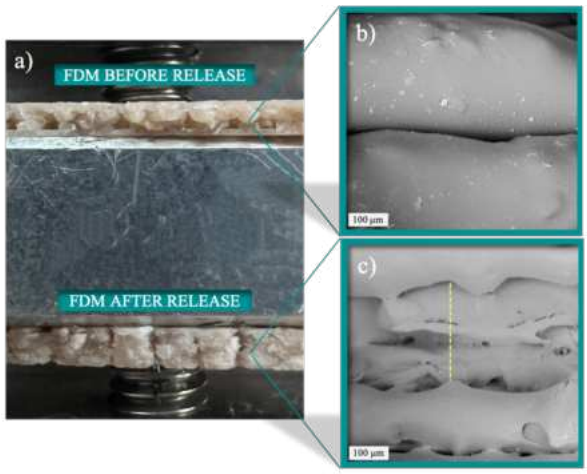

Figure 4.3.4.12 *Optical image (a) and SEM micrograph of good adhesion between layers in FDM samples before NPK release (b) and layers detachment in FDM samples after soaking in water for 30 days due to occurrence of swelling (c).*

6.3.4.9 Mechanical characterization of CRF devices after NPK release

Mechanical performance of samples after 30 days of NPK release was investigated by tensile tests and the values of elastic modulus (E), tensile strength (TS) and elongation at break (EB) are reported in Table 4.3.4.5. Samples without NPK were also immersed in DI water for 30 days and then tested for comparison. Regarding compression moulded samples, all the specimen without NPK (CM_MB, CM_MB/OFI-A, CM_MB/OFI-B) showed an increase in Young's modulus (statistically

significant, being $p < 0.05$) reasonably imputable to the degradation of the biopolymeric matrix [222]. Concerning CM_MB/NPK-A and CM_MB/NPK-B, no difference in E can be observed before and after the fertilizer release (variation not statistically significant, being $p > 0.05$), in fact, both showed a Young's modulus of ~ 95 MPa. This behaviour could be read as the result of the decrease of E due to the filler (NPK) loss during the release phase and a simultaneous increase of it imputable to the degradation of the matrix. On the contrary, hybrid composites (CM_MB/OFI-A/NPK-A and CM_MB/OFI-B/NPK-B) exhibited a slight decrease in Young's modulus (statistically significant, being $p < 0.05$). In this case, the effect of the filler loss during the release phase predominate on the biodegradation effect considering that the total amount of filler for these latter is 20% and no more 10%. Moreover, the weakening of filler/matrix interfacial interactions due to water and the poorer filler properties could influence the mechanical performance inducing a reduction in stiffness [211].

Table 4.3.4.5 Elastic modulus (E), tensile strength (TS), and elongation at break (EB) of sample obtained by compression moulding and FDM after NKP release.

Sample code name	E (MPa)	TS (MPa)	EB (%)
CM_MB	128 ± 1.6	6.1 ± 1.8	7.3 ± 2.1
CM_MB/OFI-A	135 ± 11	5.4 ± 0.0	8.9 ± 1.6
CM_MB/OFI-B	150 ± 3.1	5.7 ± 0.8	6.4 ± 0.4
CM_MB/NPK-A	94.6 ± 0.8	5.3 ± 0.6	8.4 ± 0.0
CM_MB/NPK-B	95.4 ± 3.7	5.7 ± 0.4	7.8 ± 0.8
CM_MB/OFI-A/NPK-A	137 ± 3.9	6.3 ± 0.3	7.5 ± 0.4
CM_MB/OFI-B/NPK-B	143 ± 9.5	4.8 ± 2.2	4.7 ± 2.0
FDM_MB	85.6 ± 1.1	5.9 ± 0.6	13 ± 1.4
FDM_MB/OFI-A	101 ± 1.7	5.2 ± 0.4	7.8 ± 1.4
FDM_MB/OFI-B	114 ± 0.5	5.6 ± 1.7	7.4 ± 0.7
FDM_MB/NPK-A	90.7 ± 1.5	5.9 ± 1.3	8.9 ± 1.3
FDM_MB/NPK-B	101 ± 0.7	6.1 ± 0.2	8.4 ± 0.3
FDM_MB/OFI-A/NPK-A	105 ± 0.4	5.9 ± 1.5	8.9 ± 0.8
FDM_MB/OFI-B/NPK-B	104 ± 1.4	5.7 ± 1.2	8.4 ± 1.6

Concerning FDM sample it is also necessary to take into account that the high porosities induced by the process, not only promote the water transport across the samples allowing the release of the NPK also from the more inner layer of the composites but also leads to a relevant increase of water uptake and swelling if compared to compression molded samples [211]. FDM_MB, in fact, showed a slight decrease in E value (statistically significant, being $p < 0.05$) probably imputable to its hygroscopic behaviour. This decrease was even more marked in OFI and / or NPK containing samples were also the effect of filler loss during the release phase should be considered. In detail, FDM_MB/OFI-A and FDM_MB/OFI-B displayed a decrease in Young's modulus from 113 to 101 MPa and from 128 to 114 MPa respectively (statistically significant, being $p < 0.05$). When only NPK is added to the biopolymeric matrix (FDM_MB/NPK-A and FDM_MB/NPK-B) the decrease in E value is more marked (statistically significant, being $p < 0.05$). This behaviour could be reasonably imputable to the higher filler loss due to the better solubility of NPK if compared with OFI one. Moreover, FDM_MB/OFI-A/NPK-A and FDM_MB/OFI-B/NPK-B showed the highest decrease in Young's modulus value (statistically significant, being $p < 0.05$) due to the even higher filler loss that occurs for these samples. Should be considered, in fact, that the total amount of filler for these latter is 20% and no more 10% (since 10% of OFI and 10% of NPK is present).

6.3.4.10 Conclusions

An innovative green composite with CRFs performance was produced by adding NPK flour to a biodegradable polymer (Mater-Bi®) with or without OFI particles. The final devices were successfully fabricated both for compression moulding and FDM using all the prepared formulation. Both filler and fertilizer displayed good dispersion in the composites, excellent adhesion with the polymeric matrix and effectively acted as reinforcement. FDM samples, moreover, showed higher mechanical properties if compared with compression moulded ones. Release tests of CRF devices reveal the ability of all the obtained composites to slow the release rate of NPK (up to 30 days), which

proved to be tunable by modifying formulation, flours granulometry and production techniques. The porous structure of FDM samples, induced by the process itself, promote the water transport across the devices allowing the release of the NPK also from the more inner layer. In particular, FDM_MB/OFI-A/NPK-A act as the best CRF device showing a remarkable burst delivery with about 70% of NPK released in the first 24 hours and a 100% release after 30 days. Compression molded specimens showed the same behaviour of FDM ones but the compact structure of them significantly slow down the release of NPK. Considering release kinetics results, it is possible to conclude that by adding filler, varying fertilizer and filler granulometry and by employing different production technique it is possible to tune NPK release in order to be suitable to crops different life cycle or to environmental conditions of specific soils or climates. More in detail, by addig OFI particles to the polymeric matrix and select 75 μm NPK and OFI particles it is possible to obtain CRFs devices characterized by a faster release. Biodegradable, cost effective and easy to produce CRF green composites could be prepared through FDM by adding NPK and OFI flours to a biodegradable polymeric matrix. The addition of OFI, in fact, leads to a decrease of the amount of polymer needed and consequently to a lowering in the cost of the final device. Moreover, by using FDM it is possible to reduce production time and costs, create extremely elaborated geometries as well as easy tune the NPK release rate.

6.3.5 Multifunctional 3D-Printed Composites Based on Biopolymeric Matrices and Tomato Plant (Solanum Lycopersicum) Waste for Contextual Fertilizer Release And Cu(II) Ions Removal

The subsequent text and images have been fully extracted from the published article authored by the candidate "Scaffaro, R., Gulino, E.F. & Citarrella, M.C. Multifunctional 3D-printed composites based on biopolymeric matrices and tomato plant (Solanum lycopersicum) waste for contextual fertilizer release and Cu(II) ions removal. Adv Compos Hybrid Mater 7, 95 (2024). https://doi.org/10.1007/s42114-024-00908-4 [223]" and are reproduced here with the necessary permissions from Elsevier.

Author contribution: writings—original draft, writing—review and editing, software, formal analysis, investigation, visualization, conceptualization, data curation, methodology, validation.

6.3.5.1 Abstract

The production of tomatoes faces significant challenges, including the high amount of waste generated during the harvest stage and copper-contaminated soil due to pesticide use. To address these issues and to promote a more sustainable agriculture, innovative biodegradable green composites for contextual controlled soil fertilization and Cu removal were produced by 3D-printing technology. These composites were made by incorporating NPK fertilizer flour and tomato plant waste particles (SLP) into three different biodegradable polymeric matrices: polylactic acid (PLA); a commercial blend of biodegradable co-polyesters (Mater-Bi®, MB) and their blend (MB/PLA, 50:50). Rheological characterization suggested the potential processability of all of the composites by FDM. Morphological analysis of printed samples confirmed the good dispersion of both filler and fertilizer, which also acted as reinforcement for MB and MB/PLA composites. SLP and NPK moduli were evaluated by powder nanoindentation and, for almost composites, the theoretical Halpin-Tsai model satisfactorily fitted the actual tensile moduli. The decrease in NPK fertilize release rate and the increase in Cu(II) removal efficiency were achieved using whole 3D-printed composites. By selecting the appropriate matrix and incorporating SLP particles, it was possible to tune the NPK release rate and achieve copper absorption efficiency. Notably, MB samples containing SLP particles displayed the fastest release and the highest Cu(II) removal efficiency.

6.3.5.2 Preparation of MB, PLA and MB/PLA neat and composites filaments

Aiming to obtain a good dispersion of the fillers and achieve good printability, specific amounts of SLP and NPK were chosen to prepare hybrid bio-composites, not overcoming a total amount of 20 wt% of filler added. More in detail, nine different formulation were prepared. An internal mixer was used in order to melt mix 10% of SPL and (or) 10 % of NPK to all the selected matrices. The three neat matrices (MB, PLA, and MB/PLA) were also processed under identical conditions for the purpose of comparison. The obtained formulations were then extruded and a conveyor belt system (6 m/min) was used to draw the output extrudate aiming to obtain filaments with a diameter of ~ 1.75 mm. The filaments were named based on the selected matrix and their filler contents. Formulations of the matrices and the produced composites, together with their code names, are reported in Table 4.3.5.1.

Table 4.3.5.1 Formulations of used polymeric matrices and prepared bio-composites.

Sample code name	MB [wt%]	PLA [wt%]	SLP [wt%]	NPK [wt%]
MB	100	0	0	0
PLA	0	100	0	0
MB/PLA	50	50	0	0
MB-SLP	90	0	10	0
MB-NPK	90	0	0	10
MB-SLP-NPK	80	0	10	10
PLA-SLP	0	90	10	0
PLA-NPK	0	90	0	10
PLA-SLP-NPK	0	80	10	10
MB/PLA-SLP	45	45	10	0
MB/PLA-NPK	45	45	0	10
MB/PLA-SLP-NPK	40	40	10	10

6.3.5.3 Morphology of SPL and NPK powders

After the drying process, small pieces of tomato plant stems were examined using SEM to evaluate their internal morphological structure. SEM images (Figure 4.3.5.1a, 4.3.5.1b) revealed that the tomato plants used in this work are characterized by circular and square-shaped voids regularly distributed along the entire length of the stem. These features could be particularly useful to achieve

infiltration of the polymeric matrices into the filler, thereby potentially obtaining a mechanical reinforcing effect with the formation of an interphase [224,225].

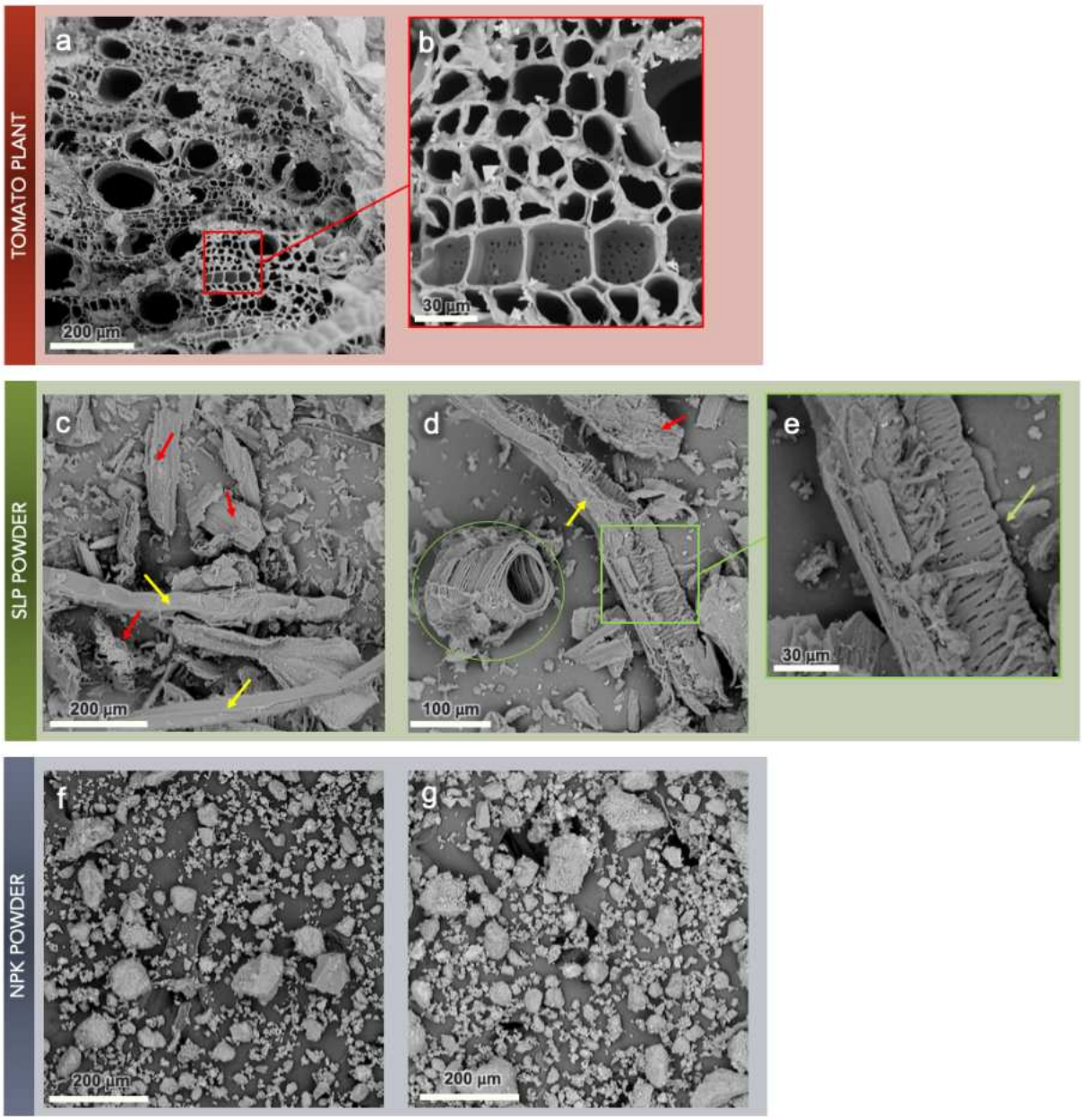

Figure 4.3.5.1 *SEM micrographs of tomato plant steam (a) and close-up view (b); SLP powder (c, d) and close-up view (e) and NPK powder (f, g). Highlighted area in panel b and e providing a detailed examination of the material's microstructure.*

After this preliminary characterization, the plant was then ground into fine particles and the obtained powder was sieved, selecting the fraction under 150 µm. Relevant SEM micrographs of SLP powder are shown in Figure 4.3.5.1c and 4.3.5.1d. SLP flour is characterized by an hybrid

morphology: some particles showed a fibrous shape (yellow arrows), while others had a flakes-like geometry (red arrows) due to the fact that whole tomato plant was ground as received without separating the different parts: the fibrous-shaped particles likely belong to the stems, while the flakes-like ones belong to the leaves. Moreover, fibrous-shaped particles are characterized by lengths greater than 150 μm but with high aspect ratio. This feature allowing them to pass through the sieve when aligned perpendicularly to the mesh. SEM images in Figure 4.3.5.1d and 4.3.5.1e (close-up view and arrow) revealed that the porous structure of the stem was partially preserved even after grinding, and that some skein-shaped particles (green circle) were also sporadically present.

Relevant micrographs of ground NPK fertilizer particles are shown in Figure 4.3.5.1f and 4.3.5.1g. Although they displayed some inhomogeneity in shape and size, they all exhibited a rounded geometric shape. Furthermore, NPK and SLP particles have distinct morphologies.

6.3.5.4 Processing and morphological analysis of filaments

First, all the different formulations (included neat MB and PLA) were melt-mixed for two minutes (T = 160 °C for MB and MB/PLA series and T = 190 °C for PLA series). The obtained mixtures were ground into pellets and then extruded into filaments using a cylindrical nozzle and a conveyor belt system. Melt mixing was performed aiming to improve the dispersion of the fillers in the polymeric matrices. This preliminary mixing enables the production of composite filaments with a homogeneous dispersion of the filler and a rounded shape, improving properties and printing performance of them. Both neat matrices and SLP and/or NPK-containing filament (diameter: ~ 1.75 mm) were successfully extruded, their morphology was analyzed, and relative optical images and SEM micrograph of their cryofractured cross section are reported in Figure 4.3.5.2.

SEM micrographs confirm that all the filament showed a diameter of ~ 1.75 mm and an almost regular cylindrical shape (Figure 4.3.5.2a-c; e-g; i-k) but -SLP-NPK ones that exhibited a non-totally uniform and quite rough surface (Figure 4.3.5.2d, h, l). More in detail, MB (Figure 4.3.5.2a), PLA

(Figure 4.3.5.2e) and MB/PLA (Figure 4.3.5.2i) neat filaments showed a very regular cylindrical shape.

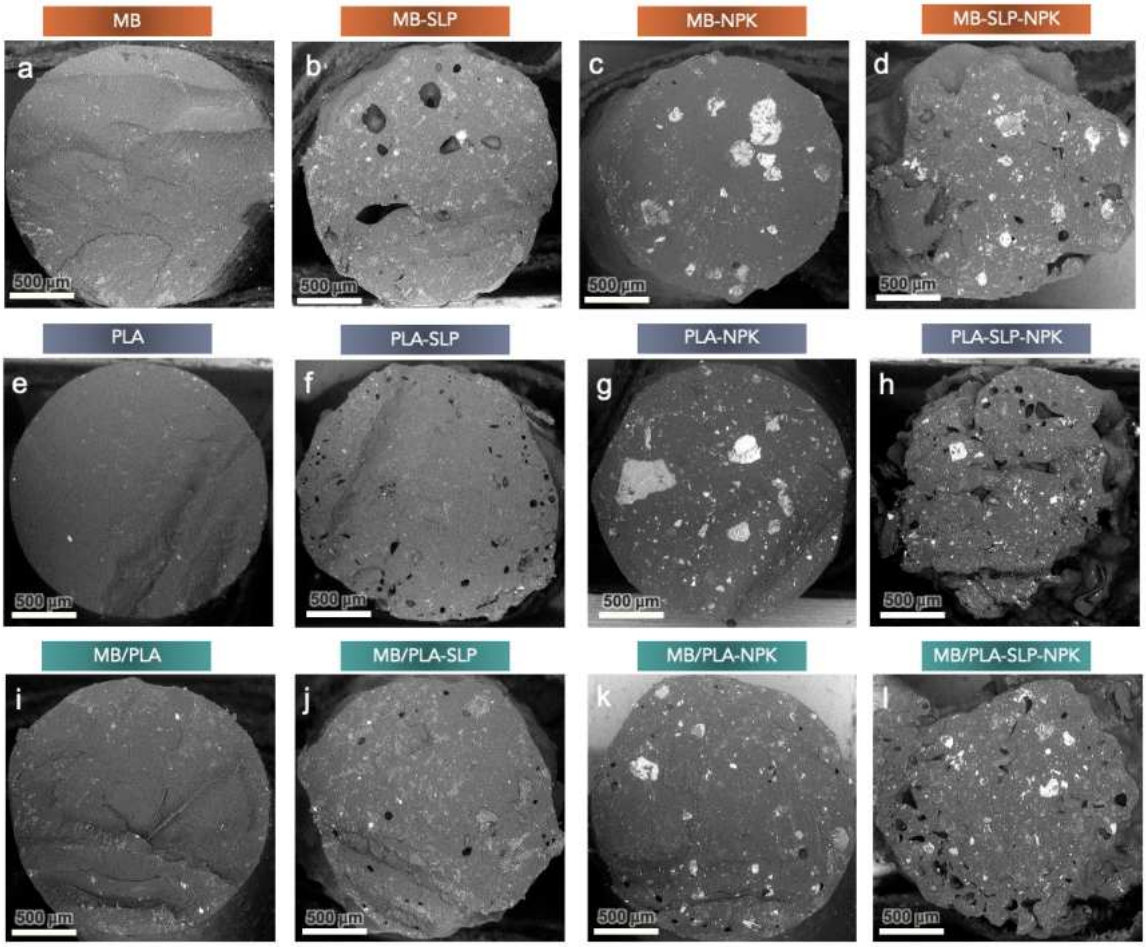

Figure 4.3.5.2 *SEM micrograph of MB (a); MB-SLP (b); MB-NPK (c); MB-SLP-NPK (d); PLA (e); PLA-SLP (f); PLA-NPK (g); PLA-SLP-NPK (h); MB/PLA (i); MB/PLA-SLP (j); MB/PLA-NPK (k); MB/PLA-SLP-NPK (l) filaments cross section.*

Furthermore, when blend together, MB and PLA, form an apparently homogeneous structure, at least at this scale, as shown in Figure 4.3.5.2i. When just SLP is added to the different polymeric matrices (Figure 4.3.5.2b; f; j), the regular cylindrical shape and homogeneous dispersion of filler are almost preserved. SLP exhibited a good adhesion with the matrices and limited presence of voids can be noted in all the three filament samples. On the other hand, the addition of NPK (Figure 4.3.5.2c; g; k), had no adverse effect on the geometric regularity of the filament. Moreover, in all filament samples, an almost homogeneous dispersion of the fertilizer with very limited presence of voids could

be noted and the interfacial adhesion between the particles and the polymeric matrices seems to be good. MB-SLP-NPK (Figure 4.3.5.2d), PLA-SLP-NPK (Figure 4.3.5.2h) and MB/PLA-SLP-NPK (Figure 4.3.5.2l) exhibit uneven edges with some voids along them. This can be explained taking into account that in this latter case the total amount of fillers (i.e. SLP and NPK) is 20%, and no more 10%. However, the cylindrical shape is sufficiently preserved in order to be 3D printed, and both the filler and the fertilizer are homogeneously dispersed throughout the filaments. The neat matrices and the SLP and(or) NPK containing formulations showed morphology potentially suitable for FDM printing process.

6.3.5.5 Rheological behaviours and thermal properties of filaments

Filaments printability by FDM technology is strongly related to their rheological behaviour [199]. Therefore, rheological analyses were investigated by using rotational rheometer and results are reported in Figure 4.3.5.3a-c.

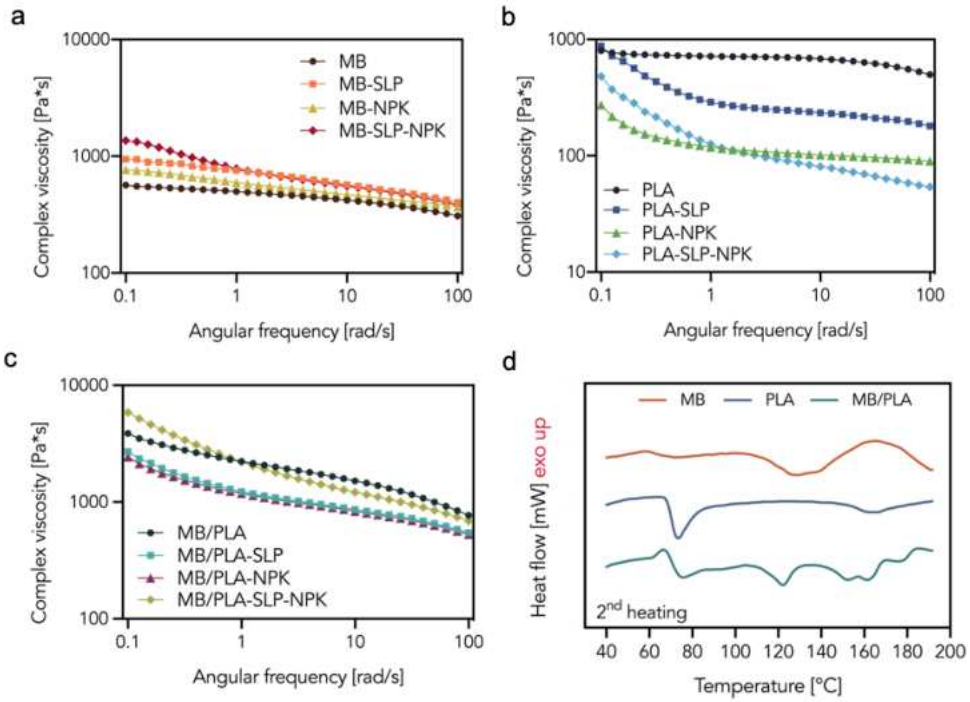

Figure 4.3.5.3 *Complex viscosities of MB (a), PLA (b) and MB/PLA (c) series performed at 160 °C, 190 °C and 160 °C respectively and DSC curves (d) of the polymeric matrices.*

Based on our previous works [202,226], all the formulations based on MB, PLA, and MB/PLA displayed viscosity values that are potentially suitable for be 3D-printed. More in detail, MB (Figure 4.3.5.3a) shows an almost Newtonian behaviour at lower frequencies and a shear-thinning behaviour at higher ones. The presence of SLP or NPK lead to an increase in viscosity values across the whole range of frequency, and a more pronounced non-Newtonian behaviour. When compared to MB-NPK, MB-SLP displayed higher viscosity value, possibly due to the porous and spongy structure of SLP particles that allows the polymeric matrix to infiltrate it. This tendency further increases when both SLP and NPK were present in the composite and the onset of yield stress phenomena could be observed. In this latter case, it is necessary to consider that the total amount of the dispersed phase was 20% (10 % SLP and 10 % NPK) and no more 10% (SLP or NPK only) like in the previous analyzed systems. On the other hand, neat PLA (Figure 4.3.5.3b) displayed its typical [227,228] Newtonian behaviour at lower frequencies and a slight shear-thinning in the higher region. The addition of SLP or NPK into the PLA matrix significantly lowered the complex viscosity over the entire investigated frequencies range (0.1–100 rad/s), as already reported for similar composite systems [199], suggesting a decrease of the molecular weight (M_w) due to a deterioration of the polymer phase upon processing. In the PLA composites filament (Figure 4.3.5.3b), a slight change in the shape of the curve was observed: PLA-SLP, PLA-NPK and PLA-SLP-NPK exhibited a non-Newtonian behaviour at lower angular frequencies and pronounced shear-thinning behaviour at higher frequencies. Moreover, for PLA-SLP-NPK the presence of yield stress phenomena could be observed. The presence of yield stress, in fact, is typical of composites systems. In Figure 4.3.5.3c, the complex viscosities of the MB/PLA series are reported. The rheological behaviour of MB/PLA blend was mostly influenced by the PLA phase. In the case of MB/PLA series, in fact, it should be considered that the temperature of 160 °C (used for filament preparation and sample printing), was chosen in order to limit MB thermal degradation. Therefore, at this temperature, the PLA phase was not completely molten. Due to the presence of this partially molten phase, neat MB/PLA exhibited a non-Newtonian behaviour characterized by a shear-thinning behaviour at high angular frequencies

and the onset of yield stress phenomena at lower frequencies. The presence of SLP or NPK leads to a decrease in viscosity values across the entire frequency range, but almost no change in the shape of the curve was observed. When both SLP and NPK were present in the composite (MB/PLA-SLP-NPK), a more pronounced non-Newtonian behaviour and yield stress phenomenon could be noted.

The results suggest that the rheological behaviours of all the composite filaments were compatible with the 3D printing process, especially those of the MB/PLA series. Shear-thinning properties are fundamental for lowering viscosity values, aiming to improve filament printability for 3D printing.

In order to deeply investigated the behaviour of the blend, DSC measurements were performed on the neat matrices and the obtained results are presented in the form of thermogram plots in Figure 4.3.5.3d. MB and PLA exhibited the same glass transition temperature of about 75 °C and melting point of 130 °C and 165 °C respectively. MB/PLA showed almost the same glass transition temperature of the single polymeric component (about 75 °C) and two different melting points: the first at about 125 °C followed by a second at about 160 °C likely related to the melting of the PLA phase. Considering that MB is a blend of aromatic and aliphatic biodegradable co-polyesters reasonably including PLA [229], the total melting enthalpy of the different matrices could be compared in order to obtain information about the crystallinity of the materials. The thermal properties of PLA confirm a typical almost amorphous behaviour of PLA, while MB exhibited a much higher melting enthalpy value showing similar results to other research studies [229]. When MB and PLA are mixed together a higher melting enthalpy is observed reasonably due to the occurrence of a nucleation effect as already reported for similar systems [230].

6.3.5.6 3D printing and morphological analysis of composites

MB, PLA and MB/PLA composites filament with 10% of SLP and/or NPK powders were successfully extruded obtaining a diameter of about 1.75 mm. Pure MB, PLA and MB/PLA filaments

were also produced using identical procedure for comparison. All filaments were easily 3D printed for FDM as was predicted considering SEM analysis (Figure 4.3.5.2) and their rheological behaviours (Figure 4.3.5.3a-c). The FDM process, in fact, proceeded smoothly, without any interruption, (also for -SLP-NPK ones despite the non-uniform surface of the filaments) and no nozzle clogging occurred. All the composites formulations could be actually printed without varying the temperature normally used for MB and PLA pure matrices (160 °C and 190 °C respectively). Neat MB/PLA and its composites have been fluidly printed at 160 °C. Specimens of 60×10×1 mm have been successfully printed with all the prepared formulations.

Morphological characterization was conducted on the cryofractured cross section of 3D printed composite samples, see SEM micrographs in Figure 4.3.5.4.

A relatively uniform dispersion of both natural filler and fertilizer was observed in all the composites (Figure 4.3.5.4a-i). In MB (Figure 4.3.5.4a-c) and PLA based composites (Figure 4.3.5.4d-f), imperfect adhesion was observed between the matrices and both SLP and NPK particles, as noted by the presence of many voids in the fracture surface. This behaviour was more pronounced with SLP particles. On the other hand, both SLP and NPK particles appeared to be well-embedded in the MB/PLA matrix (Figure 4.3.5.4g-i) and the adhesion between matrices and particles seemed to be good, especially for SLP particles (see red circle and arrow in Figure 4.3.5.4g and 4.3.5.4i respectively). In this latter case, the matrix penetrated inside the SLP particles pores, anchoring the particles to the matrix and achieving excellent adhesion. Moreover, all FDM-printed samples exhibited a porous structure created by the separation points among adjacent raster layers due to the selected raster angle (± 45°). The production of porous devices is really interesting because it allows water transport across the samples, enhancing fertilizer release and pollutant removal [154,231].

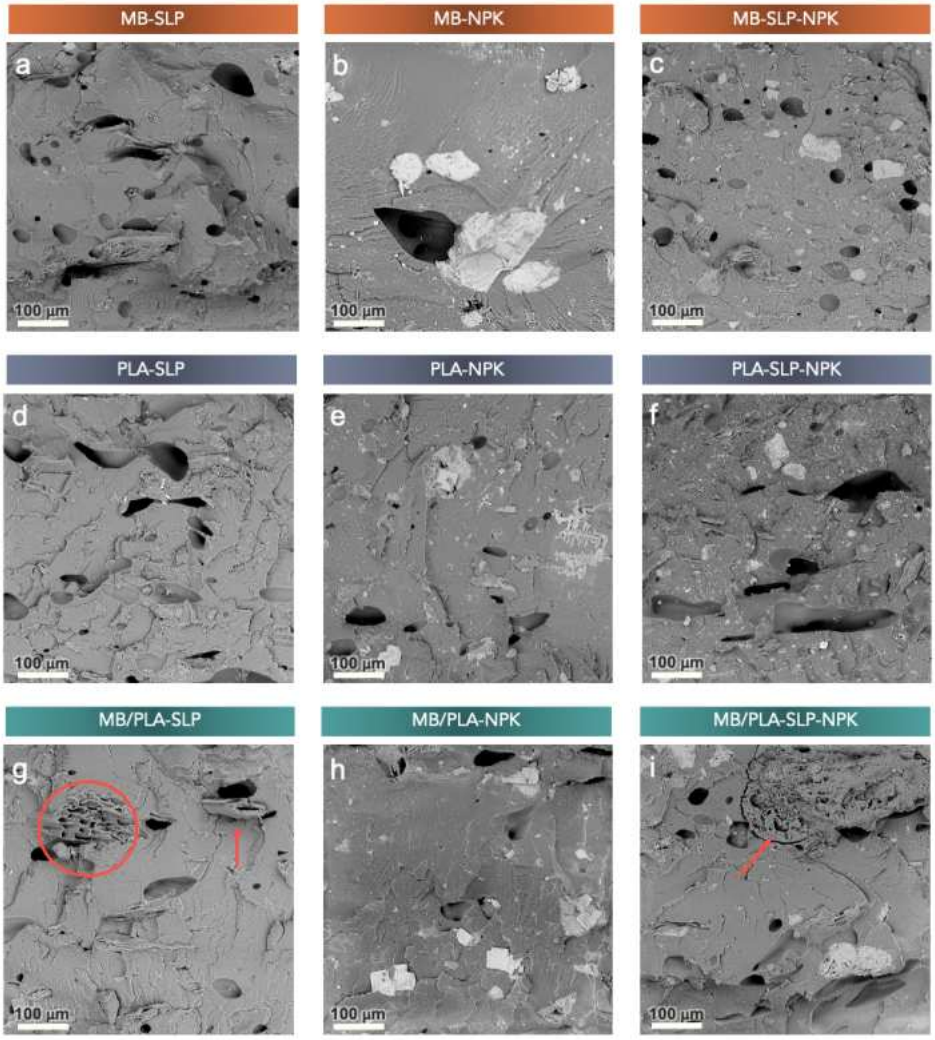

Figure 4.3.5.4 *SEM micrograph of MB-SLP (a); MB-NPK (b); MB-SLP-NPK (c); PLA-SLP (d); PLA-NPK (e); PLA-SLP-NPK (f); MB/PLA-SLP (g); MB/PLA-NPK (h); MB/PLA-SLP-NPK (i) cross section of 3D printed samples.*

6.3.5.7 Nanoindentation of SLP and NPK powders

Elastic modulus (E) of SLP and NPK particles have been investigated using nanoindentation. The nanoindentation test showed that the elastic modulus of NPK fertilizer is significantly higher than that of SLP. Specifically, Young's modulus of NPK was found to be 12708(± 8.7) MPa, while SLP one was 171(± 0.1) MPa. This difference in stiffness between NPK and SLP can be attributed to the materials nature: NPK, in fact, is composed of a mixture of nitrogen, phosphorus, and potassium salts, which are known for their hardness and strength. On the other hand, SLP is made up of organic compounds, which tend to be relatively soft.

6.3.5.8 Mechanical properties of 3D printed composites and Halpin-Tsai model

The mechanical performance of 3D-printed composites samples was investigated through tensile tests and the outcomes of composite elastic modulus, normalized to those of each matrix, are shown in Figure 4.3.5.5. The addition of SLP particles to MB (Figure 4.3.5.5a, first group of bars) did not lead to any statistical relevant variation in the E value. To address this behaviour, the fractured cross-section of MB-SLP was analyzed by SEM. As shown in Figure 4.3.5.5b, during the fracture phase, SLP particles were pulled out of the polymeric matrix limiting their reinforcing effect. On the other hand, the addition of NPK to MB (MB-NPK and MB-SLP-NPK) led to a slight but statistically significant increase in E, going from 89 MPa of neat MB to 94 and 95 MPa of MB-NPK and MB-SLP-NPK respectively.

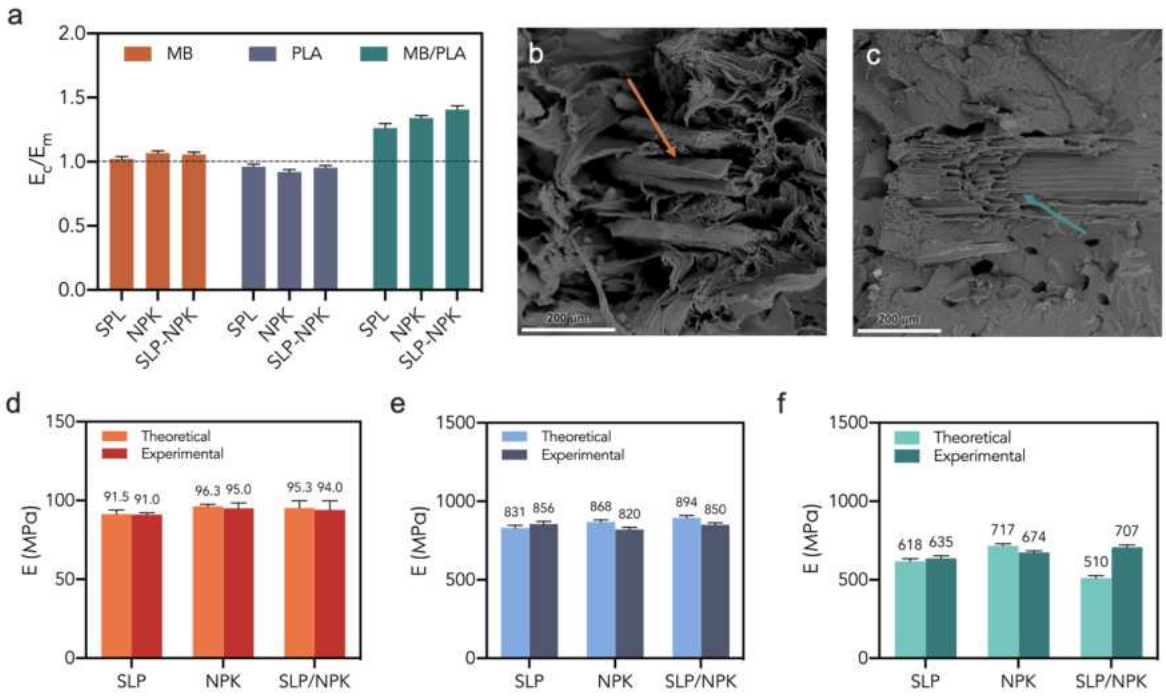

Figure 4.3.5.5 *Reduced elastic modulus of the composites (E_c, i.e. normalized to those of each matrix E_m), dashed line refers to neat matrices value of the reduced property (a); SEM micrograph of SLP particles behaviour during tensile fracture in MB-SLP (b) and MB/PLA-SLP (c) printed samples; (b) theoretical and experimental elastic modulus of MB (d), PLA (e) and MB/PLA (f) composites.*

Regarding the PLA series (Figure 4.3.5.5a, second group of bars), the addition of SLP or NPK particles, or both contextually, to PLA led to a slight but statistically significant decrease in E, going

from 891 MPa of neat PLA to 852, 820 and 850 MPa of PLA-SLP, PLA-NPK and PLA-SLP-NPK respectively. These results appear to be in full agreement with those obtained during rheological characterization. MB/PLA blend showed a different mechanical behaviour (Figure 4.3.5.5a, third group of bars). The addition of SLP particles led to an increase in E, going from 503 MPa of neat MB/PLA to 635 MPa of MB-SLP. In fact, the filler is currently well-integrated into the polymeric matrix, acting as a reinforcement (see SEM images in Figure 4.3.5.4). This is evident from the observed fracture behaviour during tensile testing (Figure 4.3.5.5c), where SLP particles tend to break rather than pull out from the matrix. These results suggest that the filler-matrix interface is strong, allowing efficient load transfer and improved mechanical properties of the composite, in accordance with the morphological analysis, (Figure 4.3.5.4h). The same trend was also observed when NPK is added to the matrix, reaching a Young's modulus of 674 MPa. Similarly, the hybrid composite (MB/PLA-SLP-NPK) exhibited the highest increase in Young's modulus, exhibiting an E value of 707 MPa due to the fact that the total amount of particles (SLP and NPK) is 20%. For MB/PLA series, all variations were statistically significant and the tensile behaviours seems to be mainly influenced by the reinforcing effect given by the fillers that stiffen the composites reducing their flexural deformability.

Nevertheless, it should be considered that the tensile properties of these types of systems can be optimized if a raster angle of 0° is chosen. In fact, in a previous work [198], we prepared green composites based on MB and tomato plant and we printed them with a 0° or ±45° raster angle in order to evaluate its influence on the tensile properties of the composites. Tensile test result reveal that the 0° raster angle definitively optimizes the tensile properties, confirming data from the literature, obtained on similar systems, where 0° raster angle usually optimizes tensile properties [232]. However, in this case, a raster angle of ±45° was chosen aiming to produce a more porous structure by creating separation points among adjacent raster layers. This promotes NPK release and Cu absorption, generates channels along the devices, and allows water to be conveyed inside the sample.

The experimental data obtained in tensile tests and those predicted by Halpin–Tsai model, were analyzed. E_{SLP} and E_{NPK} were determined by nanoindentation, as reported in the experimental part. Density measurements were performed on matrices, SLP and NPK. Figure 4.3.5.5d-f provides a comparison between the experimentally measured tensile moduli of MB, PLA and MB/PLA printed composites and those predicted by the Halpin-Tsai model. For MB based composites, the theoretical model satisfactorily fitted the actual tensile moduli. On the other hand, for PLA composites, the theoretical model almost fitted the tensile modulus of PLA-SLP but overestimated PLA-NPK and PLA-SLP-NPK ones. This behaviour could be attributed to the imperfect adhesion between the matrix and filler and the variable aspect ratio of the fillers, especially SLP. For MB/PLA blend composites a similar behaviour to that observed for PLA was noticed for MB/PLA-SLP and MB/PLA-NPK. However, for MB/PLA-SLP-NPK, the theoretical model clearly underestimated the actual tensile modulus. This issue could be addressed by considering that some SLP fibers were uniaxially oriented in tensile direction (see Figure 4.3.5.6), while the used Halpin-Tsai model fitted composites reinforced with randomly oriented fibers only.

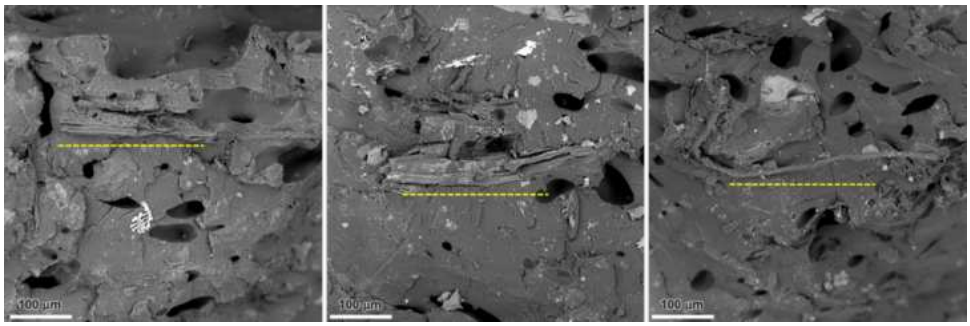

Figure 4.3.5.6 *SEM micrograph of MB/PLA-SLP-NPK cross section of printed samples fractured in liquid nitrogen lengthwise.*

The performances of SLP-filled composites in tensile test were strongly influenced by uniaxially oriented fibers. Moreover, the presence of SLP, NPK or both during the preparation of the

MB/PLA composites blend led to the production of matrices that were slightly different from the neat one, allowing to obtain a finer dispersion of one polymeric phase in the other.

6.3.5.9 NPK release and Peppas-Korsmeyer model

Conductivity measurements were used to determine the release profile of NPK from the 3D-printed samples. More in detail, electrolyte resistance was measured and correlated to the total concentration of electrolytes in solution. All tests were performed in water at 25 °C. It should be noted that this evaluation method, performed in water, may overestimate the NPK release compared to what typically occurs in soil. As a control, conductivity measurements were also performed for free NPK and for composites that do not contain NPK (see Figure 4.3.5.7a). When immersed in water, free NPK immediately achieved a plateau region, releasing all fertilizer within the first 24 hours. Devices without NPK (MB, MB-SLP, PLA, PLA-SLP, MB/PLA, MB/PLA-SLP) did not release any significant concentration of electrolytes after 30 days of immersion.

Conductivity tests were also conducted on NPK-filled composites to determine their release kinetics and the results are shown in Figure 4.3.5.7b. The NPK release kinetics of all the 3D-printed composites were characterized by three phases: a burst release in the initial 24 hours of immersion, a subsequent phase of progressive and slower release, and a final plateau region observed after 15 days of immersion, in agreement with already reported similar systems [203,233]. The sustained release of NPK fertilizer was achieved for both composites (-NPK) and hybrid composites (SLP-NPK) prepared using the three different matrices. All composites showed a significant reduction in the amount of released NPK and therefore in conductivity values, especially in the first 24 hours, compared to free NPK. Moreover, the NPK release rate could be modulated by adding SPL particles. In detail, MB-SLP-NPK showed the fastest delivery with about 80% of NPK released in the first week of the test, followed by PLA-SLP-NPK with 70% of NPK released. Other composites exhibited a lower release of NPK: after 7 days, MB/PLA-SLP-NPK released about 60% of NPK while all the

composited that not contain SLP released about 55% of it. In fact, when the samples were immersed in water, SLP particles were also released into the aqueous medium, generating channels along the devices and allowing the water to be conveyed inside the sample.

This suggests that NPK particles, found within the interior of the samples, may have a higher potential to be released. Moreover, a weak adhesion between matrix and filler would promote filler and fertilize release, thus justifying the more inhibited release of MB/PLA systems. Therefore, the results imply that, if a faster and complete release is required, SLP particles should be added to the composites and MB should be preferred as polymeric matrix. MB-SLP-NPK system, in fact, release 100% of NPK after 30 day of immersion, achieving a complete release of the fertilize. When compared to other controlled-release fertilizer devices mentioned in the scientific literature, the devices produced in this study displayed a remarkable capacity to reduce the release rate of NPK, as evident in Figure 4.3.5.7c [234–236].

The obtained NPK release data was evaluated by plotting logarithmic graphs as a function of time (Figure 4.3.5.7d) to gain a better understanding of the fertilizer release mechanism. During the firsts 24 hours of release test, burst release was observed. This phase can be divided in two sub-phases: at first the fertilizer available on composites surface was rapidly delivered (within the first 15 minutes) and subsequently the delivery was driven by diffusive phenomena (colored portion of the plot).

As the release progressed, the release curves showed an increase in slope likely due to the occurrence of swelling phenomena across the polymeric matrix possibly caused by the higher porosity induced by the printing process that reasonably led to a relevant increase in water uptake for FDM structures [203]. In the final stage, fertilizer delivery was reasonably governed by both swelling and diffusive phenomena. Peppas-Korsmeyer mathematical model [128] was used to fit the obtained release data and confirm the hypotheses on NPK release mechanism [219].

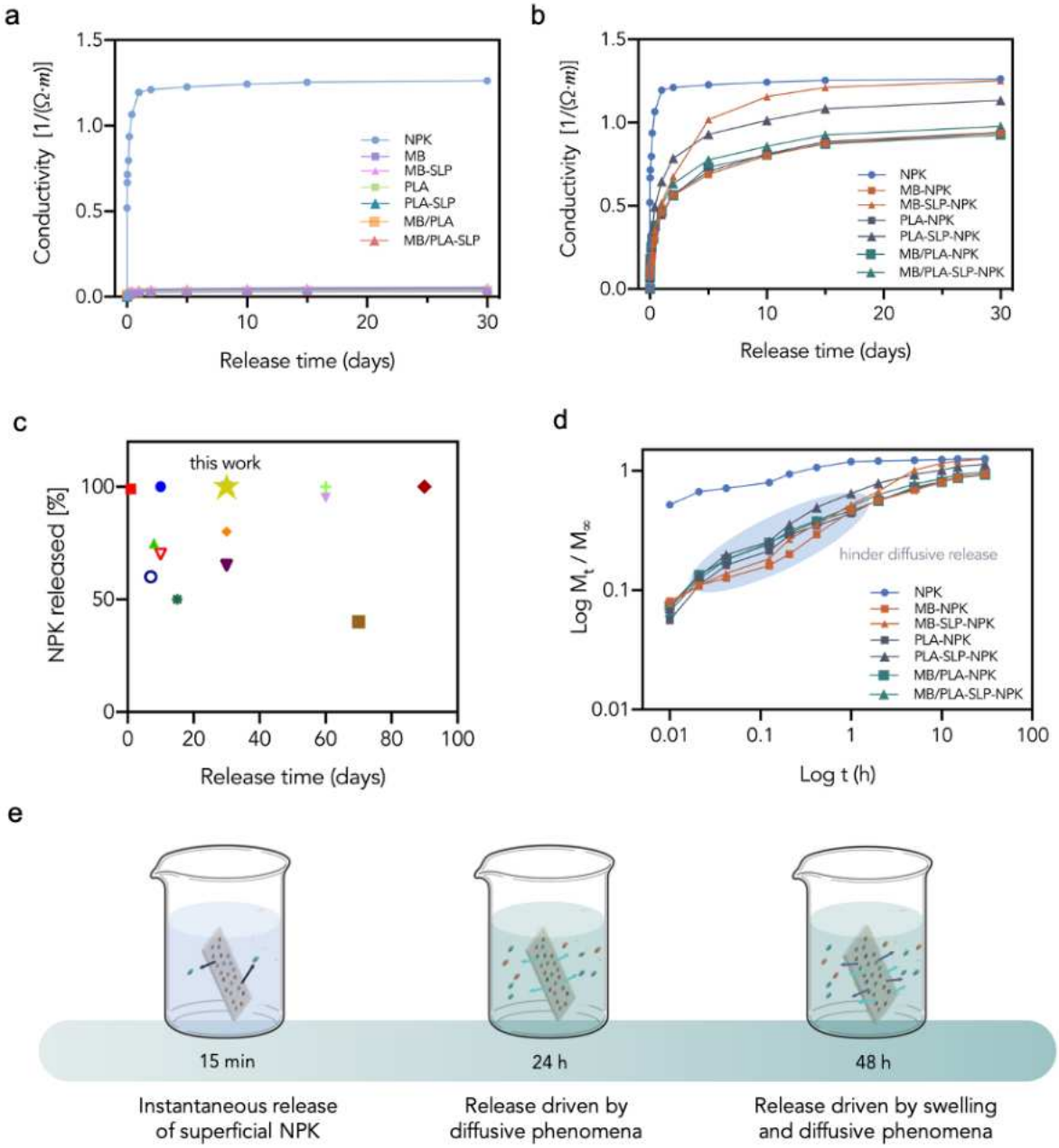

Figure 4.3.5.7 *Fertilizer release as function of time for free NPK, composites that not contain NPK (a) and 3D-printed devices (b); comparison of release rate of MB-SLP-NPK with other CRFs device obtained with different methods (c); logarithmic plots of Peppas-Korsmeyer model power law applied to the release data collected in the burst region, $M_t/M_\infty < 0.6$ was highlighted by colored portion of the plot (d); pictorial description of NPK release mechanism (e).*

This model has previously been successfully used to describe fertilizer release kinetics from CRFs devices [203,221]. The values of K and n of the different formulations were determined and reported Table 4.3.5.2.

Table 4.3.5.2 Values of slopes (n) and intercepts (k) of fitting of power law applied to the release data collected in the burst region ($M_t / M_\infty < 0.6$).

Sample	K	n
MB-NPK	0.46	0.42
MB-SLP-NPK	0.41	0.43
PLA-NPK	0.48	0.33
PLA-SLP-NPK	0.59	0.41
MB/PLA-NPK	0.48	0.32
MB/PLA-SLP-NPK	0.53	0.36

By analysing the calculated n value is possible to make assumption about the release mechanism: n approximately 0.5 indicate a diffusion-driven release; when $n = 1$ swelling occurs and when n values are between 0.5 and 1 both swelling and diffusive phenomena occurs [54]. A value of $n < 0.5$ may indicate that the matrix hinders the diffusion of the particles. As seen previously, the release curves of all composites are characterized by a burst region that represent two different effect: NPK particles readily available on the device's surface are immediately delivered in the aqueous media (t = 15 min); the real capability of the 3D-printed devices to perform a controlled release. In this second region all the systems displayed $n < 0.5$ (see n value in Table 3), therefore the fillers could indeed slow the fertilizer release. In general, in the first 24 hours, all the composites showed a hindered diffusion of the NPK, especially PLA-NPK, MB/PLA-NPK and MB/PLA-NPK ($n = 0.33$, 0.32, 0.36 respectively). CRFs composites showed an almost diffusive release mechanism, unlike NPK grains. In fact, in this latter case, NPK is immediately released for erosive dissolution. Figure 4.3.5.7e provides a pictorial representation of the release mechanism of the CRFs composites described above.

Morphology of CRFs devices were analyzed also after 30 days of soaking in water. Optical image (Figure 4.3.5.8a-f) and SEM micrograph (Figure 4.3.5.8a'-f') of the 3D-ptinted samples before (Figure 4.3.5.8a-c and 4.3.5.8a'-c') and after (Figure 4.3.5.8d-f and 4.3.5.8d'-f') NPK release were

reported. Before the release all the samples exhibited a satisfying adhesion of adjacent layer especially MB/PLA one (Figure 4.3.5.8c and 4.3.5.8c') that also showed an excellent print definition.

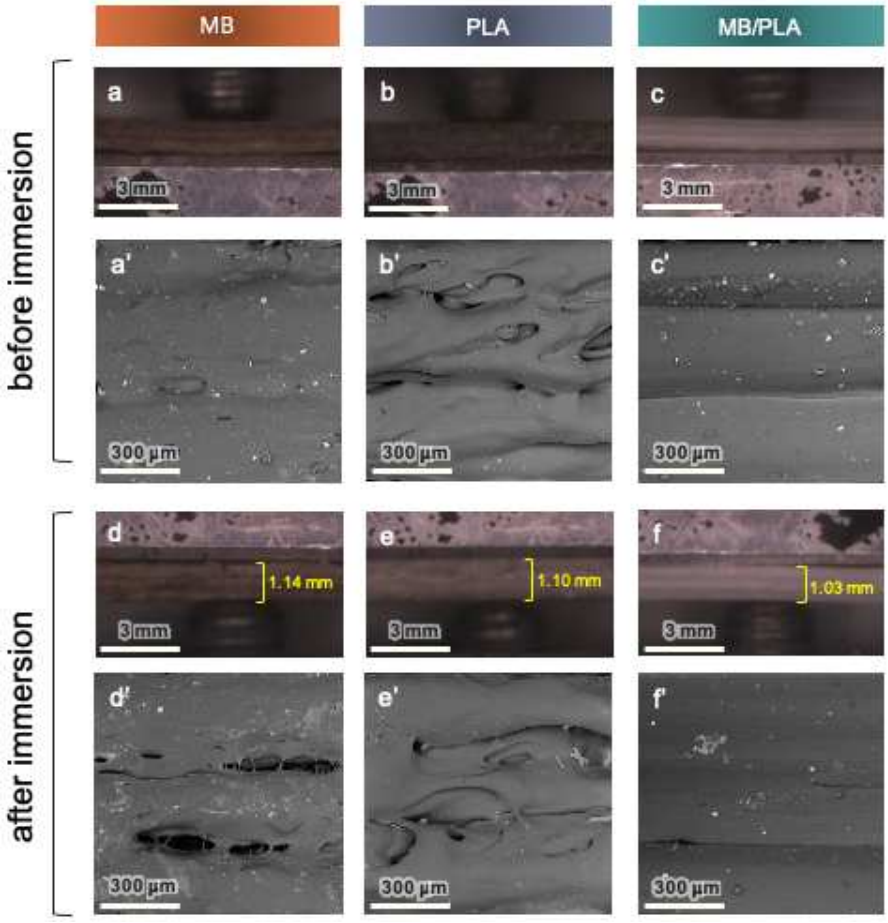

Figure 8. *Optical image (a-f) and SEM micrograph (a'-f') of good adhesion between layers in FDM samples before NPK release (a-c and a'-c') and layers detachment in FDM samples after soaking in water for 30 days due to occurrence of swelling (d-f and d'-f').*

After soaking in water for 30 days, instead, PLA sample (Figure 4.3.5.8e and 4.3.5.8e') showed a clear detachment of the layers, which was even more marked for MB one (Figure 4.3.5.8d and 4.3.5.8d'). This behaviour testifies the occurrence of swelling of the polymeric matrices confirming the supposed mechanism of release. Moreover, the PLA samples appear discoloured after release, likely due to filler loss, as observed by comparing the optical images in Figure 4.3.5.8b and 4.3.5.8e. With regard to the MB/PLA samples, the swelling phenomenon was less evident compared

to MB and PLA ones. From the SEM micrograph in Figure 4.3.5.8e', it is possible to observe that the layers do not show any detachment, but on the contrary, they appear to be better adherent to each other. Once again, this different behaviour may be caused by the greater crystallinity of the blend compared to the one of the single components. Moreover, this behaviour reasonably explains the slower NPK release obtained for the MB/PLA samples compared to that recorded for MB and PLA ones.

6.3.5.10 Cu(II) absorption

All the 3D-printed green composites were separately immersed in copper sulfate aqueous solutions for 30 days. UV spectroscopy was employed to test the Cu(II) ion removal efficiency of the samples and the outcomes are reported in Figure 4.3.5.9a. All the green composites exhibited a significant increment in the removal efficiency over the neat MB, PLA and MB/PLA that were 14, 10 and 8 % respectively. Despite plastics are considered inert, previous studies have reported the adsorption of metal ions onto various biopolymeric material, including PLA and PBAT [237,238]. The highest removal efficiency for all the three type of matrices was observed for the -SLP an -SLP-NPK composites. In detail, the maximum removal efficiency was achieved by MB-SLP-NPK with 78% of Cu removed from the aqueous solution, followed by MB-SLP with 74%. MB-NPK showed a removal efficiency of 46%. Both PLA and MB/PLA composites showed the same trend. However, in both cases, a lower removal efficiency was achieved, especially for MB/PLA composites, which exhibited the lowest values. This behaviour can be explained by considering the more compact structure of the MB/PLA samples, which remains almost unchanged after immersion in water for 30 days, preventing water from being conveyed inside the sample and thus reducing the surface area available for the absorption.

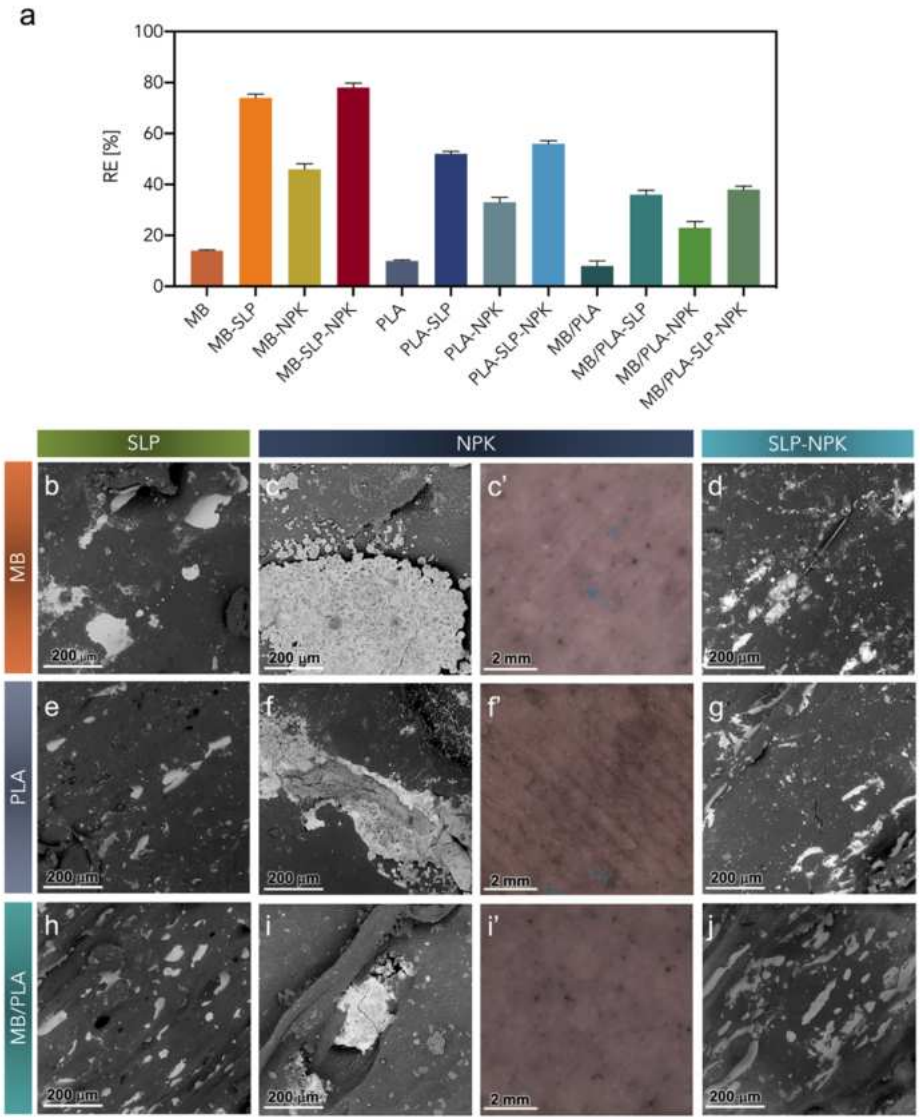

Figure 4.3.5.9 *Removal efficiency of the devices (a) and SEM micrographs (b-j) and optical images (c', f', i') of the green composites after the immersion in copper sulfate aqueous solutions for 30 days.*

These results clearly demonstrated that Cu removal efficiency of the composites could be modulated by adding SPL particles. Indeed, the composites that do not contain SLP exhibited the lowest removal efficiency values of the series. This behaviour could be reasonably explained by taking into account that, SLP contain natural compounds such as cellulose, lignin, and hemicellulose that have a high affinity for metal ions [239,240]. It is reasonable to assume that these compounds can absorb copper ions, effectively removing them from the aqueous solution. Moreover, the release of NPK particles generated channels along the polymeric matrices, facilitating the water to be conveyed inside the sample. This promoted the contact with more SLP particles, resulting in higher

removal efficiency for -SLP-NPK samples. SEM images in Figure 4.3.5.9b-j reveal that, for the -SLP and -SLP-NPK samples, the majority of the copper was absorbed by the SLP particles, identifiable as white spots in the micrographs (confirmed by punctual EDAX analysis; sample test identifying copper on white spots). On the other hand, for the -NPK samples (as shown in SEM and optical images in Figure 4.3.5.9c-c', f-f' and i-i') Cu(II) clusters formed on the polymeric matrices (confirmed by punctual EDAX analysis; sample test identifying copper on white spots) which could also be easily identified through visual inspection thanks to the pale colour of the composites.

6.3.5.11 Conclusions

Biodegradable green composites for contextual controlled soil fertilization and Cu removal were produced by 3D-printing. NPK fertilizer flour and tomato plant waste particles (SLP) were added to three different biodegradable polymeric matrices: polylactic acid (PLA), a commercial blend of biodegradable co-polyesters (Mater-Bi®, MB) and their blend (MB/PLA, 50:50). All the obtained filaments were successfully printed by FDM, in agreement with morphological analysis and rheological characterization. Morphological analysis performed on the cross section of 3D printed composite samples confirmed a relatively uniform dispersion of both natural filler and fertilizer in all composite samples. Moreover, MB and MB/PLA samples displayed good adhesion between the fillers and the matrix, unlike PLA ones where imperfect adhesion was observed. These behaviours affect the mechanical performance of the composites. For MB and MB/PLA the filler and the fertilize effectively act as reinforcement. SLP and NPK elastic moduli were evaluated by powder nanoindentation and, for the majority of the composites, the theoretical Halpin-Tsai model satisfactorily fitted the actual tensile moduli. NPK release tests showed the ability of all the obtained composites to slow the release rate of the fertilize up to 30 days. Moreover, it was possible to tune the release kinetics by changing the polymeric matrix and adding the natural filler (SLP). Cu(II) removal tests confirmed that all the green composites exhibited a significant increment in the removal

efficiency over the neat matrices. More in detail, the Cu removal efficiency could be increased by adding SPL particles that, as expected, have been very successful in absorbing copper. MB-SLP-NPK showed 100 % release of NPK after 30 days and the highest copper removal ability with 78 % of Cu removed from the aqueous solution. Moreover, the addition SLP particles leads to a decrease in the amount of polymer needed, resulting in a lower cost of the final device. In addition, the use of FDM as the selected production technique allows to reduce production time and costs. Considering the release kinetics results and Cu absorption test, it is possible to conclude that by adding tomato plant waste particles to polymeric matrices, it was possible to produce biodegradable, cost-effective and easy-to-produce devices for contextual and efficient fertilizer release and Cu(II) ions capture.

6.3.6 Green composites based on biodegradable polymers and anchovy (Engraulis Encrasicolus) waste suitable for 3D printing applications

Note: This study is ongoing, with further application tests planned to enhance and finalize the research findings.

The subsequent text and images have been fully extracted from the published article authored by the candidate "Roberto Scaffaro, Maria Clara Citarrella, Anna Catania, Luca Settanni, Green composites based on biodegradable polymers and anchovy (Engraulis Encrasicolus) waste suitable for 3D printing applications, Composites Science and Technology, Volume 230, Part 1, 2022, 109768, ISSN 0266-3538, https://doi.org/10.1016/j.compscitech.2022.109768. [226]" and are reproduced here with the necessary permissions from Elsevier. However, this paragraph also includes additional experimental results that were obtained after the publication and have not been previously reported.

Author contribution: Methodology, Software, Validation, Formal Analysis, Investigation, Data Curation, Writing - Original Draft, Writing -Review & Editing, Visualization.

6.3.6.1 Abstract

Every day large amounts of fish waste are produced and grossly discarded in markets around the world causing environmental and hygiene issue. The use of these scraps for the production of materials with higher added value can definitely contributed to solve this problem. In this work, 10% and 20% of anchovy fishbone powder (EE), obtained by market waste, were microbiological and mechanical tested and subsequently added to polylactic acid (PLA) and to a commercial blend of biodegradable co-polyesters (Mater-Bi®). Rheological characterization suggests the potential printability of all prepared composites filaments. 10% EE filled composites showed outstanding printability. Morphological analysis confirmed the obtainment of good dispersion of the filler and the excellent adhesion of EE particles with the matrices in the composites filament and in 10% printed samples. The filler effectively acted as reinforcement in flexural and impact test: for MB and PLA, the addition of EE leads to an increase of flexural modulus of about 23% and 32% respectively. In tensile test both composites turn out to be influenced by the oil contained in the filler that act as plasticizer: the elongation at break of MB increased by 364% when 10% of EE was added. The experimental data obtained by tensile tests showed an opposites behaviour than those predicted by Halpin–Tsai model, presumably due to the presence of residual fish oil acting as internal slipping agent.

6.3.6.2 Preparation of EE flour, processing of EE composites and 3D printing

Firstly, anchovy fishbone flour (EE) was obtained by anchovy scraps collected directly at the market following the process reported in Scheme 4.3.6.1. Fish wastes were first immersed in water and cleaned individually at room temperature. Subsequently, they were air dried on paper and then oven-dried for 30 minutes at 100 °C at room pressure. After that, they were removed from the oven and let to air dry for 100 hours at room temperature. The dried fishbones were then finely ground for 3 min in a mixer and the obtained particles were sieved selecting the mesh sizes under 75 μm. Particle size were selected to be suitable for the 3D printer trying to prevent nozzle obstruction. In order to achieve good printability and homogeneous dispersion of the filler, two different amounts of fillers (10 wt% and 20 wt%) were tested.

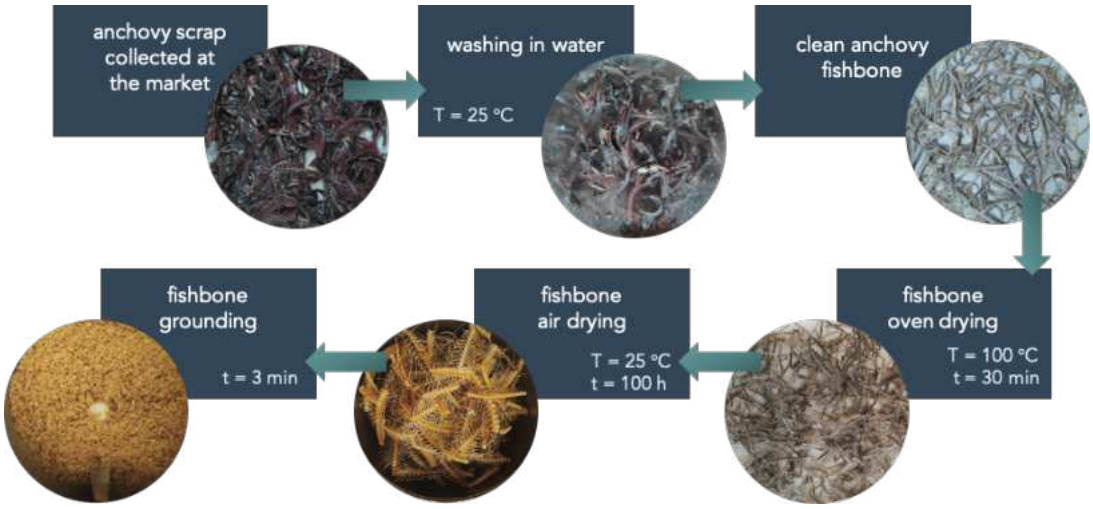

Scheme 4.3.6.1 *Schematic representation of anchovy fishbone flour preparation.*

Four different formulations were prepared by melt mixing 10 or 20 wt% of EE to MB and PLA in a Brabender internal mixer. Pure MB and PLA were melt mixed under the same conditions for comparison. Both the obtained blends and the pure matrices were then extruded. In order to obtain filaments suitable to be used for the 3D printer (diameter ~ 1.75 mm), the output extrudate were then

drawn using a conveyor belt system. The composite filaments were named according to matrix and their EE contents: MB/EE10, MB/EE20, PLA/EE10 and PLA/EE20. In addition, neat MB and neat PLA filaments, used as a control, were extruded using the same parameter.

For each neat matrix and EE composites, the following specimens were designed and printed using a Sharebot Next Generation (Italy) 3D printer: 60 mm × 10 mm × 1 mm for tensile tests, 60 mm × 13 mm × 3 mm for flexural tests and 80 mm × 13 mm × 3 mm for impact tests. A rectilinear infill pattern with a 0° raster angle was chosen to optimize the tensile properties while ± 45° raster angle was chosen to optimize mechanical properties in flexural and impact tests; 80% infill rate and 45 mm/s printing speed were chosen as a compromise solution between better properties and higher production rate.

6.3.6.3 EE powder microbiological analysis

Viable count technique did not show the presence of any pathogenic bacterium or mold. Detectable levels of food contaminants were only detected among yeasts and TMM. Barely, yeasts developed at levels of 102 colony forming units (CFU)/g, while TMM at little higher levels (103 CFU/g). Both groups represent environmental microorganisms [241–243] and the levels registered are quite negligible in terms of risks for humans. Although fishbones from various edible species have been characterized for their content in lipids, proteins, minerals and ash [244], this is the first work aimed to characterize the microbiological profile of this fish by-product.

6.3.6.4 EE particles characterizations

Morphology of EE particles were analyzed by SEM. Optical image and relevant micrographs of the natural filler are shown in Figure 4.3.6.1a and 4.3.6.1b respectively. EE particles displayed a peculiar morphology: the filler is composed by heterogeneously shaped particles that form heaps of

different dimensions due to the presence of oily phase contained in the fishbone powder. Elemental composition of EE particles (Figure 4.3.6.1c) revealed that calcium and phosphorus were the main mineral components, in accordance with the scientific literature [245,246]. The chemical composition of anchovy fishbone powder was also analyzed through FTIR spectroscopy and results are reported in Figure 4.3.6.1d. In the spectra the characteristic bands of group of PO_4^{3-} can be easily identifiable in the peaks at 1070, 1015 and 860 cm^{-1}, according to previous studies on anchovy fishbone [246]. Peaks at 1533 and 1628 cm^{-1} can be assigned to the amide-II (bending vibration of N–H groups and stretching vibrations of C–N groups) and amide-I (C=O stretching/hydrogen bonding coupled with COO) respectively [245]. The band at 3251 cm^{-1} is assigned to –OH stretching [246]. Band at 3016 cm^{-1} is assigned to C–H stretching of cis-alkene (–HC=CH–) that represent unsaturated fatty acids in the oil, while bands at 2921 and 2851 cm^{-1} are assigned to stretching vibrations of $–CH_2$ of methyl and methylene groups of lipids in anchovy oil and band at 1740 cm^{-1} is assigned to C=O stretching of ester groups [247]. The presence of these latter bands certifies a residual presence of anchovy oil in the filler.

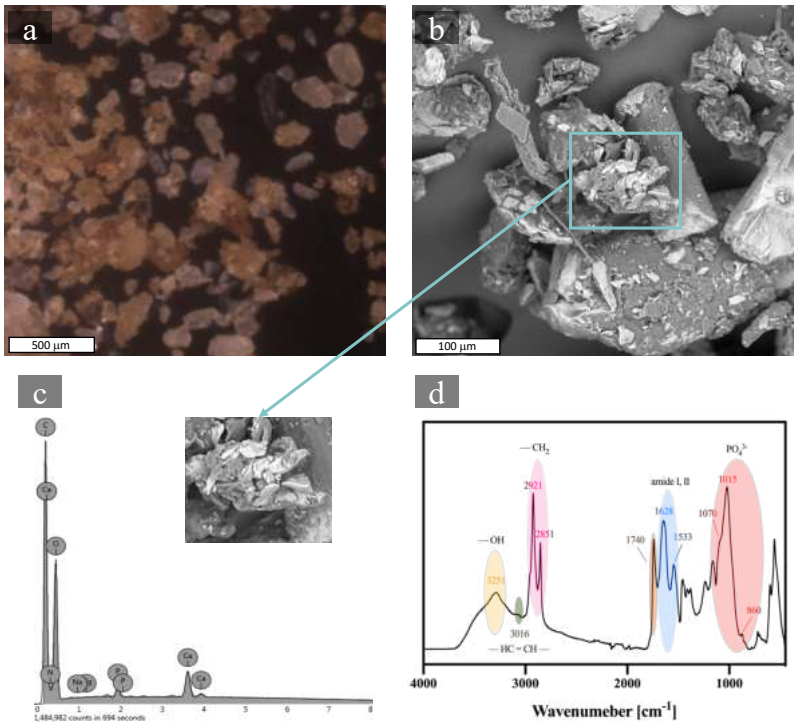

Figure 4.3.6.1 *(a) optical image; (b) SEM micrograph; (c) EDS spectrum; (d) FTIR spectra of EE powder.*

6.3.6.5 Processing and morphological analysis of EE composites filament

MB and PLA with 10% or 20% of EE were preliminary melt mixed for two minutes at 160 and 190 °C respectively and the four obtained formulations were ground into pellets and subsequently extruded in filaments. The mixing process enable to produce pellets in which the filler is already well dispersed in the polymeric matrices allowing to obtain, in the extrusion process, composites filament with homogeneous composition and shape. All filament displayed a quite regular cylindrical shape with a diameter suitable for 3D printing (~ 1.75 mm) except for MB/EE20 for which it is possible to notice uneven edges and the presence of many voids along its entire length. Morphology of composites filaments were also analyzed by SEM and micrograph of their cross section are reported in Figure 4.3.6.2a-d. It is possible to observe an almost homogeneous dispersion of filler in all filament samples with limited voids. Moreover, EE particles appear well embedded in the polymeric matrices and presenting a good interfacial adhesion with them. However, more agglomerations of anchovy fishbone were present in composites filament with 20% of EE (Figure 4.3.6.2b, d).

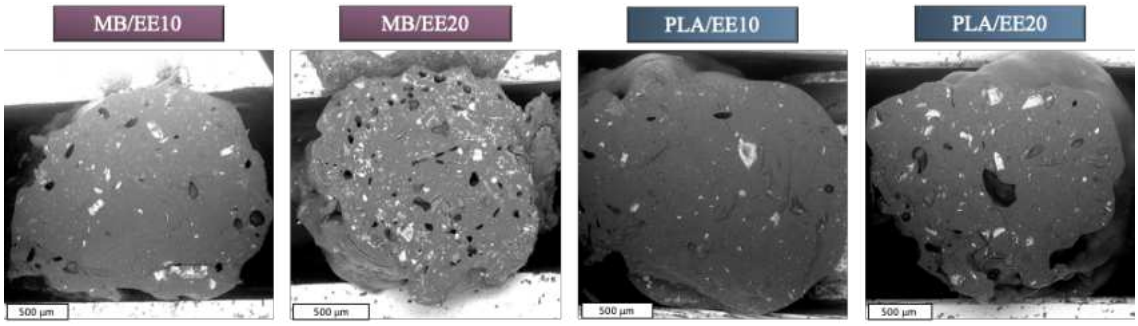

Figure 4.3.6.2 *SEM micrograph of composites filaments cryo-fractured cross section.*

6.3.6.6 FTIR spectroscopy and rheological behaviours of EE composites filament

The effects of EE addition to MB and PLA polymeric matrices have been analyzed through FTIR spectroscopy and outcomes are reported in Figure 4.3.6.3. In MB series (Figure 4.3.6.3a), the influence of the filler on the chemical groups of the composites can be observed due to the presence of band at 1628 cm^{-1}, assigned to amide-I, in EE and MB/EE spectra but not in neat MB ones and

the presence of the band at 1740 cm^{-1}, assigned to C=O stretching of ester groups. Moreover, bands at 2921 and 2851 cm^{-1} (stretching vibrations of $–CH_2$ of methyl and methylene groups of lipids in anchovy oil) in the MB/EE spectra appear more evident if compared with neat MB one, reasonably because of the presence of the filler and its oil. For PLA series (Figure 4.3.6.3b), a band at 3251 cm^{-1}, assigned to –OH stretching, can be observed in EE and PLA/EE spectra but not in neat PLA ones. The same behaviour can be noticed also for bands at 1533 and 1628 cm^{-1} (amide-II and amide-I respectively). The presence of these peaks in PLA/EE sample confirm that the addition of filler leads to some change in the matrices response and behaviour, reasonably due to the presence of the oily phase, that may have influenced its viscosity of the composites.

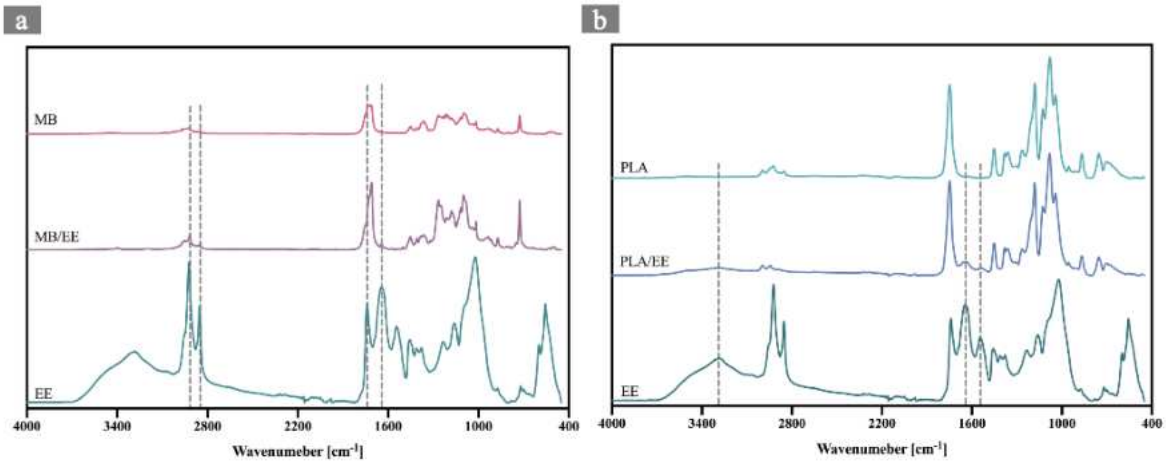

Figure 4.3.6.3 *FTIR spectra of the effect of EE addition on MB composites (a) and PLA composites (b).*

In order to go deeper inside this aspect and considering that printability is strongly related with their rheological behaviours [199], rheological analysis of the extruded filaments were performed and results are reported in Figure 4.3.6.4.

Neat MB (Figure 4.3.6.4a) displays a pseudoplastic behaviour. In MB/EE composites the appearance of yield in the low frequency region can be noted probably due to a reinforcing effect of the filler. Moreover, in the high frequencies region, viscosity decreases on increasing EE content, in

agreement with what occurs in other similar composites structured in the melt [248]. Neat PLA (Figure 4.3.6.4b) displays a Newtonian behaviour at lower frequencies regions and a slight shear thinning at higher ones. In PLA/EE composites, even if a slight change in the shape of the curve can be noted due to the reinforcing effect of the filler, it seems to be predominant, in the whole frequency range, the effect likely given by the oily component contained in the filler that lead to a lowering of viscosity value in the whole investigated range of frequencies. It is necessary to consider that, in general, rheological behaviour of fish oil is characterized by a shear-thinning non-Newtonian behaviour with a strong decrease in viscosity on increasing the shear rate [249–251]. Moreover, this behaviour is enhanced reasonably due to the decomposition of the lighter oil components that occurs at 240 °C [249,250]. Based on our previous works [190,202], all composites formulations displayed viscosity values potentially compatible with FDM printing process. Shear-thinning properties, in fact, improving filament printability for 3D printing (FDM) [252].

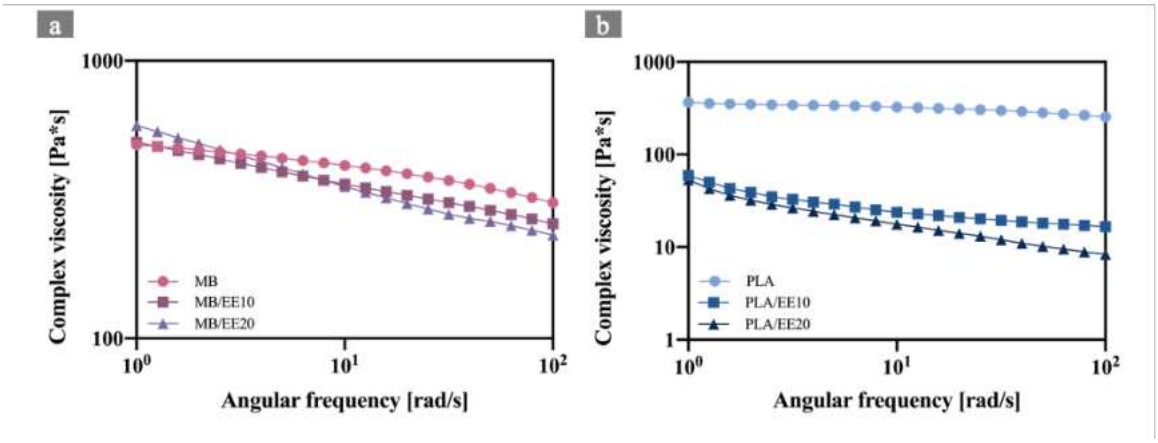

Figure 4.3.6.4 *Complex viscosities of MB/EE composites (a) and PLA/EE composites (b) performed at 160 °C and 240 °C respectively.*

6.3.6.7 Mechanical properties of EE composites filament

Filament printability is also related with their mechanical properties [253]. Tensile tests were performed on composites filaments and the values of elastic modulus (E), tensile strength (TS) and elongation at break (EB) are reported in Figure 4.3.6.5. Tensile properties of MB composites

filaments (Figure 4.3.6.5a) were affected by the filler content and their morphological structure. The addition of 10% of filler leads to a slight decrease in E and TS and a remarkable increase in EB (going from 185.5 to 284 %) probably due to the predominant plasticizing effect of the oily phase compared to the reinforcement given by EE powder (all variations were statistically significant). However, when 20% of EE is added to the matrix, an inversion of mechanical properties behaviour of the composites filament can be noted. Elastic modulus value of MB/EE20 drastically increase if compared with the pure MB one (going from 48.7 to 183 MPa), while EB decrease to 112.7 % (both variations were statistically significant). This behaviour could be reasonably ascribed to a dominant reinforcement effect of the filler over the plasticizing oil and to the poor morphology of the extruded filament, full of voids along its entire length. This latter is likely responsible of the observed EB drop. The non-uniform and void-rich structure of MB/EE20, moreover, suggests that the composite is unlikely to be printed. For PLA based systems, the situation is different, the addition of EE to PLA matrix lead to a monotonically increase in E value and a contextual monotonically decrease in TS and EB on increase the filler content (Figure 4.3.6.5b; all variations were statistically significant). In this case, EE powder effectively acted as reinforcement deeply prevailing on the oil plasticization. Furthermore, moving from 10% to 20% of filler added, no dramatic difference can be noted in TS and EB value, only the increase in E can be considered significant.

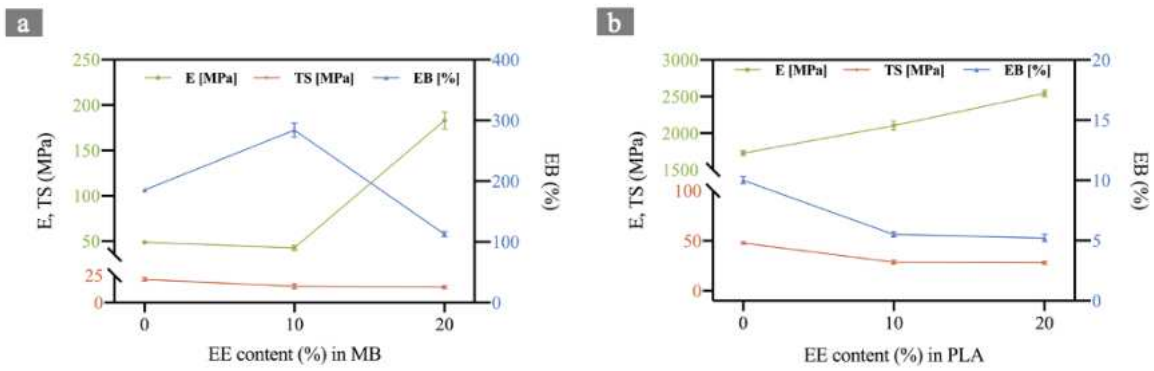

Figure 4.3.6.5 *Effects of EE contents on mechanical properties of MB/EE (a) and PLA/EE (b) composites filaments.*

6.3.6.8 EE composites filament printing process

MB/EE and PLA/EE composites filament (diameter: ~ 1.75 mm) with 10% and 20% of anchovy fishbone powder were successfully extruded. Also pure MB and PLA filaments were produced with the same procedure for comparison. MB/EE10 and PLA/EE10 composite filaments were able to be 3D printed for FDM into flat (Figure 4.3.6.6a) or geometrically complex (Figure 4.3.6.6b) products. For pure MB, MB/EE10, PLA and PLA/EE10 the printing process proceeded smoothly and no clogging of the nozzle was observed. MB/EE10 can be easily printed using the same temperature usually adopted for pure MB (160 °C). PLA/EE10, instead, needs higher temperatures to be fluidly printed than that commonly used for pure PLA (190-220 °C). After some trial, it was found out that the optimum temperature for PLA/EE10 printing is 240 °C.

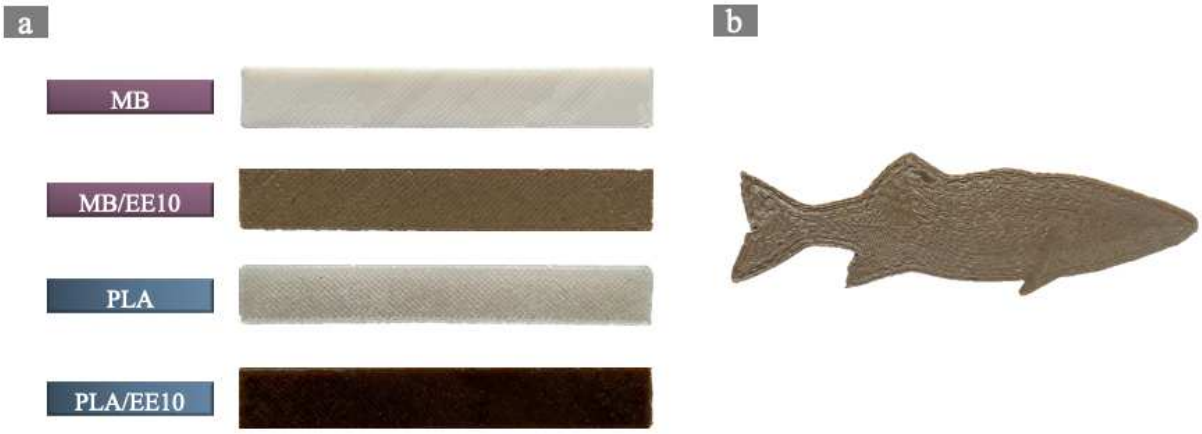

Figure 4.3.6.6 *Specimen for impact test 3D printed for FDM (a) and product with complex geometry printed with MB/EE10 composites filament (b).*

As predicted by observing the morphology of the filament, MB/EE20 cannot be printed for FDM. The filament, in fact, due to the voids present along its entire length, is not strong enough to push itself inside the melting chamber but, instead, it bends on itself, twisting around the gear. PLA/EE20 composite filament can actually be printed for FDM, as predicted by its good mechanical and rheological behaviour. However, clogging of the nozzle occurs sporadically due to the high filler content. This occlusion, actually, resolves itself after a few seconds, probably thanks to the presence

of the oily phase which facilitates the blocked anchovy particles to get out of the nozzle. This behaviour, however, leads to the production of defective specimens.

6.3.6.9 Morphological analysis of EE 3D printed composites

The effects of the addition of EE filler on the morphology of 3D-printed MB/EE10 and PLA/EE10 composites are shown in Figure 4.3.6.7. MB/EE10 and PLA/EE10 exhibited relatively uniform filler dispersion with limited voids (Figure 4.3.6.7a and c respectively). Moreover, EE particles appear well embedded in the polymeric matrices and a good interfacial adhesion between anchovy fishbone particles and the polymeric matrices can be noticed in Figure 4.3.6.7b and 4.3.6.7d.

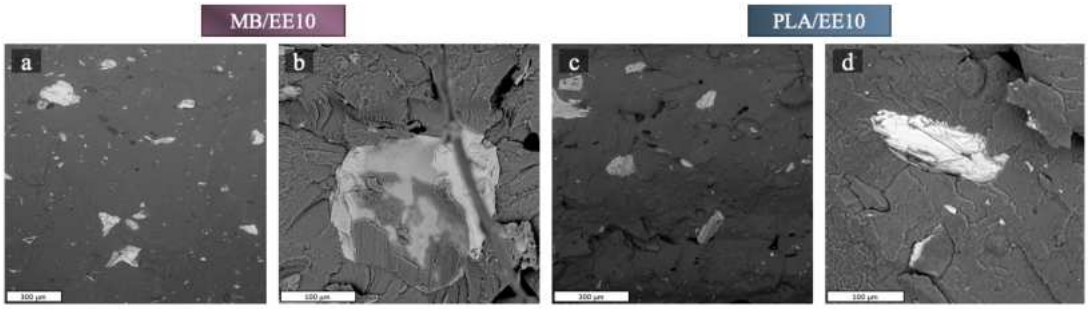

Figure 4.3.6.7 *SEM micrograph of cryo-fractured cross-section of 3D-printed MB/EE10 (a) and PLA/EE10 (c) with a relatively close-up of an embedded EE particle (b and d respectively).*

In Figure 4.3.6.8, it is possible to notice that good adhesion between layers was achieved for samples printed with raster angle of ± 45° (Figure 4.3.6.8a) and 90° (figure 4.3.6.8b) both. Moreover, when a raster angle of ± 45° is selected, it is possible to obtain a porous structure by creating separation points among adjacent raster layers. The possibility of obtaining porous structures can be of particular interest in order to obtain devices to be potentially used for controlled release applications [54,203].

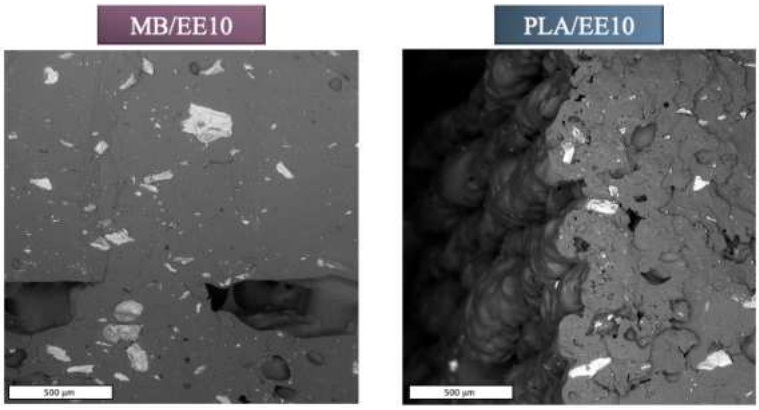

Figure 4.3.6.8 *SEM micrograph of cryofractured cross-section of MB/EE10 printed with raster angle of ± 45° and PLA/EE10 printed with raster angle of 90°.*

6.3.6.10 Mechanical properties of PLA-EE and MB-EE 3D printed composites

In order to evaluate the influence of the filler on the mechanical performance of the composites, tensile, flexural and impact tests were performed on printed samples and outcomes are reported in Figure 4.3.6.9, 4.3.6.10 and 4.3.6.11 respectively. In Figure 4.3.6.9a can be noted that the addition of 10% of EE to MB lead to a decrease in E and TS but the ductility of the composite displayed a strong increase if compared with pure matrices, with EB value going from 55.6 to 258% (all variations were statistically significant), reasonably due to the presence of the oily phase in the filler that act as plasticizer. Pure MB and MB/EE10 fractured cross-section were analyzed with SEM. Micrograph of the neat matrix (Figure 4.3.6.9b) and the EE composite (Figure 4.3.6.9c) showed both a typical ductile fracture. Likewise, the addition of 10% of anchovy fishbone to PLA (Figure 4.3.6.9d), leads to a decrease in E (going from 2885 to 2437 MPa) and TS value and a slight increase in ductility, with EB going from 3.8 to 5.6 % (all variations were statistically significant). From SEM micrographs of fractured cross-section of the printed sample, in fact, could be noted that PLA (Figure 4.3.6.9e) displayed a typical brittle fracture while PLA/EE10 (Figure 4.3.6.9f) showed a more ductile fracture. Considering these results, tensile performances of MB/EE10 and PLA/EE10 composite seem to be mainly influenced by the oily phase contained in the filler that effectively act as plasticizer improving composites elongation. The existing differences in mechanical behaviours of extruded-

filaments and 3D-printed samples can be mainly attributed to voids and grooves present in the specimen that can induce inter-layer weakness lowering composites strength [254,255].

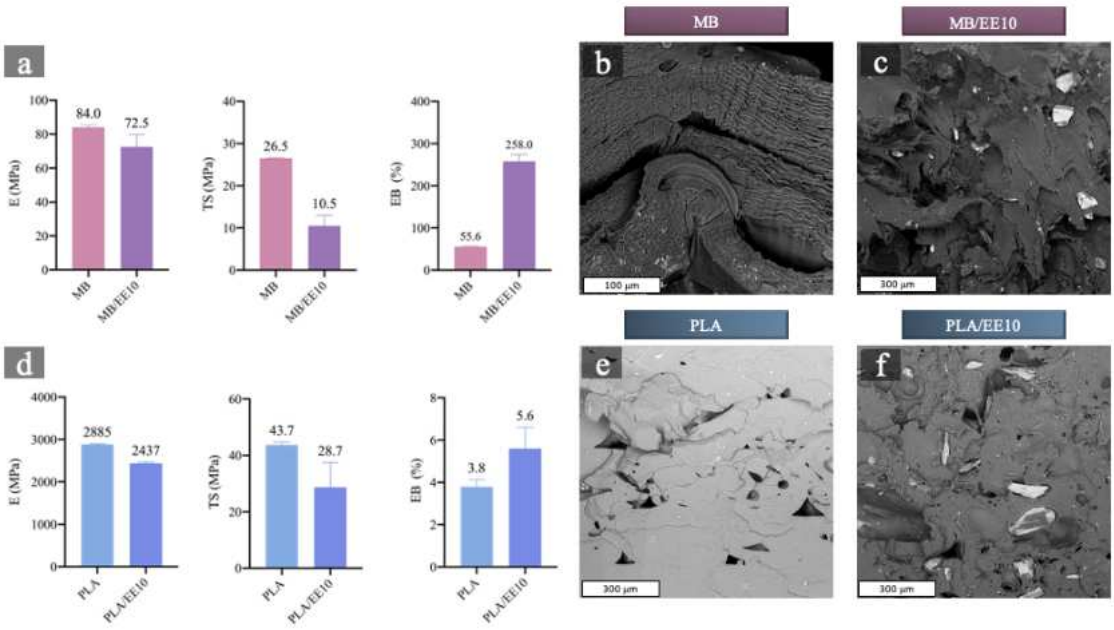

Figure 4.3.6.9 *Elastic modulus (E), tensile strength (TS), and elongation at break (EB) of 3D-printed MB and MB/EE10 (a) and relative SEM micrograph of their fractured cross-section (b, c); elastic modulus (E), tensile strength (TS), and elongation at break (EB) of 3D-printed PLA and PLA/EE10 (d) and relative SEM micrograph of their fractured cross-section (e, f).*

In Figure 4.3.6.10a the values of flexural modulus (E), flexural strength (FS) and flexural break (FB) of EE composites is reported. Only flexural modulus is present for MB series since no fracture occurs either for MB or MB/EE10 due to their ductile behaviour. However, a slight but statistically significant increase of E can be noted when 10% of EE is added to MB. The same behaviour can be found in PLA/EE10, in which the addition of the filler leads to an increase of flexural modulus and flexural strength and a slight decrease in flexural break (all variations were statistically significant). Flexural performance of PLA/EE10 seems to be mainly influenced by the reinforcing effect given by the filler that stiffen the composite reducing its flexural deformability.

Optical images and SEM micrographs of PLA and PLA/EE10 flexural fracture cross section are reported in Figure 4.3.6.10b, 4.3.6.10c and Figure 4.3.6.10d, 4.3.6.10e respectively. In each of

them it is possible to clearly distinguish zones that were under compression (top) and tensile (bottom) during the flexural test. In detail, SEM micrograph of PLA/EE10 after flexural testing shows regular fracture of particles all over the matrix (Figure 4.3.6.10e) with limited voids confirming good interfacial adhesion between anchovy fishbone particles and the polymeric matrix. However, some voids, also present in neat PLA sample (Figure 4.3.6.10c), are inevitably created between rasters and layers due to the peculiar morphology imparted by the 3D printed process itself [256]. The fracture of the EE particles in the matrix confirms that the stress is well propagated between the filler and PLA matrix, resulting in an increase flexural modulus and flexural strength [257].

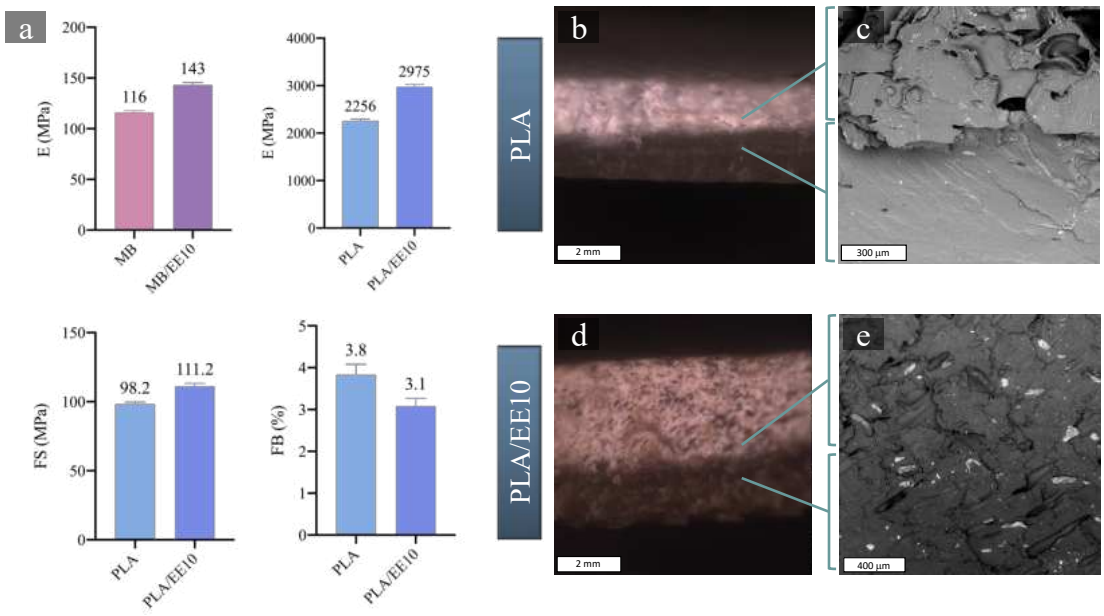

Figure 4.3.6.10 *Flexural modulus (E) of 3D-printed MB and MB/EE10 and flexural modulus (E), flexural strength (FS) and flexural break (FB) of 3D-printed PLA and PLA/EE10 (a). Optical images (b, d) and SEM micrographs (c, e) of 3D-printed PLA and PLA/EE10 flexural fracture cross-section.*

Impact properties of EE composites were measured by Charpy tests and result are reported in Figure 4.3.6.11. Again, no fractur occur either for MB or MB/EE10 due to their ductile behaviour. The addition of 10% of anchovy fishbone scraps to PLA lead to an increase in impact strength (statistically significant) as shown in Figure 4.3.6.11a. SEM micrograph of PLA (Figure 4.3.6.11b) and PLA/EE10 (Figure 4.3.6.11c) after impact testing shows that, also in this case, a regular fracture of particles all over the matrix is obtained confirming their contribution in impact strength increase.

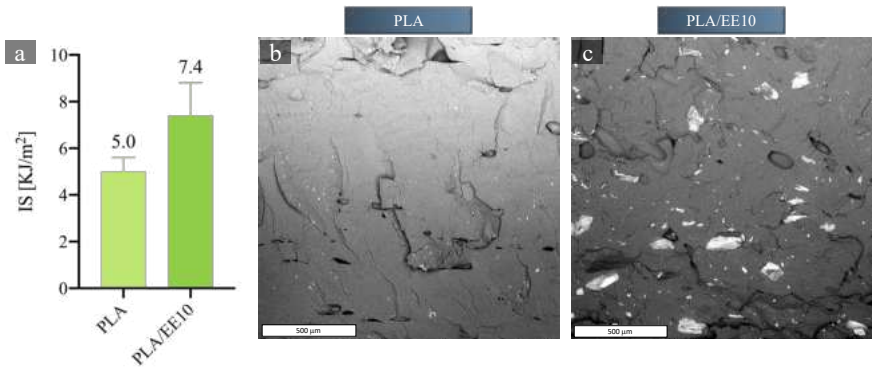

Figure 4.3.6.11 *Impact strength (IS) of PLA and PLA/EE10 (a) and relative SEM micrograph of their impact fractured cross-section (b, c).*

6.3.6.11 Halpin-Tsai model

The experimental data carried out by tensile tests on 3D printed EE composites were compared with those predicted by Halpin–Tsai model, for composites reinforced with fibers randomly oriented. E_f was determined by performing tensile tests on 20 dried fishbones taken from the spine column of different anchovy waste, prior to be grounded, and it was found to be equal to 640 ± 3.6 MPa. Density measurements were performed on MB, PLA and EE giving as a result 1.26 ± 0.0, 1.27 ± 0.0, 1.69 ± 0.1 g/cm^3 respectively. Aspect ratio (l/d) of anchovy fishbone particles tour out to be equal to 2.17 ± 0.8. Figure 4.3.6.12 provides a comparison between the tensile moduli experimentally measured for MB/EE10 and PLA/EE10 printed composites and those predicted by the Halpin-Tsai model and the above reported data. Can be noted that this model is not able to describe the behaviour of either MB or PLA EE composites. These could be easily explained considering that Halpin-Tsai model only takes into account the effect of the filler, intended as a solid particle, for predicted the mechanical behaviour of the composites. However, EE composites performance in tensile test are strongly influenced by the oil phase contained in the anchovy powder that is not considered in the model. The model, therefore, overestimated mechanical performance of the composites ignoring the plasticizing effect given by the oil.

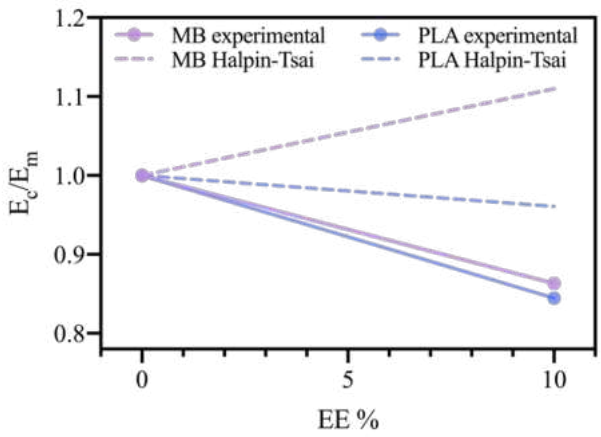

Figure 4.3.6.12 *Comparison of Halpin–Tsai model (dashed lines) and experimental results (solid lines) for tensile modulus of MB/EE10 and PLA/EE10 3D printed samples.*

6.3.6.12 Cu(II) absorption (ongoing tests)

PLA/EE10 and MB/EE10 3D-printed green composites were separately immersed in copper sulphate aqueous solutions for 30 days. UV spectroscopy will be employ to test the Cu(II) ion removal efficiency of the samples.

6.3.6.13 Conclusions

In this work, innovative and green composites filaments were produced by adding 10 or 20% of anchovy fishbone waste to two different biopolymeric matrices (PLA and MB). For both matrices, formulation with 10% of filler turned out to be easy printable for FDM. Moreover, considering that:

a) microbiological analyses revealed that anchovy fishbone powder does not contain microorganisms which, by type or quantity, may represent a risk to human health and, therefore, the filler is safe to handle;
b) all prepared composites formulation displayed viscosity values potentially compatible for be processed by 3D printing;
c) good interfacial adhesion between anchovy fishbone particles and the polymeric matrices is obtained;

d) in tensile performance the addition of 10% of fishbone waste allow to improve elongation (in both matrices) due to the anchovy oil that act as plasticizer;
e) consideration about mechanical behaviour were confirmed by Halpin–Tsai model;
f) as regards flexural and impact performance of the composites the filler proved to reinforce the composites leading to an increase of flexural modulus, flexural strength and impact strength;

utilizing 10% of anchovy fishbone waste to produce composite filaments for 3D printing is a feasible and value-added prospect of dispose such scraps that usually accumulate in fish markets, generating bad odours and attracting insects, with a high risk of bacterial proliferation. The produced composite filaments, in fact, can be employed for the manufacture for 3D printing (FDM) fields that need biodegradable, renewable and cost-effective raw material.

6.3.7 3D-printed bio-composites based on PLA and Juncus Maritimus Plant for heavy metals removal

Note: In this study characterizations and heavy metals removal tests are currently ongoing.

6.3.7.1 Abstract

Heavy metal contamination poses a significant threat to both environmental and human health due to its persistence, bioaccumulation, and toxicity. Addressing this issue requires efficient and sustainable solutions for heavy metal removal from soil. In this study, biodegradable and environmentally friendly composite were developed by combining polylactic acid (PLA) *with Juncus Maritimus* plant (JMP), that is naturally abundant in salt marshes. The JMP stems were utilized in their entirety and as separated outer sheaths and inner cores to explore the influence of morphological and compositional variations on metal adsorption efficiency. JM fillers (10% by weight) were mixed with polylactide acid (PLA) to produce composite filaments, followed by the fabrication of 3D-printed devices using fused deposition modelling (FDM). The materials will be characterized in detail, with analyses of their morphology, rheological properties and mechanical behaviour. Additionally, the tensile properties of the composites will be modelled using the Halpin-Tsai equations to predict the contribution of JM fillers to the mechanical performance of the composites. Preliminary tests assessed their printability and structural integrity. The adsorption capacity of the 3D-printed devices will be evaluated using heavy metals solutions (Cu, Mn, Ni, and Fe) under controlled conditions. The removal efficiency will be monitored over 30 days.

6.3.7.2 Preparation of JM fibers

In this study, the stems of JMP were processed in two configurations: as whole stems and separated into their outer sheath and inner core. The outer sheath, primarily composed of lignin and cellulose, provides structural rigidity, while the inner core contains polysaccharides and proteins,

giving it a more porous and flexible nature [258,259]. These structural and compositional differences were hypothesized to influence the heavy metals adsorption capacity. The JMP were firstly cleaned by immersing them in water at room temperature. After cleaning, the plants were dried under sun light for 7 days and then further oven-dried overnight at 40°C to ensure complete drying. The whole stems (JMP) the outer sheath (JMPS) and the inner core (JMPC) were separated, chopped and then ground in a ball milling for 30 minutes at 20 Hz. The obtained product was composed of powder and fibers. The fibers were separated from the powder sieving them selecting a mesh size under 500 μm aiming to achieve a smooth printing avoid nozzle clogging during the 3D printing process (diameter of the nozzle is 0.4 mm).

6.3.7.3 Preparation of composites filaments

In order to produce the composites filaments, as first step 10 % of JMP, JMPS and JMPC were separately mixed with PLA. The neat PLA was also processed under identical conditions for the purpose of comparison. The obtained formulations were then extruded aiming to obtain filaments with a diameter of ~ 1.75 mm. The filaments were named based on the selected matrix and their type of filler as: PLA/JMP, PLA/JMPS and PLA/JMPC.

6.3.7.4 Characterization and heavy metal removal test

The characterization and heavy metals removal tests are currently ongoing.

Conclusions

This thesis has explored the development of bio-polymeric devices for the removal of pollutants from air, water, and soil, emphasizing sustainability and the valorisation of natural waste biomass. By integrating biodegradable polymers such as PLA and Mater-Bi® with fillers derived from vegetal and animal waste, innovative bio-composite membranes and 3D-printed devices were fabricated using advanced manufacturing techniques, including electrospinning, solution blow spinning, and 3D printing. The results demonstrated that these materials effectively capture particulate matter from the air, adsorb dyes, oils, and greases from wastewater, and facilitate soil remediation by trapping heavy metals while simultaneously providing controlled fertilize release.

One of the major strengths of this work lies in its sustainability approach, as the use of biodegradable materials combined with waste-derived fillers significantly reduces environmental impact and promotes circular economy principles. The ability to repurpose biomass waste into functional materials for pollution remediation highlights an innovative and eco-friendly alternative to conventional synthetic filtration technologies. Moreover, the integration of advanced fabrication methods allowed for the precise control of structural properties, leading to high-performance filtration systems adaptable to different environmental contexts.

However, despite these advantages, one of the main limitations concerns the hydrolytic degradation of the biodegradable polyesters used in the study. Since these materials are susceptible to hydrolysis in humid environments, their long-term stability is limited, particularly in aqueous applications [260,261]. Experimental observations showed that after approximately five reuse cycles, the filtration/removal efficiency of the devices began to decline, likely due to both fouling effects and polymer degradation. This issue represents a challenge for the widespread application of these bio-based filters, as their durability remains a critical factor.

To address this limitation, the literature suggests several strategies that could be explored in future studies. Increasing the crystallinity of the polymer matrix could reduce its susceptibility to hydrolysis, as more crystalline regions tend to be less permeable to water. Another promising approach involves the incorporation of natural additives, which may enhance mechanical properties while slowing down the degradation process. Additionally, the use of eco-friendly chemical modifications or surface treatments could be investigated to create a protective barrier that delays hydrolysis while maintaining the material's biodegradability. These potential improvements align with the broader goal of developing sustainable and efficient filtration systems without compromising environmental compatibility [262].

In conclusion, while some challenges remain regarding the long-term stability of biodegradable polyesters, this research provides a solid foundation for the development of advanced bio-based filtration devices. By integrating sustainable materials, innovative processing techniques, and environmental remediation applications, this work contributes to the growing field of eco-friendly technologies for pollution control.

Future work

This research has established a solid foundation for the development of bio-polymeric filtration devices for pollutant removal in air, water, and soil. However, several aspects remain to be explored to enhance the efficiency and applicability of these systems. Future work will focus on completing ongoing studies, improving the hydrolytic stability of biodegradable polyesters, and integrating advanced fabrication techniques with artificial intelligence to optimize filtration performance. A key challenge to address in future studies is the hydrolytic degradation of biodegradable polyesters, which limits their long-term stability and reusability. Since these materials are inherently susceptible to hydrolysis, particularly in humid environments, research efforts will focus on strategies to enhance their resistance while preserving their eco-friendly nature. The incorporation of natural additives, preferably sourced from agro-industrial waste, represents a promising approach. Specific attention will be given to bio-based fillers capable of reinforcing the polymer matrix, hydrophobic agents that can reduce water absorption, and surface modifications that slow down degradation. These solutions could extend the life of bio-polymeric device, enabling their reuse for additional reuse cycles and increasing their practical applicability.

Beyond material improvements, the next stage of research will integrate advanced manufacturing techniques with artificial intelligence-driven optimization. The combination of 3D printing, electrospinning, and solution blow spinning has already demonstrated the potential to create highly efficient filtration structures. Future developments will focus on refining these methods to achieve precise control over the structural and functional properties of the filters, maximizing their efficiency in pollutant removal. The introduction of computational modelling and machine learning techniques will further enhance this process by enabling predictive optimization of material formulations, filter geometries, and operational conditions. By leveraging data-driven approaches, it

will be possible to design intelligent devices capable of adapting to different environmental conditions and improving performance over time.

The ultimate goal of these future investigations is to develop scalable and high-performance bio-based pollutant removal technologies that combine sustainability, durability, and efficiency. By addressing the key challenges related to material stability and process optimization, this research will contribute to the advancement of next-generation pollutant removal systems that align with circular economy principles and provide innovative solutions for environmental remediation.

References

[1] R. Scaffaro, M.C. Citarrella, Nanofibrous Polymeric Membranes for Air Filtration Application: A Review of Progress after the COVID-19 Pandemic, Macromol Mater Eng 308 (2023) 2300072. https://doi.org/10.1002/MAME.202300072.

[2] F. Russo, R. Castro-Muñoz, S. Santoro, F. Galiano, A. Figoli, A review on electrospun membranes for potential air filtration application, J Environ Chem Eng 10 (2022) 108452. https://doi.org/10.1016/J.JECE.2022.108452.

[3] J.L. Domingo, J. Rovira, Effects of air pollutants on the transmission and severity of respiratory viral infections, Environ Res 187 (2020) 109650. https://doi.org/10.1016/J.ENVRES.2020.109650.

[4] J. de Bont, S. Jaganathan, M. Dahlquist, Å. Persson, M. Stafoggia, P. Ljungman, Ambient air pollution and cardiovascular diseases: An umbrella review of systematic reviews and meta-analyses, J Intern Med 291 (2022) 779–800. https://doi.org/10.1111/JOIM.13467.

[5] J. Lelieveld, J.S. Evans, M. Fnais, D. Giannadaki, A. Pozzer, The contribution of outdoor air pollution sources to premature mortality on a global scale, Nature 2015 525:7569 525 (2015) 367–371. https://doi.org/10.1038/nature15371.

[6] F. Dutheil, J.S. Baker, V. Navel, COVID-19 as a factor influencing air pollution?, Environmental Pollution 263 (2020) 114466. https://doi.org/10.1016/J.ENVPOL.2020.114466.

[7] T. Mathys, F.T. de Souza, D. da S. Barcellos, I. Molderez, The relationship among air pollution, meteorological factors and COVID-19 in the Brussels Capital Region, Science of The Total Environment 857 (2023) 158933. https://doi.org/10.1016/J.SCITOTENV.2022.158933.

[8] J.L. Domingo, M. Marquès, J. Rovira, Influence of airborne transmission of SARS-CoV-2 on COVID-19 pandemic. A review, Environ Res 188 (2020) 109861. https://doi.org/10.1016/J.ENVRES.2020.109861.

[9] M. Marquès, J.L. Domingo, Positive association between outdoor air pollution and the incidence and severity of COVID-19. A review of the recent scientific evidences, Environ Res 203 (2022) 111930. https://doi.org/10.1016/J.ENVRES.2021.111930.

[10] C.E. Rodriguez-Martinez, M.P. Sossa-Briceño, J.A. Cortés, Decontamination and reuse of N95 filtering facemask respirators: A systematic review of the literature, Am J Infect Control 48 (2020) 1520–1532. https://doi.org/10.1016/j.ajic.2020.07.004.

[11] A. Bałazy, M. Toivola, A. Adhikari, S.K. Sivasubramani, T. Reponen, S.A. Grinshpun, Do N95 respirators provide 95% protection level against airborne viruses, and how adequate are surgical masks?, Am J Infect Control 34 (2006) 51–57. https://doi.org/10.1016/j.ajic.2005.08.018.

[12] L. Setti, F. Passarini, G. de Gennaro, P. Barbieri, M.G. Perrone, M. Borelli, J. Palmisani, A. di Gilio, V. Torboli, F. Fontana, L. Clemente, A. Pallavicini, M. Ruscio, P. Piscitelli, A. Miani, SARS-Cov-2RNA found on particulate matter of Bergamo in Northern Italy: First evidence, Environ Res 188 (2020) 109754. https://doi.org/10.1016/J.ENVRES.2020.109754.

[13] P. Piscitelli, A. Miani, L. Setti, G. de Gennaro, X. Rodo, B. Artinano, E. Vara, L. Rancan, J. Arias, F. Passarini, P. Barbieri, A. Pallavicini, A. Parente, E.C. D'Oro, C. de Maio, F. Saladino, M. Borelli, E. Colicino, L.M.G. Gonçalves, G. di Tanna, A. Colao, G.S. Leonardi, A. Baccarelli, F. Dominici, J.P.A. Ioannidis, J.L. Domingo, The role of outdoor and indoor air quality in the spread of SARS-CoV-2: Overview and recommendations by the research group on COVID-19 and particulate matter (RESCOP commission), Environ Res 211 (2022) 113038. https://doi.org/10.1016/J.ENVRES.2022.113038.

[14] X. Wu, R.C. Nethery, M.B. Sabath, D. Braun, F. Dominici, Air pollution and COVID-19 mortality in the United States: Strengths and limitations of an ecological regression analysis, Sci Adv 6 (2020). https://doi.org/10.1126/SCIADV.ABD4049/SUPPL_FILE/ABD4049_SM.PDF.

[15] Y. Zhu, J. Xie, F. Huang, L. Cao, Association between short-term exposure to air pollution and COVID-19 infection: Evidence from China, Science of The Total Environment 727 (2020) 138704. https://doi.org/10.1016/J.SCITOTENV.2020.138704.

[16] M.A. Abdulhamid, K. Muzamil, Recent progress on electrospun nanofibrous polymer membranes for water and air purification: A review, Chemosphere 310 (2023) 136886. https://doi.org/10.1016/J.CHEMOSPHERE.2022.136886.

[17] Y.W. Li, W.L. Ma, Photocatalytic oxidation technology for indoor air pollutants elimination: A review, Chemosphere 280 (2021) 130667. https://doi.org/10.1016/J.CHEMOSPHERE.2021.130667.

[18] D. Lv, M. Zhu, Z. Jiang, S. Jiang, Q. Zhang, R. Xiong, C. Huang, Green Electrospun Nanofibers and Their Application in Air Filtration, Macromol Mater Eng 303 (2018) 1800336. https://doi.org/10.1002/MAME.201800336.

[19] P.R. Yaashikaa, P. Senthil Kumar, S. Karishma, Review on biopolymers and composites – Evolving material as adsorbents in removal of environmental pollutants, Environ Res 212 (2022) 113114. https://doi.org/10.1016/J.ENVRES.2022.113114.

[20] C. Mukherjee, D. Varghese, J.S. Krishna, T. Boominathan, R. Rakeshkumar, S. Dineshkumar, C.V.S. Brahmananda Rao, A. Sivaramakrishna, Recent advances in biodegradable polymers – Properties, applications and future prospects, Eur Polym J 192 (2023) 112068. https://doi.org/10.1016/J.EURPOLYMJ.2023.112068.

[21] D. Ji, Y. Lin, X. Guo, B. Ramasubramanian, R. Wang, N. Radacsi, R. Jose, X. Qin, S. Ramakrishna, Electrospinning of nanofibres, Nature Reviews Methods Primers 2024 4:1 4 (2024) 1–21. https://doi.org/10.1038/s43586-023-00278-z.

[22] R.J. Souza, J.E. Soares Filho, T.A. Simões, J.E. Oliveira, E.S. Medeiros, Experimental Investigation of Solution Blow Spinning Nozzle Geometry and Processing Parameters on Fiber Morphology, ACS Appl Polym Mater 6 (2024) 9735–9743. https://doi.org/10.1021/ACSAPM.4C01273/ASSET/IMAGES/LARGE/AP4C01273_0007.JPEG.

[23] S.A.V. Dananjaya, V.S. Chevali, J.P. Dear, P. Potluri, C. Abeykoon, 3D printing of biodegradable polymers and their composites – Current state-of-the-art, properties, applications, and machine learning for potential future applications, Prog Mater Sci 146 (2024) 101336. https://doi.org/10.1016/J.PMATSCI.2024.101336.

[24] S. Siddiqui, S. Surananai, K. Sainath, M. Zubair Khan, R. Raja Pandiyan Kuppusamy, Y. Kempaiah Suneetha, Emerging trends in development and application of 3D printed nanocomposite polymers for sustainable environmental solutions, Eur Polym J 196 (2023) 112298. https://doi.org/10.1016/J.EURPOLYMJ.2023.112298.

[25] X.H. Qin, S.Y. Wang, Filtration properties of electrospinning nanofibers, J Appl Polym Sci 102 (2006) 1285–1290. https://doi.org/10.1002/APP.24361.

[26] M. Zhu, J. Han, F. Wang, W. Shao, R. Xiong, Q. Zhang, H. Pan, Y. Yang, S.K. Samal, F. Zhang, C. Huang, Electrospun Nanofibers Membranes for Effective Air Filtration, Macromol Mater Eng 302 (2017) 1600353. https://doi.org/10.1002/MAME.201600353.

[27] P. Li, C. Wang, Y. Zhang, F. Wei, Air Filtration in the Free Molecular Flow Regime: A Review of High-Efficiency Particulate Air Filters Based on Carbon Nanotubes, Small 10 (2014) 4543–4561. https://doi.org/10.1002/SMLL.201401553.

[28] H. Liu, C. Cao, J. Huang, Z. Chen, G. Chen, Y. Lai, Progress on particulate matter filtration technology: basic concepts, advanced materials, and performances, Nanoscale 12 (2020) 437–453. https://doi.org/10.1039/C9NR08851B.

[29] C. Yang, Aerosol Filtration Application Using Fibrous Media—An Industrial Perspective, Chin J Chem Eng 20 (2012) 1–9. https://doi.org/10.1016/S1004-9541(12)60356-5.

[30] A.-B.; Wang, X.; Zhang, L.-J.; Gao, T.; Zhang, H.-J.; Xu, Y.-J. Bi, A.-B. Wang, X. Zhang, L.-J. Gao, T. Zhang, H.-J. Xu, Y.-J. Bi, A Review of Filtration Performance of Protective Masks, International Journal of Environmental Research and Public Health 2023, Vol. 20, Page 2346 20 (2023) 2346. https://doi.org/10.3390/IJERPH20032346.

[31] B. Archer, V.R. Shaumbwa, D. Liu, M. Li, T. Iimaa, U. Surenjav, Nanofibrous Mats for Particulate Matter Filtration, Ind Eng Chem Res 60 (2021) 7517–7534. https://doi.org/10.1021/ACS.IECR.1C00829/ASSET/IMAGES/MEDIUM/IE1C00829_0009.GIF.

[32] T. Lu, J. Cui, Q. Qu, Y. Wang, J. Zhang, R. Xiong, W. Ma, C. Huang, Multistructured Electrospun Nanofibers for Air Filtration: A Review, ACS Appl Mater Interfaces 13 (2021) 23293–23313. https://doi.org/10.1021/ACSAMI.1C06520/ASSET/IMAGES/LARGE/AM1C06520_0018.JPEG.

[33] C. Zhu, C.H. Lin, C.S. Cheung, Inertial impaction-dominated fibrous filtration with rectangular or cylindrical fibers, Powder Technol 112 (2000) 149–162. https://doi.org/10.1016/S0032-5910(99)00315-0.

[34] R.A. Yapaulo, E. Wirojsakunchai, T. Orita, D.E. Foster, M. Akard, L.R. Walker, M.J. Lance, Impact of filtration velocities and particulate matter characteristics on diesel particulate filter wall loading, Http://Dx.Doi.Org/10.1243/14680874JER03509 10 (2009) 287–304. https://doi.org/10.1243/14680874JER03509.

[35] C. sen Wang, Electrostatic forces in fibrous filters—a review, Powder Technol 118 (2001) 166–170. https://doi.org/10.1016/S0032-5910(01)00307-2.

[36] J. Zhang, S. Gong, C. Wang, D.Y. Jeong, Z.L. Wang, K. Ren, Biodegradable Electrospun Poly(lactic acid) Nanofibers for Effective PM 2.5 Removal, Macromol Mater Eng 304 (2019). https://doi.org/10.1002/MAME.201900259.

[37] P. Capkova, M. Kormunda, Z. Kolska, J. Trögl, M. Munzarova, P. Rysanek, Electrospun Antimicrobial PVDF-DTAB Nanofibrous Membrane for Air Filtration: Effect of DTAB on Structure, Morphology, Adhesion, and Antibacterial Properties, Macromol Mater Eng 303 (2018). https://doi.org/10.1002/MAME.201700415.

[38] K. Li, C. Li, H. Tian, L. Yuan, A. Xiang, C. Wang, J. Li, A.V. Rajulu, Multifunctional and Efficient Air Filtration: A Natural Nanofilter Prepared with Zein and Polyvinyl Alcohol, Macromol Mater Eng 305 (2020). https://doi.org/10.1002/MAME.202000239.

[39] J. Lee, K.J. Lee, Colloid Syringeless Electrospinning toward Nonwoven Nanofiber Web Containing a Massive Amount of Inorganic Fillers, Macromol Mater Eng 307 (2022). https://doi.org/10.1002/MAME.202100818.

[40] J. Xiong, W. Shao, L. Wang, C. Cui, Y. Jin, H. Yu, P. Han, Y. Gao, F. Liu, Q. Ni, J. He, PAN/FPU Composite Nanofiber Membrane with Superhydrophobic and Superoleophobic Surface as a Filter Element for High-Efficiency Protective Masks, Macromol Mater Eng 306 (2021). https://doi.org/10.1002/MAME.202100371.

[41] F. Liu, M. Li, F. Li, K. Weng, K. Qi, C. Liu, Q. Ni, X. Tao, J. Zhang, W. Shao, J. He, Preparation and Properties of PVDF/Fe3O4 Nanofibers with Magnetic and Electret Effects and their Application in Air Filtration, Macromol Mater Eng 305 (2020). https://doi.org/10.1002/MAME.201900856.

[42] M.C. Han, H.W. He, W.K. Kong, K. Dong, B.Y. Wang, X. Yan, L.M. Wang, X. Ning, High-performance Electret and Antibacterial Polypropylene Meltblown Nonwoven Materials Doped with Boehmite and ZnO Nanoparticles for Air Filtration, Fibers and Polymers 23 (2022) 1947–1955. https://doi.org/10.1007/S12221-022-4786-8/METRICS.

[43] Z. Feng, S.J. Cao, A newly developed electrostatic enhanced pleated air filters towards the improvement of energy and filtration efficiency, Sustain Cities Soc 49 (2019) 101569. https://doi.org/10.1016/J.SCS.2019.101569.

[44] F. Liu, M. Li, W. Shao, W. Yue, B. Hu, K. Weng, Y. Chen, X. Liao, J. He, Preparation of a polyurethane electret nanofiber membrane and its air-filtration performance, J Colloid Interface Sci 557 (2019) 318–327. https://doi.org/10.1016/J.JCIS.2019.08.099.

[45] Z. Peng, J. Shi, X. Xiao, Y. Hong, X. Li, W. Zhang, Y. Cheng, Z. Wang, W.J. Li, J. Chen, M.K.H. Leung, Z. Yang, Self-charging electrostatic face masks leveraging triboelectrification for prolonged air filtration, Nature Communications 2022 13:1 13 (2022) 1–10. https://doi.org/10.1038/s41467-022-35521-w.

[46] S.A. Hosseini, H.V. Tafreshi, 3-D simulation of particle filtration in electrospun nanofibrous filters, Powder Technol 201 (2010) 153–160. https://doi.org/10.1016/J.POWTEC.2010.03.020.

[47] B. Xu, X. Yu, Y. Wu, Z. Lin, Experimental investigation of air pressure affecting filtration performance of fibrous filter sheet, Https://Doi.Org/10.1080/09593330.2016.1202328 38 (2016) 558–565. https://doi.org/10.1080/09593330.2016.1202328.

[48] Y.; Zhou, Y.; Liu, M.; Zhang, Z.; Feng, D.-G.; Yu, K. Wang, J.L. Arias, U. Scherf, M.M. El-Hammadi, Y. Zhou, Y. Liu, M. Zhang, Z. Feng, D.-G. Yu, K. Wang, Electrospun Nanofiber Membranes for Air Filtration: A Review, Nanomaterials 2022, Vol. 12, Page 1077 12 (2022) 1077. https://doi.org/10.3390/NANO12071077.

[49] G. Liu, M. Xiao, X. Zhang, C. Gal, X. Chen, L. Liu, S. Pan, J. Wu, L. Tang, D. Clements-Croome, A review of air filtration technologies for sustainable and healthy building ventilation, Sustain Cities Soc 32 (2017) 375–396. https://doi.org/10.1016/J.SCS.2017.04.011.

[50] H. Dai, X. Liu, C. Zhang, K. Ma, Y. Zhang, Electrospinning Polyacrylonitrile/Graphene Oxide/Polyimide nanofibrous membranes for High-efficiency PM2.5 filtration, Sep Purif Technol 276 (2021) 119243. https://doi.org/10.1016/J.SEPPUR.2021.119243.

[51] R.S. Barhate, S. Ramakrishna, Nanofibrous filtering media: Filtration problems and solutions from tiny materials, J Memb Sci 296 (2007) 1–8. https://doi.org/10.1016/J.MEMSCI.2007.03.038.

[52] M. Chai, W. Tong, Z. Wang, S. Zhao, Y. Zhang, Air Purification Using Polymer Fiber Filters, Macromol Mater Eng 307 (2022). https://doi.org/10.1002/MAME.202100753.

[53] D. Lv, G. Tang, L. Chen, M. Zhang, J. Cui, R. Xiong, C. Huang, Multifunctional Gas-Spinning Hierarchical Architecture: A Robust and Efficient Nanofiber Membrane for Simultaneous Air and Water Contaminant Remediation, ACS Appl Polym Mater 2 (2020) 5686–5697. https://doi.org/10.1021/ACSAPM.0C00988/ASSET/IMAGES/LARGE/AP0C00988_0010.JPEG.

[54] E.F. Gulino, M.C. Citarrella, A. Maio, R. Scaffaro, An innovative route to prepare in situ graded crosslinked PVA graphene electrospun mats for drug release, Compos Part A Appl Sci Manuf 155 (2022) 106827. https://doi.org/10.1016/J.COMPOSITESA.2022.106827.

[55] L. Zhang, L. Li, L. Wang, J. Nie, G. Ma, Multilayer electrospun nanofibrous membranes with antibacterial property for air filtration, Appl Surf Sci 515 (2020) 145962. https://doi.org/10.1016/J.APSUSC.2020.145962.

[56] H. Zhang, L. Jia, P. Li, L. Yu, Y. Liu, W. Zhao, H. Wang, B. Li, Large-Scale Blow Spinning of Nanofiber Membranes for Highly Efficient Air Mechanical Filtration with Antibacterial Activity, ACS Appl Polym Mater 4 (2022) 2081–2090. https://doi.org/10.1021/ACSAPM.1C01916/SUPPL_FILE/AP1C01916_SI_001.PDF.

[57] Z. Yang, X. Zhang, Z. Qin, H. Li, J. Wang, G. Zeng, C. Liu, J. Long, Y. Zhao, Y. Li, G. Yan, Airflow Synergistic Needleless Electrospinning of Instant Noodle-like Curly Nanofibrous Membranes for High-Efficiency Air Filtration, Small 18 (2022) 2107250. https://doi.org/10.1002/SMLL.202107250.

[58] A.M. Grancaric´1, G. Grancaric´1, I. Jerkovic´1, J. Jerkovic´1, V. Koncar, C. Cochrane, F.M. Kelly, D. Soulat, X. Legrand, Conductive polymers for smart textile applications, 48 (2018) 612–642. https://doi.org/10.1177/1528083717699368.

[59] R. Scaffaro, A. Maio, M.C. Citarrella, Ionic tactile sensors as promising biomaterials for artificial skin: Review of latest advances and future perspectives, Eur Polym J 151 (2021) 110421. https://doi.org/10.1016/J.EURPOLYMJ.2021.110421.

[60] S. Nambiar, J.T.W. Yeow, Conductive polymer-based sensors for biomedical applications, Biosens Bioelectron 26 (2011) 1825–1832. https://doi.org/10.1016/J.BIOS.2010.09.046.

[61] Y. Cao, T. Feng, J. Xu, C. Xue, Recent advances of molecularly imprinted polymer-based sensors in the detection of food safety hazard factors, Biosens Bioelectron 141 (2019) 111447. https://doi.org/10.1016/J.BIOS.2019.111447.

[62] A.G. Ayankojo, J. Reut, V. Ciocan, A. Öpik, V. Syritski, Molecularly imprinted polymer-based sensor for electrochemical detection of erythromycin, Talanta 209 (2020) 120502. https://doi.org/10.1016/J.TALANTA.2019.120502.

[63] M.M. Hasan, M.A. Shenashen, M.N. Hasan, H. Znad, M.S. Salman, M.R. Awual, Natural biodegradable polymeric bioadsorbents for efficient cationic dye encapsulation from wastewater, J Mol Liq 323 (2021) 114587. https://doi.org/10.1016/J.MOLLIQ.2020.114587.

[64] A. Kornyushchenko, V. Perekrestov, G. Wilde, Gas nanosensors, Nanosensors for Smart Cities (2020) 267–283. https://doi.org/10.1016/B978-0-12-819870-4.00015-3.

[65] M. Kumar, A. v. Agrawal, M. Moradi, R. Yousefi, Nanosensors for gas sensing applications, Nanomaterials for Air Remediation (2020) 107–130. https://doi.org/10.1016/B978-0-12-818821-7.00006-3.

[66] H. Saleem, S.J. Zaidi, A.F. Ismail, P.S. Goh, Advances of nanomaterials for air pollution remediation and their impacts on the environment, Chemosphere 287 (2022). https://doi.org/10.1016/J.CHEMOSPHERE.2021.132083.

[67] Y. Zhang, Y. Zhao, Y. Wu, Y. Liu, Y. Deng, R. Li, Y.Q. Liu, Z. Liu, H. Xiao, R. Xiong, C. Huang, A biomass-derived Schiff base material composited with polylactic acid nanofiber membrane as selective fluorescent ‘turn off/on’ platform for Pb2+ quantitative detection and characterization, Int J Biol Macromol 214 (2022) 414–425. https://doi.org/10.1016/J.IJBIOMAC.2022.06.089.

[68] Y. Zhang, Y. Zhao, B. Song, K. Liu, J. Gu, Y. Yue, R. Xiong, C. Huang, UV-fluorescence probe for detection Ni2+ with colorimetric/spectral dual-mode analysis method and its practical application, Bioorg Chem 114 (2021) 105103. https://doi.org/10.1016/J.BIOORG.2021.105103.

[69] X. Zhang, Q. Qu, A. Yang, J. Wang, W. Cheng, Y. Deng, A. Zhou, T. Lu, R. Xiong, C. Huang, Chitosan enhanced the stability and antibiofilm activity of self-propelled Prussian blue micromotor, Carbohydr Polym 299 (2023) 120134. https://doi.org/10.1016/J.CARBPOL.2022.120134.

[70] Y. Deng, T. Lu, J. Cui, S. Keshari Samal, R. Xiong, C. Huang, Bio-based electrospun nanofiber as building blocks for a novel eco-friendly air filtration membrane: A review, Sep Purif Technol 277 (2021) 119623. https://doi.org/10.1016/J.SEPPUR.2021.119623.

[71] L.M. Henning, A. Abdullayev, C. Vakifahmetoglu, U. Simon, H. Bensalah, A. Gurlo, M.F. Bekheet, Review on Polymeric, Inorganic, and Composite Materials for Air Filters: From Processing to Properties, Advanced Energy and Sustainability Research 2 (2021) 2100005. https://doi.org/10.1002/AESR.202100005.

[72] J. Song, Z. Liu, Z. Li, H. Wu, Continuous production and properties of mutil-level nanofiber air filters by blow spinning, RSC Adv 10 (2020) 19615–19620. https://doi.org/10.1039/D0RA01656J.

[73] X. Cheng, L. Zhao, Z. Zhang, C. Deng, C. Li, Y. Du, J. Shi, M. Zhu, Highly efficient, low-resistant, well-ordered PAN nanofiber membranes for air filtration, Colloids Surf A Physicochem Eng Asp 655 (2022) 130302. https://doi.org/10.1016/J.COLSURFA.2022.130302.

[74] H. Liu, S. Zhang, L. Liu, J. Yu, B. Ding, A Fluffy Dual-Network Structured Nanofiber/Net Filter Enables High-Efficiency Air Filtration, Adv Funct Mater 29 (2019) 1904108. https://doi.org/10.1002/ADFM.201904108.

[75] S.M. Ji, A.P. Tiwari, H.J. Oh, H.Y. Kim, ZnO/Ag nanoparticles incorporated multifunctional parallel side by side nanofibers for air filtration with enhanced removing organic contaminants and antibacterial properties, Colloids Surf A Physicochem Eng Asp 621 (2021) 126564. https://doi.org/10.1016/J.COLSURFA.2021.126564.

[76] Y. Cui, Z. Jiang, C. Xu, M. Zhu, W. Li, C. Wang, Preparation, filtration, and photocatalytic properties of PAN@g-C3N4 fibrous membranes by electrospinning, RSC Adv 11 (2021) 19579–19586. https://doi.org/10.1039/D1RA03234H.

[77] W. Xu, Y. Chen, Y. Liu, Directional water transfer janus nanofibrous porous membranes for particulate matter filtration and volatile organic compound adsorption, ACS Appl Mater Interfaces 13 (2021) 3109–3118. https://doi.org/10.1021/ACSAMI.0C18526/SUPPL_FILE/AM0C18526_SI_007.MP4.

[78] H. Kim, S.K. Hong, H. Lee, Y. Jeong, S.J. Cho, A reusable nanofibrous air filter with anti-wetting microbead coating, J Clean Prod 382 (2023) 134972. https://doi.org/10.1016/J.JCLEPRO.2022.134972.

[79] H. Liu, S. Zhang, L. Liu, J. Yu, B. Ding, High-Performance PM0.3 Air Filters Using Self-Polarized Electret Nanofiber/Nets, Adv Funct Mater 30 (2020) 1909554. https://doi.org/10.1002/ADFM.201909554.

[80] B. Zaarour, H. Tina, L. Zhu, X.Y. Jin, Branched nanofibers with tiny diameters for air filtration via one-step electrospinning, Journal of Industrial Textiles 51 (2022) 1105S-1117S. https://doi.org/10.1177/1528083720923773/ASSET/IMAGES/LARGE/10.1177_1528083720923773-FIG2.JPEG.

[81] C. Liu, Z. Dai, R. Zhou, Q. Ke, C. Huang, Fabrication of Polypropylene-g-(Diallylamino Triazine) Bifunctional Nonwovens with Antibacterial and Air Filtration Activities by Reactive Extrusion and Melt-Blown Technology, J Chem 2019 (2019). https://doi.org/10.1155/2019/3435095.

[82] C. Yang, X. Jiang, X. Gao, H. Wang, L. Li, N. Hussain, J. Xie, Z. Cheng, Z. Li, J. Yan, M. Zhong, L. Zhao, H. Wu, Saving 80% Polypropylene in Facemasks by Laser-Assisted Melt-Blown Nanofibers, Nano Lett 22 (2022) 7212–7219. https://doi.org/10.1021/ACS.NANOLETT.2C02693/SUPPL_FILE/NL2C02693_SI_002.ZIP.

[83] L. Zhang, Q. Zheng, X. Ge, H. Chan, G. Zhang, K. Fang, Y. Liang, Preparation of Nylon-6 micro-nanofiber composite membranes with 3D uniform gradient structure for high-efficiency air filtration of ultrafine particles, Sep Purif Technol 308 (2023) 122921. https://doi.org/10.1016/J.SEPPUR.2022.122921.

[84] C. Liu, P.C. Hsu, H.W. Lee, M. Ye, G. Zheng, N. Liu, W. Li, Y. Cui, Transparent air filter for high-efficiency PM2.5 capture, Nature Communications 2015 6:1 6 (2015) 1–9. https://doi.org/10.1038/ncomms7205.

[85] H.K. Kang, H.J. Oh, J.Y. Kim, H.Y. Kim, Y.O. Choi, Effect of Process Control Parameters on the Filtration Performance of PAN–CTAB Nanofiber/Nanonet Web Combined with Meltblown Nonwoven, Polymers 2021, Vol. 13, Page 3591 13 (2021) 3591. https://doi.org/10.3390/POLYM13203591.

[86] B. Zaarour, W. Zhang, L. Zhu, X.Y. Jin, C. Huang, Maneuvering surface structures of polyvinylidene fluoride nanofibers by controlling solvent systems and polymer concentration, Https://Doi.Org/10.1177/0040517518792748 89 (2018) 2406–2422. https://doi.org/10.1177/0040517518792748.

[87] G. dong Kang, Y. ming Cao, Application and modification of poly(vinylidene fluoride) (PVDF) membranes – A review, J Memb Sci 463 (2014) 145–165. https://doi.org/10.1016/J.MEMSCI.2014.03.055.

[88] Z. Shao, G. Kang, H. Chen, J. Jiang, X. Wang, W. Li, Y. Liu, G. Zheng, Preparation, characterization, and air filtration property of electrospun bimodal fibrous membrane based on low conductivity blended polymers solution, Mater Today Commun 34 (2023) 105014. https://doi.org/10.1016/J.MTCOMM.2022.105014.

[89] A. Wang, X. Li, T. Hou, Y. Lu, J. Zhou, X. Zhang, B. Yang, High efficiency, low resistance and high temperature resistance PTFE porous fibrous membrane for air filtration, Mater Lett 295 (2021) 129831. https://doi.org/10.1016/J.MATLET.2021.129831.

[90] Y.A. Nanehkaran, Z. Licai, M. Azarafza, S. Talaei, X. Jinxia, J. Chen, R. Derakhshani, The predictive model for COVID-19 pandemic plastic pollution by using deep learning method, Scientific Reports 2023 13:1 13 (2023) 1–14. https://doi.org/10.1038/s41598-023-31416-y.

[91] P. Pandit, S. Maity, K. Singha, Annu, M. Uzun, M. Shekh, S. Ahmed, Potential biodegradable face mask to counter environmental impact of Covid-19, Clean Eng Technol 4 (2021) 100218. https://doi.org/10.1016/J.CLET.2021.100218.

[92] H.J. Kim, D.I. Choi, S.K. Sung, S.H. Lee, S.J. Kim, J. Kim, B.S. Han, D.I. Kim, Y. Kim, Eco-friendly poly(vinyl alcohol) nanofiber-based air filter for effectively capturing particulate matter, Applied Sciences (Switzerland) 11 (2021) 3831. https://doi.org/10.3390/APP11093831/S1.

[93] M. Zhu, R. Xiong, C. Huang, Bio-based and photocrosslinked electrospun antibacterial nanofibrous membranes for air filtration, Carbohydr Polym 205 (2019) 55–62. https://doi.org/10.1016/J.CARBPOL.2018.09.075.

[94] D. Lv, R. Wang, G. Tang, Z. Mou, J. Lei, J. Han, S. de Smedt, R. Xiong, C. Huang, Ecofriendly Electrospun Membranes Loaded with Visible-Light-Responding Nanoparticles for Multifunctional Usages: Highly Efficient Air Filtration, Dye Scavenging, and Bactericidal Activity, ACS Appl Mater Interfaces 11 (2019) 12880–12889. https://doi.org/10.1021/ACSAMI.9B01508/ASSET/IMAGES/LARGE/AM-2019-015085_0006.JPEG.

[95] W. Han, D. Rao, H. Gao, X. Yang, H. Fan, C. Li, L. Dong, H. Meng, Green-solvent-processable biodegradable poly(lactic acid) nanofibrous membranes with bead-on-string structure for effective air filtration: "Kill two birds with one stone," Nano Energy 97 (2022) 107237. https://doi.org/10.1016/J.NANOEN.2022.107237.

[96] S. Wanwong, W. Sangkhun, P. Jiamboonsri, Electrospun Cyclodextrin/Poly(L-lactic acid) Nanofibers for Efficient Air Filter: Their PM and VOC Removal Efficiency and Triboelectric Outputs, Polymers (Basel) 15 (2023) 722. https://doi.org/10.3390/POLYM15030722/S1.

[97] Q.F. Lim, R.C.C. Yap, C.P. Teng, J.C.C. Yeo, M.Y. Tan, J.P.W. Toh, Q. Zhu, W. Thitsartarn, C. He, S. Liu, J. Kong, Electrospray-on-Electrospun Breathable, Biodegradable, and Robust Nanofibrous Membranes with Photocatalytic Bactericidal Activity, ACS Appl Nano Mater 6 (2022) 1828–1838. https://doi.org/10.1021/ACSANM.2C04776/ASSET/IMAGES/LARGE/AN2C04776_0008.JPEG.

[98] L. Wang, Y. Gao, J. Xiong, W. Shao, C. Cui, N. Sun, Y. Zhang, S. Chang, P. Han, F. Liu, J. He, Biodegradable and high-performance multiscale structured nanofiber membrane as mask filter media via poly(lactic acid) electrospinning, J Colloid Interface Sci 606 (2022) 961–970. https://doi.org/10.1016/J.JCIS.2021.08.079.

[99] Z. Wang, Z. Pan, J. Wang, R. Zhao, A Novel Hierarchical Structured Poly(lactic acid)/Titania Fibrous Membrane with Excellent Antibacterial Activity and Air Filtration Performance, J Nanomater 2016 (2016). https://doi.org/10.1155/2016/6272983.

[100] L.Y. Wang, L.E. Yu, J.Y. Lai, T.S. Chung, Developing ultra-high gas permeance PVDF hollow fibers for air filtration applications, Sep Purif Technol 205 (2018) 184–195. https://doi.org/10.1016/J.SEPPUR.2018.05.036.

[101] L.Y. Wang, W.F. Yong, L.E. Yu, T.S. Chung, Design of high efficiency PVDF-PEG hollow fibers for air filtration of ultrafine particles, J Memb Sci 535 (2017) 342–349. https://doi.org/10.1016/J.MEMSCI.2017.04.053.

[102] L.Y. Wang, L.E. Yu, J.Y. Lai, T.S. Chung, Effects of Pluronic F127 on phase inversion and membrane formation of PAN hollow fibers for air filtration, J Memb Sci 584 (2019) 137–147. https://doi.org/10.1016/J.MEMSCI.2019.05.001.

[103] M. Li, Y. Feng, K. Wang, W.F. Yong, L. Yu, T.S. Chung, Novel Hollow Fiber Air Filters for the Removal of Ultrafine Particles in PM2.5 with Repetitive Usage Capability, Environ Sci Technol 51 (2017) 10041–10049. https://doi.org/10.1021/ACS.EST.7B01494/SUPPL_FILE/ES7B01494_SI_001.PDF.

[104] J. Li, D. Zhang, T. Yang, S. Yang, X. Yang, H. Zhu, Nanofibrous membrane of graphene oxide-in-polyacrylonitrile composite with low filtration resistance for the effective capture of PM2.5, J Memb Sci 551 (2018) 85–92. https://doi.org/10.1016/J.MEMSCI.2018.01.025.

[105] R. Roche, F. Yalcinkaya, Electrospun Polyacrylonitrile Nanofibrous Membranes for Point-of-Use Water and Air Cleaning, ChemistryOpen 8 (2019) 97–103. https://doi.org/10.1002/OPEN.201800267.

[106] R. Scaffaro, L. Settanni, E.F. Gulino, Release Profiles of Carvacrol or Chlorhexidine of PLA/Graphene Nanoplatelets Membranes Prepared Using Electrospinning and Solution Blow Spinning: A Comparative Study, Molecules 2023, Vol. 28, Page 1967 28 (2023) 1967. https://doi.org/10.3390/MOLECULES28041967.

[107] D. Zong, X. Zhang, X. Yin, F. Wang, J. Yu, S. Zhang, B. Ding, Electrospun Fibrous Sponges: Principle, Fabrication, and Applications, Advanced Fiber Materials 2022 4:6 4 (2022) 1434–1462. https://doi.org/10.1007/S42765-022-00202-2.

[108] S. Abdolkarim, H. Ravandi, M. Sadrjahani, A. Valipouri, F. Dabirian, F.K. Ko, Recently developed electrospinning methods: a review, Textile Research Journal 2022 (n.d.) 5130–5145. https://doi.org/10.1177/00405175211069880.

[109] S.S. Ayati, M. Karevan, E. Stefanek, M. Bhia, M. Akbari, Nanofibers Fabrication by Blown-Centrifugal Spinning, Macromol Mater Eng 307 (2022) 2100368. https://doi.org/10.1002/MAME.202100368.

[110] H. Xu, S. Yagi, S. Ashour, L. Du, M.E. Hoque, L. Tan, A Review on Current Nanofiber Technologies: Electrospinning, Centrifugal Spinning, and Electro-Centrifugal Spinning, Macromol Mater Eng (2022). https://doi.org/10.1002/MAME.202200502.

[111] Y. Gao, J. Zhang, Y. Su, H. Wang, X.X. Wang, L.P. Huang, M. Yu, S. Ramakrishna, Y.Z. Long, Recent progress and challenges in solution blow spinning, Mater Horiz 8 (2021) 426–446. https://doi.org/10.1039/D0MH01096K.

[112] Y. Kara, K. Molnár, Revealing of process–structure–property relationships of fine polypropylene fiber mats generated via melt blowing, Polym Adv Technol 32 (2021) 2416–2432. https://doi.org/10.1002/PAT.5270.

[113] H. Zhang, Q. Zhen, Y. Liu, R. Liu, Y. Zhang, One-step melt blowing process for PP/PEG micro-nanofiber filters with branch networks, Results Phys 12 (2019) 1421–1428. https://doi.org/10.1016/J.RINP.2019.01.012.

[114] J. Lim, S. Choi, H.S. Kim, Behavior of melt electrospinning/blowing for polypropylene fiber fabrication, Polym Int 72 (2023) 120–125. https://doi.org/10.1002/PI.6453.

[115] X. Hao, Y. Zeng, A review on the studies of air flow field and fiber formation process during melt blowing, Ind Eng Chem Res 58 (2019) 11624–11637. https://doi.org/10.1021/ACS.IECR.9B01694/ASSET/IMAGES/LARGE/IE-2019-01694K_0008.JPEG.

[116] R. Rashid, I. Shafiq, P. Akhter, M.J. Iqbal, M. Hussain, A state-of-the-art review on wastewater treatment techniques: the effectiveness of adsorption method, Environmental Science and Pollution Research 2021 28:8 28 (2021) 9050–9066. https://doi.org/10.1007/S11356-021-12395-X.

[117] M. Khodakarami, M. Bagheri, Recent advances in synthesis and application of polymer nanocomposites for water and wastewater treatment, J Clean Prod 296 (2021) 126404. https://doi.org/10.1016/J.JCLEPRO.2021.126404.

[118] H. Lin, Z. Wang, C. Liu, Y. Dong, Technologies for removing heavy metal from contaminated soils on farmland: A review, Chemosphere 305 (2022) 135457. https://doi.org/10.1016/J.CHEMOSPHERE.2022.135457.

[119] R. Shrestha, S. Ban, S. Devkota, S. Sharma, R. Joshi, A.P. Tiwari, H.Y. Kim, M.K. Joshi, Technological trends in heavy metals removal from industrial wastewater: A review, J Environ Chem Eng 9 (2021) 105688. https://doi.org/10.1016/J.JECE.2021.105688.

[120] N.H. Ismail, W.N.W. Salleh, A.F. Ismail, H. Hasbullah, N. Yusof, F. Aziz, J. Jaafar, Hydrophilic polymer-based membrane for oily wastewater treatment: A review, Sep Purif Technol 233 (2020) 116007. https://doi.org/10.1016/J.SEPPUR.2019.116007.

[121] S. Cairone, H.M. Hegab, H. Khalil, L. Nassar, V.S. Wadi, V. Naddeo, S.W. Hasan, Novel eco-friendly polylactic acid nanocomposite integrated membrane system for sustainable wastewater treatment: Performance evaluation

and antifouling analysis, Science of The Total Environment 912 (2024) 168715. https://doi.org/10.1016/J.SCITOTENV.2023.168715.

[122] A.T. Hoang, S. Nižetić, X.Q. Duong, L. Rowinski, X.P. Nguyen, Advanced super-hydrophobic polymer-based porous absorbents for the treatment of oil-polluted water, Chemosphere 277 (2021) 130274. https://doi.org/10.1016/J.CHEMOSPHERE.2021.130274.

[123] L.Y. Ng, H.S. Chua, C.Y. Ng, Incorporation of graphene oxide-based nanocomposite in the polymeric membrane for water and wastewater treatment: A review on recent development, J Environ Chem Eng 9 (2021) 105994. https://doi.org/10.1016/J.JECE.2021.105994.

[124] L. Baraldi, D. De Angelis, R. Bosi, R. Pennini, I. Bassanetti, A. Benassi, G.E. Bellazzi, Mechanical Characterization of Pharmaceutical Powders by Nanoindentation and Correlation with Their Behavior during Grinding, Pharmaceutics 2022, Vol. 14, Page 1146 14 (2022) 1146. https://doi.org/10.3390/PHARMACEUTICS14061146.

[125] C.M. Messina, R. Gaglio, M. Morghese, M. Tolone, R. Arena, G. Moschetti, A. Santulli, N. Francesca, L. Settanni, Microbiological Profile and Bioactive Properties of Insect Powders Used in Food and Feed Formulations, Foods 8 (2019). https://doi.org/10.3390/FOODS8090400.

[126] L.-C. Tang, H. Zhang, S. Sprenger, L. Ye, Z. Zhang, Fracture mechanisms of epoxy-based ternary composites filled with rigid-soft particles, Compos Sci Technol 72 (2012) 558–565. https://doi.org/https://doi.org/10.1016/j.compscitech.2011.12.015.

[127] Z. Peng, K. Jiang, Y. Qin, M. Li, N. Balar, B.T. O'Connor, H. Ade, L. Ye, Y. Geng, Modulation of Morphological, Mechanical, and Photovoltaic Properties of Ternary Organic Photovoltaic Blends for Optimum Operation, Adv Energy Mater 11 (2021) 2003506. https://doi.org/10.1002/AENM.202003506.

[128] P.L. Ritger, N.A. Peppas, A simple equation for description of solute release II. Fickian and anomalous release from swellable devices, Journal of Controlled Release 5 (1987) 37–42. https://doi.org/10.1016/0168-3659(87)90035-6.

[129] R. Scaffaro, M.C. Citarrella, Stable and reusable electrospun bio-composite fibrous membranes based on PLA and natural fillers for air filtration applications, Sustainable Materials and Technologies (2024) e01146. https://doi.org/10.1016/J.SUSMAT.2024.E01146.

[130] L. Li, Y. Gao, G. Nie, X. Yan, S. Wang, T. Zhang, S. Ramakrishna, Y.Z. Long, W. Han, Biodegradable Poly (L-Lactic acid) Fibrous Membrane with Ribbon-Structured Fibers and Ultrafine Nanofibers Enhances Air Filtration Performance, Small (2024) 2402317. https://doi.org/10.1002/SMLL.202402317.

[131] J. Ge, D. Han, S. Li, J. Li, S. Hong, C. Wang, P. Hu, S. Ramakrishna, Y. Liu, Electrospun membrane of PLA/calendula with improved UV protection and stable filtration performance, Sep Purif Technol 344 (2024) 127310. https://doi.org/10.1016/J.SEPPUR.2024.127310.

[132] C. Zhang, J. Sun, S. Lyu, Z. Lu, T. Li, Y. Yang, B. Li, H. Han, B. Wu, H. Sun, D. Li, J. Huang, D. Sun, Poly(lactic acid)/artificially cultured diatom frustules nanofibrous membranes with fast and controllable degradation rates for air filtration, Adv Compos Hybrid Mater 5 (2022) 1221–1232. https://doi.org/10.1007/S42114-022-00474-7/FIGURES/8.

[133] R. Scaffaro, A. Maio, E.F. Gulino, Hydrolytic degradation of PLA/Posidonia Oceanica green composites: A simple model based on starting morpho-chemical properties, Compos Sci Technol 213 (2021) 108930. https://doi.org/10.1016/J.COMPSCITECH.2021.108930.

[134] M.R.V. Fontes, M.P. da Rosa, L.M. Fonseca, P.H. Beck, E. da Rosa Zavareze, A.R.G. Dias, Thermal stability, hydrophobicity and antioxidant potential of ultrafine poly (lactic acid)/rice husk lignin fibers, Brazilian Journal of Chemical Engineering 38 (2021) 133–144. https://doi.org/10.1007/S43153-020-00083-1/FIGURES/5.

[135] N. Dalton, R.P. Lynch, M.N. Collins, M. Culebras, Thermoelectric properties of electrospun carbon nanofibres derived from lignin, Int J Biol Macromol 121 (2019) 472–479. https://doi.org/10.1016/J.IJBIOMAC.2018.10.051.

[136] R. Casasola, N.L. Thomas, A. Trybala, S. Georgiadou, Electrospun poly lactic acid (PLA) fibres: Effect of different solvent systems on fibre morphology and diameter, Polymer (Guildf) 55 (2014) 4728–4737. https://doi.org/10.1016/J.POLYMER.2014.06.032.

[137] Y. Liu, T. Hu, Z. Wu, G. Zeng, D. Huang, Y. Shen, X. He, M. Lai, Y. He, Study on biodegradation process of lignin by FTIR and DSC, Environmental Science and Pollution Research 21 (2014) 14004–14013. https://doi.org/10.1007/S11356-014-3342-5/FIGURES/9.

[138] T.U. Rashid, R.E. Gorga, W.E. Krause, Mechanical Properties of Electrospun Fibers—A Critical Review, Adv Eng Mater 23 (2021). https://doi.org/10.1002/ADEM.202100153.

[139] M. Jafari, E. Shim, A. Joijode, Fabrication of Poly(lactic acid) filter media via the meltblowing process and their filtration performances: A comparative study with polypropylene meltblown, Sep Purif Technol 260 (2021) 118185. https://doi.org/10.1016/J.SEPPUR.2020.118185.

[140] G. Zhu, C. Wang, T. Yang, N. Gao, Y. Zhang, J. Zhu, X. He, J. Shao, S. Li, M. Zhang, S. Zhang, J. Gao, H. Xu, Bio-inspired gradient poly(lactic acid) nanofibers for active capturing of PM0.3 and real-time respiratory monitoring, J Hazard Mater 474 (2024) 134781. https://doi.org/10.1016/J.JHAZMAT.2024.134781.

[141] C. Wang, X. He, G. Zhu, X. Li, X. Zhu, R. Chen, S. Tian, X. Li, J. Zhu, J. Shao, J. Gao, G.J. Zhong, H. Xu, Extreme Orientation of Stereocomplexed Poly(lactic acid) Induced Ultrafine Electroactive Nanofibers for Respiratory Healthcare and Intelligent Diagnosis, ACS Sustain Chem Eng (2024). https://doi.org/10.1021/ACSSUSCHEMENG.4C02720/ASSET/IMAGES/LARGE/SC4C02720_0005.JPEG.

[142] X. Song, M. Tang, C. Wang, X. Li, J. Zhu, J. Shao, S. Huang, B. Wang, X.P. Li, H. Li, H. Xu, Stereocomplexation-Enhanced Electroactivity of Poly(lactic acid) Nanofibrous Membranes for Long-Term PM Capturing and Remote Respiratory Monitoring, ACS Sustain Chem Eng 12 (2024) 3554–3564. https://doi.org/10.1021/ACSSUSCHEMENG.3C06327/SUPPL_FILE/SC3C06327_SI_007.MP4.

[143] Y. Wang, X. Zhang, X. Jin, W. Liu, An in situ self-charging triboelectric air filter with high removal efficiency, ultra-low pressure drop, superior filtration stability, and robust service life, Nano Energy 105 (2023) 108021. https://doi.org/10.1016/J.NANOEN.2022.108021.

[144] M.H. Wolf, N. Izaguirre, B. Pascual-José, R. Teruel-Juanes, J. Labidi, A. Ribes-Greus, Dielectric characterisation of chitosan-based composite membranes containing fractionated kraft and organosolv lignin, React Funct Polym 196 (2024) 105833. https://doi.org/10.1016/J.REACTFUNCTPOLYM.2024.105833.

[145] L. Jiang, X. Zhu, J. Li, J. Shao, Y. Zhang, J. Zhu, S. Li, L. Zheng, X.P. Li, S. Zhang, H. Li, G.J. Zhong, H. Xu, Electroactive and breathable protective membranes by surface engineering of dielectric nanohybrids at poly(lactic acid) nanofibers with excellent self-sterilization and photothermal properties, Sep Purif Technol 339 (2024) 126708. https://doi.org/10.1016/J.SEPPUR.2024.126708.

[146] T. Yang, X. Zhu, Y. Zhang, L. Ke, J. Zhu, R. Huang, S. Li, Y. Zhu, S. Zhang, G.J. Zhong, H. Xu, Nanopatterning of beaded poly(lactic acid) nanofibers for highly electroactive, breathable, UV-shielding and antibacterial protective membranes, Int J Biol Macromol 260 (2024) 129566. https://doi.org/10.1016/J.IJBIOMAC.2024.129566.

[147] H. Li, Z. Wang, H. Zhang, Z. Pan, Nanoporous PLA/(Chitosan Nanoparticle) Composite Fibrous Membranes with Excellent Air Filtration and Antibacterial Performance, Polymers 2018, Vol. 10, Page 1085 10 (2018) 1085. https://doi.org/10.3390/POLYM10101085.

[148] M. Zhu, Y. Deng, Y. Zheng, X. Hu, W. Xu, R. Xiong, C. Huang, Tribo-charge enhanced and cellulose based biodegradable nanofibrous membranes with highly fluffy structure for air filtration and self-powered respiration monitoring systems, J Hazard Mater 468 (2024) 133770. https://doi.org/10.1016/J.JHAZMAT.2024.133770.

[149] P. Santhra Krishnan, A. Salian, S. Dutta, S. Mandal, A roadmap to UV-protective natural resources: classification, characteristics, and applications, Mater Chem Front 5 (2021) 7696–7723. https://doi.org/10.1039/D1QM00741F.

[150] G. Petruk, F. Di Lorenzo, P. Imbimbo, A. Silipo, A. Bonina, L. Rizza, R. Piccoli, D.M. Monti, R. Lanzetta, Protective effect of Opuntia ficus-indica L. cladodes against UVA-induced oxidative stress in normal human keratinocytes, Bioorg Med Chem Lett 27 (2017) 5485–5489. https://doi.org/10.1016/J.BMCL.2017.10.043.

[151] A.M. Mannino, C. Micheli, Ecological Function of Phenolic Compounds from Mediterranean Fucoid Algae and Seagrasses: An Overview on the Genus Cystoseira sensu lato and Posidonia oceanica (L.) Delile, Journal of Marine Science and Engineering 2020, Vol. 8, Page 19 8 (2020) 19. https://doi.org/10.3390/JMSE8010019.

[152] W. Ma, Y. Ding, M. Zhang, S. Gao, Y. Li, C. Huang, G. Fu, Nature-inspired chemistry toward hierarchical superhydrophobic, antibacterial and biocompatible nanofibrous membranes for effective UV-shielding, self-cleaning and oil-water separation, J Hazard Mater 384 (2020) 121476. https://doi.org/10.1016/J.JHAZMAT.2019.121476.

[153] D.D. da Silva Parize, M.M. Foschini, J.E. de Oliveira, A.P. Klamczynski, G.M. Glenn, J.M. Marconcini, L.H.C. Mattoso, Solution blow spinning: Parameters optimization and effects on the properties of nanofibers from poly(lactic acid)/dimethyl carbonate solutions, J Mater Sci 51 (2016) 4627–4638. https://doi.org/10.1007/S10853-016-9778-X/TABLES/4.

[154] R. Scaffaro, E.F. Gulino, M.C. Citarrella, Biodegradable Membrane with High Porosity and Hollow Structure Obtained via Electrospinning for Oil Spill Clean-up Application, J Polym Environ 31 (2023) 3965–3981. https://doi.org/10.1007/S10924-023-02876-0/FIGURES/12.

[155] Y. Xu, P. Guo, A.T. Akono, Novel Wet Electrospinning Inside a Reactive Pre-Ceramic Gel to Yield Advanced Nanofiber-Reinforced Geopolymer Composites, Polymers (Basel) 14 (2022) 3943. https://doi.org/10.3390/POLYM14193943/S1.

[156] A. Maio, M. Gammino, E.F. Gulino, B. Megna, P. Fara, R. Scaffaro, Rapid One-Step Fabrication of Graphene Oxide-Decorated Polycaprolactone Three-Dimensional Templates for Water Treatment, ACS Appl Polym Mater 2 (2020) 4993–5005. https://doi.org/10.1021/ACSAPM.0C00852/ASSET/IMAGES/LARGE/AP0C00852_0010.JPEG.

[157] B. Zhang, C. Lu, Y. Liu, P. Zhou, Wet spun polyacrylontrile-based hollow fibers by blending with alkali lignin, Polymer (Guildf) 149 (2018) 294–304. https://doi.org/10.1016/J.POLYMER.2018.07.019.

[158] R. Scaffaro, F.E. Gulino, F. Lopresti, Structure–property relationship and controlled drug release from multiphasic electrospun carvacrol-embedded polylactic acid/polyethylene glycol and polylactic acid/polyethylene oxide nanofiber mats:, Https://Doi.Org/10.1177/1528083718801359 49 (2018) 943–966. https://doi.org/10.1177/1528083718801359.

[159] J. Doshi, D.H. Reneker, Electrospinning process and applications of electrospun fibers, J Electrostat 35 (1995) 151–160. https://doi.org/10.1016/0304-3886(95)00041-8.

[160] R. Scaffaro, G. Lo Re, S. Rigogliuso, G. Ghersi, 3D polylactide-based scaffolds for studying human hepatocarcinoma processes in vitro, Http://Www.Tandfonline.Com/Action/JournalInformation?Show=aimsScope&journalCode=tsta20#.VmBmuzZFCUk 13 (2012) 12. https://doi.org/10.1088/1468-6996/13/4/045003.

[161] Y. Zhou, G.Z. Tan, Y. Zhou, G.Z. Tan, Core–Sheath Wet Electrospinning of Nanoporous Polycaprolactone Microtubes to Mimic Fenestrated Capillaries, Macromol Mater Eng 305 (2020) 2000180. https://doi.org/10.1002/MAME.202000180.

[162] N.I. Farkas, L. Marincaș, R. Barabás, L. Bizo, A. Ilea, G.L. Turdean, M. Toșa, O. Cadar, L. Barbu-Tudoran, Preparation and Characterization of Doxycycline-Loaded Electrospun PLA/HAP Nanofibers as a Drug Delivery System, Materials 2022, Vol. 15, Page 2105 15 (2022) 2105. https://doi.org/10.3390/MA15062105.

[163] R. Ghafari, R. Scaffaro, A. Maio, E.F. Gulino, G. Lo Re, M. Jonoobi, Processing-structure-property relationships of electrospun PLA-PEO membranes reinforced with enzymatic cellulose nanofibers, Polym Test 81 (2020) 106182. https://doi.org/10.1016/j.polymertesting.2019.106182.

[164] B. Darbasizadeh, S.A. Mortazavi, F. Kobarfard, M.R. Jaafari, A. Hashemi, H. Farhadnejad, B. Feyzi-barnaji, Electrospun Doxorubicin-loaded PEO/PCL core/sheath nanofibers for chemopreventive action against breast cancer cells, J Drug Deliv Sci Technol 64 (2021) 102576. https://doi.org/10.1016/J.JDDST.2021.102576.

[165] Ş. Melda Eskitoros-Togay, Y.E. Bulbul, S. Tort, F. Demirtaş Korkmaz, F. Acartürk, N. Dilsiz, Fabrication of doxycycline-loaded electrospun PCL/PEO membranes for a potential drug delivery system, (2019). https://doi.org/10.1016/j.ijpharm.2019.04.073.

[166] S. Goettems Kuntzler, J.A. Vieira Costa, M. Greque De Morais, Development of electrospun nanofibers containing chitosan/PEO blend and phenolic compounds with antibacterial activity, (2018). https://doi.org/10.1016/j.ijbiomac.2018.05.224.

[167] S. Li, I. Molina, M. Bueno Martinez, M. Vert, Hydrolytic and enzymatic degradations of physically crosslinked hydrogels prepared from PLA/PEO/PLA triblock copolymers, J Mater Sci Mater Med 13 (2002) 81–86. https://doi.org/10.1023/A:1013651022431/METRICS.

[168] T.A.M. Valente, D.M. Silva, P.S. Gomes, M.H. Fernandes, J.D. Santos, V. Sencadas, Effect of sterilization methods on electrospun poly(lactic acid) (PLA) fiber alignment for biomedical applications, ACS Appl Mater Interfaces 8 (2016) 3241–3249. https://doi.org/10.1021/ACSAMI.5B10869/ASSET/IMAGES/ACSAMI.5B10869.SOCIAL.JPEG_V03.

[169] T. Abudula, U. Saeed, A. Memic, K. Gauthaman, M.A. Hussain, H. Al-Turaif, Electrospun cellulose Nano fibril reinforced PLA/PBS composite scaffold for vascular tissue engineering, Journal of Polymer Research 26 (2019) 1–15. https://doi.org/10.1007/S10965-019-1772-Y/FIGURES/11.

[170] L. Moradkhannejhad, M. Abdouss, N. Nikfarjam, M.H. Shahriari, V. Heidary, The effect of molecular weight and content of PEG on in vitro drug release of electrospun curcumin loaded PLA/PEG nanofibers, J Drug Deliv Sci Technol 56 (2020) 101554. https://doi.org/10.1016/J.JDDST.2020.101554.

[171] A. Mehrvarz, J. Khalil-Allafi, M. Etminanfar, S. Mahdavi, The study of morphological evolution, biocorrosion resistance, and bioactivity of pulse electrochemically deposited Hydroxyapatite/ZnO composite on NiTi superelastic alloy, Surf Coat Technol 423 (2021) 127628. https://doi.org/10.1016/J.SURFCOAT.2021.127628.

[172] B. Xiong, J. Li, C. He, X. Tang, Z. Lv, X. Li, X. Yan, Effect of pore morphology and surface roughness on wettability of porous titania films, Mater Res Express 7 (2020) 115013. https://doi.org/10.1088/2053-1591/ABC770.

[173] J. Lin, Y. Shang, B. Ding, J. Yang, J. Yu, S.S. Al-Deyab, Nanoporous polystyrene fibers for oil spill cleanup, Mar Pollut Bull 64 (2012) 347–352. https://doi.org/10.1016/J.MARPOLBUL.2011.11.002.

[174] Y. fan Deng, N. Zhang, T. Huang, Y. zhou Lei, Y. Wang, Constructing tubular/porous structures toward highly efficient oil/water separation in electrospun stereocomplex polylactide fibers via coaxial electrospinning technology, Appl Surf Sci 573 (2022) 151619. https://doi.org/10.1016/J.APSUSC.2021.151619.

[175] S. Mantripragada, S. Gbewonyo, D. Deng, L. Zhang, Oil absorption capability of electrospun carbon nanofibrous membranes having porous and hollow nanostructures, Mater Lett 262 (2020) 127069. https://doi.org/10.1016/J.MATLET.2019.127069.

[176] J.W. Liang, G. Prasad, S.C. Wang, J.L. Wu, S.G. Lu, Enhancement of the Oil Absorption Capacity of Poly(Lactic Acid) Nano Porous Fibrous Membranes Derived via a Facile Electrospinning Method, Applied Sciences 2019, Vol. 9, Page 1014 9 (2019) 1014. https://doi.org/10.3390/APP9051014.

[177] J.C.C. Yeo, D. Kai, C.P. Teng, E.M.J.R. Lin, B.H. Tan, Z. Li, C. He, Highly Washable and Reusable Green Nanofibrous Sorbent with Superoleophilicity, Biodegradability, and Mechanical Robustness, ACS Appl Polym Mater 2 (2020) 4825–4835. https://doi.org/10.1021/ACSAPM.0C00786.

[178] B. Ye, C. Jia, Z. Li, L. Li, Q. Zhao, J. Wang, H. Wu, Solution-blow spun PLA/SiO2 nanofiber membranes toward high efficiency oil/water separation, J Appl Polym Sci 137 (2020) 49103. https://doi.org/10.1002/APP.49103.

[179] G. Zhang, P. Wang, X. Zhang, C. Xiang, L. Li, Preparation of hierarchically structured PCL superhydrophobic membrane via alternate electrospinning/electrospraying techniques, J Polym Sci B Polym Phys 57 (2019) 421–430. https://doi.org/10.1002/POLB.24795.

[180] J. Gao, X. Song, X. Huang, L. Wang, B. Li, H. Xue, Facile preparation of polymer microspheres and fibers with a hollow core and porous shell for oil adsorption and oil/water separation, Appl Surf Sci 439 (2018) 394–404. https://doi.org/10.1016/J.APSUSC.2018.01.013.

[181] A.-Y. Jiang, Z.-J. Pan, Cross-sectional Porosity and Oil Sorption of PLA Nanofibers with Hollow and Lotus Root-like Structures, Journal of Fiber Bioengineering and Informatics 13 (2020) 51–60. https://doi.org/10.3993/jfbim00335.

[182] J.L. Viana, T. França, C. Cena, Solution Blow Spinning Poly(vinyl alcohol) Sub-microfibers Produced from Different Solvents, Orbital: The Electronic Journal of Chemistry 12 (2020) 1–6. https://doi.org/10.17807/ORBITAL.V12I1.1169.

[183] J.E. Domínguez, A. Kasiri, J. González-Benito, Wettability behavior of solution blow spun polysulfone by controlling morphology, J Appl Polym Sci 138 (2021) 50200. https://doi.org/10.1002/APP.50200.

[184] M.R.V. Fontes, M.P. da Rosa, L.M. Fonseca, P.H. Beck, E. da Rosa Zavareze, A.R.G. Dias, Thermal stability, hydrophobicity and antioxidant potential of ultrafine poly (lactic acid)/rice husk lignin fibers, Brazilian Journal of Chemical Engineering 38 (2021) 133–144. https://doi.org/10.1007/S43153-020-00083-1/FIGURES/5.

[185] H. Ding, W. Yang, W. Yu, T. Liu, H. Wang, P. Xu, L. Lin, P. Ma, High hydrophobic poly(lactic acid) foams impregnating one-step Si–F modified lignin nanoparticles for oil/organic solvents absorption, Composites Communications 25 (2021) 100730. https://doi.org/10.1016/J.COCO.2021.100730.

[186] M. Mikriukova, J. Lahti, J. Kuusipalo, Permeation of vegetable oils and slippery properties of extrusion coated paperboard, Packaging Technology and Science 35 (2022) 445–458. https://doi.org/10.1002/PTS.2642.

[187] E.D. Revellame, D.L. Fortela, W. Sharp, R. Hernandez, M.E. Zappi, Adsorption kinetic modeling using pseudo-first order and pseudo-second order rate laws: A review, Clean Eng Technol 1 (2020) 100032. https://doi.org/10.1016/J.CLET.2020.100032.

[188] Y. Wang, Z. Liu, X. Wei, K. Liu, J. Wang, J. Hu, J. Lin, An integrated strategy for achieving oil-in-water separation, removal, and anti-oil/dye/bacteria-fouling, Chemical Engineering Journal 413 (2021) 127493. https://doi.org/10.1016/J.CEJ.2020.127493.

[189] T. Wang, W. Wang, C. Hu, J. Zheng, B. Liu, Z. Zhu, Mechanically durable, recyclable polyvinyl alcohol/lignin-based aerogel for efficient oil/water separation and solar-powered removal of high-viscosity oil, Ind Crops Prod 219 (2024) 119131. https://doi.org/10.1016/J.INDCROP.2024.119131.

[190] R. Scaffaro, M.C. Citarrella, E.F. Gulino, M. Morreale, Hedysarum coronarium-Based Green Composites Prepared by Compression Molding and Fused Deposition Modeling, Materials 2022, Vol. 15, Page 465 15 (2022) 465. https://doi.org/10.3390/MA15020465.

[191] G. Cicala, D. Giordano, C. Tosto, G. Filippone, A. Recca, I. Blanco, Polylactide (PLA) Filaments a Biobased Solution for Additive Manufacturing: Correlating Rheology and Thermomechanical Properties with Printing Quality, Materials 2018, Vol. 11, Page 1191 11 (2018) 1191. https://doi.org/10.3390/MA11071191.

[192] N.R. Rajendran Royan, J.S. Leong, W.N. Chan, J.R. Tan, Z.S.B. Shamsuddin, Current State and Challenges of Natural Fibre-Reinforced Polymer Composites as Feeder in FDM-Based 3D Printing, Polymers 2021, Vol. 13, Page 2289 13 (2021) 2289. https://doi.org/10.3390/POLYM13142289.

[193] P. Wang, B. Zou, S. Ding, C. Huang, Z. Shi, Y. Ma, P. Yao, Preparation of short CF/GF reinforced PEEK composite filaments and their comprehensive properties evaluation for FDM-3D printing, Compos B Eng 198 (2020) 108175. https://doi.org/10.1016/J.COMPOSITESB.2020.108175.

[194] R. Scaffaro, E.F. Gulino, M.C. Citarrella, A. Maio, Green Composites Based on Hedysarum coronarium with Outstanding FDM Printability and Mechanical Performance, Polymers 2022, Vol. 14, Page 1198 14 (2022) 1198. https://doi.org/10.3390/POLYM14061198.

[195] I. Živković, C. Fragassa, A. Pavlović, T. Brugo, Influence of moisture absorption on the impact properties of flax, basalt and hybrid flax/basalt fiber reinforced green composites, Compos B Eng 111 (2017) 148–164. https://doi.org/10.1016/J.COMPOSITESB.2016.12.018.

[196] A.H. Hassanin, T. Hamouda, Z. Candan, A. Kilic, T. Akbulut, Developing high-performance hybrid green composites, Compos B Eng 92 (2016) 384–394. https://doi.org/10.1016/J.COMPOSITESB.2016.02.051.

[197] R. Scaffaro, A. Maio, Integrated ternary bionanocomposites with superior mechanical performance via the synergistic role of graphene and plasma treated carbon nanotubes, Compos B Eng (2019). https://doi.org/10.1016/j.compositesb.2019.03.076.

[198] R. Scaffaro, M.C. Citarrella, M. Morreale, Green Composites Based on Mater-Bi® and Solanum lycopersicum Plant Waste for 3D Printing Applications, Polymers 2023, Vol. 15, Page 325 15 (2023) 325. https://doi.org/10.3390/POLYM15020325.

[199] Y. Tao, M. Liu, W. Han, P. Li, Waste office paper filled polylactic acid composite filaments for 3D printing, Compos B Eng 221 (2021) 108998. https://doi.org/10.1016/J.COMPOSITESB.2021.108998.

[200] H. Singh, N.K. Batra, I. Dikshit, Development of new hybrid jute/carbon/fishbone reinforced polymer composite, Mater Today Proc 38 (2021) 29–33. https://doi.org/10.1016/J.MATPR.2020.05.520.

[201] J.C.H. Affdl, J.L. Kardos, The Halpin-Tsai equations: A review, Polym Eng Sci 16 (1976) 344–352. https://doi.org/10.1002/PEN.760160512.

[202] R. Scaffaro, A. Maio, E.F. Gulino, B. Megna, Structure-property relationship of PLA-Opuntia Ficus Indica biocomposites, Compos B Eng 167 (2019) 199–206. https://doi.org/10.1016/J.COMPOSITESB.2018.12.025.

[203] R. Scaffaro, M.C. Citarrella, E.F. Gulino, Opuntia Ficus Indica based green composites for NPK fertilizer controlled release produced by compression molding and fused deposition modeling, Compos Part A Appl Sci Manuf 159 (2022) 107030. https://doi.org/10.1016/J.COMPOSITESA.2022.107030.

[204] R. Scaffaro, A. Maio, E.F. Gulino, G. Alaimo, M. Morreale, Green composites based on pla and agricultural or marine waste prepared by fdm, Polymers (Basel) 13 (2021) 1–17. https://doi.org/10.3390/polym13091361.

[205] K.L. Alvarez C., R.F. Lagos C., M. Aizpun, Investigating the influence of infill percentage on the mechanical properties of fused deposition modelled ABS parts, Ingenieria e Investigacion 36 (2016) 110–116. https://doi.org/10.15446/ing.investig.v36n3.56610.

[206] S. Mahmood, A.J. Qureshi, K.L. Goh, D. Talamona, Tensile strength of partially filled FFF printed parts: Experimental results, Rapid Prototyp J 23 (2017) 122–128. https://doi.org/10.1108/RPJ-08-2015-0115.

[207] H.K. Dave, N.H. Patadiya, A.R. Prajapati, S.R. Rajpurohit, Effect of infill pattern and infill density at varying part orientation on tensile properties of fused deposition modeling-printed poly-lactic acid part, Proc Inst Mech Eng C J Mech Eng Sci 235 (2021) 1811–1827. https://doi.org/10.1177/0954406219856383.

[208] A. Haryńska, I. Carayon, P. Kosmela, K. Szeliski, M. Łapiński, M. Pokrywczyńska, J. Kucińska-Lipka, H. Janik, A comprehensive evaluation of flexible FDM/FFF 3D printing filament as a potential material in medical application, Eur Polym J 138 (2020) 109958. https://doi.org/10.1016/j.eurpolymj.2020.109958.

[209] U. Modi, S. Prakash, Wettability of 3D printed polylactic acid (PLA) parts, AIP Conf Proc 2148 (2019). https://doi.org/10.1063/1.5123974.

[210] A. Mehrvarz, J. Khalil-Allafi, A.K. Khosrowshahi, Biocompatibility and antibacterial behavior of electrochemically deposited Hydroxyapatite/ZnO porous nanocomposite on NiTi biomedical alloy, Ceram Int (2022). https://doi.org/10.1016/J.CERAMINT.2022.02.183.

[211] A. le Duigou, M. Castro, R. Bevan, N. Martin, 3D printing of wood fibre biocomposites: From mechanical to actuation functionality, Mater Des 96 (2016) 106–114. https://doi.org/10.1016/j.matdes.2016.02.018.

[212] K. Lubkowski, A. Smorowska, M. Sawicka, E. Wróblewska, A. Dzienisz, M. Kowalska, M. Sadłowski, Ethylcellulose as a coating material in controlled-release fertilizers, Polish Journal of Chemical Technology 21 (2019) 52–58. https://doi.org/10.2478/PJCT-2019-0010.

[213] L.L. Messa, R. Faez, Spray-dried chitosan/nanocellulose microparticles: synergistic effects for the sustained release of NPK fertilizer, Cellulose 27 (2020) 10077–10093. https://doi.org/10.1007/S10570-020-03482-2/FIGURES/9.

[214] A. Olad, H. Zebhi, D. Salari, A. Mirmohseni, A. Reyhani Tabar, Slow-release NPK fertilizer encapsulated by carboxymethyl cellulose-based nanocomposite with the function of water retention in soil, Materials Science and Engineering: C 90 (2018) 333–340. https://doi.org/10.1016/J.MSEC.2018.04.083.

[215] M. Baki, J. Abedi-Koupai, Preparation and characterization of a superabsorbent slow-release fertilizer with sodium alginate and biochar, J Appl Polym Sci 135 (2018) 45966. https://doi.org/10.1002/APP.45966.

[216] G. Rozo, L. Bohorques, J. Santamaría, Controlled release fertilizer encapsulated by a κ-carrageenan hydrogel, Polimeros 29 (2019). https://doi.org/10.1590/0104-1428.02719.

[217] J. de GUZMAN, K. dela Peña, J. Ytac Dorothy, T. Tumolva, Synthesis and Characterization of Ionically-Crosslinked κ- Carrageenan/Sodium Alginate/Carboxymethyl Cellulose Hydrogel Blends for Soil Water Retention and Fertilizer Release, Solid State Phenomena 304 (2020) 59–65. https://doi.org/10.4028/WWW.SCIENTIFIC.NET/SSP.304.59.

[218] P. Costa, J.M. Sousa Lobo, Modeling and comparison of dissolution profiles, European Journal of Pharmaceutical Sciences 13 (2001) 123–133. https://doi.org/https://doi.org/10.1016/S0928-0987(01)00095-1.

[219] I.Y. Wu, S. Bala, N. Škalko-Basnet, M.P. di Cagno, Interpreting non-linear drug diffusion data: Utilizing Korsmeyer-Peppas model to study drug release from liposomes, European Journal of Pharmaceutical Sciences 138 (2019) 105026. https://doi.org/10.1016/j.ejps.2019.105026.

[220] S. Noppakundilograt, N. Pheatcharat, S. Kiatkamjornwong, Multilayer-coated NPK compound fertilizer hydrogel with controlled nutrient release and water absorbency, J Appl Polym Sci 132 (2015). https://doi.org/10.1002/app.41249.

[221] Y.C. Chen, Y.H. Chen, Thermo and pH-responsive methylcellulose and hydroxypropyl hydrogels containing K2SO4 for water retention and a controlled-release water-soluble fertilizer, Science of the Total Environment 655 (2019) 958–967. https://doi.org/10.1016/j.scitotenv.2018.11.264.

[222] R. Scaffaro, M. Morreale, G. lo Re, F.P. la Mantia, Degradation of Mater-Bi®/wood flour biocomposites in active sewage sludge, Polym Degrad Stab 94 (2009) 1220–1229. https://doi.org/10.1016/j.polymdegradstab.2009.04.028.

[223] R. Scaffaro, E.F. Gulino, M.C. Citarrella, Multifunctional 3D-printed composites based on biopolymeric matrices and tomato plant (Solanum lycopersicum) waste for contextual fertilizer release and Cu(II) ions removal, Adv Compos Hybrid Mater 7 (2024) 1–16. https://doi.org/10.1007/S42114-024-00908-4/FIGURES/9.

[224] J.M. de O. Cremonezzi, G.M. Pinto, R. Mincheva, R.J.E. Andrade, J.M. Raquez, G.J.M. Fechine, The micromechanics of graphene oxide and molybdenum disulfide in thermoplastic nanocomposites and the impact to the polymer-filler interphase, Compos Sci Technol 243 (2023). https://doi.org/10.1016/j.compscitech.2023.110236.

[225] K. Baek, H. Shin, M. Cho, Multiscale modeling of mechanical behaviors of Nano-SiC/epoxy nanocomposites with modified interphase model: Effect of nanoparticle clustering, Compos Sci Technol 203 (2021). https://doi.org/10.1016/j.compscitech.2020.108572.

[226] R. Scaffaro, M.C. Citarrella, A. Catania, L. Settanni, Green composites based on biodegradable polymers and anchovy (Engraulis Encrasicolus) waste suitable for 3D printing applications, Compos Sci Technol 230 (2022) 109768. https://doi.org/10.1016/J.COMPSCITECH.2022.109768.

[227] Z. Liu, Q. Lei, S. Xing, Mechanical characteristics of wood, ceramic, metal and carbon fiber-based PLA composites fabricated by FDM, Journal of Materials Research and Technology 8 (2019) 3743–3753. https://doi.org/10.1016/j.jmrt.2019.06.034.

[228] J. Kiendl, C. Gao, Controlling toughness and strength of FDM 3D-printed PLA components through the raster layup, Compos B Eng 180 (2020) 107562. https://doi.org/10.1016/J.COMPOSITESB.2019.107562.

[229] A.M. Borrero-López, C. Valencia-Barragán, E.C. Triviño, A. Tenorio-Alfonso, C. Delgado-Sánchez, C. Villegas, S. Martínez, A. Torres, A. Rojas, R. Araya, A. Guarda, M.J. Galotto, Processing, Characterization and Disintegration Properties of Biopolymers Based on Mater-Bi® and Ellagic Acid/Chitosan Coating, Polymers 2023, Vol. 15, Page 1548 15 (2023) 1548. https://doi.org/10.3390/POLYM15061548.

[230] J. Andrzejewski, J. Cheng, A. Anstey, A.K. Mohanty, M. Misra, Development of Toughened Blends of Poly(lactic acid) and Poly(butylene adipate- co-terephthalate) for 3D Printing Applications: Compatibilization Methods and Material Performance Evaluation, ACS Sustain Chem Eng 8 (2020) 6576–6589. https://doi.org/10.1021/ACSSUSCHEMENG.9B04925/ASSET/IMAGES/LARGE/SC9B04925_0008.JPEG.

[231] Y. Tang, A. Varyambath, Y. Ding, B. Chen, X. Huang, Y. Zhang, D. Yu, I. Kim, W. Song, Porous organic polymers for drug delivery: hierarchical pore structures, variable morphologies, and biological properties, Biomater. Sci. 10 (2022) 5369–5390. https://doi.org/10.1039/D2BM00719C.

[232] H.L. Boudjema, H. Bendaikha, U. Maschke, Green composites based on Atriplex halimus fibers and PLA matrix, Journal of Polymer Engineering 40 (2020) 693–702. https://doi.org/10.1515/polyeng-2020-0068.

[233] J. de L. Souza, C.G. Chiaregato, R. Faez, Green Composite Based on PHB and Montmorillonite for KNO3 and NPK Delivery System, J Polym Environ 26 (2018) 670–679. https://doi.org/10.1007/s10924-017-0979-4.

[234] A. El Gharrak, Y. Essamlali, O. Amadine, S. Aboulhrouz, A. Hafnaoui, H. Ghalfi, M. Zahouily, Tunable physicochemical properties of lignin and rapeseed oil-based polyurethane coatings with tailored release property of coated NPK fertilizer, Prog Org Coat 170 (2022) 106982. https://doi.org/10.1016/J.PORGCOAT.2022.106982.

[235] G.B. Ramírez-Rodríguez, G. Dal Sasso, F.J. Carmona, C. Miguel-Rojas, A. Pérez-De-Luque, N. Masciocchi, A. Guagliardi, J.M. Delgado-López, Engineering Biomimetic Calcium Phosphate Nanoparticles: A Green Synthesis of Slow-Release Multinutrient (NPK) Nanofertilizers, ACS Appl Bio Mater 3 (2020) 1344–1353. https://doi.org/10.1021/ACSABM.9B00937/ASSET/IMAGES/LARGE/MT9B00937_0008.JPEG.

[236] S.K. Das, G.K. Ghosh, Developing biochar-based slow-release N-P-K fertilizer for controlled nutrient release and its impact on soil health and yield, Biomass Convers Biorefin 1 (2021) 1–13. https://doi.org/10.1007/S13399-021-02069-6/TABLES/5.

[237] F.G. Torres, D.C. Dioses-Salinas, C.I. Pizarro-Ortega, G.E. De-la-Torre, Sorption of chemical contaminants on degradable and non-degradable microplastics: Recent progress and research trends, Science of The Total Environment 757 (2021) 143875. https://doi.org/10.1016/J.SCITOTENV.2020.143875.

[238] N. Fijoł, A. Aguilar-Sánchez, M.X. Ruiz-Caldas, J. Redlinger-Pohn, A. Mautner, A.P. Mathew, 3D printed polylactic acid (PLA) filters reinforced with polysaccharide nanofibers for metal ions capture and microplastics separation from water, Chemical Engineering Journal 457 (2023) 141153. https://doi.org/10.1016/J.CEJ.2022.141153.

[239] T. Zhou, M. Zhao, X. Zhao, Y. Guo, Y. Zhao, Simultaneous remediation and fertility improvement of heavy metals contaminated soil by a novel composite hydrogel synthesized from food waste, Chemosphere 275 (2021) 129984. https://doi.org/10.1016/J.CHEMOSPHERE.2021.129984.

[240] R. Jiménez-Ballesta, S. Bravo, J.A. Amorós, C. Pérez-de-los-Reyes, J. García-Pradas, M. Sanchez, F.J. García-Navarro, Soil and Leaf Mineral Element Contents in Mediterranean Vineyards: Bioaccumulation and Potential Soil Pollution, Water Air Soil Pollut 233 (2022) 1–13. https://doi.org/10.1007/S11270-021-05485-6/FIGURES/2.

[241] A.M. Grumezescu, A.M. Holban, Microbial contamination and food degradation, (n.d.) 487.

[242] C.P. Gerba, I.L. Pepper, Microbial Contaminants, Environmental and Pollution Science (2019) 191–217. https://doi.org/10.1016/B978-0-12-814719-1.00013-6.

[243] L.L. Fu, J.R. Li, Microbial Source Tracking: A Tool for Identifying Sources of Microbial Contamination in the Food Chain, Https://Doi.Org/10.1080/10408398.2011.605231 54 (2013) 699–707. https://doi.org/10.1080/10408398.2011.605231.

[244] J. Toppe, S. Albrektsen, B. Hope, A. Aksnes, Chemical composition, mineral content and amino acid and lipid profiles in bones from various fish species, Comp Biochem Physiol B Biochem Mol Biol 146 (2007) 395–401. https://doi.org/10.1016/J.CBPB.2006.11.020.

[245] T. Yin, H. Du, J. Zhang, S. Xiong, Preparation and Characterization of Ultrafine Fish Bone Powder, Http://Dx.Doi.Org/10.1080/10498850.2015.1010128 25 (2016) 1045–1055. https://doi.org/10.1080/10498850.2015.1010128.

[246] B. Kizilkaya, A.A. Tekinay, Y. Dilgin, Adsorption and removal of Cu (II) ions from aqueous solution using pretreated fish bones, Desalination 264 (2010) 37–47. https://doi.org/10.1016/J.DESAL.2010.06.076.

[247] B. Wang, B. Adhikari, M. Mathesh, W. Yang, C.J. Barrow, Anchovy oil microcapsule powders prepared using two-step complex coacervation between gelatin and sodium hexametaphosphate followed by spray drying, Powder Technol 358 (2019) 68–78. https://doi.org/10.1016/J.POWTEC.2018.07.034.

[248] M.C. Mistretta, L. Botta, R. Arrigo, F. Leto, G. Malucelli, F.P. la Mantia, Bionanocomposite Blown Films: Insights on the Rheological and Mechanical Behavior, Polymers 2021, Vol. 13, Page 1167 13 (2021) 1167. https://doi.org/10.3390/POLYM13071167.

[249] I.A. Adeoti, K. Hawboldt, M.R. Santos, Thermal and flow properties of fish oil blends with bunker fuel oil, Fuel 158 (2015) 641–649. https://doi.org/10.1016/J.FUEL.2015.06.019.

[250] J. Huang, S. Sathivel, Thermal and rheological properties and the effects of temperature on the viscosity and oxidation rate of unpurified salmon oil, J Food Eng 89 (2008) 105–111. https://doi.org/10.1016/J.JFOODENG.2008.03.007.

[251] P. Jayasinghe, I. Adeoti, K. Hawboldt, A Study of Process Optimization of Extraction of Oil from Fish Waste for Use as A Low-Grade Fuel, J Am Oil Chem Soc 90 (2013) 1903–1915. https://doi.org/10.1007/S11746-013-2321-1.

[252] X. Xiao, V.S. Chevali, P. Song, D. He, H. Wang, Polylactide/hemp hurd biocomposites as sustainable 3D printing feedstock, Compos Sci Technol 184 (2019) 107887. https://doi.org/10.1016/J.COMPSCITECH.2019.107887.

[253] Y. Tao, L. Pan, D. Liu, P. Li, A case study: Mechanical modeling optimization of cellular structure fabricated using wood flour-filled polylactic acid composites with fused deposition modeling, Compos Struct 216 (2019) 360–365. https://doi.org/10.1016/J.COMPSTRUCT.2019.03.010.

[254] W. Wu, P. Geng, G. Li, D. Zhao, H. Zhang, J. Zhao, Influence of Layer Thickness and Raster Angle on the Mechanical Properties of 3D-Printed PEEK and a Comparative Mechanical Study between PEEK and ABS, Materials 2015, Vol. 8, Pages 5834-5846 8 (2015) 5834–5846. https://doi.org/10.3390/MA8095271.

[255] J. Allum, A. Gleadall, V. v. Silberschmidt, Fracture of 3D-printed polymers: Crucial role of filament-scale geometric features, Eng Fract Mech 224 (2020) 106818. https://doi.org/10.1016/J.ENGFRACMECH.2019.106818.

[256] B. Akhoundi, A.H. Behravesh, Effect of Filling Pattern on the Tensile and Flexural Mechanical Properties of FDM 3D Printed Products, Exp Mech 59 (2019) 883–897. https://doi.org/10.1007/S11340-018-00467-Y/FIGURES/20.

[257] K.B. Adhikary, S. Pang, M.P. Staiger, Dimensional stability and mechanical behaviour of wood–plastic composites based on recycled and virgin high-density polyethylene (HDPE), Compos B Eng 39 (2008) 807–815. https://doi.org/10.1016/J.COMPOSITESB.2007.10.005.

[258] C.M.R. Almeida, A.P. Mucha, M.T.S.D. Vasconcelos, Influence of the sea rush Juncus maritimus on metal concentration and speciation in estuarine sediment colonized by the plant, Environ Sci Technol 38 (2004) 3112–3118. https://doi.org/10.1021/ES049932J/ASSET/IMAGES/LARGE/ES049932JF00003.JPEG.

[259] C. Santín, M. González-Pérez, X.L. Otero, P. Vidal-Torrado, F. Macías, M.Á. Álvarez, Characterization of humic substances in salt marsh soils under sea rush (Juncus maritimus), Estuar Coast Shelf Sci 79 (2008) 541–548. https://doi.org/10.1016/J.ECSS.2008.05.007.

[260] A. Rosato, A. Romano, G. Totaro, A. Celli, F. Fava, G. Zanaroli, L. Sisti, Enzymatic Degradation of the Most Common Aliphatic Bio-Polyesters and Evaluation of the Mechanisms Involved: An Extended Study, Polymers (Basel) 14 (2022) 1850. https://doi.org/10.3390/POLYM14091850/S1.

[261] R. Muthuraj, M. Misra, A.K. Mohanty, Hydrolytic degradation of biodegradable polyesters under simulated environmental conditions, J Appl Polym Sci 132 (2015) 42189. https://doi.org/10.1002/APP.42189.

[262] Y. Wang, R.J. van Putten, A. Tietema, J.R. Parsons, G.J.M. Gruter, Polyester biodegradability: importance and potential for optimisation, Green Chemistry 26 (2024) 3698–3716. https://doi.org/10.1039/D3GC04489K.